UNIVERSITAT POLITÈCNICA DE VALÈNCIA

Departamento de Máquinas y Motores Térmicos

DOCTORAL THESIS:

Contribution to the Experimental Characterization and 1-D Modelling of Turbochargers for IC Engines

---

by

Miguel Ángel Reyes Belmonte

in fulfillement of the requirements for the degree of

Doctor of Philosophy
(Mechanical Engineering)

Supervisor: Prof. Dr. Francisco José Arnau Martínez

Valencia, 2013

DOCTORAL THESIS

Contribution to the Experimental Characterization and 1-D Modelling of Turbochargers for IC Engines

AUTHORS

Written by: Dipl. Ing. Miguel Ángel Reyes Belmonte
Supervised by: Prof. Dr. Francisco José Arnau Martínez

DEFENSE COMMITTEE

Chairman: Prof. Dr. José Ramón Serrano Cruz
Universidad Politécnica de Valencia
Members: Prof. Dr. Guillermo Paniagua
Von Karman Institute
Prof. Dr. Juan José Hernández Adrover
Universidad de Castilla la Mancha

DISSERTATION READERS

Prof. Dr. Angelo Onorati
Politecnico di Milano
Prof. Dr. Guillermo Paniagua
Von Karman Institute
Prof. Dr. Magín Lapuerta Amigo
Universidad de Castilla la Mancha

Abstract

At the end of the 19^{th} Century, the invention of the Internal Combustion Engine (ICE) marked the beginning of our current lifestyle. Soon after the first ICE patent, the importance of increasing air pressure upstream the engine cylinders was revealed. At the beginning of the 20^{th} Century turbo-machinery developments (which had started time before), met the ICE what represented the beginning of turbocharged engines. Since that time, the working principle has not fundamentally changed. Nevertheless, stringent emissions standards and oil depletion have motivated engine developments; among them, turbocharging coupled with downsized engines has emerged as the most feasible way to increase specific power while reducing fuel consumption.

Turbocharging has been traditionally a complex problem due to the high rotational speeds, high temperature differences between working fluids (exhaust gases, compressed air, lubricating oil and cooling liquid) and pulsating flow conditions. To improve current computational models, a new procedure for turbochargers characterization and modelling has been presented in this Thesis. That model divides turbocharger modelling complex problem into several sub-models for each of the non-recurring phenomenon; i.e. heat transfer phenomena, friction losses and acoustic non-linear models for compressor and turbine. A series of ad-hoc experiments have been designed to aid identifying and isolating each phenomenon from the others. Each chapter of this Thesis has been dedicated to analyse that complex problem proposing different sub-models.

First of all, an exhaustive literature review of the existing turbocharger models has been performed. Then a turbocharger 1-D internal Heat Transfer Model (HTM) has been developed. Later geometrical models for compressor and turbine have been proposed to account for acoustic effects. A physically based methodology to extrapolate turbine performance maps has been developed too. That model improves turbocharged engine prediction since turbine instantaneous behaviour moves far from the narrow operative range provided in manufacturer maps. Once each separated model has been developed and validated, a series of tests considering all phenomena combined have been performed. Those tests have been designed to check model accuracy under likely operative conditions.

The main contributions of this Thesis are the development of a 1-D heat transfer model to account for internal heat fluxes of automotive turbochargers; the development of a physically-based turbine extrapolation methodology; the several tests campaigns that have been necessary to study each phenomenon isolated from others and the integration of experiments and models in a comprehensive characterization procedure designed to provide 1-D predictive turbocharger models for ICE calculation.

Resumen

Al final del Siglo XIX, la invención del Motor de Combustión Interna Alternativo (MCIA) marcó el principio del estilo actual de vida. Poco después de la primera patente del MCIA, se demostró la importancia de aumentar la presión del aire antes del cilindro. A comienzos del Siglo XX los desarrollos en turbomaquinaria se unieron al MCIA lo que representó el comienzo de la turbosobrealimentación de motores. Desde ese momento, el principio de funcionamiento prácticamente no ha cambiado. Sin embargo, las exigentes normativas medioambientales y la disminución en las reservas de petroleo han motivado el desarrollo de nuevos conceptos; entre ellos, la turbosobrealimentación unida a motores *downsized* ha emergido como la alternativa más factible para incrementar la potencia específica del motor y la reducción en consumo.

La turbosobrealimentación ha sido tradicionalmente un problema complejo debido al alto regimen de giro, las elevadas diferencias de temperatura entre los fluidos de trabajo (gases de escape, aire, aceite de lubricación y refrigerante) y las condiciones de flujo pulsante. Con el objetivo de mejorar los modelos actuales de simlación, un nuevo procedimiento para la caracterización de turbogrupos y su modelado ha sido presentado en esta Tesis. Este modelo divide el problema complejo de modelado en turbogrupos en varios submodelos para cada uno de los fenomenos existentes; i.e. transmisión de calor, pérdidas por fricción y modelos acústicos no lineales para el compresor y la turbina. Una serie de experimentos *ad-hoc* ha sido diseñada para ayudar a identificar y aislar cada fenomeno del resto. Cada capítulo de esta Tesis ha sido dedicado a analizar este complejo problema proponiendo diferentes sub-modelos.

Primero de todo una exhaustiva revisión bibliográfica de los modelos existentes de turbogrupos ha sido llevada a cabo. Luego un modelo 1-D de transmisión de calor interna (HTM) ha sido desarrollado. Después modelos geométricos para el compresor y la turbina han sido propuestos para tener en cuenta efectos acústicos. Una metodología física para extrapolar los mapas de funcionamiento de la turbina ha sido desarrollada también. Este modelo mejora el la predicción de motores sobrealimentados ya que el funcionamiento instantáneo de la turbina se mueve lejos del estrecho rango proporcionado en los mapas del fabricante. Una vez que cada modelo independiente ha sido desarrollado y validado, una serie de ensayos considerando todos los fenómenos combinados ha sido llevada a cabo. Estos tests han sido diseñados para chequear la precisión del modelo bajo condiciones realistas de operación.

Las principales contribuciones de esta Tesis son el desarrollo de un modelo 1-D de transmisión de calor para tener en cuenta los flujos de calor internos en turbogrupos de automoción; el desarrollo de una metodología física para la extrapolación de mapas de turbina; el desarrollo de diversas campañas experimentales necesarias para estudiar cada fenómeno de forma aislada y la integración de experimentos y modelos en un procedimiento diseñado para proporcionar modelos 1-D de turbogrupo para el cálculo de motores.

Resum

A la fi del Segle XIX, l'invenció del Motor de Combustió Interna Alternatiu (MCIA) va marcar l'inici de l'actual estil de vida. Poc després de la primera patent del MCIA, la importància d'augmentar la pressió d'aire abans del cilindre va ser demostrada. A començaments del Segle XX els desenvolupaments en turbomaquinària, es van unir al MCIA el que va representar el començament de la turbosobrealimentació dels motors. Des d'aquest moment, el principi de funcionament pràcticament no ha canviat gens. No obstant, les exigents normatives mediambientals i la disminució en les reserves petroli han motivat el desenvolupament de nous conceptes de motor; entre ells, la turbosobrealimentació unida als motors *downsized* ha emergit com l'alternativa més factible per incrementar la potència específica del motor i la reducció del consum.

La turbosobrealimentació ha sigut tradicionalment un problema complexe degut a l'alt règim de gir del turbogrup, les elevades diferencies de temperatura entre els fluids de trebal (gassos, aire, oli de lubricació i liquid refrigerant) i les condicions de flux polsant. A fi de millorar els models actuals de simulació, un nou procediment per a caracteriztzar i modelar els turbogrups ha sigut presentat en aquesta Tesis. Aquest model divideix el complex problema de modelat en turbogrups en diversos sub-models per a cadascun dels fenòmens existents; i.e. transmisió de calor, perdugues per fricció i models acustics no lineals per al compressor i la turbina. Una sèrie d'experiments *ad-hoc* ha sigut dissenyada per ajudar a identificar i aïllar cada fenomen. Cada capítol d'aquesta Tesis ha sigut dedicat a analitzar el complex problema proposant diferent sub-models.

Primer de tot una exhaustiva revisió bibliogràfica del models existents de turbogrups ha sigut realitzada. Després un model 1-D de transmissió de calor interna (HTM) ha sigut desenvolupat. Després models geomètrics per al compressor i la turbina han sigut proposats per tindre en compte els efectes acústics. Una metodologia física per extrapolar els mapes de funcionament de la turbina ha sigut desenvolupat també. Aquest model millora la predicció de motors turbosobrealimentats ja que el funcionament instantani de la turbina es mou lluny de l'estret rang proporcionat als mapes del fabricant. Una vegada que cada model independent ha sigut desenvolupat i validat, una sèrie d'assajos considerant tots els fenòmens de manera combinada ha sigut dut a terme. Aquests tests han sigut dissenyat per comprovar la precisió del model baix condicions realistes d'operació.

Les principals contribucions d'aquesta Tesis son el desenvolupament d'un model 1-D de transmissió de calor per als fluxos de calor interns en turbogrups d'automoció; el desenvolupament d'una metodologia física per a l'extrapolació de mapes de turbina; el desenvolupament de diverses campanyes experimentals necessàries per estudiar cada fenomen de forma aïllada i l'integració dels experiments i models en un procediment disenyat per a proporcionar models 1-D de turbogrup per al càlcul de motors.

Acknowledgements

First of all I would like to thank CMT-Motores Térmicos for giving me the opportunity of being part of such a prestigious research team. I extend those sincere acknowledgements to the whole group from technicians, researchers, students, lecturers, professors and staff administration. I especially would like to thank my tutor Francisco José Arnau for monitoring the research work presented in this Thesis. And also Professor José Ramón Serrano and Pablo Olmeda, without their continuous help the work presented here had not been possible. I would also like to thank technicians Valentín Ucedo, Miguel Ortiz and José "the lathe operator" for their worthy assistance on the machining and for their dedicated work controlling turbocharger test rigs.

There is a long list of students that have collaborated keeping going this work and other research while doing their final project degree here. I would like to gratefully thank them for their friendship during these years. They are *Guillermo, Vincenzo, Angel, Daniel, Edu, Álvaro, Paula, Víctor, Ramón and Nicolás*. There is even a bigger list of friends and work-mates that I have had the pleasure to work with and share both the good moments and the busy ones. They are the students *Paloma, Adrián, José Vicente and Carles* and the international PhD students team formed by *Olivier Varnier, Ricardo Lang, Oscar García, Emanuelle Angiolini, Artem Dombrovsky and Richard Burke (research fellow from Bath University)*. I would also like to thank Luis Miguel García-Cuevas for his worthy computing assistance and his tutor Andrés Tiseira for our experiments on the wind tunnel.

Eventually I would like to thank my parents and my sister for their infinite support and affection during these years.

"If we knew what it was we were doing,
it would not be called research,
would it?"

Albert Einstein

"Research is what I'm doing when
I don't know what I'm doing."

Wernher von Braun

A mis padres, Miguel y María
y a mi hermana Mari Carmen

Contents

Nomenclature

Acronyms

0-D	Zero-Dimensional
1-D	One-Dimensional
3-D	Tri-Dimensional
BP	Back-Plate
CAD	Crank Angle Degree
CFD	Computational Fluid Dynamics
COT	Compressor Outlet Temperature
CVT	Commercial Vaned Turbine
EGR	Exhaust Gas Recirculation
ER	Expansion Ratio
FEA	Finite Element Analysis
FEM	Finite Elements Method
FFT	Fast Fourier Transform
FGT	Fixed Geometry Turbine
HD	Heavy Duty
HTM	Heat Transfer Model
HVAC	Heat Ventilation Air Conditioning
ICE	Internal Combustion Engine
IER	Modified Expansion Ratio
LOLIMOT	Local Linear Model Trees
LSTT	Large Size Truck Turbine
MSTT	Medium Size Truck Turbine
NEDC	New European Driving Cycle
NS	Navier-Stokes
PID	Proportional Integrative Derivative
RTD	Resistance Temperature Detector
SPL	Sound Pressure Losses
SSTT	Small Size Truck Turbine
TOT	Turbine Outlet Temperature
VGT	Variable Geometry Turbine
ZSLM	Zero Slope Line Method

Latin symbols

A	area
A_A	entropy level
Air	air node (referring to compressor conditions after adiabatic compression process)
C	thermal capacitance or compressor measurement plane (depending on the context)
c	specific heat capacity
c_p	specific heat at constant pressure
c_s	isentropic gas velocity
c_v	specific heat at constant volume
D	diameter
e	error
f	frequency
g	acceleration due to Earth's gravity
Gas	gas node (referring to turbine inlet conditions)
Gr	Grashof number
H	housing measurement plane
$\dot{H}$	enthalpy change
h	heat transfer coefficient, oil film thickness or enthalpy (depending on the context)
I	inertial moment
k	correcting factor
K	conductance
L	length
m	mass
$\dot{m}$	mass flow rate
M	Mach number
n	engine speed
N	turbocharger speed
Nu	Nusselt number
Oil	oil node (referring to oil inlet conditions)
p	pressure
Pr	Prandtl number
$\dot{Q}$	heat transfer
r	radius
R	ideal gas constant

Ra	Rayleigh number
Re	Reynolds number
s	entropy
S	cross sectional area
Str	Strouhal number
t	time
T	temperature or turbine measurement plane (depending on the context)
u	linear velocity
u_1^*	corrected rotor tip speed
W	Water node
$\dot{W}$	mechanical power
z	number of blades
Z	engine order

Greek symbols

α	thermal diffusivity
α_1	flow angle at rotor inlet
β	thermal expansion coefficient
β_2	flow angle at rotor outlet
η	efficiency
γ	adiabatic exponent
κ	thermal conductivity
μ	dynamic viscosity or corrector term (depending on the context)
ν	kinematic viscosity
Φ	normalized flow rate
Π	pressure ratio
Ψ	head parameter
ρ	density
σ	blade speed ratio
θ	dimensionless temperature

Subscripts and superscripts

$*$	corrected parameter (with references)

0	stagnation conditions or turbine inlet port (depending on the context)
1	compressor inlet conditions or housing plane near turbine (depending on the context)
2	compressor outlet conditions or housing central plane (depending on the context)
3	turbine inlet conditions or housing plane near compressor (depending on the context)
4	turbine outlet conditions
ad	adiabatic process
amb	ambient conditions
bc	boundary conditions
C	Compressor
$comp$	composed pressure wave
$cond$	conductive process
$conv$	convective process
$corr$	corrected parameter
$crit$	critical conditions
dia	diabatic process
eff	effective
i	calculation node
inc	incident pressure wave
ins	instantaneous parameter
IT	turbine inlet (after subtracting heat)
j	calculation node
l	fluid node
m	mechanical losses
max	maximum
$meas$	measured
min	minimum
mod	modelled
O	oil
OC	compressor outlet
OD	compressor outlet diffuser
OI	oil inlet conditions
OO	oil outlet conditions
p	turbine inlet port
q	final state after receiving heat

R	turbine rotor
r	reflected pressure wave
$r2$	2nd reflected pressure wave
red	reduced parameter (without references)
ref	reference conditions
s	isentropic process or referring to the shaft (depending on the context)
S	turbine stator
st	static conditions
t	time instant or transmitted pressure wave (depending on the context)
tv	turbine volute
T	Turbine
w	wall

Groups

$$K_1 = 2 \cdot \left(\frac{r_2}{r_1}\right)^2$$

$$K_2 = 2 \cdot \left(\tan\alpha_1 + \left(\frac{r_2}{r_1}\right) \cdot \tan\beta_2\right)$$

$$K_3 = \frac{(\gamma-1)\cdot u_1^{*2}}{2\cdot\gamma\cdot R} = \frac{u_1^{*2}}{2\cdot c_p}$$

Chapter 1

Introduction

Contents

1.1 Background

HISTORY of modern Internal Combustion Engines (ICE) begins in 1876 when German engineer Nicolaus Otto obtained the patent named *Gasmotor* with number DE 532 for the company *Gasmotorenfabrik Deutz AG*. That engine put in practice the concept of a four stroke thermal engine with compression of the mixture before ignition that had been invented and patented in 1861 by French engineer Alphonse Beau de Rochas. That engine was designed to run with volatile fuels such the gasoline where the mixture was ignited by the action of an electric spark plug. In 1893 German engineer Rudolf Diesel obtained the patent for his compression ignition engine, where only air was compressed before injecting fuel in the combustion chamber and heat of air compression was the required to ignite fuel. It was in 1885 when German engineer Gottlieb Daimler presented a patent justifying the use of forced induction to force air into the internal combustion engine. Two decades later, in 1905 Swiss engineer Alfred Büchi patented a forced inducted ICE where engine exhaust gases moved a turbine coupled to a compressor, it was the beginning of *turbocharging* history. Working principles of ICE have remained unaltered over the last century despite the spectacularly technological sophistication of the last few decades to meet with legislation, manufacturers competitive cost products and users performance demands. In current financial and technological scenario the former concept of ICE has been updated to deal with the following challenges:

- Strong increase in fossil-fuel demands, mainly from emerging economies such as India or China. It is expected that by the year 2030, their oil demands will be more than twice world current consumption.
- Despite recent increase in oil reserves, extraction from new oil fields is only achievable at an expensive price using latests technologies. Moreover fuel is a non-renewable source an oil depletion would be expected in a long term future [11].
- As a consequence of previous topics joined to political instabilities on production regions, oil price has been increasing over the last few decades as showed in top part of figure 1.1.
- More and more tighten standards on engine emissions as it is observed in bottom part of figure 1.1 [1, 2, 3].

- Despite new developments in hydrogen vehicles field [108] and electrification tendencies [84], those technologies are still at a high price showing a lower autonomy compared to the classical ICE engine.

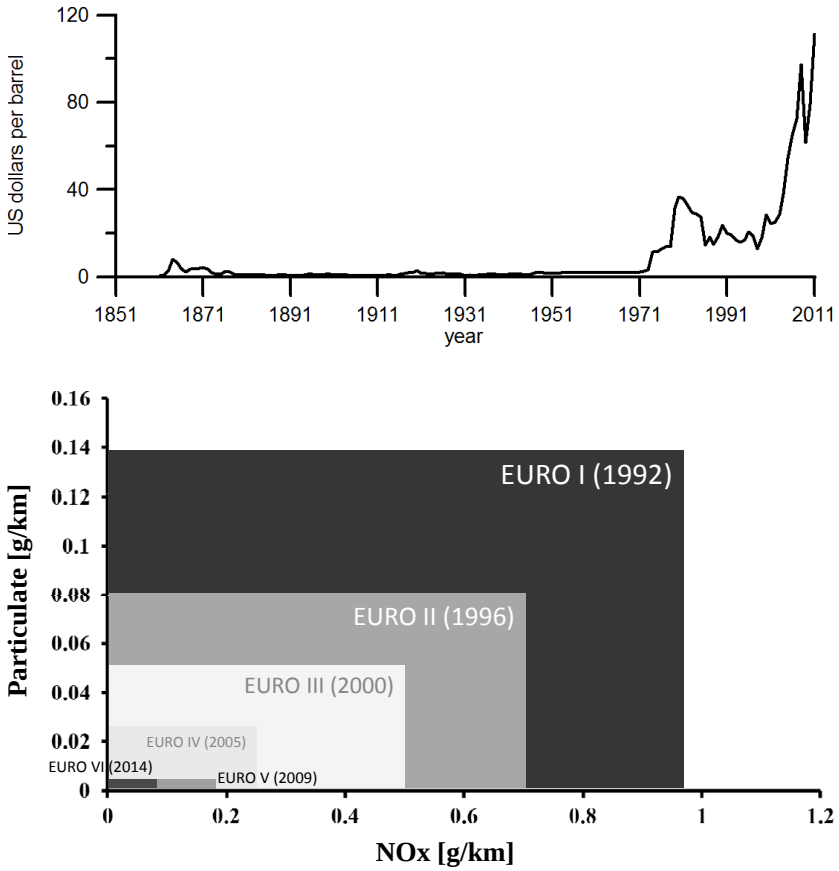

Figure 1.1: Top: Oil's market data [26], increase in oil price since 1861. Down: Euro Standards

In that demanding context the internal combustion engine (ICE) remains as the only feasible option at least for the next two decades to meet with users demands and tighten legislation standards. In order to do so, advanced engine technologies reducing fuel consumption, pollutant and particles emissions but keeping high engine performance must be considered. Among engine current technologies used to overcome those limitations the following topics can be highlighted.

- Improvement in combustion processes [52].
- High-pressure injection systems [181].
- Multiple injections [123].
- High EGR ratios [185, 72].
- Variable valve timing [61].
- High swirl ratios [138].
- New clean fuels [95].
- Improvement in engine control [96].
- Energy recovery systems [191, 180, 50, 149].
- Advanced Diesel particulate filters [71, 174].
- High boosting pressure [8].

Devices allowing air pressure increase are key in current engine developments. All new diesel engines used in Europe feature boosting technologies, and it is expected that 50% of gasoline engines will be force inducted [161]. Those technologies enable emissions and fuel consumption reduction, in that context downsizing the ICE coupled to high pressure direct injection systems and high pressure boosting devices becomes the most promising technology [69, 24]. Downsizing techniques are based on engine capacity reduction but keeping same engine power. Fuel reduction is a consequence of mechanical losses diminishing due to the small rotating assembly and the higher engine loading. Heat transfer and pumping losses are reduced too what ensures a lower fuel consumption. That technology is being used by most of engine manufacturers to replace former engines to small ones, for example from 2.0 litres into 1.6 or 1.4 engines. Nowadays more severe downsized engines are being developed by manufacturers. For example replacing 1.6 litres engines into 1.0 litres applying that technology to turbocharged - direct injected gasoline engines [62]. Turbocharging coupled to downsized engines must provide high performance characteristics under such stringent environment:

- High pulsating flow, mainly for downsized engines using 2 or 3 cylinders.

- High temperature at turbine inlet, mainly turbocharging gasoline engines.
- High temperature at compressor outlet, since high pressure ratios are desired.
- High pressure differences between compressor and turbine, since rise in boosting pressure is desired for a wider range of engine operative conditions.

1.2 General Motivations

Turbocharger performance prediction is a key factor for ICE design. Well understanding of occurring physical phenomena during turbocharger operation is essential to achieve users demands following the emissions standards. With that aim manufacturers and researchers have developed mathematical models in order to reproduce accurately what occurs with turbocharger performance in real-life engines operation. These mathematical models range from the really fast in calculation but less accurate in solution Look-up Tables models to the highly precise Computational Fluid Dynamics' models (CFD) but with their inherent drawback of the expensive time calculation requirements. Among both limits there are some other engine modelling tools as figure 1.2 shows for a general engine modelling approach.

Traditionally, turbocharger one-dimensional modelling has been used due to its good compromise between results accuracy and computational time. Nevertheless, current turbocharger models have shown a lack of accuracy mainly simulating operative points corresponding to engine partial load conditions or during transients. That is due to the fact that manufacturer maps have been used as the standard source of information for those models. Data from those maps have demonstrated not to be good enough to understand or to predict many important operative conditions on engine service, corresponding to off-design points for the turbocharger. These are:

- Engine tip in, under such conditions turbocharger works with low blade speed ratios having thermal inertia an important role.
- Engine tip out, where compressor surge becomes important.

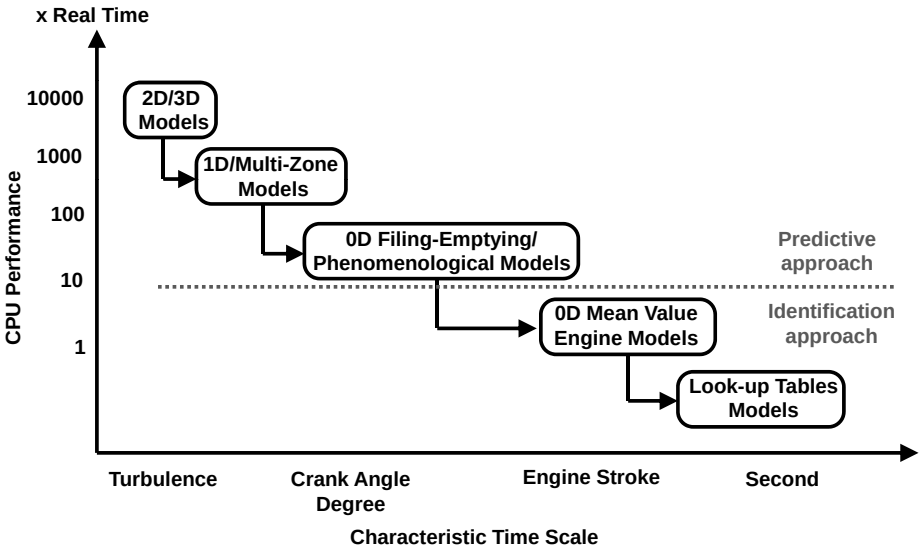

Figure 1.2: Engine Modelling tools [74]

- Partial loads at urban driving conditions, where heat transfer and friction losses become important.
- Cold start and warm up, where friction in journal and/or in thrust bearings can be quite considerable due to the high viscosity of lubricating oil.
- Turbine pulsating flow, can lead to big instantaneous variations in blade speed ratio and bearing thrust changes.

Lack of accuracy of current turbocharger models come from the fact that turbocharger performance maps are measured under other conditions for gas and lubricating oil temperatures but also under steady flow conditions. Those features cannot be assured to keep the same for the off-design points sorted above. When turbocharger is working at those conditions, heat transfer, friction losses and pulsating flow effects can be quite important compared to turbine or compressor mechanical power. For that reason, models to well understand those phenomena will help to accurately predict turbocharger performance. In addition, those operative conditions correspond to the area of interest for homologation cycles and so are of great interest for turbomachinery and engine manufacturers.

Several previous researches on turbocharger modelling have been carried out by CMT-Motores Térmicos in previous decades. From the first studies of Payri [124], to the recent studies focusing on some particular aspects of turbocharger modelling. Some of those works were focused on the transient response of the turbocharged engine as the Thesis of Serrano [146] or the modelling of variable geometry turbines as the works presented at Cervelló Thesis [29]. Others works, focused on compressor modelling under surge conditions as the works of Tiseira [169] and Lang [102]. Recently some CFD works have investigated effects of pulsating flow in the turbine of a passenger car turbocharger as the Thesis of Fajardo [57]. In addition new trends and limits of two-stage boosting system have been recently investigated by Varnier [176].

1.3 Objectives

The general objective of this PhD-Thesis has been the development of a global 1-D turbocharger model taking into account main thermo-fluid dynamic processes occurring during turbocharger operation when it is coupled to an internal combustion engine (ICE). The understanding and modelling of each one of the following phenomena represents a primary objective needed to achieve the general objective of this Thesis. These are:

- Heat transfer effects.
- Pulsating flow in compressor side.
- Pulsating flow in turbine side.
- Mechanical friction losses in turbocharger shaft.

That model has been later programmed into one-dimensional (1-D) gas-dynamic engine simulation code OpenWAM^{TM}[189, 68] to accurately reproduce conditions measured in test cells. In order to achieve the first objective (heat transfer modelling), an extensive experimental methodology has been performed to develop and validate turbocharger heat transfer model. For getting the second and third objectives, compressor and turbine geometrical models have been proposed to take into account acoustic effects. Both models have been designed using 0-D and 1-D elements keeping performance maps as the

basic source of information to be introduced into 1-D engine simulation codes. In addition, a physically based extrapolation methodology to extend turbine performance maps has been developed. That procedure allows covering the whole operative range of the turbine using the narrow range of information provided by manufacturers. That tool has demonstrated its potential modelling turbine steady and pulsating flow allowing average and instantaneous performance prediction. Finally, a mechanical losses model for turbocharger shaft [153, 154] has been coupled to proposed turbocharger model. Interactions between friction losses and heat transfer models have been considered since the increase in lube oil temperature is due to both friction and heat transfer effects. In addition, friction model needs receiving information from compressor and turbine sub-models since thrust bearing losses are affected by pressure variations at turbine and compressor machines.

Once different sub-models have been developed and validated accounting the aforesaid effects, they can be used to reproduce any turbocharger operative conditions. Two possible paths can be followed in turbocharger modelling, they have been named from here on as the *direct problem* and the *inverse problem* and they are schematically shown on figure 1.3.

- The *direct problem* is shown on the top diagram of figure 1.3. It consists of turbocharger modelling using isentropic maps for compressor and turbine as the basic source of information. Those maps contain information about pure aerodynamic behaviour of both turbomachines, and so the efficiency showed there remains invariant under any operative conditions. Proposed methodology for turbine maps extrapolation is used then to extend performance maps. That methodology needs turbine geometrical information apart from the data stored at turbine isentropic maps. Turbine geometrical model accounting for acoustic effects is geometrically based too. Compressor isentropic map will be corrected using compressor geometry to get a map without pressure losses in equivalent geometrical (and a compressor geometrical model) able to account for the acoustic effects. Once turbine and compressor isentropic maps have been extrapolated and adapted to account for acoustics, they will be used in conjunction with heat transfer and mechanical losses model to predict turbocharger performance. Both models have been based on turbochager geometry but also need information from occurring operative conditions (temperatures, pressures, mass flows ...) since those effects are particular for every tested situation. All those models will be applied

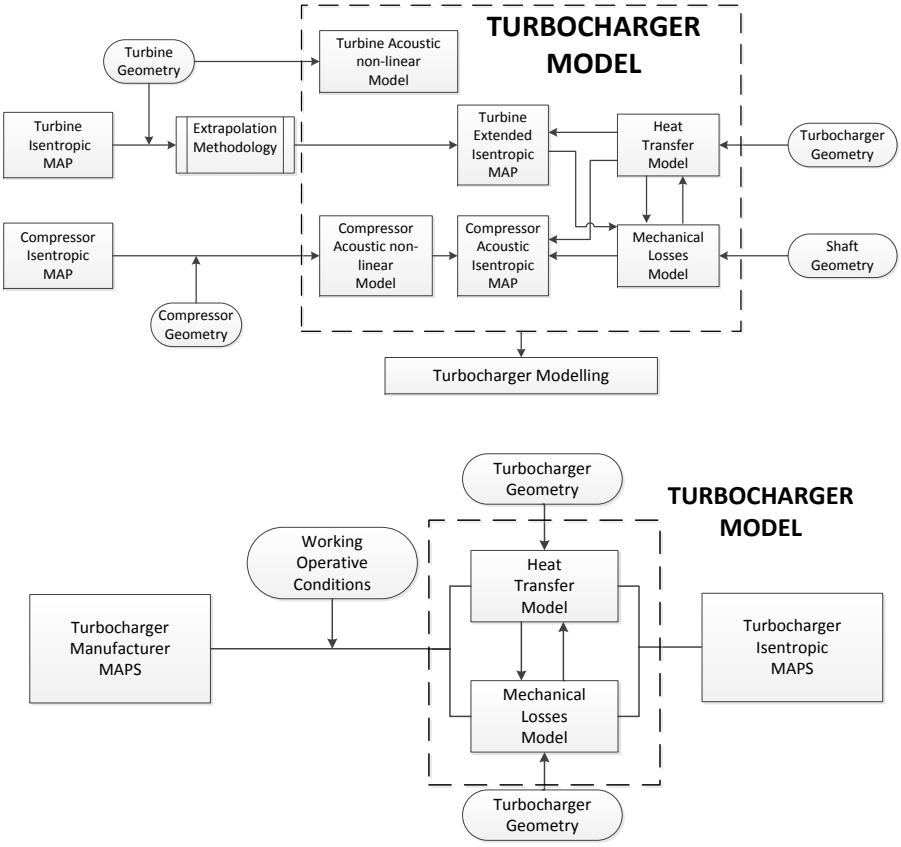

Figure 1.3: Turbocharger modelling possibilities proposed in this Thesis. Top: Direct problem. Bottom: Inverse problem.

later in quasi-steady or non-steady way in gas dynamic simulation code OpenWAM^{TM} to accurately simulate turbocharger performance.

- Turbocharger performance maps provided by manufacturers are usually far from the assumption of isentropic behaviour. That is due to the fact that those maps are usually measured using a hot gas stand. Particular heat transfer and mechanical losses occurring during those tests have been traditionally included on turbocharger performance maps information. For that reason, those maps only provide accurate results in turbocharger modelling under similar operative conditions as the appearing when turbocharger maps were measured. Nevertheless that assumption is difficult to ensure, mainly for points corresponding to the off-design

conditions presented above. For those reasons turbocharger models proposed in this Thesis are an original tool to obtain turbocharger isentropic maps using manufacturer ones. That methodology has been named from here on as the *inverse problem*. That configuration has been represented on the bottom diagram of figure 1.3, where heat transfer and mechanical losses models have been applied to turbocharger manufacturer maps. Doing so heat transfer and mechanical friction can be discounted from the efficiency provided at those maps. In order to do so, geometrical information from the turbocharger and working operative conditions when turbocharger maps were measured are necessary to precisely discount both effects. Once turbocharger isentropic maps have been obtained, they can be used to simulate any turbocharger operative conditions using the direct problem way showed on the top diagram of figure 1.3.

1.4 Methodology

In order to achieve the global objective mentioned in section 1.3 (to develop a turbocharger 1-D global model), it has been necessary the study of main thermo-fluid dynamic processes taking place in a turbocharger for automotive applications. These are:

- Study of heat transfer phenomena. Despite typical high rotational speeds of the turbocharger and the general assumption of its adiabatic behaviour, the importance of heat transfer effects has been demonstrated in this Thesis. Mainly for urban driving conditions, turbochargers of reduced size or turbochargers for petrol engine applications.

- Study of mechanical losses phenomena. Its importance is supported by the high occurring rotational speeds and the small size of the internal components of the turbocharger. A previously developed tool has been introduced into turbocharger simulations in order to close the energy problem.

- Study of compressor and turbine working performance under non-steady flow conditions, focusing in the importance of wave propagation in both elements. Importance of map extrapolation techniques has been demonstrated in turbine pulsating flow characteristics prediction.

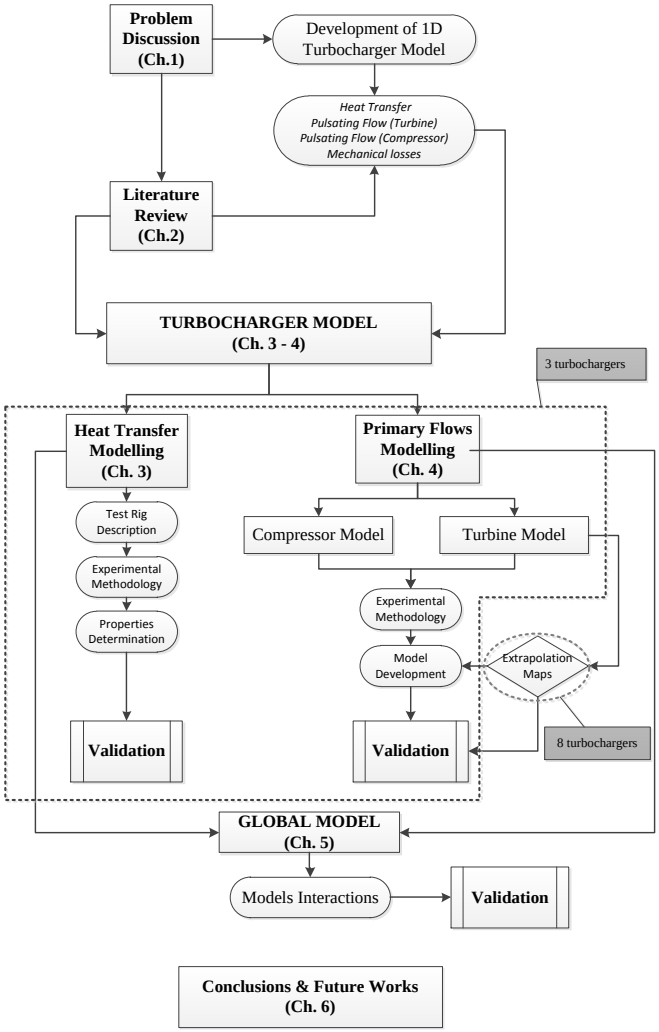

Figure 1.4: Schematic view of Thesis document.

Once those processes have been studied, the Thesis has been focused in the development and validation of several turbochargers sub-models to account for the aforesaid phenomena. To improve turbocharger current models, a series of ad-hoc experiments have been designed to analyse each of those previous topics without the interference of the others. That methodology will increase the accuracy of later turbocharger prediction. Thesis document has been struc-

tured around those objectives into the following chapters. The flux diagram presented in figure 1.4 has been introduced to outline Thesis structure.

Chapter 2 has been dedicated to the literature survey on turbocharger modelling. Particular attention has been paid to current works for turbocharger heat transfer modelling, compressor and turbine non-steady modelling focusing in the proposals to extrapolate performance maps. A review on turbocharger mechanical losses determination has been carried out too.

Chapter 3 has been dedicated to the study of turbocharger heat transfer phenomena. That analysis has been focused into the study of internal heat transfer mechanisms. A one-dimensional lumped model based on the electrical analogy has been developed to account for the internal heat transfer. That model has been separated into the study of heat fluxes between turbocharger solid components(via conduction mechanism) and those fluxes between turbocharger cases and working fluids (via convection mechanism). In addition heat accumulation during transient processes has been considered too. Particular experiments have being designed for turbocharger heat transfer model development and validation. An original experimental methodology consisting of filling up turbocharger cases with thermal oil at different temperature levels has been proposed. That methodology has been used in order to determine metal conduction between different turbocharger components, but also their thermal inertia. Later, turbocharger has been measured in a gas stand by modifying working fluids parameters (turbine gases, compressor air, lubricating oil and coolant) as desired (mass flow, inlet temperatures and pressure ratios). That extensive information has been used to complete heat transfer model with internal convective characterization. Heat transfer studies have been repeated for three different turbochargers (in size and configuration) in order to make the study more general. Finally it will be showed how heat transfer model can be used to obtain adiabatic maps from manufacturer information (the *inverse problem*). That tool will be key if operative conditions, far from the ones occurring when manufacturer maps were measured, want to be simulated.

Chapter 4 has been dedicated to the study of primary flows of the turbocharger. What means the effect of gas and air flow through the turbine and compressor respectively, paying special attention to pulsating flow in both machines. That chapter has been divided into two sections, first one dedicated to compressor non-steady characterization and second one to the turbine analysis. Geometrical models accounting for acoustic effects on compressor and

turbine side have been proposed. Those models have been developed using 0-D and 1-D elements in order to integrate them into 1-D simulation codes like OpenWAM^{TM}. Both models have been developed and validated using an extensive experimental test campaign using quasi-adiabatic pulsating flow on the element under study (whether turbine or compressor). Meanwhile the other element (compressor or turbine) was tested under steady flow conditions to isolate it from pulsating phenomena. That methodology has been carried out using a gas stand and a rotary valve for pulsating flow generation with pulses frequency and amplitude as desired. Those studies have been repeated for the three turbochargers presented on Chapter 3. Special interest has been focused into an innovative physically-based methodology to extrapolate turbine performance maps. That methodology allows the extension of turbine maps far from the traditionally narrow region covered by manufacturer maps. Getting information for the whole operative range of the turbine will be important in turbine pulsating characterization. Under such conditions, pressure pulses modify instantaneously turbine operative conditions far from the region showed on conventional performance maps. Apart from the three turbochargers used in previous chapters, other five turbines, have been used to complete extrapolation validation.

Chapter 5 of this Thesis has been dedicated to turbocharger model validation working under more realistic operative conditions, where above-presented phenomena will occur. Interactions between proposed turbocharger sub-models have been analysed there too. It will be demonstrated the potential of that tool predicting turbine and compressor outlet temperatures mainly for turbocharger operative conditions corresponding to urban driving conditions. It will be demonstrated the potential of presented turbocharger model since it will be able to predict accurately turbocharger main characteristics even under pulsating flow and hot operative conditions without including any corrector term, nor for the engine speed neither the load to tune turbocharger performance prediction. In addition the influence of pulsating characteristics (frequency and amplitude) on turbine and mechanical efficiencies have been studied. It will be demonstrated how turbine extension maps tool coupled to mechanical friction losses model can be used in a quasi-steady way to predict accurately turbine performance under pulsating flow conditions.

Chapter 6 has been dedicated to summarize most relevant topics, highlight conclusions of this Thesis and to proposing some future works to improve turbocharger current modelling tools.

References

[1] *" Council Directive 91/441/EEC of 26 June 1991 on the Approximation of the Laws of the Member States Relating to Measures to Be Taken Against Air Pollution by Emissions from Motor Vehicles"*. Official Journal of the European Union, 30/08/1991, pp. 1-106, 1991. (Cit. on p. 2).

[2] *" Council Directive 98/69/EEC of 13 October 1998 on the Approximation of the Laws of the Member States Relating to Measures to be Taken Against Air Pollution by Emissions from Motor Vehicles"*. Official Journal of the European Union, 28/12/1998, pp. 1-65, 1998. (Cit. on p. 2).

[3] *" Regulation 715/2007 of the European Parliament and of the Council of 20 June 2007 on Type Approval of Motor Vehicles with Respect to Emissions from Light Passenger and Commercial Vehicles (Euro 5 and Euro 6) and on Access to Vehicle Repair and Maintenance Information"*. Official Journal of the European Union, 29/06/2007, pp. L171/1-16, 2007. (Cit. on p. 2).

[8] I. Al-Hinti, M. Samhouri, A. Al-Ghandoor, and A. Sakhrieh. "The effect of boost pressure on the performance characteristics of a diesel engine: A neuro-fuzzy approach". In: *Applied Energy* 86 (2009), pp. 113–121 (cit. on p. 4).

[11] T. Appenzeller. "End of Cheap Oil". In: *National Geographic Magazine* June (2004) (cit. on p. 2).

[24] A. Boretti. "Towards 40directly injected, turbocharged, spark ignition ethanol engines". In: *Energy Conversion and Management* 57.0 (2012), pp. 154 –166. ISSN: 0196-8904. DOI: 10.1016/j.enconman.2011.12.011. URL: http://www.sciencedirect.com/science/article/pii/S0196890411003657 (cit. on p. 4).

[26] BP. *BP Statistical Review of World Energy June 2012* (cit. on p. 3).

[29] C. Cervelló. "Contribución a la caracterización experimental y al modelado de turbinas de geometría variable en grupos de sobrealimentación". PhD thesis. Universidad Politécnica de Valencia, 2005 (cit. on p. 7).

[50] V. Dolz, R. Novella, A. García, and J. Sánchez. "HD Diesel engine equipped with a bottoming Rankine cycle as a waste heat recovery system. Part 1: Study and analysis of the waste heat energy". In: *Applied Thermal Engineering* 36.0 (2012), pp. 269 –278. ISSN: 1359-4311. DOI: 10.1016/j.applthermaleng.2011.10.025. URL: http://www.sciencedirect.com/science/article/pii/S1359431111005631 (cit. on p. 4).

[52] Pierre Duret, ed. *New Generation of Engines Combustion Processes for the Future?* Entretiens IFP Series. Editions Technip, 2002, p. 179. URL: ISBN-13:9782710808121 (cit. on p. 4).

[57] P. Fajardo. "Methodology for the Numerical Characterization of a Radial Turbine under Steady and Pulsating Flow". PhD thesis. Universidad Politécnica de Valencia, 2012 (cit. on p. 7).

[61] G. Fontana and E. Galloni. "Variable valve timing for fuel economy improvement in a small spark-ignition engine". In: *Applied Energy* 86.1 (2009), pp. 96 –105. ISSN: 0306-2619. DOI: 10.1016/j.apenergy.2008.04.009. URL: http://www.sciencedirect.com/science/article/pii/S0306261908001013 (cit. on p. 4).

[62] R. Friedfeldt, T. Zenner, R. Ernst, and A. Fraser. "Three-cylinder Gasoline Engine with Direct Injection". In: *MTZ worldwide Edition* 05 (2012) (cit. on p. 4).

[68] J. Galindo, J.R. Serrano, F.J. Arnau, and P. Piqueras. "Description of a Semi-Independent Time Discretization Methodology for a One-Dimensional Gas Dynamics Model". In: *Journal of engineering for gas turbines and power* 131 (2009). DOI: 10.1115/1.2983015 (cit. on pp. 7, 218).

[69] J. Galindo, J.R. Serrano, H. Climent, and O. Varnier. "Impact of two-stage turbocharging architectures on pumping losses of automotive engines based on an analytical model". In: *Energy Conversion and Management* 51.10 (2010), pp. 1958 –1969. ISSN: 0196-8904. DOI: 10.1016/j.enconman.2010.02.028. URL: http://www.sciencedirect.com/science/article/pii/S0196890410000944 (cit. on p. 4).

[71] J. Galindo, J.R. Serrano, P. Piqueras, and O. García-Afonso. "Heat transfer modelling in honeycomb wall-flow diesel particulate filters". In: *Energy* 43.1 (2012). 2nd International Meeting on Cleaner Combustion (CM0901-Detailed Chemical Models for Cleaner Combustion), pp. 201 –213. ISSN: 0360-5442. DOI: 10.1016/j.energy.2012.04.044. URL: http://www.sciencedirect.com/science/article/pii/S0360544212003428 (cit. on p. 4).

[72] E. Galloni, G. Fontana, and R. Palmaccio. "Numerical analyses of {EGR} techniques in a turbocharged spark-ignition engine". In: *Applied Thermal Engineering* 39.0 (2012), pp. 95 –104. ISSN: 1359-4311. DOI: 10.1016/j.applthermaleng.2012.01.040. URL: http://www.sciencedirect.com/science/article/pii/S1359431112000592 (cit. on p. 4).

[74] P. Gautier, A. Albrecht, P. Moulin, A. Chasse, L. Fontvieille, A. Guinois, and L. Doleac. *"A New Simulation Step Towards Virtual Bench Through the Challenging Case of Two-Stage Turbocharger Diesel Engine Control Design"*. SAE Technical Paper 2008-01-0355, 2008. (Cit. on p. 6).

[84] K.G. Høyer. "The history of alternative fuels in transportation: The case of electric and hybrid cars". In: *Utilities Policy* 16.2 (2008), pp. 63 –71. ISSN: 0957-1787. DOI: 10.1016/j.jup.2007.11.001. URL: http://www.sciencedirect.com/science/article/pii/S0957178707000768 (cit. on p. 3).

[95] B. Kegl. "Influence of biodiesel on engine combustion and emission characteristics". In: *Applied Energy* 88.5 (2011), pp. 1803 –1812. ISSN: 0306-2619. DOI: 10.1016/j.apenergy.2010.12.007. URL: http://www.sciencedirect.com/science/article/pii/S0306261910005143 (cit. on p. 4).

[96] U. Kiencke and L. Nielsen. "Automotive Control Systems: For Engine, Driveline, and Vehicle". In: *Measurement Science and Technology* 11.12 (2000), p. 1828. URL: http://stacks.iop.org/0957-0233/11/i=12/a=708 (cit. on p. 4).

[102] R. Lang. "Contribución a la Mejora del Margen de Bombeo en Compresores Centrífugos de Sobrealimentación". PhD thesis. Departamento de Máquinas y Motores Térmicos - UPV, 2011 (cit. on p. 7).

[108] A. Mohammadi, M. Shioji, Y. Nakai, W. Ishikura, and E. Tabo. "Performance and combustion characteristics of a direct injectionSI hydrogen engine". In: *International Journal of Hydrogen Energy* 32.2 (2007), pp. 296 –304. ISSN: 0360-3199. DOI: 10.1016/j.ijhydene.2006.06.005. URL: http://www.sciencedirect.com/science/article/pii/S0360319906002084 (cit. on p. 3).

[123] S. Park, S. Yoon, and C. Lee. "Effects of multiple-injection strategies on overall spray behavior, combustion and emissions reduction characteristics of biodiesel fuel". In: *Applied Energy* 88 (2011), pp. 88–98 (cit. on p. 4).

[124] F. Payri. "Predicción de las actuaciones de los grupos de sobrealimentación para motores diesel de automoción". PhD thesis. Universidad Politécnica de Madrid, 1973 (cit. on p. 7).

[138] B.V.V.S.U. Prasad, C.S. Sharma, T.N.C. Anand, and R.V. Ravikrishna. "High swirl-inducing piston bowls in small diesel engines for emission reduction". In: *Applied Energy* 88.7 (2011), pp. 2355 –2367. ISSN: 0306-2619. DOI: 10.1016/j.apenergy.2010.12.068. URL: http://www.sciencedirect.com/science/article/pii/S030626191000588X (cit. on p. 4).

[146] J.R. Serrano. "Análisis y modelado de transitorios de carga en MEC turboalimentados". PhD thesis. Universidad Politécnica de Valencia, 1999 (cit. on p. 7).

[149] J.R. Serrano, V. Dolz, R. Novella, and A. García. "HD Diesel engine equipped with a bottoming Rankine cycle as a waste heat recovery system. Part 2: Evaluation of alternative solutions". In: *Applied Thermal Engineering* 36.0 (2012), pp. 279 –287. ISSN: 1359-4311. DOI: 10.1016/j.applthermaleng.2011.10.024. URL: http://www.sciencedirect.com/science/article/pii/S135943111100562X (cit. on p. 4).

[153] J.R. Serrano, P. Olmeda, A. Tiseira, L.M. García-Cuevas, and A. Lefebvre. "Importance of mechanical losses modeling in the performance prediction of radial turbochargers under pulsating flow conditions". In: *SAE Int. J. Engines 6(2)* 6(2) (2013), pp. 729–738. DOI: 10.4271/2013-01-0577 (cit. on pp. 8, 46, 48, 49, 93, 132, 157, 189, 216, 217, 255).

[154] J.R. Serrano, P. Olmeda, A. Tiseira, L.M. García-Cuevas, and A. Lefebvre. "Theoretical and experimental study of mechanical losses in automotive turbochargers". In: *Energy* 55 (2013), pp. 888 –898 (cit. on pp. 8, 46, 48, 49, 93, 132, 157, 189, 216, 217, 223, 233, 255, 271).

[161] S.M. Shahed. "Gasoline engine downsizing and boosting for CO2 emission reduction, California Air Resource Board, Climate Change". In: *International Vehicle Technology Symposium, Sacramento CA*. 2003 (cit. on p. 4).

[169] A. Tiseira. "Caracterización Experimental y Modelado de Bombeo en Compresores Centrífugos de Sobrealimentación". PhD thesis. Departamento de Máquinas y Motores Térmicos - UPV, 2008 (cit. on p. 7).

[174] A. Torregrosa, J.R. Serrano, F.J. Arnau, and P. Piqueras. "A fluid dynamic model for unsteady compressible flow in wall-flow diesel particulate filters". In: *Energy* 36.1 (2011), pp. 671 –684. ISSN: 0360-5442. DOI: 10.1016/j.energy.2010.09.047. URL: http://www.sciencedirect.com/science/article/pii/S0360544210005268 (cit. on p. 4).

[176] O. Varnier. "Trends and Limits of Two-Stage Boosting Systems for Automotive Diesel Engines". PhD thesis. Universidad Politecnica de Valencia, 2012 (cit. on pp. 7, 60).

[180] T. Wang, Y. Zhang, J. Zhang, G. Shu, and Z. Peng. "Analysis of recoverable exhaust energy from a light-duty gasoline engine". In: *Applied Thermal Engineering* 0 (2012), pp. 414–419. ISSN: 1359-4311. DOI: 10.1016/j.applthermaleng.2012.03.025. URL: http://www.sciencedirect.com/science/article/pii/S1359431112002098 (cit. on p. 4).

[181] X. Wang, Z. Huang, W. Zhang, O. Kuti, and K. Nishida. "Effects of ultra-high injection pressure and micro-hole nozzle on flame structure and soot formation of impinging diesel spray". In: *Applied Energy* 88 (2011), pp. 1620–1628 (cit. on p. 4).

[185] H. Wei, T. Zhu, G. Shu, L. Tan, and Y. Wang. "Gasoline engine exhaust gas recirculation - A review". In: *Applied Energy* 99 (2012), pp. 534–544 (cit. on p. 4).

[189] *www.Openwam.org*. OpenWAM, CMT-Motores Térmicos; Universitat Politècnica de València (UPV). 2012 (cit. on pp. 7, 152, 188, 214, 218, 228, 253).

[191] W. Yan, Y. Xiaoli, and L. Guodong. "Experimental Measurement and Analysis of Performance of Heat Pipe Heat Exchanger Used in a Turbocharged Engine with Intercooling". In: *Heat Transfer Engineering* 33-14 (2012), pp. 1207–1216. DOI: 10.1080/01457632.2012.677727 (cit. on p. 4).

Chapter 2

Literature Review of Turbochargers Modelling

Contents

2.1 Introduction

TURBOCHARGING has become one of the keys for automotive engines improvement in the last years for both diesel and petrol engines. New turbocharging systems allowing higher boosting capabilities have yielded to new downsized engines with lower consumption and pollutant emissions. However, current turbochargers are now constrained to harder operating conditions, including higher pulsating flow at the turbine side, higher operating temperature or more likeability of surge occurrence. One of the most important tools used by automotive engineers for the engine gas-exchange and boosting system developments are gas-dynamic models able to predict the engine flows characteristics and thus the engine performance. These models need to be fed with the turbocharger information, mainly turbine and compressor performance maps. In the last years, a lack of accuracy has been noticed in those models. The reason is that the phenomena mentioned above, pulsating flow, heat transfer and mechanical losses; have not been considered in those models.

In the following section a literature survey about turbochargers modelling aspects related with present Thesis objectives will be discussed.

2.2 Models to Characterize Heat Transfer Phenomena in Turbochargers

Traditionally heat transfer effects have been neglected in turbomachinery studies due to the relative small exchange surface and the occurring high flows. Nevertheless that assumption was only valid for large turbomachines, but not true for the small turbocharger used in passenger car applications, mainly at engine low load operative points and transient conditions [159, 65]. Such conditions correspond to urban traffic conditions according to NEDC tests (New European Driving Cycle) where turbocharger speed is lower than 100,000 rpm. In such conditions heat transfer to the compressor (from the turbine and oil) can equal the energy consumed by the compression process [137]. Improvement in turbocharger simulation codes and engine matching becomes vital in the automotive division since turbocharging the downsized engine is the most feasible way to keep effective power while reducing fuel consumption and pollutant emissions [77, 165]. In order to get those objectives, a good data source

for the turbocharger is needed. Nevertheless, the information provided in turbocharger manufacturers maps is affected by heat transfer effects. Those heat fluxes will be particular from turbine and oil working conditions when turbocharger map was measured. So that the efficiency given in a turbocharger map is not the one defined as isentropic since it is also containing the influence of heat transfer. Nonetheless if the overall simulation of the turbocharger and engine matching wants to be improved, it will be desirable obtaining information about its isentropic efficiency [111]. Since that efficiency will remain the same for any given configuration (in a gas stand or in an engine) because it is subject only to the internal gas dynamic processes occurring in the machine. Nevertheless turbocharger maps are not usually measured under isentropic conditions due to the difficulties and limitations of the adiabatic testing procedure. That methodology will allow measuring turbocharger performance without undesirable heat transfer effects. If a direct parametrization of the turbocharger using extrapolation from turbocharger maps information is used, unsatisfactory modelling results will be obtained as showed by Guzzella [76]. For the aforementioned reasons having a turbocharger heat transfer model would be important when manufacturer maps will be used. That case is the standard for engine simulation codes. In such conditions a heat transfer model will be able to provide turbocharger isentropic efficiency by discounting heat fluxes occurring when the map was measured.

Looking insight of heat transfer phenomena in turbochargers, several studies have shown that the turbocharger is part of a complex thermal system containing different heat flows between compressor, turbine, engine housing, lubrication oil and environment [111, 156]. In normal operative conditions heat flows from the turbine to the turbocharger housing arriving later to the compressor worsening its efficiency [140, 160, 177]. For instance when turbine inlet temperature increases from 50°C to 500°C a nearly 15% of lower compressor efficiency is measured for turbocharger speeds lower than the 50% of the maximum tip speed [35]. Those results were also confirmed by Shaaban and Seume [157] who showed how the deviation between compressor non-adiabatic and adiabatic efficiency increased significantly with the decreasing in rotational speed. At the housing, heat is partially removed by the lubricating oil and the coolant circuit in case it exists. In addition the turbocharger exchanges energy to the surroundings by means of radiation and a mixed convection (free and forced depending on its set-up). An schematic diagram of turbocharger main energy fluxes is represented in figure 2.1. As it is observed, the whole energy drop on the turbine side is divided into a mechanical power

term ($\Delta\dot{W}_T$) that will drive the compressor ($\Delta\dot{W}_C$) once mechanical losses in the shaft have been discounted ($\dot{W}_{MechLoss}$). But another part of that available energy will be translated into a heat flux that will be exchanged with the surroundings ($\dot{Q}_{T(Rad,Conv)}$) and to the housing where it will be transmitted to the lubricating oil ($\dot{Q}_{H/Oil}$) or to the surroundings ($\dot{Q}_{H(Rad,Conv)}$). Eventually part of that heat flux will arrive to the compressor side where an amount of that heat will increase air temperature and another part will be exchanged with the surroundings ($\dot{Q}_{C(Rad,Conv)}$).

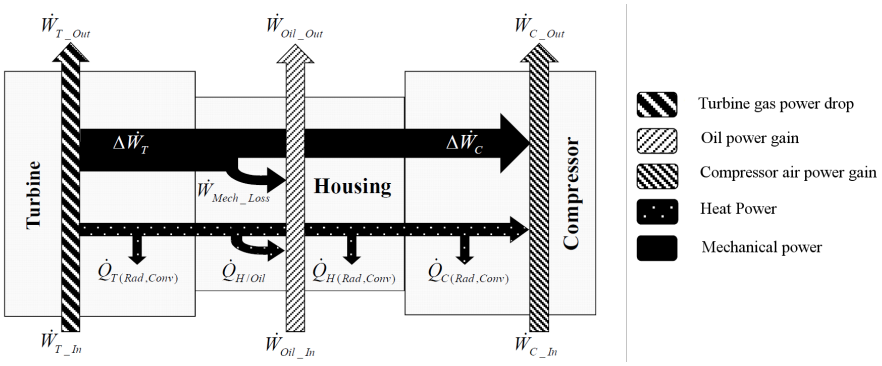

Figure 2.1: Main energy fluxes inside a turbocharger [132].

Several methodologies for turbocharger heat transfer phenomena characterization have been proposed in the literature survey. They can range from fast one-dimensional models for the whole turbocharger to the accurate FEM-CFD models analysing the separated components from the turbocharger. They will be explained in next sections.

2.2.1 One-Dimensional Models

Zero and one-dimensional models used to characterize both the internal and external heat transfer of turbochargers are based in the thermodynamic analysis of their adiabatic and diabatic processes. Figure 2.2 shows both processes compared to the ideal one (isentropic).

The isentropic evolution on the compressor side (from 10 to 20_s) reflects the ideal situation of a compression process taking place under the assumptions of being adiabatic and reversible. Compressor outlet temperature in that situation is calculated using isentropic evolution statement and the state

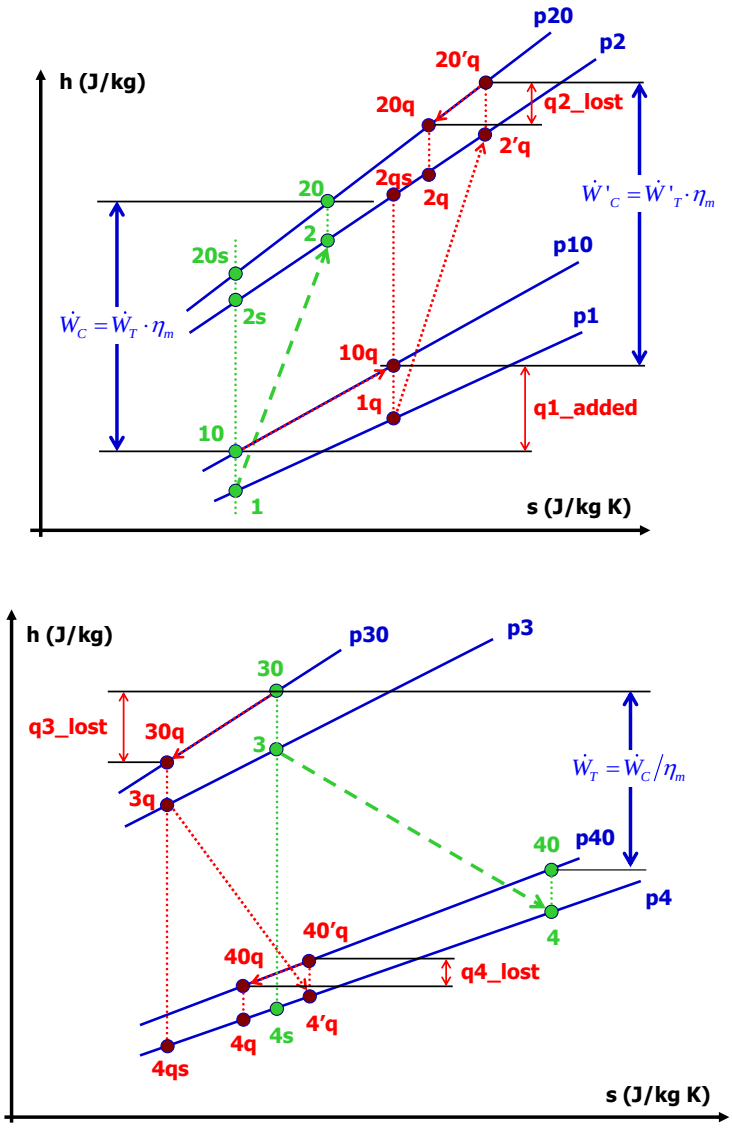

Figure 2.2: Entropic diagrams for the compressor (top) and turbine (bottom) [150].

equation between initial and final conditions as showed by equation 2.1 [183].

$$T_{20s} = T_{10} \cdot \Pi_C^{\frac{\gamma-1}{\gamma}} \tag{2.1}$$

Where Π_C represents the pressure ratio between final and initial states (p_{20}/p_{10}) and γ the adiabatic exponent.

If the compressor process is assumed to be adiabatic but not reversible, compressor outlet temperature (T_{20}) will increase compared to the one provided by the isentropic assumption (T_{20s}). The ratio of enthalpy changes between both processes is known as compressor isentropic efficiency defined by equation 2.2.

$$\eta_{C,is} = \frac{\Delta h_s}{\Delta h_{ad}} = \frac{T_{20s} - T_{10}}{T_{20} - T_{10}} = \frac{T_{10} \cdot \left(\Pi_C^{\frac{\gamma-1}{\gamma}} - 1 \right)}{T_{20} - T_{10}} \tag{2.2}$$

Furthermore, if it is assumed that compressor is exchanging some heat with turbocharger unit (q1 added and q2 lost), its real outlet temperature could be even higher (T_{20q}) than adiabatic outlet temperature (T_{20}). In the case showed on the top part of figure 2.2, from Serrano et al. [150], points marked with the subtitle q are those from the diabatic compression process (when heat transfer phenomena is considered). Being points 10 and $20q$ initial and final states of the real (diabatic) compression process. According to that diagram, air at compressor inlet (T_{10}) is receiving some heat (q1 added) what increases its temperature (T_{10q}). Later, compression adiabatic process will take place ($T_{20'q}$) where compressor and turbine powers must be equal but discounting mechanical losses ($\dot{W}'_C = \dot{W}'_T \cdot \eta_m$). Finally compressor outlet temperature is reduced as consequence of losing some heat (q2 lost) to the cooler housing (T_{20q}).

Baines et al. [14] observed that compressor air could be heated up or cooled down depending on turbocharger operative conditions, same conclusions were achieved by Bohn et al. [21]. So, heat transfer effects to the compressor always exist and its behaviour cannot be considered fully adiabatic under any circumstances [158]. For low rotational speeds Shaaban and Seume [158] pointed out how compressor air received heat from the turbocharger housing what increased its outlet temperature. Nevertheless, at a certain point (moderate to high high rotational speeds), heat transfer process will reverse. When compressed air temperature will be higher than its casing temperature, heat exchange will occur from the air to compressor casing what will reduce air's temperature (T_{20q}). In such conditions, compressor outlet temperature T_{20q} (once heat losses have been discounted) could be even lower than the adiabatic

outlet temperature (T_{20}). Nevertheless heat transfer effects will be minor at high rotational speeds in comparison with its mechanical power.

A new efficiency definition is given comparing the ratio of enthalpy changes between the ideal situation (isentropic) and the real one (diabatic). That diabatic efficiency is simply known as compressor efficiency and it is typically provided in manufacturer maps (equation 2.3).

$$\eta_C = \frac{\Delta h_s}{\Delta h_{dia}} = \frac{T_{20s} - T_{10}}{T_{20q} - T_{10}} = \frac{T_{10} \cdot \left(\Pi_C^{\frac{\gamma-1}{\gamma}} - 1 \right)}{T_{20q} - T_1} \tag{2.3}$$

One of the consequences of this thermal energy transferred to the compressor will be the reduction in compressor efficiency given in manufacturer maps (mainly for low load conditions) due to the increase in the air outlet temperature. That temperature increase should be taken into account for intercooler designs. Heat transfer effects become important at engine starting, idle and partial-load engine operation. In those situations heat transfer to the compressor will increase due to the low rotational speeds and even worst at the proximity of engine operating points to the compressor surge line [139] due to the lower mass flow (longer residence time).

Same processes can be distinguished on the turbine side. In the case shown on the bottom part of figure 2.2, the reversible and adiabatic expansion process (isentropic) is shown between points 30_q and 4_{qs}. Turbine isentropic outlet temperature can be calculated using equation 2.4.

$$T_{4qs} = T_{30q} \cdot \left(\frac{1}{\Pi_T} \right)^{\frac{\gamma-1}{\gamma}} \tag{2.4}$$

When the expansion process keeps adiabatic but not reversible, another final state is defined with the name of adiabatic (point 4'q, which is based on keeping constant turbine effective power). The ratio of enthalpy change between the adiabatic and the isentropic states will be used to define turbine isentropic efficiency showed in equation 2.5.

$$\eta_{T,s} = \frac{\Delta h_{ad}}{\Delta h_s} = \frac{T_{30q} - T_{4'q}}{T_{30q} - T_{4qs}} = \frac{T_{30q} - T_{4'q}}{T_{30q} \cdot \left(1 - \left[\frac{1}{\Pi_T}\right]^{\frac{\gamma-1}{\gamma}}\right)} \tag{2.5}$$

If a diabatic evolution is considered (between points 30 and 4q), turbine total outlet temperature could be even lower than the value predicted by the adiabatic evolution (4'q). That is justified as the real evolution is cooled and so turbine efficiency defined between initial and final states using equation 2.6 will be higher than the adiabatic one, and could be even higher than one.

$$\eta_T = \frac{\Delta h_{dia}}{\Delta h_{is}} = \frac{T_{30} - T_{4q}}{T_{30} - T_{4s}} = \frac{T_{30} - T_{4q}}{T_{30} \cdot \left(1 - \left[\frac{1}{\Pi_T}\right]^{\frac{\gamma-1}{\gamma}}\right)} \tag{2.6}$$

A relevant discrepancy between existing one-dimensional turbine and compressor heat transfer models is whether the heat flux is added/removed to the system after or before the extraction of power, or even a combination of both possibilities [21, 78, 157]. For example the model proposed by Baines et al. [14] assumed that the heat transferred from the compressed air to the surroundings and to the rest of the turbocharger unit occurred after the compression process, taking place in the diffuser and the volute. That proposal was justified by the larger exposed surface to the air in that section compared to the impeller area. Although heat transfer might exist in the impeller due to conduction along the shaft, it should be small due to the lubrication oil and the small diameter of the shaft.

That hypothesis was confirmed by the studies presented by Chesse et al. [33] who proposed a simple experimental methodology to study heat transfer effects on turbocharger compressor performance. For that purpose a gas stand was used to measure compressor characteristics under adiabatic conditions and later using two temperature levels at turbine inlet. First of all, compressor adiabatic map was obtained by minimizing internal and external heat transfer. For this purpose, both the turbocharger and the test rig were fully insulated in order to avoid external convection and radiation. In addition turbine inlet temperature for each operative point was adjusted keeping the average temperature from the expansion process equal to the average temperature for the compression process. Once compressor adiabatic map had been obtained, measurements were repeated modifying turbine inlet temperatures

(300°C and 500°C). From direct comparison between the three maps, it was observed that constant speed lines were not modified while turbine inlet temperature was increased, what ensured that aerodynamic losses did not depend on heat transfer. That supported the assumption that heat transfer in compressor takes place in the diffuser (after the impeller), as many authors have already suggested [14]. However, efficiency lines from those measurements showed an important change what confirmed the existence of a heat flux from the hot turbine to the cold compressor. Those differences were bigger at the low load area, where compressor works far from the hypothesis of an adiabatic machine as other authors also confirmed [150, 157]. Due to the fact that heat transfer occurred after the impeller, compressor mechanical power should be the same for any turbine inlet temperature. Heat fluxes to the compressor were determined by direct comparison between cold and hot measurements in the gas stand. Comparing compressor heat fluxes to its mechanical power, the non-adiabatic behaviour at low loads was confirmed. For instance at 30,000 rpm with 300°C at turbine inlet, heat fluxes to the compressor side were half the mechanical power. But when turbine inlet temperature was increased up to 500°C, what would represent engine real operative conditions, its value was in the same magnitude than compressor mechanical power. As rotational speed increased, relative importance of compressor heat fluxes reduced (lower than 5% for rotational speeds over 120,000 rpm [150]).

Model proposed by Baines et al. [14] was focused on turbocharger convective heat transfer phenomena meanwhile internal conduction and external radiation were not particularly studied. Literature values for casing thermal conductivities and surface emissivities were used instead in turbocharger global characterization [23]. Turbocharger internal and external convection were studied using different values for turbine inlet temperature and ventilation velocity. Internal convection among working fluids (exhausted gases, air and oil) and their cases (turbine, compressor and housing) was characterized by means of Nusselt number correlation (equation 2.7).

$$\mathrm{Nu} = \mathrm{a} \cdot \mathrm{Re}^{\mathrm{b}} \cdot \mathrm{Pr}^{\mathrm{c}} \tag{2.7}$$

Where,

$$\mathrm{Nu} = \frac{\mathrm{h} \cdot \mathrm{L}_{\mathrm{eff}}}{\kappa} \tag{2.8}$$

$$\mathrm{Pr} = \frac{\mathrm{c_p} \cdot \mu}{\kappa} \tag{2.9}$$

$$\mathrm{Re} = \frac{\rho \cdot \mathrm{u} \cdot \mathrm{D}}{\mu} \tag{2.10}$$

Where L_{eff} is a characteristic length, h represents convective heat transfer coefficient while parameters a, b and c were fitted using experimental data.

External convection was studied fitting the same parameters of equation 2.7 for cases with ventilation (forced convection). For free convection cases (without ventilation), equation 2.11 was used instead.

$$\mathrm{Nu} = \mathrm{d} \cdot \mathrm{Gr^e} \cdot \mathrm{Pr^f} \tag{2.11}$$

Where,

$$\mathrm{Gr} = \frac{\mathrm{g} \cdot \beta \cdot \mathrm{L^3} \cdot (\mathrm{T_w} - \mathrm{T_l})}{\nu^2} \tag{2.12}$$

Being g gravity acceleration, β the thermal expansion coefficient, meanwhile T_w represented surface temperature and T_l bulk temperature.

The study was repeated using three different turbochargers for truck applications, importance of lubricating oil removing part of turbocharger internal heat fluxes was revealed. That conclusion was get comparing results from hot tests to the corresponding points tested under adiabatic conditions. Oil temperature increase across the turbocharger was due to a combination of friction losses and heat transfer effects. Lubricating oil importance was also shown since compressor heat fluxes were not so strong dependent on turbine inlet temperature as it was pointed out by Payri et al. [132].

Similar results were obtained by Yamagata et al. [190] focusing in high turbocharger speeds without thermal insulation. That study concluded that metal temperatures from compressor components (back plate, impeller back and impeller hub) proportionally varied with compressed air temperature. Meanwhile turbine inlet temperature or lube oil effects were relatively small as figure 2.3 shows. That showed out that lube oil passing through the housing minimized the heat transfer from the turbine to the compressor.

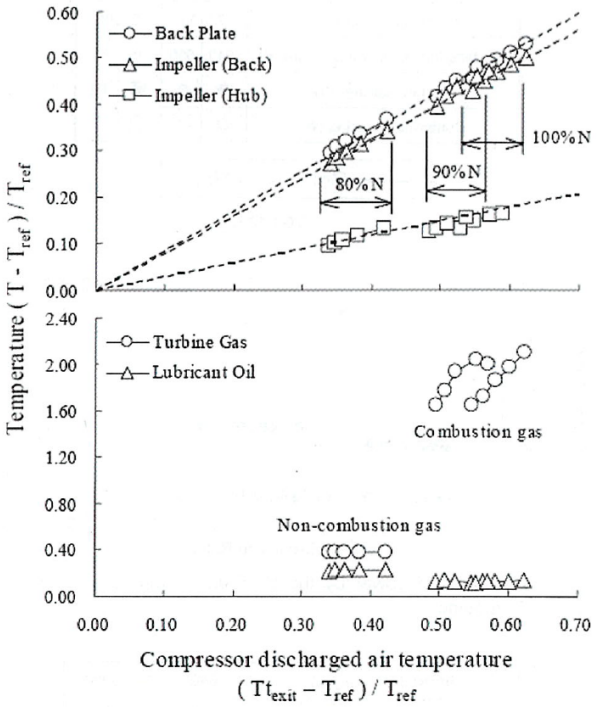

Figure 2.3: Dependence of compressor components temperature with its outlet temperature [190].

Using the same argument of exposed areas but applied to the turbine side, biggest heat transfer should take place up to turbine tongue and at volute occurring so before the extraction of power in the rotor. In that case, heat transfer affected work transfer process. Main advantage of that model was the simplicity for later programming in engine computational code, since the whole heat transfer occurred in one place. In addition, experimental instrumentation was easier and so it was model validation.

A similar study to the one presented by Baines et al. [14] was performed by Diango et al. [48] but focusing on heat exchange by convection mechanism in gas turbine cases. Internal convection in the turbine volute was studied using Sieder-Tate correlation [99] (equation 2.13).

$$\mathrm{Nu} = 0.023 \cdot \mathrm{Re}^{0.8} \cdot \mathrm{Pr}^{0.3} \tag{2.13}$$

Same correlation was used for external forced convection but Morgan correlation based on Rayleigh number (Ra) was used for the external free convection [121] (equation 2.14).

$$\mathrm{Nu} = \mathrm{a} \cdot \mathrm{Ra}^{\mathrm{b}} \tag{2.14}$$

Where,

$$\mathrm{Ra} = \mathrm{Gr} \cdot \mathrm{Pr} = \frac{\mathrm{g} \cdot \beta \cdot \mathrm{L}^3 \cdot (\mathrm{T_w} - \mathrm{T_l})}{\alpha \cdot \nu} \tag{2.15}$$

Being α thermal diffusivity defined as $\kappa / c_p \cdot \rho$.

Serrano et al. [150] assumed that heat transfer on the turbocharger took place before and after the rotor impeller as the top part of figure 2.2 shows. On the compressor side, heat flux was added before compression process ($q1_{added}$). Later adiabatic compression occurred and eventually another amount of heat was added/removed at compressor outlet (after compression process) depending on turbocharger working conditions. For the case showed in figure 2.2 heat was lost ($q2_{lost}$). The same approach was previously proposed by Shaaban [156, 157], Bohn [22, 21] and Hagelstein [78]. On the turbine side Serrano proposed that heat flux was lost at turbine inlet ($q3_{lost}$), later the adiabatic expansion occurred (from $30q$ to $4'q$). Finally another amount of heat flux was lost at turbine outlet ($q4_{lost}$) after the expansion process. With that level of detail, difficulties in instrumentation for experimental characterization increased.

Models presented by Sidorow et al. [162] proposed also the division of compression and expansion processes into three stages. That work investigated the reliability of integrating a turbocharger model into onboard fault diagnosis. Turbocharger thermodynamic approach was based on Euler's turbomachinery equation for adiabatic enthalpy calculations in compressor and turbine [183, 192] but considering heat transfer in the housing [163].

For the compression process shown on the left side of figure 2.4, diabatic enthalpy difference ($\Delta h_{c,dia}$) was obtained from measured temperatures between compressor inlet (T_1) and outlet (T_{2c}). This diabatic process included the intrinsically compression process but also heat transfer phenomena. Heat transfer was considered to occur at two locations on the flow path. A first heat

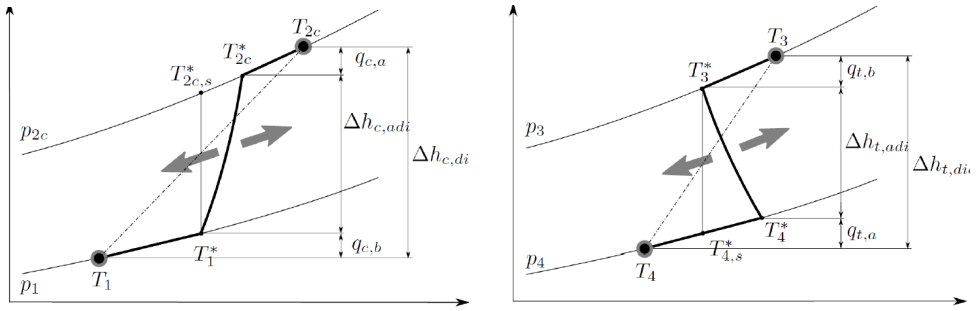

Figure 2.4: Diabatic processes in a turbocharger from Sidorow et al.[162]. Left: Compression process. Right: Expansion process.

flux ($q_{c,b}$) increased compressor inlet temperature (from T_1 to T_1^*) before the compression process. After that, adiabatic compression occurred increasing temperature from T_1^* to T_{2c}^*. Finally the third step included another source of heat flux after the compression ($q_{c,a}$) which increased adiabatic outlet temperature (T_{2c}^*) up to the measured outlet temperature $T_{2,c}$. In that study heat fluxes to the compressor were considered only as an inflow increasing its temperature for any given operative condition. Diabatic enthalpy difference was calculated using equation 2.16. Where $c_{p,a}$ represented specific heat capacity at constant pressure for the fresh air (it was assumed a constant value).

$$\begin{aligned}\Delta h_{c,dia} = c_{p,a} \cdot (T_{2c} - T_1) = q_{c,b} + \Delta h_{c,adi} + q_{c,a} = \\ c_{p,a} \cdot \left[(T_1^* - T_1) + (T_{2c}^* - T_1^*) + (T_{2c} - T_{2c}^*)\right]\end{aligned} \tag{2.16}$$

The same approach was considered for the turbine side, firstly a heat flux was released at turbine inlet conditions ($q_{t,b}$). Next, adiabatic expansion between temperature levels T_3^* and T_4^* took place. Finally, another heat flux was released ($q_{t,a}$), being T_4 the measured outlet temperature. Whole process was expressed in equation 2.17.

$$\begin{aligned}\Delta h_{t,dia} = c_{p,e} \cdot (T_3 - T_4) = q_{t,b} + \Delta h_{t,adi} + q_{t,a} = \\ c_{p,e} \cdot \left[(T_3 - T_3^*) + (T_3^* - T_4^*) + (T_4^* - T_4)\right]\end{aligned} \tag{2.17}$$

Temperatures before (T_1^* and T_3^*) and after (T_{2c}^* and T_4^*) the adiabatic work exchange were calculated using Newton's cooling law.

$$T_1^* = T_1 + \frac{h_{q,c,b} \cdot A_{c,b}}{c_{p,a} \cdot \dot{m}_c} \cdot (T_3 - T_1) \tag{2.18}$$

$$T_{2c}^* = T_{2c} - \frac{h_{q,c,a} \cdot A_{c,a}}{c_{p,a} \cdot \dot{m}_c} \cdot (T_3 - T_2) \tag{2.19}$$

Equations 2.18 and 2.19 show, how unmeasured temperatures T_1^* and T_{2c}^* were calculated using turbine inlet temperature (T_3) and heat transfer coefficients ($h_{q,c,b}$ and $h_{q,c,a}$). Temperatures before and after adiabatic expansion process (T_3^* and T_4^*) were calculated using equations 2.20 and 2.21.

$$T_3^* = T_3 - \frac{h_{q,t,b} \cdot A_{t,b}}{c_{p,e} \cdot \dot{m}_t} \cdot (T_3 - T_1) \tag{2.20}$$

$$T_4^* = T_4 + \frac{h_{q,t,a} \cdot A_{t,a}}{c_{p,e} \cdot \dot{m}_t} \cdot (T_4 - T_1) \tag{2.21}$$

As it is observed unmeasured temperatures (T_3^* and T_4^*) were determined using compressor inlet measured temperature (T_1) and heat transfer coefficients ($h_{q,t,b}$ and $h_{q,t,a}$). Adiabatic compressor outlet temperature (T_{2c}^*) was calculated from isentropic exit temperature (equation 2.1) and isentropic efficiency definition (equation 2.2), both expressions lead to,

$$\eta_c = \frac{c_{p,a} \cdot T_1^* \cdot \left(\left[\frac{p_{2c}}{p_1} \right]^{\frac{\gamma-1}{\gamma}} - 1 \right)}{\Delta h_{c,adi}} \tag{2.22}$$

Same procedure was followed in turbine adiabatic enthalpy calculation, as showed by equation 2.23.

$$\eta_t = \frac{\Delta h_{t,ad}}{c_{p,e} \cdot T_3^* \cdot \left(1 - \left[\frac{p_4}{p_3} \right]^{\frac{\gamma-1}{\gamma}} \right)} \tag{2.23}$$

Isentropic efficiency from equation 2.22 was modelled as a neuronal net of type LOLIMOT (Local Linear Model Trees) for nonlinear dynamic system

identification [115]. That neuronal net depended on turbocharger corrected speed and compressor corrected mass flow. Turbine isentropic efficiency defined in terms of turbine blade speed ratio (equation 2.24) and stator vanes geometry [76] was interpolated using polynomials as proposed by Sidorow et al. [163] and modelled by means of neuronal net LOLIMOT.

$$\sigma = \frac{u}{c_s} = \frac{\pi \cdot D_T \cdot N}{\sqrt{2 \cdot c_{p,e} \cdot T_{30} \cdot \left(1 - \left[\frac{p_3}{p_4}\right]^{\frac{1-\gamma}{\gamma}}\right)}} \tag{2.24}$$

Being u blade tip speed velocity and c_s isentropic gas velocity. As equations 2.22 and 2.23 show, temperatures before the work exchange process (T_1^* and T_3^*) were needed. Those temperatures depended on heat transfer coefficients h and heat transfer areas A both for the turbine and compressor, before and after the work process. Those parameters were fitted using experimental data in the proposed model.

Romagnoli et al. [141] studied turbocharger internal heat transfer phenomena by means of an extensive experimental campaign on an engine test cell. Turbocharger internal heat transfer paths according to those works are represented in figure 2.5.

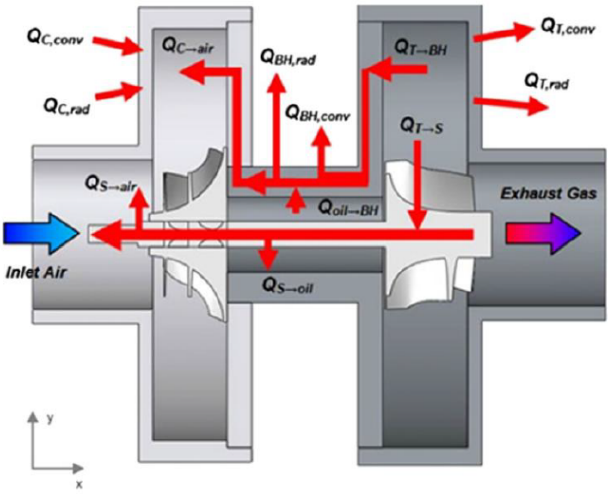

Figure 2.5: Energy fluxes in a turbocharger [141]

Turbocharger was instrumented using several thermocouples to measure internal and external wall temperatures for compressor, turbine and housing. Turbocharger thermocouples were installed at three positions; near the engine, in the top part and in the external side. That set-up confirmed that turbine and compressor surface temperatures were not uniform when the turbocharger was installed in an engine layout. Besides, a clear difference between inner and external temperature for any given position in the turbocharger was observed. That phenomena justified that heat was conducted through the wall and later was dissipated by radiation and convection to the surroundings. Compression process was divided into three stages, being compression within the impeller considered as adiabatic. The addition of external heat transfer was split into two parts, one before the compression and the other after that. One of the main contributions of that model was the proposal of a correlation for compressor outlet temperature. To calculate that temperature, the model assumed that heat transferred to the compressed air after the impeller arrived through the compressor back-plate. In that case, back-plate temperature (T_{BP}) was equal to housing surface temperature. Heat flux added after the compression was calculated using equation 2.25.

$$\dot{Q} = h \cdot A_{BP} \cdot (T_{BP} - T_{2,adi}) = \dot{m}_a \cdot c_{p,a} \cdot (T_2 - T_{2,adi}) \tag{2.25}$$

Being A the wetted area and h the film coefficient. Rearranging for compressor outlet temperature (T_2),

$$T_2 = T_{2,adi} + \frac{h \cdot A_{BP}}{\dot{m}_a \cdot c_{p,a}} \cdot (T_{BP} - T_{2,adi}) \tag{2.26}$$

Temperature after adiabatic compression ($T_{2,adi}$) and back-plate temperature (T_{BP}) were unknown in equation 2.26. To simplify that problem, heat transferred before compression was assumed negligible due to the small exposed area at compressor inlet. Being impeller inlet temperature equal to compressor inlet temperature. That simplification allowed the calculation of adiabatic compression temperature ($T_{2,adi}$). On the other hand, experimental results showed a linear trend between housing wall temperature and turbine inlet temperature, both assumptions allowed for compressor outlet temperature calculation. That model considered too the heat flux to the wheels due to their gradient of temperature during expansion/compression processes.

That heat flux was transmitted along the shaft, and later partially removed by forced convection with the lubricating oil.

Studies from Shaaban et al. [158] proposed turbocharger measurements in a gas stand with cold (adiabatic) and hot (non-adiabatic) conditions to develop a heat transfer model. A large number of infinitesimal compression stages were assumed. Compression process in each infinitesimal stage was assumed to be adiabatic allowing its outlet temperature calculation, meanwhile heat transfer was considered to occur between infinitesimal stages. Thermal energy transferred to the compressor was assumed by the model. That amount was recalculated until compressor outlet temperature prediction and measured value converged. The study pointed out the importance of heat transfer in compressor performance, mainly for low rotational speeds. For instance at 60,000 rpm thermal energy transferred to the compressor represented 35% of total enthalpy increase across the compressor.

2.2.2 Empirical Models

Among the existing empirical models to account for heat transfer phenomena in automotive turbochargers, the proposal of Aghaali and Angstrom [7] has been pointed out. The study was based on an extensive experimental methodology of a water cooled turbocharger installed in a 2.0 litres spark turbocharged engine. Heat transfer phenomena was correlated with engine and turbocharger operative conditions. In order to do so, two test campaigns were carried out and later simulated using whole engine model in GT-Power^{TM} [73]. Analysis including or not heat transfer effects were performed, it was assumed that thermal flux occurred after the compressor impeller and before the turbine rotor. According to that proposal, heat transfer was simulated in GT-Power^{TM} adding a heat sink before the turbine expansion (placed in the volute) and a heat source after the compression (placed in the scroll). To avoid any disturbance in pulsating prediction, the extra added length was compensated reducing the length of adjacent pipes. A PID controller was introduced to fit compressor and turbine simulated outlet temperatures to the measured ones. In case heat transfer phenomena was not considered, multiplier coefficients were used to modify compressor and turbine efficiencies fitting so simulated outgoing temperatures.The following conclusions were obtained using the proposed empirical model.

- Turbocharger heat transfer becomes important as engine speed and load increases (higher exhaust gases temperatures and mass flows).
- Compressor receives more heat from housing when no water is used (water circuit works as a heat barrier between turbine and compressor).
- Radiation from turbine back to compressor back has no significant effect (small areas).
- Simulations without heat transfer model needed multiplier coefficients far from one to fit compressor and turbine outlet temperatures. Those multipliers were loading dependent what reduced simulation predictability.
- Linear correlation between compressor heat transfer and compressor power was found (for water-cooled turbochargers). Second order correlation was proposed for no water-cooled turbochargers. Both trends turned into second order degree relation in case compressor heat flux was correlated to engine brake power.
- Logarithmic relation between turbine heat transfer and its power was found in both water cooled and no water cooled simulations. That trend turned into a linear tendency with engine brake power.

Two last features allowed heat transfer correlation extrapolation to non-measured operative conditions, making that empirical proposal more reliable in engine simulation codes.

2.2.3 CFD Models

Several studies using CFD models to investigate heat transfer phenomena inside small turbochargers have been done to analyse its impact on the overall performance. For instance, model proposed by Verstraete et al. [177] studied 3-D conduction using finite element analysis (FEA) inside the rotor and stator of three different sized micro gas turbines. 3-D flow in the radial compressor, turbine and gap between stator and rotor was calculated by means of non-adiabatic Navier-Stokes (NS) solver. Main advantage of that proposal was that the standard solvers and grid generators were used. Nevertheless the non-coinciding grids at the common interface made necessary an iterative process

to pass information between both boundaries. Heat transfer areas of the gas turbine are shown on the left side of figure 2.6, those areas correspond to the description given in table 2.1. One of the important contributions of that work was the analysis of temperature distribution in a turbomachine cutting as figure 2.6 shows on its right. Despite big differences in temperature between turbine rotor and compressor impeller, only a small heat flux was transferred along the shaft of the turbomachine.

Those results supported the general assumption done by other studies considering neither the heat flux between turbine and compressor by means of conduction along the shaft (path E) nor the internal convection to the wheels (paths H and B) [14]. In that case the problem was simplified by considering only internal convection from the exhaust gases to the turbine volute (path F). That heat flux was transmitted by conduction along the turbocharger housing passing later to compressor diffuser due to its higher exposed area (path D) what increased compressed air temperature. Relative importance of external convection at compressor case (path A), mainly for the smallest turbocharger, was also observed. Effect of compressor blow-by, due to pressure differences between compressor and turbine was also studied. This cold blow-by acted like a coolant taking away heat from the stator.

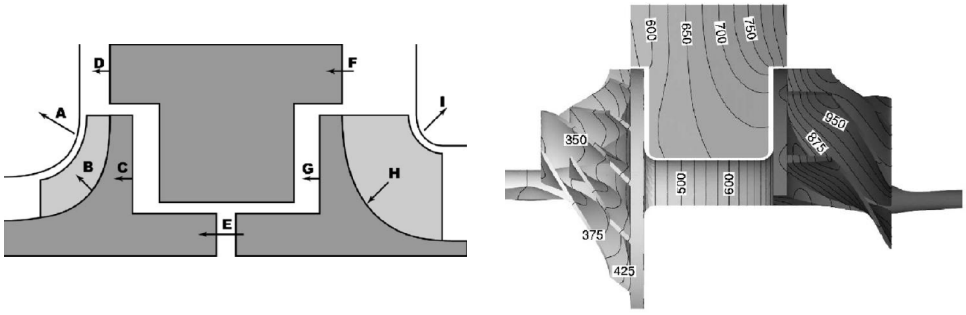

Figure 2.6: Heat transfer studies from Verstraete et al. [177], Left: Calculation domain, Right: Temperature distribution (in K degrees).

Among other CFD works investigating heat transfer phenomena in automotive turbochargers, the research from Bohn et al. [22] can be highlighted. In that work, compressor heat transfer problem was computed using CFD codes. Twelve different operative conditions [23] changing turbine inlet temperature and compressor mass flow were studied. Several topics can be pointed out

Table 2.1: Heat transfer analysis from Verstraete et al. [177].

Region	Description	Relative importance (%)			Heat fluxes (W)		
		small	**medium**	**large**	**small**	**medium**	**large**
A	Heat flux from compressor case to the surroundings (convection)	25.9	23.4	17.6	84	217	490
B	Heat flux from the compressor impeller to the air (convection)	9.3	8.2	7.6	30	76	213
C	Heat flux from the compressor back to the compressor wheel (convection)	3.7	3.8	4.2	12	35	116
D	Heat flux in compressor diffuser from the stator conduction (convection)	15.4	15.1	13.7	50	140	382
E	Heat flux from turbine wheel to compressor wheel (conduction along the shaft)	3.7	2.7	1.6	12	25	44
F	Heat flux into the stator from turbine volute (convection)	22.2	22.4	23.5	72	208	655
G	Heat flux from turbine wheel to turbine back (convection)	3.1	5.0	6.1	10	46	169
H	Heat flux from the exhaust gases to the turbine rotor (convection)	8.0	9.2	9.2	26	85	257
I	Heat flux from turbine case to the surroundings (convection)	8.6	10.2	16.6	28	95	462
					324	**927**	**2788**

from that work,

- Turbocharger heat transfer paths were described according to the diagram on the left side of figure 2.7. As it is observed, turbocharger model was divided into turbine, central housing and compressor planes. One part of the enthalpy drop across the turbine was converted into mechanical power (P_T). Then it was transmitted along the shaft to the compressor wheel. Only a part of that mechanical power get to the compressor (P_C), the remaining heated up the lubricating oil due to friction losses (Q_{oil}). Remaining turbine energy (that was not converted into mechanical power) was transmitted as a heat flux. Whether to the surroundings by means of natural convection ($Q_{nC,T}$) and thermal radiation ($Q_{R,T}$) or by conduction along the turbocharger housing ($Q_{T,H}$). Only a part of that heat get to the compressor side since turbocharger housing exchanged heat with the surroundings by means of natural convection ($Q_{nC,H}$) and radiation ($Q_{R,H}$) but also increased lube oil temperature due to forced convection (Q_{OC}).
- No differences in radial surface temperature along the turbocharger were observed (right side of figure 2.7). What meant that heat transfer phenomena was conducted only by temperature differences in the axial direction (from hot turbine to cold compressor) being negligible the heat

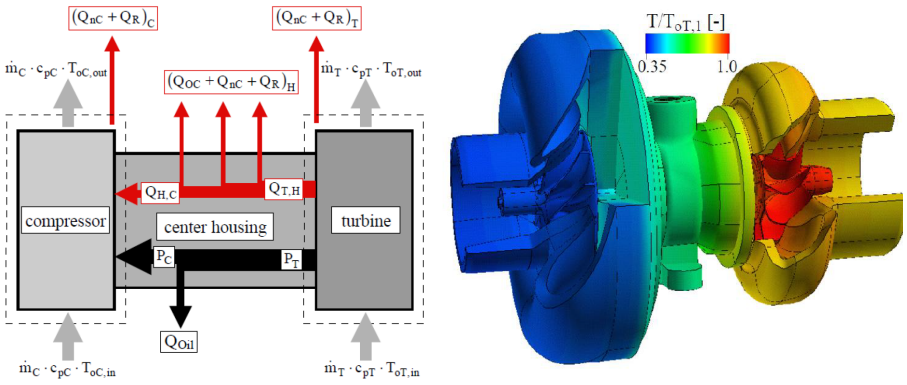

Figure 2.7: Heat transfer studies from Bohn et al. [22], Left:Heat transfer paths, Right:Surface temperature distribution.

transfer in the radial direction. That assumption allowed heat transfer simplification into a one-dimensional analysis.

- A total of 60 cutting planes were introduced at compressor side in order to analyse heat transfer phenomena in detail (left side of figure 2.8). It was observed that heat fluxes in the compressor side become important at the second half of the compressor proposed model. What meant from position 0.5 to 0.75 (blades section) and from position 0.75 to 1 (diffuser section).

- Compressed air at the diffuser could be heated up or cooled down depending on compressor operative conditions. First occurred for small compressor mass flows and the second for higher compressor ratios where compressed air temperature was higher than compressor casing temperature.

- Compressor heat transfer calculation was based on an artificial Reynolds number correlation. It was based on compressor internal geometry and the temperature drop between compressor inlet (T_{01}^C) and turbine inlet (T_{01}^T). General expression used to calculate that heat was given by equation 2.27, where temperature drop (ΔT_0) and contact area (A_C) were defined in equations 2.28 and 2.29. Compressor geometry was defined on the right side of figure 2.8.

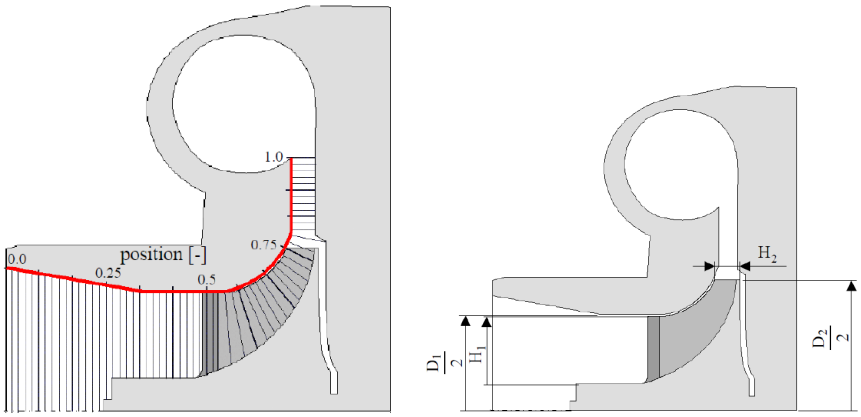

Figure 2.8: Heat transfer studies at compressor side by Bohn et al.[22], Left:Cutting planes, Right:Geometry for heat transfer characterization.

$$Q_C = h_C \cdot \Delta T_0 \cdot A_C \tag{2.27}$$

$$\Delta T_0 = T_{01}^T - T_{01}^C \tag{2.28}$$

$$A_C = \frac{\pi}{2} \cdot (D_2 - D_1 + 2 \cdot H_1)^2 \tag{2.29}$$

Using Nusselt number definition,

$$Nu_C = \frac{h_C \cdot l_c}{\kappa} \tag{2.30}$$

Where thermal conductivity (κ) of the air passing through the compressor was determined at the mean temperature between compressor and turbine inlet. Characteristic length (l_C) for Nusselt correlation was calculated using equation 2.31.

$$l_c = \frac{\pi}{4} \cdot (D_2 - D_1 + 2 \cdot H_1) \tag{2.31}$$

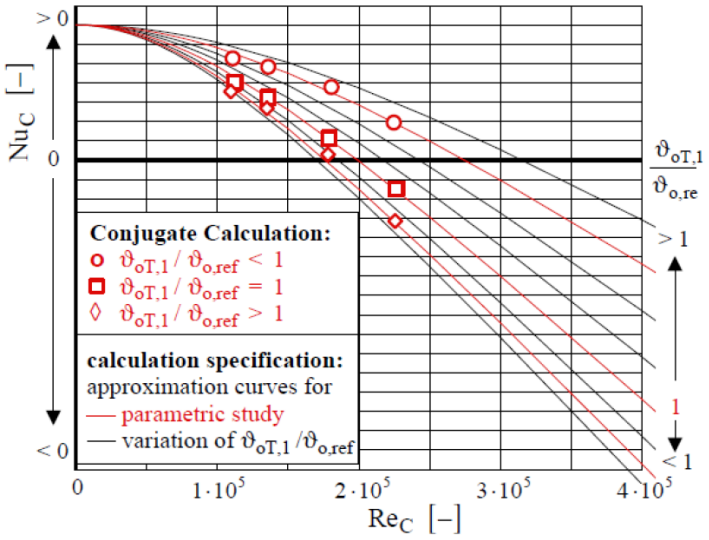

Figure 2.9: Modelling results from Bohn et al. [22], relation between Nu and Re.

Compressor Nusselt number calculated with equations above was represented in figure 2.9 versus Reynolds artificial number according to equation 2.32. A trend between compressor Nusselt number (conducting internal heat transfer) and Reynolds number calculated at inlet conditions (including operative conditions)was found as shown in equation 2.33.

$$\mathrm{Re_C} = \frac{\dot{m}_c}{\mu_{c,1}} \cdot \frac{\mathrm{D_2 - D_1 + 2 \cdot H_1}}{4 \cdot \mathrm{D_2 \cdot H_2}} \tag{2.32}$$

$$\mathrm{Nu_C} = \mathrm{Nu_0} - \sqrt{\mathrm{p^2} - \left(\frac{\mathrm{Re_C^2}}{1 - \varepsilon^2}\right)} \tag{2.33}$$

Where parameter ϵ^2 was defined as,

$$\varepsilon^2 = \varepsilon_0 \cdot e^{\frac{-T_{01}^T}{\varepsilon_1}} + \varepsilon_2 \cdot T_{01}^T \tag{2.34}$$

Being p, Nu_0, ϵ_0, ϵ_1, ϵ_2 fitting constants.

Previous equations allowed compressor heat transfer calculations for any operative conditions.

2.3 Models to Characterize Mechanical Losses in Turbochargers

Mechanical losses in turbochargers are produced in the bearings placed at the connecting shaft which holds the turbine and the compressor wheels. Most of current turbochargers include two kinds of bearings as it is shown in cutting figure 2.10. The two journal bearings are designed to reduce friction losses due to the high rotational speeds. Meanwhile the double-acting axial thrust bearing (near the compressor inducer) bears with the axial load due to the force unbalance between compressor and turbine wheels.

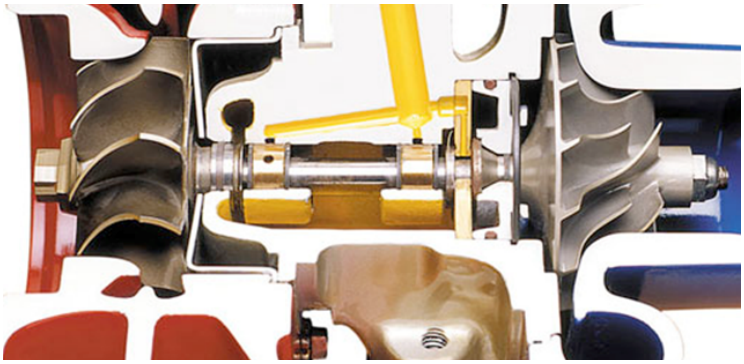

Figure 2.10: Detailed view of turbocharger bearings.

Mechanical friction losses produced in the turbocharger during operative conditions are commonly given in terms of non-dimensional variables. In such way turbocharger mechanical efficiency (η_m) is introduced. This efficiency is generally defined as the ratio of mechanical powers between the conducted machine (compressor) and the driving machine (turbine) as equation 2.35 shows.

$$\eta_m = \frac{\dot{W}_C}{\dot{W}_T} \tag{2.35}$$

Turbocharger manufacturers do not usually provide reliable information

about mechanical friction losses. What is traditionally given by manufacturers in a turbine efficiency map is the global value of both turbine (isentropic) and turbocharger (mechanical) efficiencies together but also including heat transfer effects as equation 2.36 shows.

$$\eta_T = \frac{\dot{W}_C}{\dot{W}_{T,s}} \tag{2.36}$$

In general, when a mechanical efficiency value is needed, with neither the heat transfer effects nor the turbine isentropic efficiency, a typical constant value of 0.9 is assumed. Nevertheless that assumption is no longer valid for rotational speeds lower than 100,000 krpm [46] such as the occurring for urban driving conditions [145]. When turbocharger off-design operative conditions are studied, such a big approximation in mechanical efficiency cannot be done as showed by Galindo et al. [64].

Several studies have been done up to this moment in order to determine experimentally and later to characterize mechanical friction losses, both in terms of efficiency and in terms of power. In the following sections both aspects will be summarized.

2.3.1 Experimental identification of friction losses

As it has been mentioned before, the knowledge of mechanical friction losses is key for turbocharger lower operation speeds [145]. Accurate measurements in that area becomes a difficult task since sensitive measuring devices are needed. Several experimental techniques allowing mechanical friction losses determination have been investigated.

2.3.1.1 Indirect measuring

One of the traditional ways to determine turbocharger friction losses derives from the indirect measurements in a test cell. Those techniques are widespread in turbocharger research providing good results in a range from medium to high turbocharger rotational speeds. Nevertheless, that mechanical efficiency has been determined indirectly from the measurement of other turbocharger

parameters, and so the lower is the load (reduced speeds) the more difficult becomes the measurement procedure. In those cases, uncertainties from measurements and error propagation can exceed the magnitude of parameter under evaluation. For those reasons a carefully experimental methodology is required if the region of low loads is under study [132]. Among the indirect methodologies for mechanical friction losses determination, measurement of lube oil enthalpy variation and the unbalance between compressor and turbine mechanical powers point out over the others.

- Enthalpy variation of the lubricating oil

  This technique requires the installation of the turbocharger unit into a test cell where compressor, turbine and oil temperatures and mass flows can be controlled as desired [132, 104]. This procedure allows friction losses determination as the rate of change of lubricating oil enthalpy across the turbocharger using equation 2.37 [18]. Advantages of this technique can be summarized in its low price (if the gas-stand exists) and the easy controlled tests. But in the drawbacks side, technique's accuracy is comprised to measurements accuracy since small magnitudes are measured at low turbocharger speeds. In addition, having a good measure of oil outlet temperature is a difficult task due to the mixing flow with the blow-by coming from the turbine side.

  $$\dot{W}_m = \dot{m}_{oil} \cdot c_{p,oil} \cdot \left(T_{oil}^{out} - T_{oil}^{in}\right) \tag{2.37}$$

  If accurate measurements are needed, this technique must be enhanced avoiding internal heat transfer phenomena [44]. One of the proposals from the literature is the almost-adiabatic methodology presented by Payri et al. [132]. It consisted of minimising turbocharger external heat transfer to the surroundings by fully insulating the turbocharger unit. Meanwhile the internal heat transfer was reduced imposing the same temperature at turbine inlet, lubricating oil inlet and compressor outlet. Doing so the absorbed energy by the lubricating oil comes mainly from heat generated by friction [14, 36] since turbocharger behaviour is almost adiabatic and turbine blow-by is at the same temperature than oil inlet. If adiabatic assumption could not be assumed, due to turbocharger operative conditions, an exergy analysis should be used instead [49].

- Power unbalance between compressor and turbine

Other way to determine turbocharger friction losses indirectly is based in the power balance shown in equation 2.38. That method provides good results only if gas evolution inside turbine and compressor are adiabatic. As in the method presented above, accuracy of that technique improves if the turbocharger is fully insulated and operating temperatures are chosen to reduce heat transfer exchange.

$$\dot{W}_m = \dot{W}_T - \dot{W}_C \tag{2.38}$$

In case compressor wheel is removed, friction power can be determined directly as the power extracted by the turbine since no compression work is done [101].

2.3.1.2 Direct measuring

Accurate measurement of mechanical friction losses can be directly obtained, mainly at the low loads area, measuring the friction torque. That can be done by installing a rotating torquemeter between the driving (turbine wheel or an electric motor) and the central housing containing the bearings. Experiments carried out by Povedin et al. [135, 136, 137] about turbocharger performance at low speeds showed the difficulty of measuring friction losses at those conditions. They showed also the importance of oil characteristics for correct mechanical losses determination [134] on the whole engine performance [75]. Those studies agreed with results presented by Lamquin and Gjika [101] and Shmitt et al. [144]. Torquemeter used in the studies of Povedin et al. [135, 136, 137] included an axial load system to measure alone friction forces due to the axial thrust bearing [45]. An experimental methodology for turbocharger low loads characterization was designed. Turbocharger speeds of 50,70 and 90 krpm were tested with low levels of oil inlet temperature. In case of journal bearings characterization alone, temperatures of 20°C and 40°C were tested. For the higher temperature level, three oil inlet pressure levels (2,3 and 4 bars) were used. Friction losses reduction in journal bearing was confirmed as oil inlet temperature increased (due to oil viscosity drop). It was also observed that the higher was the oil inlet pressure, the higher were friction losses. It was due to the corresponding increase in oil mass flow being higher the cooling effect of the oil stream over bearings temperature. That effect was translated into a local decrease in oil temperature inside the bearings,

increasing so oil viscosity and consequently frictional losses. Global mechanical losses were studied using two oil inlet temperatures (40°C and 60°C) with five levels of axial load forces. The study confirmed friction reduction as oil temperature increased but also revealed the increase in friction losses when axial forces increased, appearing a linear trend between both parameters for low turbocharger speeds. Finally it was pointed out the relative importance of both the journal and thrust bearings in mechanical friction losses and oil mass flow repartition. It was shown that thrust bearing weighted more than 60% of the overall losses [44, 178]. Similar studies were done but focusing on the compressor performance variation modifying lubricating oil parameters (inlet temperature and pressure) [134]. Importance of both parameters in heat transfer exchange to the compressor was demonstrated, affecting compressor efficiency determination. Similar studies using a torquemeter test bench but removing turbocharger wheels and generating axial forces with an electromagnetic device were carried out by Schmitt et al. [144].

2.3.2 Models to characterize friction losses

Several models have been presented in the literature in order to characterize mechanical friction losses in a turbocharger. They range from the empirical model proposed by Payri et al. [132] to one-dimensional models as the presented by Serrano et al. [153, 154] or models based on Computational Fluid Dynamics (CFD) as the proposed by Deligant et al. [43]. Correlations proposed in the two first models are derived from the indirect measurement of mechanical friction losses by means of oil enthalpy variation across the turbochargers.

2.3.2.1 Empirical model

Empirical model proposed by Payri et al. [132] was based on a wide experimental test campaign of the turbocharger under almost-adiabatic steady flow conditions. Experiments were focused in the region of low speed of the turbocharger in order to keep valid the hypothesis of almost-adiabatic behaviour. Four levels of oil inlet temperature (60°C, 70°C, 80°C and 90°C) and three levels of oil pressure (2, 3 and 4 bars) were studied. Mechanical friction losses were determined using aforementioned techniques of indirect measurements, i.e. oil enthalpy variation and power unbalance. Good agreement in mechani-

cal friction losses determination using both techniques was pointed out thanks to discounting the small heat fluxes from the measurements. The study proposed correlating mechanical efficiency by means of dimensionless parameters taking into account factors affecting friction losses. With that aim Reynolds number defined in equation 2.39 was introduced.

$$\mathrm{Re} = \frac{\rho_{\mathrm{oil}} \cdot \mathrm{u} \cdot \mathrm{HD}}{\mu_{\mathrm{oil}}} \tag{2.39}$$

Type of oil and mass flow were taken into account in that equation under the density (ρ) and dynamic viscosity (μ). Bearing geometry and turbocharger speed (N) were considered in equation 2.40. Where u represented shaft velocity and HD clearance factor defined as the gap between bearing internal diameter and shaft diameter.

$$u = \frac{\pi \cdot N \cdot D}{60} \tag{2.40}$$

Representing mechanical efficiency (from the indirect measurements) versus Reynolds number (defined in equation 2.39) it was observed that measurements were grouped by oil temperatures. For that reason Prandtl number was included to consider oil temperature variations. Finally, dimensionless parameter representing the axial load in the thrust bearing was introduced. According to Hu et al. [85], axial thrust of the turbocharger was mostly determined by the static pressure difference of compressor impeller and turbine's back plate, which was related to the compressor impeller outlet and turbine inlet pressure. According to previous hypothesis, dimensionless axial thrust was simplified as it is shown in equation 2.41.

$$\frac{\Delta p}{p} = \frac{p_{oil}^{in} - \left[p_3 - \left(\frac{p_1+p_2}{2}\right)\right]}{p_{oil}^{in}} \tag{2.41}$$

Being p_3 turbine inlet pressure meanwhile p_1 and p_2 were compressor inlet and outlet pressures. It was assumed that the averaged value in compressor pressures corresponded to impeller outlet pressure. Taking into account the aforesaid factors, correlation proposed by Payri et al. [132] had the form shown in equation 2.42. An exponential dependency was chosen since mechanical efficiency must lie between zero and one,.

$$\eta_{mech} = k1 \cdot \left[1 - e^{-k2 \cdot \mathrm{Re}^{k3} \cdot \mathrm{Pr}^{k4}}\right] + (1 - k1) \cdot \left[1 - e^{-k5 \cdot \left(\frac{\Delta p}{p}\right)^{k6}}\right] \tag{2.42}$$

Coefficients from $k1$ to $k6$ were determined from experimental measurements using least squares fitting method. Good agreement between measured and modelled mechanical efficiency was obtained.

2.3.2.2 One-Dimensional model

One dimensional model proposed by Serrano et al. [153, 154] was based on oil enthalpy variation across the turbocharger. That model solved the Navier-Stokes (NS) equations for both the journal bearing and the axial thrust bearing in a simplified way assuming the following hypothesis,

1. Oil behaves as an incompressible fluid.
2. Flow through the bearing is steady.
3. Bearing is long enough to consider constant behaviour on each section.
4. Flow is circumferentially symmetric.
5. Body forces are negligible.
6. Reynolds number is expected to be small enough to make the viscous stresses comparable to the inertial forces of the fluid.
7. Film thickness in the bearing is smaller than any other bearing geometry.

Mechanical losses according to that model are defined using equation 2.43. Where $\dot{W}_{jb}$ represented journal bearing losses and $\dot{W}_{tb}$ friction losses on axial thrust bearing.

$$\dot{W}_m = \dot{W}_{jb} + \dot{W}_{tb} \tag{2.43}$$

Friction losses on the radial bearing are defined according to expression 2.44. As it is observed, those losses are dependant of shaft rotational speed

(N), oil viscosity (μ), geometrical parameters like journal bearing radius (R_{jb}) and bearing length (L_{jb}), oil film thickness (h_{jb}) and fitting parameter k_{jb}.

$$\dot{W}_{jb} = 2 \cdot \pi \cdot R_{jb}^3 \cdot k_{jb} \frac{L_{jb}}{h_{jb}} \cdot \mu \left(\bar{T}_{oil}\right) \cdot N^2 \tag{2.44}$$

Meanwhile friction losses on the thrust bearing are defined using expression 2.45. Where k_{tb} is a fitting factor, $R_{tb,max}$, $R_{tb,min}$ and $\bar{R}_{tb}$ are maximum, minimum and average radius of axial thrust bearing, being φ a geometrical factor defined using those radius. F_{at} is a pressure term accounting for compressor and turbine forces acting to the thrust bearing. Finally k_m denotes the fraction of lubricating oil mass flow (m) passing through the axial bearing. Detailed physics description can be found in works from Serrano et al. [153, 154].

$$\dot{W}_{tb} = k_{tb} \cdot \pi \left(R_{tb,max}^2 - R_{tb,min}^2\right) \cdot \bar{R}_{tb}^2 \cdot \sqrt[3]{\left|\frac{F_{at} \cdot \rho}{12 \cdot k_m \cdot m \cdot \varphi \cdot \mu}\right|} \cdot \mu \cdot N^2 \tag{2.45}$$

Although that model was based on bearings geometry only, some corrector parameters were needed in order to compensate the aforementioned simplifications. Good agreement with experimental results were found for different oil inlet tested conditions (pressure and temperature) and different turbochargers (different size and bearing's configuration). Potential of that method arose in the separated study of friction losses in journal and thrust bearing. Besides it was physically based and could be applied using a reduced amount of measurements. Due to the fact that the model was derived from Navier-Stokes equations, the same methodology could be extrapolated to calculate mechanical friction losses in journal bearing of the engine that Serrano [154] and Coy [40] showed how they can reach the 40% of the total mechanical power losses.

2.3.2.3 CFD models

Recent studies have introduced Computational Fluid Dynamics (CFD) calculations to mechanical friction losses determination of the turbocharger. Among those studies the proposed by Deligant et al. [43] were only concerned to the journal bearing losses, considering half of the journal bearing geometry due

to its symmetry. That model solved equations of continuity, momentum conservation and the energy balance at each one of the calculation cells (a total of 111,600 cells). A laminar oil flow was assumed inside the bearing, if the flow could not be assumed laminar, studies of Bouard et al. [25] could be taken into account. Load in the journal bearing was assumed to be constant and no cavitation was considered. The study showed good agreement with experimental results for different oil inlet temperatures and pressures.

2.4 Models to Characterize Non-Steady Compressor Behaviour

First step to well predict turbocharger performance under non-steady behaviour begins with the development of tools allowing the extrapolation in manufacturer maps. Those maps are the source of information for current engine computational codes. Those tools are needed since manufacturer maps are poorly discretized (interpolation) and are usually given in a narrow area and only for higher turbocharger speeds typically over 90,000 rpm (extrapolation) [91, 105, 109]. Two trends in turbocharger modelling have been found in literature survey. First kind of techniques are based on physical equations as the proposed by Descombes et al. [47], Jiang et al. [90] and Nasser [114]. Second trend is based on the storage of turbocharger performance data into lookup tables using mathematical algorithms for intra-extrapolation [76, 109]. In the following sections, current methodologies and modelling tools for the unsteady characterization of compressor are analysed.

2.4.1 Compressor Extrapolation Techniques

Among existing curve fitting methods for compressor performances maps, proposals by Jensen et al. [89], Mueller [113], Kolmanovsky et al. [98], Martin et al. [105] and Nelson et.al [117] can be pointed out.

Jensen method [89] was a simplification of the model proposed by Winkler [186]. That model used dimensionless head parameter (Ψ) defined in equation 2.46 and compressor efficiency (η_C). Where u represented compressor blade tip speed.

$$\Psi = \frac{c_p \cdot T_{amb} \cdot \left[\left(\frac{p_2}{p_1} \right)^{\frac{\gamma-1}{\gamma}} - 1 \right]}{\frac{1}{2} \cdot u^2} \tag{2.46}$$

That model proposed correlating head parameter (Ψ) and compressor efficiency (η_C) with functions of normalized compressor flow rate (Φ) and Mach number (M) calculated at compressor inlet conditions defined by equations 2.47 and 2.48. Those function are showed in equations 2.49 and 2.50.

$$\Phi = \frac{\dot{m}_c}{\rho_{amb} \cdot \frac{\pi}{4} \cdot D_C^2 \cdot u} \tag{2.47}$$

$$\mathrm{M_{in}} = \frac{\mathrm{u}}{\sqrt{\gamma \cdot \mathrm{R} \cdot \mathrm{T_{amb}}}} \tag{2.48}$$

$$\Psi = \frac{k_1 + k_2 \cdot \mathrm{M_{in}} + \mathrm{k_3} \cdot \Phi + \mathrm{k_4} \cdot \mathrm{M_{in}} \cdot \Phi}{k_5 + k_6 \cdot \mathrm{M_{in}} - \Phi} \tag{2.49}$$

$$\eta_C = \frac{a_1 + a_2 \cdot \mathrm{M_{in}}}{a_3 - \mathrm{M_{in}}} \cdot \Phi^2 + \frac{a_4 + a_5 \cdot \mathrm{M_{in}}}{a_6 - \mathrm{M_{in}}} \cdot \Phi + \frac{a_7 + a_8 \cdot \mathrm{M_{in}}}{a_9 - \mathrm{M_{in}}} \tag{2.50}$$

Fitting constants k_i and a_i from equations 2.49 and 2.50 were determined via least squares fit of the experimental data. Once head parameter was known, compressor performance could be determined for a given mass flow and rotational turbocharger speed by introducing equation 2.49 into 2.46. That methodology provided stable and accurate results, nevertheless extrapolation to higher and lower speed areas were not so accurate. In addition, head parameter (Ψ) and compressor efficiency (η_C) were not physically related in the surge region what provided no coherent results in this region. Martin et al. [105] proposed a modification on Jensen compressor model to avoid those problems by introducing some physical laws in that model. In addition, fitting constants k_i and a_i from equations 2.49 and 2.50 were fitted at each compressor iso-speed line instead of fitting the whole performance with a unique set of constants. Those modifications improved considerably compressor extrapolation accuracy at the high speed region.

A modification of Jensen proposal was introduced by Andersson [10] who used equation from an ellipsis to relate head parameter (Ψ) and flow coefficient (Φ) as showed by equation 2.51.

$$1 = \left(\frac{\Phi}{a_1}\right)^2 + \left(\frac{\Psi}{a_2}\right)^2 \tag{2.51}$$

The advantage of that proposal was that there were only two fitting coefficients a_1 and a_2, but the solution should be limited to real values, what meant head parameter (Φ) could not be higher than constant a_2.

Sorenson et al. [166] stated that a linear tendency of flow coefficient (Φ) with head parameter (Ψ) divided by compressor efficiency (η_C) could be found as showed by equation 2.52. Eriksson works [55], using different compressors, showed that relation was not exactly a straight line since a slight convexity appeared mainly far from the design points.

$$\Phi = a_1 + a_2 \cdot \frac{\Psi}{\eta_C} \tag{2.52}$$

Mueller proposal [113], combined physical principles and compressor geometry, a quadratic function of head parameter (Ψ) in flow coefficient (Φ) was founded as showed by equation 2.53.

$$\Psi = A \cdot \Phi^2 + B \cdot \Phi + C \tag{2.53}$$

Being A, B and C speed dependant parameters defined in equations 2.54, 2.55 and 2.56. Where $\dot{m}_C^{top}$ represented compressor maximum mass flow for each speedline.

$$A = A_2 \cdot u^2 + A_1 \cdot u + A_0 \tag{2.54}$$

$$B = \frac{-2 \cdot A \cdot \dot{m}_C^{top}}{u} \tag{2.55}$$

$$C = C_2 \cdot u + C_1 \cdot u + C_0 \tag{2.56}$$

Another model used for compressor maps extrapolation was based on Kolmanovsky proposal [98], also named as ZSLM (Zero Slope Line Method). That model proposed a direct correlation between compressor reduced mass flow ($\dot{m}_C^{red}$), defined in equation 2.57, pressure ratio (Π_C) and reduced speed (N_C^{red}) defined by equation 2.58.

$$\dot{m}_C^{red} = \frac{\dot{m}_C \cdot \sqrt{T_{01}}}{p_{01}} \tag{2.57}$$

$$N_C^{red} = \frac{N}{\sqrt{T_{01}}} \tag{2.58}$$

Compressor performance was determined using equation 2.59 for points near the choke limit (steep slope), and using equation 2.60 for rest of cases.

$$\frac{\dot{m}_C^{red}}{\dot{m}_{C,top}^{red}} = 1 + \alpha \cdot \left(1 - e^{k_5 \cdot \left(\frac{\Pi_C}{\Pi_{C,top}} - 1\right)}\right) \tag{2.59}$$

$$\frac{\dot{m}_C^{red}}{\dot{m}_{C,top}^{red}} = 1 - \alpha \cdot k_5 \cdot \left(\frac{\Pi_C}{\Pi_{C,top}} - 1\right) \tag{2.60}$$

Being $\Pi_{C,top}$ the corresponding pressure ratio for maximum mass flow ($\dot{m}_{C,top}^{red}$) for each speed line and α a function of reduced speed as equation 2.61 shows. Quadratic functions for both terms with reduced speed were assumed as equations 2.62 and 2.63 show.

$$\alpha = k_6 \cdot e^{-k_7 \cdot N_C^{red}} \tag{2.61}$$

$$\dot{m}_{C,top}^{red} = k_1 \cdot N_C^{red} + k_2 \cdot \left(N_C^{red}\right)^2 \tag{2.62}$$

$$\Pi_{C,top} = k_3 + k_4 \cdot \left(\dot{m}_{C,top}^{red}\right)^2 \tag{2.63}$$

Neural networks have been recently applied to represent compressor performance. Despite the excellent results obtained with that methodology, the

number of fitting coefficients was large compared to manufacturer supplied data. Nelson et al. [117] reported that 21 parameters were needed for fitting purposes in case of a network with one hidden layer and five neurons was used to represent compressor flow map. Similar approach was repeated using two hidden layers [116].

Spline fitting techniques have been also used for compressor interpolation. With that technique, pairs of data points in compressor map are connected by means of cubic functions. In order to find the unique solution to the four fitting coefficients of each spline, several mathematical conditions must be accomplished [30]. For standard splines, polynomials at the interior nodes must join up (continuity at nodes), polynomials must pass along the first and last points of the series, first and second derivatives must be equal at the interior nodes and the second derivative must be zero at the end nodes. If smoothing splines are used, previous conditions must be accomplished too, but they do not need to pass through interior data points. Finally if Hermite splines are used, same conditions that in standard splines must be accomplished but discontinuities in the second derivative can appear.

Dowell et al. [51] proposed a combination of Jensen and Kristensen (J & K) method [89] with splines fitting techniques. J & K method was used to calculate pressure ratio for zero mass flow and mass flow for pressure ratio unity. Mass flow for zero compressor efficiency was also calculated with J & K method. That methodology supplied artificial points outside the measured compressor performance allowing extrapolation outside normal operative region that could be reach during transients on engine (surge and choke). Both measured and new introduced points were fitted using smoothing splines in compressor mass flow performance and cubic Hermite splines in efficiency performance. The latter ensured the monotonicity avoiding un-physical peaks between each pair of points in the efficiency map. Those peaks will lead to unreliable islands in efficiency in contour plot inside the pressure ratio vs. mass flow map.

Finally some ad-hoc correlations for compressor performance (mass flow, pressure ratio and efficiency) have been proposed fitting measuring data to polynomials expressions as Eriksson proposal [56]. Although those correlations are well-suited for 0D models due to its fast calculation, severe simplifications avoid its use when accurate results are needed.

2.4.1.1 Compressor Geometry for Acoustic non-linear Effects

In order to well predict turbocharger compressor performance under pulsating flow conditions, Torregrosa et al. [172] proposed compressor geometrical scheme shown in figure 2.11.

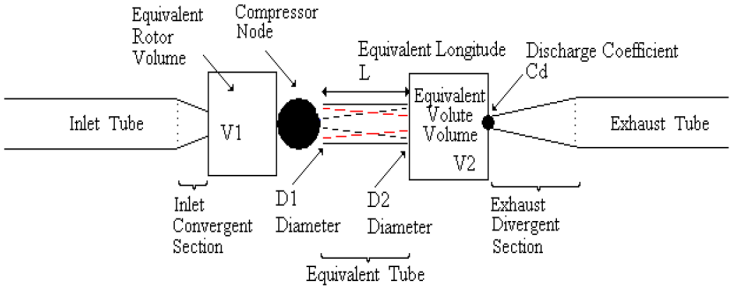

Figure 2.11: Geometrical scheme of the unsteady flow compressor model according to Torregrosa et al. [172]

That model combined pure quasi-steady approach interpolating in compressor chart (named as compressor node in that model) with unsteady elements representing compressor geometry. That assembly was achieved by proper combination of elements available in 1D gas-dynamic codes such as volumes, ducts and discharge coefficients. Magnitudes for those elements were related with real geometrical parameters. Some of them ($D1$, $D2$, L and Cd) were fitted from a multifactor variance analysis (ANOVA) using near 150 measured points from 4 different turbochargers. Best modelling results showed an equivalent length of compressor volute of 1/3 of its real length. Inlet diameter of that pipe was chosen as the diameter of a circular section equivalent to the available cross section at the rotor inlet. Best results showed that outlet diameter for that pipe should be equivalent to the volute exhaust section at compressor tongue. Model was completed with a reservoir with the equivalent volume of compressor rotor and other with the equivalent volume of compressor stator. Compressor chart was adapted subtracting pressure losses generated by elements representing internal compressor geometry due to those losses had been already included in the compressor characteristic map. Discharge coefficient between equivalent volute volume and the connection pipe at compressor outlet was set to 0.7 as it was the value providing best results according to the ANOVA analysis.

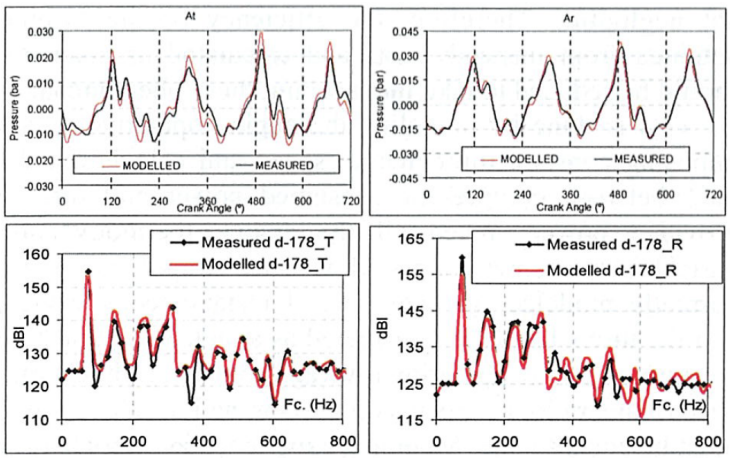

Figure 2.12: 1D unsteady compressor model of Torregrosa et al. [172] (Operation point at 178 krpm)

Figure 2.12 shows how the 1-D compressor model proposed by Torregrosa et al.[172] reproduced accurately unsteady behaviour of reflected and transmitted pressure pulses, both in time and frequency domains. Simulated results with the unsteady compressor model were compared with a model that only accounted for quasi-steady behaviour using compressor charts between two pipes. Proposed unsteady model showed better prediction for the pressure pulses travelling through the ducts upstream the compressor (noise source radiated upstream the compressor).

2.5 Models to Characterize Non-Steady Turbine Behaviour

2.5.1 Introduction

Turbine performance maps are the standard source of information for gas-dynamic engine codes. These maps are usually provided in two charts, one for mass flow parameter ($\dot{m}_T^{red}$) versus the total-to-static pressure ratio along the turbine (Π_T), defined by equations 2.64 and 2.65.

$$\dot{m}_T^{red} = \frac{\dot{m}_T \cdot \sqrt{T_{30}}}{p_{30}} \tag{2.64}$$

$$\Pi_T = \frac{p_{30}}{p_4} \tag{2.65}$$

The second chart provides turbine efficiency (η_T) traditionally defined as equation 2.36 showed, versus pressure ratio (Π_T) or blade speed ratio (σ) that was defined in equation 2.24.

Due to the fact that turbine efficiency has been defined in terms of compressor power, mechanical efficiency (η_m) has been already included in that parameter. An example of those charts is presented in figure 2.13 for a variable geometry turbine (VGT). Those turbines have moving vanes in the stator in order to improve transient torque response due to the faster increase in boosting pressure [9]. Observing those maps following conclusions can be derived.

- Measured points are grouped in both charts with turbine speed parameter defined as equation 2.66 shows.

$$N_T^{red} = \frac{N}{\sqrt{T_{30}}} \tag{2.66}$$

- Narrow range of data at constant speed is supplied on manufacturer maps for each iso-speedline, since those measurements were obtained in steady state conditions mounting the whole turbocharger. Under those conditions, compressor was driven by the turbine acting like a brake. Therefore turbine operative range was restricted by the two stable working limits of the compressor, i.e. surge and choking. Nevertheless extra information (far from those limits) could be obtained if pressure at compressor inlet circuit would be modified in order to change air density and so the absorbed power [70]. A torquimeter could be used instead of the compressor impeller in order to modify turbine load, obtaining so a wider operative range.

- The above-mentioned operative limits (imposed by the compressor) are responsible that high expansion ratios can be only achieved for high mass flow parameters and high rotational speeds. Consequently low regions in

the turbine mass flow map are only affordable for the lowest turbocharger speeds.

- For a given expansion ratio, the lower is the speed the higher is the mass flow parameter. That phenomenon agrees with centrifugal force field reduction at turbine rotor outlet.
- Turbine efficiency points versus blade speed ratio seems to collapse. Being the maximum efficiency obtained for a blade speed ratio near to 0.7. In addition turbine isentropic efficiency seems to fit with a parabolic equation as Watson [183] proposed.

Maps can be represented in terms of corrected turbine parameters, i.e. turbine corrected mass flow ($\dot{m}_T^*$) and turbine corrected speed (N_T^*), if temperature and pressure in a state of reference are chosen as shown by equations 2.67 and 2.68. Despite that change in turbine parameters definition, physics remain the same and so the shape of those maps.

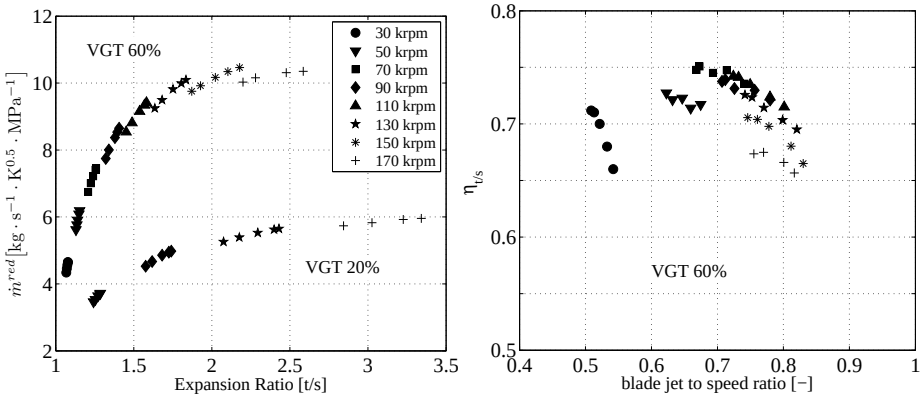

Figure 2.13: Turbine performance maps

$$\dot{m}_T^* = \dot{m}_T^{red} \cdot \frac{p_{ref}}{\sqrt{T_{ref}}} \tag{2.67}$$

$$N_T^* = N_T^{red} \cdot \sqrt{T_{ref}} \tag{2.68}$$

When the turbocharger is coupled to an ICE, its behaviour is far from that described under steady state conditions due to the high pulsating flow

at turbine inlet. Due to the fact that turbine performance maps are obtained under steady state conditions, some authors claim that those charts cannot be directly used to reproduce pulsating behaviour since errors over 20% would appear [107, 103]. For that reason, matching between turbocharger and ICE becomes the an important topic for automotive designers. In that scenario, several researches have investigated pulsating flow influence in turbine performance from the very first attempts of Wallace et al. [179] and Dale et al. [42, 41]. Some of them focused in the differences between turbine operation under steady and pulsating conditions like Masanori et al. [107]. Others paid attention onto the extrapolation techniques to improve the engine matching [155, 168]. Several studies have been done in the scenario of 1-D models due to its fast CPU time calculation [32, 31, 6, 38, 37, 148] but currently CFD works have been focused on the turbine [100, 122, 5, 81, 79, 80]. Over the last few decades, several approximations to a comprehensive characterization of radial turbine from automotive turbochargers have been done to improve computational simulations. Main problem in turbine simulation arises in the well prediction of turbine performance under pulsating flow conditions. Better prediction of mass flow rate and turbine efficiency under unsteady behaviour have been sought traditionally for researchers.

2.5.2 Turbine Modelling

Several turbine models have been proposed over the last few decades, being the main difference among them the way in which fluid-dynamic behaviour was characterized. Watson and Janota [183] proposed a simple model where turbine was replaced by a single nozzle whose equivalent area was that producing the same pressure drop for the same steady mass flow. That model provided good results modelling axial turbines with moderate expansion ratios. Nevertheless that model did not provide successful results for radial turbines with higher expansion ratios since choking conditions were predicted earlier than the obtained from measurements. Payri et al. [126, 127] proposed a turbine model consisting of two nozzles in series separated by an intermediate chamber. First nozzle represented the turbine stator which produced a first expansion on the flow, and a second nozzle representing turbine rotor which produced a second expansion. Intermediate reservoir represented the existing volume at turbine volute, although its value was not critical predicting turbine pulsating behaviour. Effective area of both nozzles was obtained from turbine measurements under steady flow conditions assuming that half of the

expansion took place in the stator and the other half in the rotor.

2.5.2.1 Turbine Modelling - Geometry for Acoustic non-linear

Due to the fact that turbocharger turbine never operates under steady flow conditions when it is coupled to an ICE (even for constant pressure arrangements), effects of unsteady flow have been widely studied. Several proposals for turbine unsteady characterization have been presented. They can be divided into Zero-Dimensional models (0-D), One-Dimensional models (1-D) and Three-Dimensional models (3-D).

0-D Models

Zero-Dimensional models (0-D) also called "filling and emptying models" are those where flow parameters depend on time only and not of a spatial variable. Wave propagation is not considered then but it is the mass accumulation. In those models, turbine volute is considered as a volume introducing a residence time into the gas dynamics. 0-D assumptions have been traditionally justified by the fact that the length of the exhaust line (including exhaust manifold and turbine volute) is relatively small and pressure waves in that system can be ignored [20, 92]. That assumption provides acceptable results [15] mainly in upstream/downstream turbine pressure traces for low to middle engine speed range were wave effects in the air path are not so pronounced. However for higher engine speeds, wave effects become more pronounced showing 0-D approaches limitations predicting turbine behaviour in those regions [176]. Main limitation of 0-D models arise when turbine chokes since simple models, considering turbine as a single nozzle, predict choking at lower pressure ratios than measured ones. To overcome that problem, Payri et al. [127] proposed a turbine model based on two nozzles in series with an intermediate volume to account for mass accumulation.

1-D Models

To overcome the aforementioned limitations of 0-D models, 1-D models have been widely spread in turbocharger modelling due to the turbine swallowing capacity was better predicted by means of 1-D models [31]. These 1-D models

solve differential equations describing flow behaviour along pipes taking into account all the involved phenomena (friction, heat transfer, changes in cross-section and pressure wave interaction).

Chen et al. [32] studied relative importance of unsteadiness effects on turbine components due to the pulsating flow, analysing the Strouhal number (equation 2.69) at turbine volute and rotor.

$$\mathrm{Str} = \frac{\tau_\mathrm{A}}{\tau_\mathrm{B}} \tag{2.69}$$

Where τ_A was the time for fluid particles to be transported through the turbine component while τ_B was the timescale of the unsteadiness of pulsating flow. Strouhal number higher than unity meant that unsteady effects dominated and so wave action propagation effects should be taken into account. Whereas Str lower than unity lead to a simplification of the problem since quasi-steady effects dominate. From the results of Chen et al. [32] a quasi-steady approach for turbine rotor was justified meanwhile dynamic effects were only necessary to be considered for the turbine volute what justifies its modelling using 1-D approach. Several 1-D models have been proposed to model the turbine volute to account for unsteadiness effects. Chen et al. [32], proposed a 1-D model where turbine volute was divided into two tapered ducts reproducing cross-sectional area reduction across the volute as scheme on the left side of figure 2.14 shows.

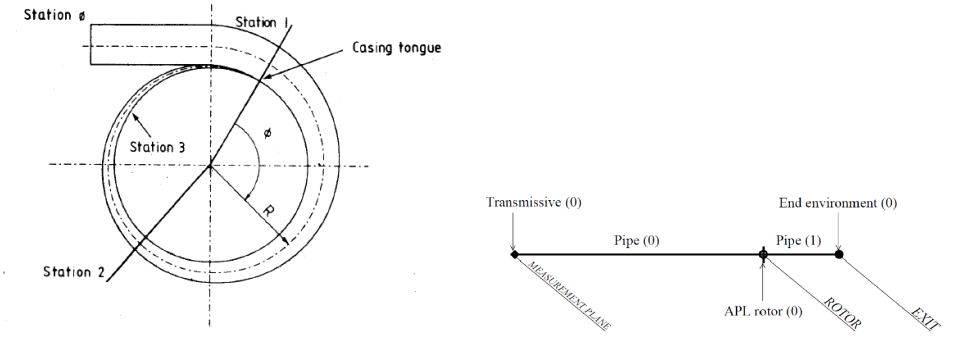

Figure 2.14: Turbine 1D models; Left: Chen et al. [32], Right: Costall et al. [37]

First pipe was defined from turbine entry (station 0) to volute tip tongue

(station 1), with diameters and length equal to measured ones. Second pipe was determined from the tip of volute tongue (station 1) up to an azimuth position of 180° degrees where the flow was assumed that reached the rotor (station 2). Length of that pipe was real length of the volute meanwhile its outlet area was determined by means of equation 2.70 and consequently its volume was arbitrary.

$$A_2 = \frac{2\pi}{(2\pi - \phi_2)} \cdot A_{2,real} \tag{2.70}$$

Where $A_{2,real}$ was the actual cross-sectional area of the casing at the azimuth angle ϕ_2. So that modelled outlet area of tapered pipe number 2 was the double of the real area measured at that point.

Later, Chen et al. [31] improved that model by introducing losses models accounting for circumferential variation, casing friction, incidence losses, rotor internal losses, clearance flow losses, exit mixing losses, bearing losses and disc friction losses. With respect to the geometrical model for the turbine, it was similar to the aforementioned. Turbine volute was modelled using two tapered pipes, first one was defined from turbine entry (station 0) to the tip of the volute tongue (station 1), with diameters and length equal to the measured ones. The second station (end of pipe 2) was placed at the same place than before keeping that real length, but being its outlet area determined keeping volume of the tapered duct equal to volute real volume.

Abidat et al. [6] modelled turbine volute as a curved pipe, assuming that its area varied linearly with the azimuth angle. Inlet diameter of that pipe was measured at the tip of the tongue while its outlet diameter was that measured at a radius equal to the mean of the volute section centroid radius. That curved pipe was divided into finite volumes where 1-D unsteady equations were solved using a second-order solution method.

Model proposed by Costall et al. [38, 37], presented turbine volute as a straight tube integrated with its inlet pipe. According to right side of figure 2.14, pipe 0 represented facility inlet pipe from measurement plane to an arbitrary section placed at 180° downstream the tip of the tongue according to Chen et al. [31]. Length and volume from that modelling pipe should be the same than the ones measured between both points. Constant diameter of pipe 0 was determined as that keeping the same volume as the real one.

Obviously that model was far from the real shape of the turbine volute but the objective was developing a simple model to be used in 1-D gas dynamics codes. Theoretically, virtual inlet to the turbine rotor should be placed at the point where half of the mass flow passing through the turbine was consumed within the chosen volute portion (from tip of the tongue to an azimuth angle ϕ) [37]. Pipe number 1 represented turbine outlet diffuser whose length and volume were measured in test facility.

2.5.2.2 Advanced 1-D Models

Several one-dimensional models for the turbine, considering both the volute and the rotor, accounting for unsteady flow effects have been presented. Hu et al. [86, 87] developed a 1-D model for vaneless twin-entry turbines based on the Ehrlich' work [53, 54]. Turbine volute was discretized into streamwise elements solving flow along the mean streamline using the method of characteristics. Each nozzle passage was treated as a separated element, their inlet conditions were determined interpolating in the adjacent volute elements. Each rotor passage was considered as a radial and an axial element, a constant flow angle at the rotor inlet was assumed as if there was a vaned diffuser to avoid 2-D calculations. Losses were calibrated from steady flow measurements and introduced as source terms in that model.

Later King [97] improved that model considering choking and using an upwind algorithm. Boundary conditions for such model were adapted to be implemented into GT-Power^{TM} [73] engine simulation code.

Serrano et al. [148] improved Payri's model of two nozzle in series with an intermediate volume, to account for stator nozzle variable effective area in case of VGT turbines. Stator effective area was determined using turbine performance parameters like reaction degree, turbine efficiency and velocity triangles.

2.5.2.3 3-D Models

Recent advances in computer modelling (calculation speed and storage devices) have allowed turbine characterization under pulsating flow conditions by means of Computational Fluid Dynamics (CFD). Those calculations are

based on the solution of time-varying Navier-Stokes equations applied to the turbine unit. First completed calculations were done by Lam et al. [100] who modelled a vaned turbine using multiple reference frames (MRF). The domain was divided into stationary and rotating subdomains applying the frozen rotor method, so the relative motion between stationary and rotating subdomains was not taken into account. That assumption was based on the fact that pulse frequency was lower than rotor passing frequency. It was found that turbine volute had an important damping effect on mass flow rate variation, what agreed with mass storage occurring in the volume. Nevertheless little damping was observed in total temperature. Later Palfreyman [122] modelled a nozzleless turbine considering the stationary and rotating meshes being coupled at each instant of time by means of a sliding plane at the interface between stator and rotor. The work of Abidat [5] showed how mass flow rate at rotor inlet and outlet was very similar what implied that rotor could be considered as quasi-steady.

2.5.3 Turbine Extrapolation Techniques

When turbine is connected to an ICE it works with high pulsating flow, which is produced by the opening and closing of cylinder exhaust valves. That mechanism causes an instantaneous variation of the pressure gas inside the exhaust manifold that will be translated into a pulsating periodical process in the expansion ratio and mass flow across the turbine. That pulsating variation affects turbine efficiency due to the associated variation in instantaneous temperature inside the exhaust manifold. Those instantaneous variations are seen on turbine charts presented in figure 2.15.

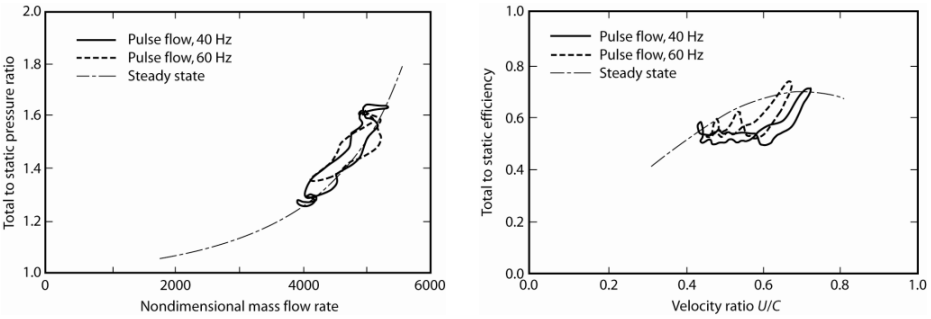

Figure 2.15: Turbine instantaneous performance (Works from Dale [41])

As it is showed in figure 2.15, turbine can move instantaneously far from the narrow region measured with steady flow conditions. For that reason, several studies have been focused on turbine maps extension.

2.5.3.1 Mass Flow Extension

Empirical Models

Empirical models are those using polynomial expressions, fitted with measured data, to describe turbine mass flow characteristics. They are traditionally simple and fast in calculation what make them appropriate in control-oriented simulations. However its accuracy is not sufficient for extrapolation performance. A simple proposal was the used by Eriksson et al. [56] to correlate turbine corrected mass flow with expansion ratio in the direct way showed by equation 2.71. Where coefficient c and exponent k were used as tuning parameters.

$$m_T^* = c \cdot \sqrt{1 - \Pi_T^k} \tag{2.71}$$

Sieros et al. [164] proposed a quadratic polynomial (equation 2.72) in turbine expansion ratio and reduced speed to determine turbine mass flow parameter.

$$\dot{m}_T^{red} = a_0 + a_1 \cdot \Pi_T + a_2 \cdot N_T^{red} + a_3 \cdot \Pi_T \cdot N_T^{red} + a_4 \cdot \Pi_T^2 + a_5 \cdot \left(N_T^{red}\right)^2 \tag{2.72}$$

Orkisz and Stawarz [120] proposed a quadratic polynomial (equation 2.73) to obtain turbine expansion ratio (Π_T) in terms of turbine mass flow parameter ($\dot{m}_T^{red}$), reduced speed (N_T^{red}) and parameter Z_T defined in equation 2.74. Where sub-index *crit* denoted critical conditions on the turbine.

$$\Pi_T = a_0 + a_1 \cdot \dot{m}_T^{red} \cdot N_T^{red} + a_2 \cdot \left(\dot{m}_T^{red} \cdot N_T^{red}\right)^2 + a_3 \cdot \dot{m}_T^{red} \cdot N_T^{red} \cdot Z_T + a_4 \cdot Z_T + a_5 \cdot Z_T^2 \tag{2.73}$$

$$Z_T = \left(\frac{\Pi_T}{\dot{m}_T^{red} \cdot N_T^{red}} \right)_{crit} \cdot \left(\frac{\dot{m}_T^{red} \cdot N_T^{red}}{\Pi_T} \right) - 1 \tag{2.74}$$

Fang et al. [59] proposed an exponential function in order to represent turbine mass flow characteristics (equation 2.75). Equation structure was chosen by doing computing tests with non-linear regression software 1stOpt [4] over several proposals among candidate correlations.

$$\varphi = a_0 + a_1 \cdot \exp\left(a_2 \cdot \left(N_T^{red} \right)^{a_3} \cdot [\Pi_T - 1] \right) \tag{2.75}$$

Where a_0, a_1, a_2 and a_3 were fitting coefficients.

GT-Power$^{\text{TM}}$ engine simulation code [73] uses a parabolic equation in blade speed ratio (σ) to extrapolate turbine performance map as equation 2.76 shows.

$$\dot{m}_T^{red} = k_3 \cdot (c + (1 - c) \cdot (k_1 \cdot \sigma)^m) \tag{2.76}$$

Where $1/k_1$ was blade speed ratio at maximum efficiency, k_3 corrected mass flow at point of maximum efficiency, c reduced mass flow at blade speed ratio equal to zero and m a parameter whose values ranged from 2 to 4 [60].

Partly Empirical Models

Turbine mass flow has been traditionally extrapolated considering the standard equation for isentropic compressible flow across a single orifice as showed in equation 2.77 [82].

$$\dot{m}_T^{red} = A_{eff} \cdot \sqrt{\frac{2 \cdot \gamma}{R \cdot (\gamma - 1)} \cdot \left[\left(\frac{1}{\Pi_T} \right)^{\frac{2}{\gamma}} - \left(\frac{1}{\Pi_T} \right)^{\frac{\gamma+1}{\gamma}} \right]} \tag{2.77}$$

Nevertheless that approximation lead turbine choking at low pressure ratio defined in equation 2.78. However, that situation is not observed with experimental measurements. That is due to the fact that turbine effectively behaves as a series of two nozzles, i.e. one for the stator vanes and the second for the rotor passages.

$$\frac{1}{\Pi_T^{crit}} = \left(\frac{2}{\gamma+1}\right)^{\frac{\gamma}{\gamma-1}} \tag{2.78}$$

In addition, equation 2.77 predicts a decreasing mass flow through a single nozzle once critical conditions have been reached, phenomenon that does not occur in real turbines. For that reason, several authors proposed modified versions of that equation which fitted better to the experimental results. Jensen et al. [89] proposed equation 2.77 for a fixed geometry turbine if the expansion ratio was below critical conditions, and equation 2.79 for higher expansion ratios.

$$\dot{m}_T^{red} = A_{eff} \cdot \sqrt{\frac{2\cdot\gamma}{R\cdot(\gamma-1)} \cdot \left[\left(\frac{1}{\Pi_T^{crit}}\right)^{\frac{2}{\gamma}} - \left(\frac{1}{\Pi_T^{crit}}\right)^{\frac{\gamma+1}{\gamma}}\right]} \tag{2.79}$$

Where turbine effective area (A_{eff}) was modelled as a function of turbine pressure ratio (Π_T) and reduced speed (N_T^{red}) as showed by equation 2.80.

$$A_{eff} = a_1 + a_2 \cdot \Pi_T + a_3 \cdot N_T^{red} + a_4 \cdot \Pi_T \cdot N_T^{red} \tag{2.80}$$

For variable geometry turbines, effective area should be modified due to the modification in stator vanes geometry. In addition equations 2.77 and 2.79 were modified introducing parameter g, representing deviation of turbine expansion ratio for zero flow. That was justified by the fact that for variable geometry turbines, zero flow was not achieved with pressure ratio unity (as nozzle equation would predict). That parameter was fitted using a quadratic function in vane position.

$$\begin{aligned} \dot{m}_T^{red} &= A_{eff} \cdot \sqrt{\frac{2\cdot\gamma}{R\cdot(\gamma-1)} \cdot \left[\left(\frac{1}{\Pi_T} - g\right)^{\frac{2}{\gamma}} - \left(\frac{1}{\Pi_T} - g\right)^{\frac{\gamma+1}{\gamma}}\right]} \\ \dot{m}_T^{red} &= A_{eff} \cdot \sqrt{\frac{2\cdot\gamma}{R\cdot(\gamma-1)} \cdot \left[\left(\frac{1}{\Pi_T^{crit}} - g\right)^{\frac{2}{\gamma}} - \left(\frac{1}{\Pi_T^{crit}} - g\right)^{\frac{\gamma+1}{\gamma}}\right]} \end{aligned} \tag{2.81}$$

Canova et al. [27, 28] proposed a modification of Jensen's approach fitting polytrophic coefficient (γ) with measured data.

Moulin et al. [110] proposed the version showed in equation 2.82, calculating turbine extrapolated mass flow without taking into account speed variations. For that reason, some errors appeared at the high speed region where the model overestimated measured mass flow [110].

$$\dot{m}_T^{red} = A_{eff} \cdot \Pi_T^{3/2} \sqrt{\frac{2 \cdot \gamma}{R \cdot (\gamma - 1)} \left[\left(\frac{1}{\Pi_T} \right)^{\frac{2}{\gamma}} - \left(\frac{1}{\Pi_T} \right)^{\frac{\gamma+1}{\gamma}} \right]} \tag{2.82}$$

Serrano et al. [155] used nozzle equation 2.77 to extrapolate turbine mass flow but assuming a linear trend on turbine effective area with blade speed ratio for a given rotational speed (equation 2.83) as suggested by Muñoz and Payri [112] and Zinner [193].

$$A_{eff} = a_1 + a_2 \cdot \sigma \tag{2.83}$$

Couderc et al. [39] proposed the introduction of a corrected pressure ratio in equation 2.77. That correction term took into account displacement of critical expansion ratio observed in turbine maps, which was caused by changes of flow relative velocity. Linear tendency (equation 2.84) with measured turbocharger speed was used to obtain the new expansion ratio used in nozzle equation.

$$\Pi_T^{corr} = a \cdot \Pi_T + b \tag{2.84}$$

Being a and b functions of turbocharger rotational speed obtained using second order polynomials. Turbine effective area A_{eff} was fitted via second order polynomial in turbocharger measured speed (equation 2.85).

$$A_{eff} = a_1 + a_2 \cdot N_T + a_3 \cdot N_T^2 \tag{2.85}$$

Fang and Dai [58] proposed a regression model of turbine mass flow rate using Taylor series to expand functions with variables having small variation. Applying that methodology to the terms involved in Euler's turbomachinery equation and doing some assumptions in velocity terms, equation 2.86 was obtained.

$$\left(\dot{m}_T^{red}\right)^2 = a_0 + a_1 \cdot z^5 \cdot \left(1 - \Pi_T^{\frac{1-\gamma}{\gamma}}\right) + a_2 \cdot \left(N_T^{red}\right)^2 \cdot z^5 + a_3 \cdot z^5 \cdot \ln \Pi_T + a_4 \cdot \left(N_T^{red}\right)^2 \cdot z^4 \cdot \left(1 - \Pi_T^{\frac{1-\gamma}{\gamma}}\right) + a_5 \cdot z^5 \cdot \left(1 - \Pi_T^{\frac{1-\gamma}{\gamma}}\right) \cdot \ln z + a_6 \cdot \left(N_T^{red}\right)^2 \cdot z^5 \cdot \ln z + a_7 \cdot \left(N_T^{red}\right)^4 \cdot z^4 \tag{2.86}$$

That equation was only valid for expansion ratios below 3.5, if it was used for higher expansion ratios, then turbine reduced speed (N_T^{red}) was chosen as the biggest measured for expansion ratio equal to 3.5 being that pressure ratio constant for higher expansion ratio region. Parameter z was calculated as showed by equation 2.87 being E a fitting parameter assumed to lie between 1.0 and 1.5.

$$z = 1 - 1.357 \cdot 10^{-6} \cdot D_T^2 \cdot E \cdot N_T^{red} \tag{2.87}$$

2.5.3.2 Efficiency Extension

Traditionally turbine isentropic efficiency has been given in terms of blade speed ratio (σ) since the appearance of that representation has the shape of an inverted parabola [183, 83]. Several authors have proposed modelling turbine efficiency using a quadratic or cubic polynomial in blade speed ratio with coefficients depending on turbine geometrical and/or operating parameters. One of the simplest approximations used in turbine efficiency extrapolation was Eriksson proposal [55]. Using a quadratic function in blade speed ratio as equation 2.88 shows. Where $\eta_{T,max}$ was the maximum measured efficiency and σ_{max} the blade speed ratio at which that maximum efficiency appeared. Advantages of that proposal were that only one coefficient must be fitted, and turbine extrapolated curve was limited by measured point (point of maximum efficiency). Nevertheless that approach showed accurate results only in the narrow range of the steady state measurements. On the drawbacks side of that simple proposals, measurements from an extended range of turbine efficiency they do not fit to the shape of quadratic functions [106].

$$\eta_T = \eta_{T,max} \cdot \left(1 - c \cdot (\sigma - \sigma_{max})^2\right) \tag{2.88}$$

Eriksson et al. [56] proposed a control-oriented correlation to model turbine isentropic efficiency (equation 2.89). It only depended on turbine expansion ratio (Π_T) and parameters a_1, a_2 and a_3 that were determined via least square fitting.

$$\eta_T = a_1 \cdot \sqrt{\frac{1}{\Pi_T} - 1} + a_2 \cdot \sqrt[4]{\frac{1}{\Pi_T} - 1} + a_3 \tag{2.89}$$

Jensen et al. [89] proposed turbine isentropic efficiency modelling using a quadratic polynomial in blade speed ratio with coefficients linearly dependant on turbine reduced speed as showed by equation 2.90.

$$\eta_T = a_0 + a_1 \cdot N_T^{red} + \left(a_2 + a_3 \cdot N_T^{red}\right) \cdot \sigma + \left(a_4 + a_5 \cdot N_T^{red}\right) \cdot \sigma^2 \tag{2.90}$$

Couderc et al. [39] proposed linear correlation 2.91 of turbine specific enthalpy change in terms of reduced mass flow. Where coefficients a and b depended on turbocharger speed, and were determined by least square method on the supplier map. Once functions for a and b had been determined, turbine efficiency extrapolation was done using equation 2.5.

$$\Delta h_{real} = a \cdot \dot{m}_T^{red} + b \tag{2.91}$$

GT-Power^{TM} engine simulation code [73] fits turbine efficiency data map to a parabolic function on blade speed ratio as shown by equation 2.92.

$$\eta_{TS} = k_2 \cdot \left(1 - (1 - k_1 \cdot \sigma)^b\right) \tag{2.92}$$

Where k_2 represented turbine maximum efficiency, $1/k_1$ is the blade speed ratio where maximum efficiency occurred and b a parameter between 1.4 and 2.2 [60].

2.5.3.3 Efficiency Fitting Coefficients to compensate for Pulsating

Turbine efficiency under pulsating flow conditions is far from values provided by manufacturer maps for steady conditions [18] . That is due to the un-

steady effects on turbine, friction and heat transfer losses. For those reasons, some authors proposed several techniques to correct turbine efficiency given in maps in order to use them into pulsating flow simulations. Nevertheless, those types of correlations took into account both causes of lower efficiency and consequently they were not physically explicit. Those correlations could be improved if heat transfer would be separated from the friction losses amd those from the unsteady flow phenomena. In the early nineties, Masanori et al. [107] studied the differences on turbine performance between the steady state and on engine conditions for several gasoline and diesel turbocharged engines. Correction coefficients for turbine efficiency and mass flow due to engine pulsation were introduced. Those parameters were used to multiply steady state turbine mass flow and efficiency in order to obtain corresponding parameters at pulsating conditions. It was observed that as the expansion ratio increased, pulsation coefficients draw to unity what meant that pulsating effects (or heat transfer and friction effects) were less important and hot steady state conditions from turbine efficiency maps could be assumed. However, at low expansion ratios pulsating and the other effects become greater and correction parameters of 1.6 for turbine efficiency and 0.9 for turbine mass flow parameter were needed. In that scenario Luján et al. [103] studied turbine efficiency drop working under pulsating flow. For that purpose, two twin entry turbines from six in-line cylinders HD engines were studied. It was observed that turbine efficiency calculated from averaged parameters measured in engine bed (η_{mean}) was lower than efficiency provided by manufacturer maps (η_{map}) (in a ratio of 13%).

Turbine real efficiency (η_{real}) calculated from instantaneous values of gases temperature and mass flow was even lower than calculated from average measured parameters. Those instantaneous parameters were obtained from accurate prediction of 1-D gas dynamics code due to the extreme difficulty of obtaining that information in an engine test bench. In order to re-adapt manufacturers efficiency for hot pulsating flow simulations, a linear correlation between efficiency ratios defined by equations 2.93 and 2.94 was found with a parameter that will take into account pulses characteristics (pulsation parameter P_F) defined as shown by equation 2.95.

$$\text{ratio}_1 = \frac{\eta_{\text{mean}}}{\eta_{\text{map}}} \tag{2.93}$$

$$EC = \frac{\eta_{real}}{\eta_{map}} \tag{2.94}$$

$$P_F = \frac{p_{\max} - p_{\min}}{p_{\text{mean}}} \cdot \frac{n}{60} \cdot Z_t \tag{2.95}$$

Where n represented engine speed, Z_t number of cylinders discharging to the turbine and subscripts max, min and $mean$ denoting maximum, minimum and average values of turbine inlet pressure pulse respectively.

Payri et al. [125] observed that for a VGT turbine there was not a correlation between pulsation parameter P_F and correction in turbine efficiency. It was observed that the presence of directional nozzles imposing a constant flow angle at the stator inlet was one of the reasons. But also for closer positions of the VGT, reduction in stator effective area caused flow lamination. Nevertheless turbine efficiency correlation coefficient EC defined by equation 2.94 was a function of independent turbocharger variables. So that, quadratic correlations of EC with mass flow rate and turbocharger speed were found, meanwhile an inverse exponential relation with mass flow rate was observed. Mathematical expression showed in equation 2.96 was used to correct turbine efficiency under hot and real pulsating flow conditions.

$$EC = k_1 \cdot \left[\operatorname{sech}\left(\frac{\dot{m}_T - k_2}{k_3} \right) + \operatorname{sech}\left(\frac{N_{TC} - k_4}{k_5} \right) \right] + k_6 - \frac{k_7}{e^{k_8 \cdot \Pi_T}} \tag{2.96}$$

Torregrosa et al. [172] proposed another efficiency correction factor for variable geometry turbines. That correction was dependant on pulses characteristics (amplitude and frequency) but also on turbocharger performance (VGT opening and turbocharger speed) as equation 2.97 shows.

$$k = k_1 + k_2 \cdot VGT + k_3 \cdot N + k_4 \cdot f_a + k_5 \cdot A_i + k_6 \cdot f \tag{2.97}$$

Where k was correcting efficiency parameter, VGT stator vanes opening, N turbocharger speed, A_i engine pulses amplitude, f engine pulses frequency and f_a factor of amplitude defined as equation 2.98 shows.

$$f_a = \frac{p_{\max} - p_{\min}}{p_{\text{mean}} - p_{\text{amb}}} \tag{2.98}$$

Good prediction of pulsating turbine efficiency was obtained but that kind of correlations should be fitted for each turbine [128].

2.6 Summary

In this section a literature review of turbochargers modelling has been carried out. In the first section, models to characterize heat transfer phenomena in turbochargers have been studied from one-dimensional to CFD models, revising empirical models too. Several proposals to introduce heat transfer into compressor/turbine fluid-dynamic models have been pointed out. Traditionally heat transfer has been introduced before or after work transfer process or even a combination of both. Typical correlations for turbocharger heat transfer modelling have been presented too. Later models to characterize mechanical losses in turbocharger have been revised. Difficulty of measuring mechanical losses in a test bench was pointed out and some of current experimental methodologies were described. Those ranged from standard indirect techniques measuring lubricating oil enthalpy drop across the turbocharger or the direct measuring using a torquimeter. First technique needed accurate temperature probes and a almost-adiabatic testing methodology to separate heat transfer effects from pure friction effects. Later a revision on friction losses modelling has been performed.

In the second part, importance of modelling turbocharger performance under non-steady flow conditions was analysed through a literature review. First compressor models to account for pulsating effects were considered, paying special attention to compressor extrapolation techniques. Later models to characterize non-steady behaviour in compressor and turbine were revised, several proposal have been sorted on the literature to model compressor and turbine volute and stator. Revision on turbine extrapolation methodologies follows, where simple empirical models and partly empirical models for mass flow and efficiency extrapolation have been studied. Finally, some efforts to deal with real pulsating flow in the turbine have been shortened to contrast past initiations with the proposal of this Thesis.

References

[4] *7D-Soft High Technology Inc. 1stOpt manual, Release 3.0, http://www.7d-soft.com/ ; April 2010.* (Cit. on p. 66).

[5] M. Abidat and M. Hachemi. "Off-design performance of a turbocharger mixed flow turbine". In: *6th European Conference on Turbomachinery, Lille, France, 7-11 March.* 2005 (cit. on pp. 59, 64).

[6] M. Abidat, M. Hachemi, M.K. Hamidou, and N. Baines. "Prediction of the steady and non-steady flow performance of a highly loaded mixed flow turbine". In: *Proceedings of the Institution of Mechanical Engineers* 212 (1998), pp. 173–184 (cit. on pp. 59, 62).

[7] H. Aghaali and HE. Angstrom. "Improving turbocharged engine simulation by including heat transfer in the turbocharger". In: *SAE Technical Paper* 2012-01-0703 (2012) (cit. on p. 35).

[9] J. Andersen, E. Karlsson, and A. Gawell. "Variable Turbine Geometry on SI Engines". In: *SAE Technical Paper* 2006-01-0020 (2006) (cit. on p. 57).

[10] P. Andersson. "Air Charge Estimation in Turbocharged Spark Ignition Engines". PhD thesis. Linköpings Universitet, 2005 (cit. on p. 52).

[14] N. Baines, K. Wygant, and A. Dris. "The analysis of Heat Transfer in Automotive Turbochargers". In: *Proceedings of ASME Turbo Expo 2009, GT2009-59618.* 2009 (cit. on pp. 24, 26, 27, 29, 37, 44, 111).

[15] N.C. Baines, A. Hajilouy-Benisi, and J.H. Yeo. "The pulse flow performance and modelling of radial inflow turbines". In: *Proceedings of the Institution of Mechanical Engineers, 5th International Conference on Turbocharging and Turbochargers* C484/006/94 (1994), pp. 209–220 (cit. on p. 60).

[18] R.S. Benson and K.H. Scrimshaw. "An experimental investigation of non-steady flow in a radial gas turbine". In: *Proceedings of the Institution of Mechanical Engineers* 180 (1965), pp. 74–85 (cit. on pp. 44, 70).

[20] F.S. Bhinder and P.S. Gulati. "A method for predicting the performance of centripetal turbines in non-steady flow". In: *Proceedings of the Institution of Mechanical Engineers, 1st International Conference on Turbocharging and Turbochargers* (1978), pp. 233–240 (cit. on p. 60).

[21] D. Bohn, T. Heuer, and K. Kusterer. "Conjugate Flow and Heat Transfer Investigation of a Turbo Charger". In: *Journal of Engineering for Gas Turbines and Power* 127.3 (2005), pp. 663–669 (cit. on pp. 24, 26, 30).

[22] D. Bohn, T. Heuer, and K. Kusterer. "Conjugate flow and heat transfer investigation of a turbocharger: Part I: Numerical results". In: *ASME paper* GT2003-38445 (2003) (cit. on pp. 30, 37, 39–41).

[23] D. Bohn, N. Moritz, and M. Wolff. "Conjugate flow and heat transfer investigation of a turbocharger: Part II: Experimental results". In: *ASME paper* GT2003-38449 (2003) (cit. on pp. 27, 37).

[25] L. Bouard, M. Fillon, and J. Frene. "Comparison between three turbulent models application to thermohydrodynamic performances of tilting-pad journal bearings". In: *Tribology International* 29 (1996), pp. 11–18 (cit. on p. 50).

[27] M. Canova. "Development and validation of a control-oriented library for the simulation of automotive engines". In: *International Journal of Engine Research* 5 (2004), pp. 219–228 (cit. on p. 67).

[28] M. Canova, S. Midlam-Mohler, Y. Guezennec, and G. Rizzoni. "Mean value modeling and analysis of HCCI diesel engines with external mixture formation". In: *Journal of Dynamic Systems, Measurement, and Control* 131 (2009), pp. 1–14 (cit. on p. 67).

[30] S.C. Chapra and R.P. Canale. *Numerical Methods for Engineers*. Ed. by New York 4th Ed. McGraw-Hill, 2002 (cit. on p. 54).

[31] H. Chen, I. Hakeem, and R. Martinez-Botas. "Modelling of a turbocharger turbine under pulsating inlet conditions". In: *Proceedings of the Institution of Mechanical Engineers, Part A: Journals of Power and Energy* 210 (1996), pp. 397–408 (cit. on pp. 59, 60, 62).

[32] H. Chen and D. Winterbone. "A method to predict performance of vaneless radial turbine under steady and unsteady flow conditions". In: *Proceedings of the Institution of Mechanical Engineers, Turbocharging and Turbochargers* (1990), pp. 13–22 (cit. on pp. 59, 61, 159).

[33] P. Chesse, D. Chalet, and X. Tauzia. "Impact of heat transfer on the performance calculations of automotive turbocharger compressor". In: *Oil & Gas Science and Technology. IFP Energies nouvelles* (2011) (cit. on p. 26).

[35] M. Cormerais, JF. Hetet, P. Chessé, and A. Maiboom. "Heat Transfer analysis in a turbocharger compressor: Modelling and Experiments". In: *SAE Technical Paper* 2006-01-0023 (2006) (cit. on p. 21).

[36] M. Cormerais, J.F. Hetet, P. Chesse, and A. Malboom. "Heat Transfers Characterization in a Variable Geometry Turbocharger: Experiments and Correlations". In: *Proceedings of ASME Internal Combustion Engine Division, Spring Technical Conference*. 2006 (cit. on p. 44).

[37] A.W. Costall, R.M. McDavid, R.F. Martinez-Botas, and N.C. Baines. "Pulse performance modelling of a twin-entry turbocharger turbine under full and unequal admission". In: *ASME paper* GT2009-59406 (2009) (cit. on pp. 59, 61–63, 159).

[38] A.W. Costall, S. Szymko, R. Martinez-Botas, D. Filsionger, and D. Ninkovic. "Assesment of unsteady behavior in turbocharger turbines". In: *ASME paper* GT2006-90348 (2006) (cit. on pp. 59, 62).

[39] C. Couderc, P. Chessé, and D. Chalet. "Comparison of the prediction performances of different models of radial turbine under steady and unsteady flow conditions". In: *Scientific Bulletin, Automotive series, year XVII, No.21(2)* (cit. on pp. 68, 70).

[40] R.C. Coy. "Practical applications of lubrication models in engines". In: *Tribology International* 31.10 (1998), pp. 563 –571. ISSN: 0301-679X. DOI: 10.1016/S0301-679X(98)00077-2. URL: http://www.sciencedirect.com/science/article/pii/S0301679X98000772 (cit. on p. 49).

[41] A. Dale. "Radial Vaneless Turbocharger Turbine Performance". PhD thesis. Imperial College, London, 1990 (cit. on pp. 59, 64, 162).

[42] A. Dale and N. Watson. "Vaneless radial turbocharger turbine performance". In: *Proceedings of the Institution of Mechanical Engineers* C110/86 (1986) (cit. on p. 59).

[43] M. Deligant, P. Podevin, and G. Descombes. "CFD model for turbocharger journal bearing performances". In: *Applied Thermal Engineering* 31.5 (2011). MNF 2009 Special Issue, pp. 811 –819. ISSN: 1359-4311. DOI: 10.1016/j.applthermaleng.2010.10.030. URL: http://www.sciencedirect.com/science/article/pii/S1359431110004692 (cit. on pp. 46, 49).

[44] M. Deligant, P. Podevin, and G. Descombes. "Experimental identification of turbocharger mechanical friction losses". In: *Energy* 39 (2012), pp. 388–394 (cit. on pp. 44, 46).

[45] M. Deligant, P. Podevin, G. Descombes, T. Lamquin, F. Vidal, and A. Marchal. "Effect of axial load on turbocharger friction losses". In: *Proceedings of the 13th EAEC European Congress, Valencia, Spain*. 2011 (cit. on p. 45).

[46] M. Deligant, P. Podevin, T. Lamquin, F. Vidal, and A. Marchal. "Experimental study of turbocharger's performances at low speeds". In: *Proceedings of the ASME 2010 Internal Combustion Engine Division Fall Technical Conference*. 2010 (cit. on p. 43).

[47] G. Descombes, F. Maroteaux, J. Jullien, and M. Pluviose. "Modelling of flow within a vaned channel in thermal engine". In: *International Journal of Thermal Sciences* 44.10 (2005), pp. 1000–1012 (cit. on p. 50).

[48] A. Diango, C. Perilhon, E. Danho, and G. Descombes. *Advances in gas turbine technology*. Ed. by Ernesto Benini. InTech, 2011. DOI: 10.5772/664 (cit. on p. 29).

[49] A. Diango, C. Perilhon, G. Descombes, and E. Danho. "Application of exergy balances for the optimization of non-adiabatic small turbomachines operation". In: *Energy* 36 (2011), pp. 2924–2936 (cit. on p. 44).

[51] P.G. Dowell and S. Akehurst. "Advanced Mapping Techniques for Radial Compressor for Use in Real-Time Engine Models". In: *SAE Technical Paper* 2010-01-1227 (2010) (cit. on p. 54).

[53] A.D. Ehrlich. "Characterization of unsteady on-engine turbocharger turbine performance". PhD thesis. Purdue University, West Lafayette, IN, 1998 (cit. on p. 63).

[54] A.D. Ehrlich, P.B. Lawless, and S. Fleeter. "On-engine turbocharger turbine inlet flow characterization". In: *SAE Technical Paper* 971565 (1997) (cit. on p. 63).

[55] L. Eriksson. "Modeling and Control of Turbocharged SI and DI Engines". In: *Oil & Gas Science and Technology. IFP Energies nouvelles* 62 (2007), pp. 523–538 (cit. on pp. 52, 69).

[56] L. Eriksson, J.B. Nielsen, F.P. Bergström, and P. Andersson. "Modeling of a Turbocharged SI Engine". In: *Annual Reviews in Control* 26 (2002), pp. 129–137 (cit. on pp. 54, 65, 70).

[58] X. Fang and Q. Dai. "Modeling of turbine mass flow rate performances using the Taylor expansion". In: *Applied Thermal Engineering* 30 (2010), pp. 1824–1831 (cit. on p. 68).

[59] X. Fang, Q. Dai, Y. Yin, and Y. Xu. "A compact and accurate empirical model for turbine mass flow characteristics". In: *Energy* 35 (2010), pp. 4819–4823 (cit. on p. 66).

[60] O. Flärdh and J. Märtensson. "Analysis of a Quasy-Steady Extension to the Turbine Model in Mean Value Engine Models". In: *SAE Technical Paper* 2010-01-1191 (2010) (cit. on pp. 66, 70).

[64] J. Galindo, H. Climent, C. Guardiola, and A. Tiseira. "On the effect of pulsating flow on surge margin of small centrifugal compressors for automotive engines". In: *Experimental Thermal and Fluid Science* 33 (2009), pp. 1163–1171 (cit. on p. 43).

[65] J. Galindo, J.M. Luján, J.R. Serrano, V. Dolz, and S. Guilain. "Description of a heat transfer model suitable to calculate transient processes of turbocharged Diesel engines with one-dimensional gas-dynamic codes". In: *Applied Thermal Engineering* 26.1 (2006), pp. 66–76 (cit. on p. 20).

[70] J. Galindo, J.R. Serrano, C. Guardiola, and C. Cervelló. "Surge limit definition in a specific test bench for the characterization of automotive turbochargers". In: *Experimental Thermal and Fluid Science* 30 (2006), pp. 449–462 (cit. on pp. 57, 162, 163).

[73] *Gamma Technologies, 2010, GT-POWER User's Manuals and Tutorials. GT-SUITE Version 7.1.* (Cit. on pp. 35, 63, 66, 70).

[75] E.G. Giakoumis. "Lubricating oil effects on the transient performance of a turbocharged diesel engine". In: *Energy* 35 (2010), pp. 864–873 (cit. on p. 45).

[76] L. Guzzella. *Introduction to modeling and control of internal combustion engine systems.* Springer, 2009 (cit. on pp. 21, 33, 50).

[77] L. Guzzella, U. Wenger, and R. Martin. "IC-engine Downsizing and Pressure-Wave Supercharging for Fuel Economy". In: *SAE Technical Paper* 2000-01-1019 (2000) (cit. on p. 20).

[78] D. Hagelstein, B. Beyer, J. Seume, M. Rautenberg, and H. Hasemann. "Heuristical view on the non-adiabatic coupling system of combustion engine and turbocharger". In: *C602/015/2002. Proceedings of 7th International Conference on Turbochargers and Turbocharging. Professional Engineering Publishing. Ltd. IMechE. London.* 2002 (cit. on pp. 26, 30).

[79] F. Hellström and L. Fuchs. "Effects of inlet conditions on the turbine performance of a radial turbine". In: *ASME paper* GT2008-51088 (2008) (cit. on p. 59).

[80] F. Hellström and L. Fuchs. "Numerical computation of the pulsatile flow in a turbocharger with realistic inflow conditions from an exhaust manifold". In: *ASME paper* GT2009-59619 (2009) (cit. on p. 59).

[81] F. Hellström and L. Fuchs. "Numerical computations of pulsatile flow in a turbo-charger". In: *AIAA Aerospace Sciences Meeting and Exhibit, Reno, Nevada,7-10 January.* 2008 (cit. on p. 59).

[82] J. Heywood. *Internal Combustion Engine Fundamentals.* Ed. by ISBN 007 028637 X. McGraw-Hill Science/Engineering/Math, 1988 (cit. on pp. 66, 163).

[83] J.H. Horlock and D.E. Winterbone. *The thermodynamics and gas dynamics of internal combustion engines. Volume II.* Oxford: Clarendon Press, 1986 (cit. on p. 69).

[85] L. Hu, C. Yang, H. Sun, E. Krivizky, L. Larosiliere, J Zhang, and M.C. Lai. "Experimental and computational analysis of impact of self recirculation casing treatment on turbocharger compressor". In: *SAE Technical Paper 2010-01-1224.* 2010 (cit. on p. 47).

[86] X. Hu. "An advanced turbocharger model for the internal combustion engine". PhD thesis. Purdue University, West Lafayette, IN, 2000 (cit. on p. 63).

[87] X. Hu and P.B. Lawless. "Predictions of on-engine efficiency for the radial turbine of a pulse turbocharged engine". In: *SAE Technical Paper* 2001-01-1238 (2001) (cit. on p. 63).

[89] J.P. Jensen, A.F. Kristensen, S.C. Sorenson, N. Houbak, and E. Hendricks. "Mean value modeling of a small turbocharged diesel engine". In: *SAE Technical Paper* 910070 (1991) (cit. on pp. 50, 54, 67, 70).

[90] W. Jiang, J. Khan, and R. Dougal. "Dynamic centrifugal compressor model for system simulation". In: *Journal of power sources* 158.2 (2006), pp. 1333–1343 (cit. on p. 50).

[91] M. Jung, R.G. Ford, K. Glover, and N. et al. Collings. "Parameterization and Transient Validation of a Variable Geometry Turbocharger for Mean-Value Modeling at Low and Medium Speed-Load Points". In: *SAE Technical Paper* 2002-01-2729 (2002) (cit. on p. 50).

[92] L.J. Kastner and F.S. Bhinder. "A method for predicting the performance of a centripetal gas turbine fitted with a nozzle-less volute". In: *ASME paper* 75-GT-65 (1975) (cit. on p. 60).

[97] A.J. King. "A turbocharger unsteady performance model for the GT-Power internal combustion engine simulation". PhD thesis. Purdue University, West Lafayette, IN, 2002 (cit. on p. 63).

[98] I. Kolmanovsky, P. Moraal, M.J. van Nieuwstadt, M. Criddle, and P. Wood. *Modelling and identification of a 2.0 l turbocharged DI diesel engine.* Tech. rep. Ford internal technical report SR-97-039, 1997 (cit. on pp. 50, 53).

[99] F. Kreith. *Principles of heat transfer.* International textbook Company Scranton, Pennsylvania, 1967 (cit. on p. 29).

[100] J. Lam, Q. Roberts, and G. McDonnell. "Flow modelling of a turbocharger turbine unser pulsating flow". In: *Proceedings of the Institution of Mechanical Engineers, Turbocharging and Turbochargers* (2002), pp. 181–197 (cit. on pp. 59, 64).

[101] T. Lamquin and K. Gjika. "Power losses identification on turbocharger hydrodynamic bearing". In: *Proceedings of ASME Turbo Expo 2009: Power for Land, Sea and Air. Orlando, FL. USA.* 2009 (cit. on p. 45).

[103] J.M. Luján, J. Galindo, and J.R. Serrano. "Efficiency Characterization of Centripetal Turbines under Pulsating Flow Conditions". In: *SAE Technical Paper* 2001-01-0272 (2001) (cit. on pp. 59, 71, 214).

[104] S. Marelli and M. Capobianco. "Steady and pulsating flow efficiency of a waste-gated turbocharger radial flow turbine for automotive application". In: *Energy* (2010) (cit. on p. 44).

[105] G. Martin, V. Talon, P. Higelin, A. Charlet, and C. Caillol. "Implementing Turbomachinery Physics into Data Map-Based Turbocharger Models". In: *SAE Technical Paper* 2009-01-0310 (2009) (cit. on pp. 50, 51, 160).

[106] R. Martinez-Botas. "Opportunities and challenges. Turbocharger trends and requirements forum". In: *Annex in the proceedings of the 8th International conference on turbochargers and turbocharging, London 15-18 May.* 2006 (cit. on pp. 69, 161, 162, 167, 170).

[107] I. Masanori, I. Nobuyuki, M. Youichi, and K. Toshiijo. "Comparison of Turbocharger Performance Between Steady Flow and Pulsating Flow on Engines". In: *SAE Technical Paper* 940839 (1994) (cit. on pp. 59, 71).

[109] P. Moraal and I. Kolmanovsky. "Turbocharger modeling for automotive control applications". In: *SAE Technical Paper* 1999-01-0908 (1999) (cit. on p. 50).

[110] P. Moulin, J. Chauvin, and B. Youssef. "Modelling and control of the air system of a turbocharged gasoline engine". In: *Proceedings of the 17th World Congress. The International Federation of Automatic Control, Seoul, Korea, July 6-11.* 2008 (cit. on p. 68).

[111] M. Mrosek and R. Isermann. "On the parametrisation of the turbocharger power and heat transfer models". In: *IFAC AAC 2010, Munich. Germany.* 2010 (cit. on p. 21).

[112] M. Muñoz and F Payri. *Motores de Combustión Interna Alternativos.* ISBN 84 86043 01 9. Madrid: Sección de Publicaciones de la E.T.S. de Ingenieros Industriales Fundación General - U.P.M, 1989 (cit. on pp. 68, 164, 166).

[113] M. Mueller. "Mean value modeling of turbocharged spark ignition engines". MA thesis. DTU, Denmark, 1997 (cit. on pp. 50, 52).

[114] S.H. Nasser and B.B. Playfoot. "A turbocharger selection computer model". In: *SAE Technical Paper* 1999-01-0559 (1999). DOI: 10.4271/1999-01-0559 (cit. on p. 50).

[115] O. Nelles. "Lolimot - local linear model trees for nonlinear dynamic system identification". In: *Automatisierungstechnik* 45 (1997), pp. 163–174 (cit. on p. 33).

[116] S.A. Nelson, Z.S. Filipi, and D.N. Assanis. "The Use of Neural Nets for Matching Fixed or Variable Geometry Compressors With Diesel Engines". In: *Journal of Engineering for Gas Turbines and Power* 125.2 (2003), pp. 572–579. DOI: 10.1115/1.1563239. URL: http://link.aip.org/link/?GTP/125/572/1 (cit. on p. 54).

[117] S.A. Nelson, Z.S. Filipi, and D.N. Assanis. "The use of neural networks for matching compressors with diesel engines". In: *Spring Technical Conference, volum ICE-26-3, pages 35-42.* 1996 (cit. on pp. 50, 54).

[120] M. Orkisz and S. Stawarz. "Modeling of turbine engine axial-flow compressor and turbine characteristics". In: *Journal of Propulsion and Power* 16 (2000), pp. 336–339 (cit. on p. 65).

[121] J. Padet. *Convection thermique et massique.* Techniques de l'ingénieur. BE 8206 (cit. on p. 30).

[122] D. Palfreyman and R. Martinez-Botas. "The pulsating flow field in a mixed flow turbocharger turbine:an experimental and computational study". In: *ASME paper* GT2004-53143 (2004) (cit. on pp. 59, 64).

[125] F. Payri, J. Benajes, J. Galindo, and J.R. Serrano. "Modelling of turbocharged diesel engines in transient operation: Part 2: wave action models for calculating the transient operation in a high speed direct injection engine". In: *Proceedings of the Institution of Mechanical Engineers, Part D: Jour* 216 (2002), pp. 479–493 (cit. on pp. 72, 145).

[126] F Payri, J. Benajes, J. Jullien, and Q. Duan. "Non-steady flow behaviour of a supercharger turbine". In: *Proceedings of the Third EAEC International Conference, pp. 347-351, Strassbourg.* 1991 (cit. on pp. 59, 159).

[127] F. Payri, J. Benajes, and M. Reyes. "Modelling of supercharger turbines in internal-combustion engines". In: *Journal of Mechanical Science* 38.8-9 (1996), pp. 835–869 (cit. on pp. 59, 60, 159, 160, 170).

[128] F. Payri, J. Galindo, J.R. Serrano, and A. Páez. "Experimental and modelling investigation on unsteady effects in compressor and turbines of current and future Diesel engines". In: *Société des Ingénieurs de l'Automobile (SIA).* 2008 (cit. on p. 73).

[132] F. Payri, J.R. Serrano, P. Olmeda, A. Páez, and F. Vidal. "Experimental methodology to characterize mechanical losses in small turbochargers". In: *Proceedings of ASME Turbo Expo 2010: Power for Land, Sea and Air. Glasgow, UK.* 2010 (cit. on pp. 22, 28, 44, 46, 47).

[134] P. Podevin, A. Clenci, and G. Descombes. "Influence of the lubricating oil pressure and temperature on the performance at low speeds of a centrifugal compressor for an automotive engine". In: *Applied Thermal Engineering* 31 (2011), pp. 194–201 (cit. on pp. 45, 46).

[135] P. Podevin, G. Descombes, A. Clenci, and C. Zaharia. "Researches regarding mechanical efficiency evaluation at turbochargers". In: *Proceeding of the International Automotive Congress, Brasov, Romania.* 2004 (cit. on p. 45).

[136] P. Podevin, G. Descombes, V. Hara, A. Clenci, and C. Zaharia. "Performances of turbocharger at low speed 1". In: *12 the EAEC Congress, Belgreade, Serbie.* 2005 (cit. on p. 45).

[137] P. Podevin, Toussaint M., Richard G., and G. Farinole. "Performances of turbocharger at low speed". In: *Proceeding of the SYMKOM02 congress, Lodz, Pologne.* 2002 (cit. on pp. 20, 45).

[139] H. Pucher, R. Berndt, and P. et al Grigoriadis. "Erweiterte darstellung und extrapolation von turbolader-Kennfeldern als randbedingung der motorprozesssimulation". In: *FVV Informationstagung Motoren Heft R513, Frankfurt, Germany.* 2001 (cit. on p. 25).

[140] M. Rautenberg, A. Mobarak, and M. Molababic. "Influence of heat transfer between turbine and compressor on the performance of small turbochargers". In: *JSME Paper 83-Tokyo-IGTC-73. International Gas Turbine Congress.* 1983 (cit. on p. 21).

[141] A. Romagnoli and R. Martinez-Botas. "Heat transfer analysis in a turbocharger turbine: An experimental and computational evaluation". In: *Applied Thermal Engineering* 38 (2012), pp. 58–77 (cit. on p. 33).

[144] S. Schmitt, W. Schmid, G. Hertweck, M. Schlegl, and S. Staudacher. "High-Precision Measurements of Friction Losses in Turbochargers". In: *Aufladetechnische Konferenz 2007, Desden, Germany.* 2007 (cit. on pp. 45, 46).

[145] N. Schorn, V. Smiljanowski, U. Späder, R. Stalman, and H. Kindl. "Turbocharger turbines in engine cycle simulation". In: *13th Supercharging Conference. Dresden, Germany.* (Cit. on p. 43).

[148] J.R. Serrano, F.J. Arnau, V. Dolz, A. Tiseira, and C. Cervelló. "A model of turbocharger radial turbines appropriate to be used in zero- and one-dimensional gas dynamics codes for internal combustion engines modelling". In: *Energy Conversion and Management* 49 (2008), pp. 3729–3745 (cit. on pp. 59, 63, 160, 170, 189, 215, 216, 231, 234, 271, 275).

[150] J.R. Serrano, C. Guardiola, V. Dolz, A. Tiseira, and C. Cervelló. "Experimental study of the turbine inlet gas temperature influence on turbocharger performance". In: *SAE Technical Paper* 2007-01-1559 (2007) (cit. on pp. 23, 24, 27, 30).

[153] J.R. Serrano, P. Olmeda, A. Tiseira, L.M. García-Cuevas, and A. Lefebvre. "Importance of mechanical losses modeling in the performance prediction of radial turbochargers under pulsating flow conditions". In: *SAE Int. J. Engines 6(2)* 6(2) (2013), pp. 729–738. DOI: 10.4271/2013-01-0577 (cit. on pp. 8, 46, 48, 49, 93, 132, 157, 189, 216, 217, 255).

[154] J.R. Serrano, P. Olmeda, A. Tiseira, L.M. García-Cuevas, and A. Lefebvre. "Theoretical and experimental study of mechanical losses in automotive turbochargers". In: *Energy* 55 (2013), pp. 888 –898 (cit. on pp. 8, 46, 48, 49, 93, 132, 157, 189, 216, 217, 223, 233, 255, 271).

[155] J.R. Serrano, B. Pla, D. Ospina, and R. Gozalbo. "Estimation of the Extended Turbine Maps for a Radial Inflow Turbine". In: *SAE Technical Paper* 2010-01-1234 (2010) (cit. on pp. 59, 68).

[156] S. Shaaban. "Experimental investigation and extended simulation of turbocharger non-adiabatic performance". PhD thesis. University of Hannover, Germany, 2004 (cit. on pp. 21, 30).

[157] S. Shaaban and J. Seume. "Analysis of turbocharger non-adiabatic performance". In: *Turbochargers and Turbocharging, Inst Mech Engineers* (2006), pp. 119–130 (cit. on pp. 21, 26, 27, 30).

[158] S. Shaaban and J. Seume. "Impact of Turbocharger Non-Adiabatic Operation on Engine Volumetric Efficiency and Turbo Lag". In: *International Journal of Rotating Machinery* 2012 (2012) (cit. on pp. 24, 35).

[159] S. Shaaban, J. Seume, R. Berndt, H. Pucher, and H.J. Linnhoff. "Part-load performance prediction of turbocharged engines". In: *C647/019. Proceedings of 8th International Conference on Turbochargers and Turbocharging. Woodhead Publishing and CRC Press LLC. London.* 2006 (cit. on pp. 20, 89).

[160] P.N. Shah and C.S. Tan. "Effect of blade passage surface heat extraction on axial compressor performance". In: *Transactions-American Society of Mechanical Engineers Journal of Turbomachinery* 129.3 (2007), p. 457 (cit. on p. 21).

[162] A. Sidorow, R. Isermann, F. Cianflone, and G. Landsmann. "Comparison of a turbocharger model based on isentropic efficiency maps with a parametric approach based on Euler's turbo-machinery equation". In: *18th IFAC World Congress. Milano (Italy) August 28 - September 2,* 2011 (cit. on pp. 30, 31).

[163] A. Sidorow, R. Isermann, F. Cianflone, and G. Landsmann. "Model based fault detection of the air and exhaust path of diesel engine including turbocharger models". In: *SAE 2011 World Congress, Detroit.* 2011 (cit. on pp. 30, 33).

[164] G. Sieros, A. Stamatis, and K. Mathioudakis. "Jet engine component maps for performance modeling and diagnosis". In: *Journal of Propulsion and Power* 13 (1997), pp. 665–674 (cit. on p. 65).

[165] P. Soltic. "Part-Load Optimized Si Engine Systems". PhD thesis. Swiss Federal Institute of Technology, Zürich, 2000 (cit. on p. 20).

[166] S. Sorenson, E. Hendricks, S. Magnusson, and A. Bertelsen. "Compact and accurate turbocharger modelling for engine control". In: *Electroni Engine Controls 2005 (SP-1975), SAE Technical Paper* 2005-01-1942 (2005) (cit. on p. 52).

[168] M. Tancrez, J. Galindo, C. Guardiola, P. Fajardo, and O. Varnier. "Turbine adapted maps for turbocharger engine matching". In: *Experimental Thermal and Fluid Science* 35.1 (2011), pp. 146 –153. ISSN: 0894-1777. DOI: 10.1016/j.expthermflusci.2010.07.018. URL: http://www.sciencedirect.com/science/article/pii/S0894177710001755 (cit. on p. 59).

[172] A. Torregrosa, J. Galindo, J.R. Serrano, and A. Tiseira. "A procedure for the unsteady characterization of turbochargers in reciprocating internal combustion engines". In: *The 4th International Symposium on Fluid Machinery and Fluid Engineering, November 24-27, 2008, Beijing, China.* 2008 (cit. on pp. 55, 56, 72, 149, 274).

[176] O. Varnier. "Trends and Limits of Two-Stage Boosting Systems for Automotive Diesel Engines". PhD thesis. Universidad Politecnica de Valencia, 2012 (cit. on pp. 7, 60).

[177] T. Verstraete, Z. Alsalihi, and R.A. Van den Braembussche. "Numerical study of the heat transfer in micro gas turbines". In: *Journal of Turbomachinery* 129 (2007), pp. 835–41 (cit. on pp. 21, 36–38).

[178] F. Vidal, A. Yammine, P. Chesse, A. Lefebvre, S. Guilain, and H. et al. Tartousi. "Diams: advanced diagnostics and modelling for turbocharging". In: *Conference internationale : Motorisations Diesel, face au defi de la competitivite. Rouen - INSA.* 2010 (cit. on p. 46).

[179] F.J. Wallace and G.P. Blair. "The pulsating-flow performance of inward radial-flow turbines". In: *Proceedings of the ASME Gas Turbine Conference and Products Show* paper 65-GT-21 (1965), pp. 1–19 (cit. on p. 59).

[183] N. Watson and S. Janota. *Turbocharging the internal combustion engine.* London: MacMillan Publishers Ltd, 1982 (cit. on pp. 23, 30, 58, 59, 69, 159, 163, 164, 173–175).

[186] G. Winkler. "Steady state and dynamic modeling of engine turbomachinery systems". PhD thesis. University of Bath, UK, 1977 (cit. on p. 50).

[190] A. Yamagata, S. Nagai, and T: Kawakubo. "Prediction and measurement of turbocharger compressor wheel temperature". In: *Proceedings of 8th International Conference on Turbochargers and Turbocharging. Woodhead Publishing and CRC Press LLC. London.* 2006 (cit. on pp. 28, 29).

[192] S. Zahn and R. Isermann. "Crank angle synchronious modelling and real-time simulation of diesel engines for ecu function development and testing". In: *AVEC.* 2008 (cit. on p. 30).

[193] K. Zinner. *Supercharging of Internal Combustion Engines.* ISBN 3 540 085440. Springer-Verlag New York, 1978 (cit. on pp. 68, 164, 168).

Chapter 3

Turbocharger Heat Transfer Modelling

Contents

3.1 Introduction

In normal operative conditions a turbocharger operates with high-pressured hot exhaust gases passing through the turbine case that are expanded in the rotor wheel in order to produce mechanical work in the shaft. In the other side of the shaft a compressor wheel transforms that mechanical energy into high-pressured air flow that is used to boost the IC engine. Even in an adiabatic process and due to the expansion process in the turbine case, exhaust gases reduce their temperature meanwhile air passing through the compressor increases its temperature while increasing its pressure. Due to the typical high rotational speeds of this kind of turbomachines (that ranges from 30,000 rpm to 250,000 rpm) it is mandatory lubricating turbocharger shaft with an oil film. That oil is delivered at engine block temperature and in a pure adiabatic process it is heated up later due to friction losses in the shaft. Recently, turbochargers for passenger car applications are including a cooling circuit in the central housing in order to isolate the hot turbine from the cold compressor. High temperature differences among the working fluids (exhaust gases moving the turbine, air passing through the compressor, lubricating oil and cooling liquid) but also the intrinsically power exchange processes in both turbomachines lead to a complex energy (heat, mass and mechanical power) transfer problem due to difficulties separating the following terms.

- Heat exchange from the hot gas passing through the turbine from the temperature reuction due to gas expansion.
- Power transferred to the oil just by heat transfer phenomena from the power transferred by friction (mechanical losses).
- Heat absorbed by cold air (compressor) due to the temperature differences from the temperature increase due to the compression process.

In order to simplify the study and to decouple the energy problem from the mechanical one, a series of experimental tests have been carried out. The presented methodology allows a detailed study on the internal heat transfer phenomena in turbochargers for passenger car applications. In order to cover a wide range of the current product market, three turbocharger models (in size and configuration) have been tested. That information has been used to develop a Heat Transfer Model (HTM) suitable to be used in one-dimensional

(1-D) engine simulation codes. Table 3.1 shows main characteristics of those turbochargers named as #1 (big size), #2 (medium size) and #3 (small size).

Table 3.1: Turbochargers identification

TURBO	**#1**	**#2**	**#3**
Turbine wheel diameter (mm)	41	38	36.5
Compressor wheel diameter (mm)	49	46	40
VGT	yes	yes	no
Water cooled	yes	no	yes
Engine type	diesel	diesel	petrol
Engine displacement (l)	2.0	1.6	1.2

3.2 Lumped Model Development

Proposed turbocharger thermal model has been based on the electrical analogy [173]. In this kind of models, the element under study is considered as a thermal network consisting of a finite number of nodes, whose thermal inertia is characterized by a thermal capacitance, and linked with other nodes by means of thermal conductances. Once the structure has been divided into nodes, energy conservation (equation 3.1) is applied to each node. It means that the sum of heat fluxes between nodes, convective heat fluxes and other heat fluxes in a time interval equals the change in sensible energy of the node.

$$\begin{aligned} & m_i \cdot c \cdot \frac{T^i_{t+\Delta t} - T^i_t}{dt} = \sum_j K_{ij} \cdot \left(T^j_{t+\Delta t} - T^i_{t+\Delta t} \right) + \sum_k q_{k \to i} + ... \\ & \sum_l h_{li} \cdot A_{li} \cdot \left(T^l_{t+\Delta t} - T^i_{t+\Delta t} \right) \end{aligned} \tag{3.1}$$

Where m_i denotes the mass of node i, c corresponds to its heat capacity, K_{ij} is the conductance between nodes i and j , h_{li} is the heat transfer coefficient between the fluid boundary l and node i while A_{li} is the corresponding contact area and $q_{k \to i}$ is a source term. On the right-hand side, temperatures at time instant $t + \Delta t$ are used (the implicit formulation). The advantage of the implicit formulation is that the solution is unconditionally stable when simulating transitory behaviour. The implicit has been chosen since the model presented here has been also used for transitory calculations.

Writing equation 3.1 for each of the n nodes results into a set of linear, implicit equations on the form of equation 3.2,

$$\left(\mathbf{K} + \frac{1}{\Delta t} \cdot \mathbf{C}\right) \cdot \mathbf{T}_{t+\Delta t} = \mathbf{Q} + \frac{1}{\Delta t} \cdot \mathbf{C} \cdot \mathbf{T}_t + \mathbf{H} \tag{3.2}$$

Where $\mathbf{T}_t$ and $\mathbf{T}_{t+\Delta t}$ are column vectors of n elements with previous and new nodes temperatures. $\mathbf{Q}$ is a column vector with the sum of heat fluxes to node i on the ith row. $\mathbf{H}$ is a column vector where the ith row, includes the sum of the product terms $T_l h_{li} A_{li}$ for the convective boundary conditions of node i. $\mathbf{K}$ and $\mathbf{C}$ are $n \times n$ conductance and capacitance matrices, respectively. In stationary conditions ($t = t + \Delta t$), equation 3.2 reduces to,

$$\mathbf{K} \cdot \mathbf{T}_t = \mathbf{Q} + \mathbf{H} \tag{3.3}$$

Where $\mathbf{K}$ is a matrix storing the whole information from the lumped model. It can be subdivided into four submatrices as equation 3.4 indicates. Assuming fluid temperature vector ($\mathbf{T_{bc}}$) as boundary conditions and rearranging equation 3.3 it can be obtained,

$$\begin{bmatrix} \mathbf{I} & \mathbf{0} \\ \mathbf{hA_{l,i}} & \mathbf{K_{i,j}} \end{bmatrix} \cdot \begin{bmatrix} \mathbf{T_{bc}} \\ \mathbf{T_{unknown}} \end{bmatrix} = \begin{bmatrix} \mathbf{T_{bc}} \\ \mathbf{0} \end{bmatrix} \tag{3.4}$$

Submatrix $\mathbf{I}$ represents the identity matrix and $\mathbf{0}$ the null matrix. Columns from submatrix $\mathbf{hA}_{l,i}$ represent each of the working fluids meanwhile there is a row for each metal node. Therefore, elements from submatrix $\mathbf{hA}_{l,i}$ are zero if there is not a physical connection between node i and fluid l. Columns and rows from submatrix $\mathbf{K}_{i,j}$ represent metal nodes. This submatrix is symmetric being elements for the main diagonal the sum of conductances (conductive and convective) connected with metal node i but with a minus sign, and elements from upper and lower diagonal are metal conductance between node i and j.

There are two methods for conductance and capacitance matrices calculation, analytical (direct method) and experimental (indirect method). In the former (direct), the conductive cases should be calculated bearing in mind the kind of connection between nodes: planar ($k_{i,j} A_{i,j} / x_{i,j}$) or radial ($2\pi k_{i,j} l_{i,j} / ln(r_j / r_i)$), while convective connections should be calculated as the

product of heat transfer coefficient and contact area ($h_{i,j}A_{i,j}$). In the latter (indirect), conductive and convective connections are adjusted by means of a set of controlled measurements of temperatures and heat fluxes. In the direct method, a comprehensive knowledge of the geometry and materials is needed to determine accurately conductances between nodes. In most cases, that knowledge is difficult to ensure, basically in the case of convective coefficients. For the aforementioned reasons, experimental fit of those connections (conductive and convective) has been performed.

Several studies about heat transfer phenomena inside automotive turbochargers demonstrated that radial temperature distribution in a cross sectional area was negligible compared to the axial temperature distribution [159]. That evidence allows the simplification of heat transfer problem inside the turbocharger considering it as a one-dimensional problem [152] instead of the three-dimensional case.

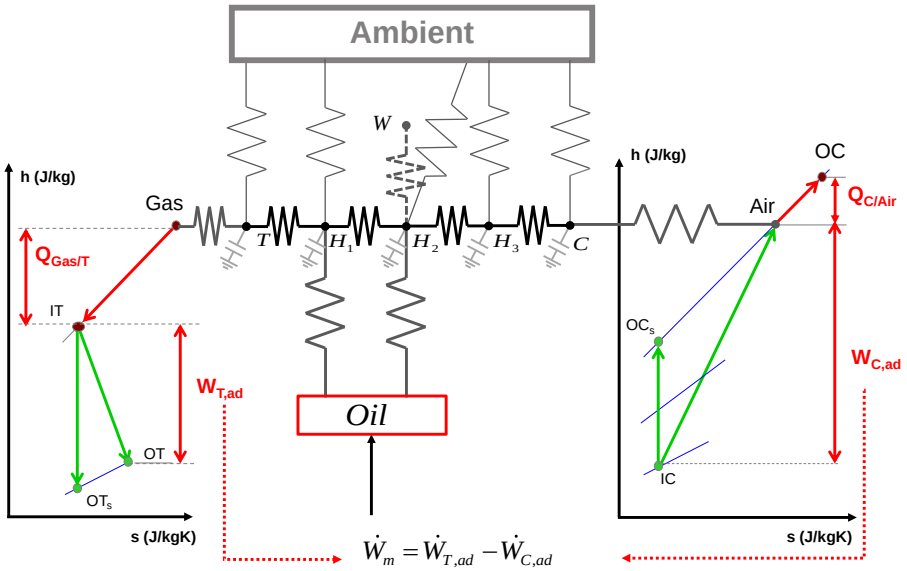

Figure 3.1: Turbocharger lumped model

Figure 3.1 shows proposed 1-D lumped model to account for heat transfer effects inside an automotive turbocharger. It includes five metal nodes that are representative for the geometry of the turbocharger. These are T (turbine case), C (compressor case) and three nodes for the turbocharger housing

named H_1 (placed near turbine case), H_2 (placed in the central part, where oil and water comes to the turbocharger) and H_3 (placed near compressor case). That division was justified by complexity of housing internal geometry but also for the simplicity studying internal heat fluxes to the lubricating oil and coolant circuit. Metal nodes are connected between them by means of conductive conductance $K_{i,j}$ being calculated the heat flux between two metal nodes using Fourier's Law (equation 3.5). Conductive conductances are represented with thermal resistors drawn in black in figure 3.1. Conductive conductance between adjacent metal nodes in the turbocharger are constant for any operative condition since that property depends only on the internal geometry and cases material.

$$\dot{Q}_{i,j}^{cond} = K_{i,j} \cdot (T_i - T_j) \tag{3.5}$$

According to presented turbocharger configuration, metal nodes can be connected to fluid nodes too by means of convective conductances ($hA_{l,i}$) being calculated the heat flux between a metal node and a fluid one using Newton's cooling law (equation 3.6). Working fluids in turbocharger model have been named from here on as *Gas* (exhaust gases moving the turbine), *Air* (compressed air by the compressor), *Oil* (lubricating oil), *W* (cooling liquid for some turbochargers) and *Ambient*.

$$\dot{Q}_{l,i}^{conv} = hA_{l,i} \cdot (T_l - T_i) \tag{3.6}$$

Connection between metal and fluid nodes is represented by grey thermal resistors in figure 3.1. Metal nodes can store energy during transient processes due to their associated mass. That phenomenon has been taken into account in the network model by means of capacitors (represented in light grey).

According to heat transfer proposal, not the whole energy from the exhaust gases upstream turbine inlet is used in power generation inside the turbine. An important part of that energy is transmitted by convection mechanism to the turbine case ($\dot{Q}_{Gas/T}$) and later to the rest of the turbocharger by means of metal conduction ($\dot{Q}_{T/H1}$). Other part of that energy is released to the surroundings as a convective and radiative heat flux ($\dot{Q}_{T/Amb}$). Finally, other part of that energy is used to heat up turbine case during transient operation (energy accumulation). In order to simplify the complex heat transfer phe-

nomena in the turbine side and taking into account the exposed areas, it has been assumed that the heat transfer phenomena occurs before the expansion process as it is shown in the left h/s diagram of figure 3.1. At compressor side, the same phenomena can be explained with the difference that the outlet air can absorb or release thermal energy ($\dot{Q}_{C/Air}$) from the compressor case depending on housing wall temperatures. In order to simplify that process and taking into account that compressor larger exposed area is at compressor volute and diffuser, it has been assumed that heat transfer phenomena occurs after the compression work. That process is shown in the h/s diagram on the right side of figure 3.1. In the presented case, compressed air is receiving heat from metal node C. Taking into account those considerations, heat transfer phenomena can be split into the following processes.

- Some of the energy from the exhaust gases (entering at Gas temperature) is transmitted to the turbine case (node T) before extracting mechanical power at the turbine rotor. This subtracted energy ($\dot{Q}_{Gas/T}$) lead to the inlet turbine (IT) temperature governing the expansion process is lower than the measured at turbine inlet (Gas).

- That energy is transmitted by pure metal conduction from metal node T to metal node H_1 ($\dot{Q}_{T/H1}$).

- At that point (node H_1), heat flux can be transmitted following three possible paths. The first one by metal conduction between metal nodes H_1 and H_2 ($\dot{Q}_{H1/H2}$). The second amount of energy is transmitted to the lubricating oil by forced convection (from H_1 to Oil, $\dot{Q}_{H1/Oil}$). The third is to the ambient $\dot{Q}_{H1/Amb}$

- Central node H_2 is connected by metal conduction with metal nodes H_1 and H_3 ($\dot{Q}_{H1/H2}$ and $\dot{Q}_{H2/H3}$) but it is also in contact with ambient ($\dot{Q}_{H2/Amb}$) and with lubricating oil ($\dot{Q}_{H2/Oil}$). In case the turbocharger will be water-cooled, extra node W will be introduced $\dot{Q}_{H2/W}$ (its convective connection is shown in dashed grey in figure 3.1).

- Housing node H_3 is connected by metal conduction with metal nodes H_2 and C ($\dot{Q}_{H2/H3}$ and $\dot{Q}_{H3/C}$) and to ambient $\dot{Q}_{H3/Amb}$.

- Compressor node (C) is connected by metal conduction with metal node H_3 ($\dot{Q}_{H3/C}$), to the ambient $\dot{Q}_{C/Amb}$ and by forced convection with a

node placed at compressor diffuser $\dot{Q}_{C/Air}$. That is final state after the adiabatic compression process is named Air.

- A scheme of the internal heat transfer fluxes in a turbocharger is shown in cutting view on the left side of figure 3.2.

- For some operative conditions temperature after adiabatic compression (node Air according to figure 3.1) can be lower than wall temperature of nodes H_3 and C (low loads). Then compressed air will receive some heat from those nodes ($\dot{Q}_{H3/C}$) and later ($\dot{Q}_{C/Air}$). At those conditions compressed air will increase its temperature up to the outlet conditions named OC (situation described in figure 3.1).

- For high loads, temperature after adiabatic compression Air can exceed temperature of the neighbouring nodes ($H3$ and C). Then heat transfer phenomena moves from air to node C (being compressor outlet temperature OC lower than adiabatic temperature, i.e. Air).

- Heat fluxes to the oil have been considered to occur according to the processes described on the right side of figure 3.2. This distinction has been done according to measured temperature differences and with the aim of simplifying energy exchange phenomena to the lubricating oil. Oil comes into the turbocharger at temperature OI, then it increases up to conditions $OI/H1$ by receiving some heat from metal node H_1 ($\dot{Q}_{H1/Oil}$). At that point oil temperature increases due to mechanical friction losses ($\dot{W}_m$) up to conditions $OO/H2$. Eventually oil will increase its temperature up to the outlet measured temperature (OO) due to heat exchange with node H_2 ($\dot{Q}_{H2/Oil}$).

- Each metal node is connected to the ambient by means of a convective branch (external radiation and convection) and by view factors to the metal nodes of the system. Those branches have been removed in previous explanation since view factors hidden clarity in the system description.

A series of ad-hoc experiments have been carried out to determine thermal properties of proposed lumped model. Those properties have been divided into the ones depending only on geometrical considerations (weight, material, lengths...) but not on turbocharger operative conditions. And the other group depending on both geometrical parameters (lengths, diameters...) but also on

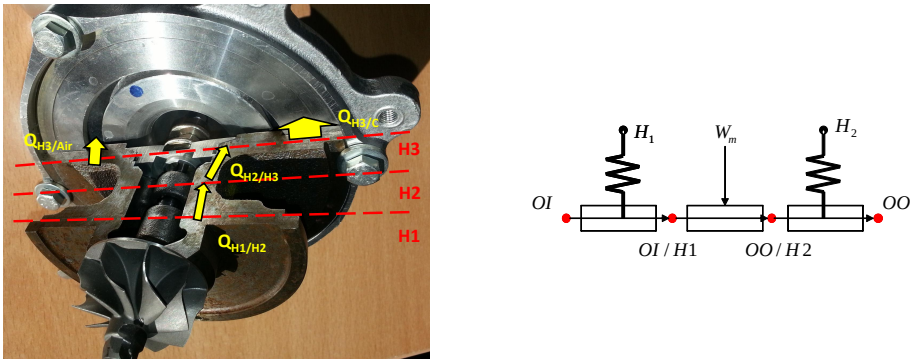

Figure 3.2: Left: Cutting view of a non-water cooled turbocharger; Rigth: Heat fluxes to the lubricating oil

the operative conditions (mass flow, rotational speed, temperature...). Conductive conductances (between metal nodes) and thermal capacitances belong to the first group. Convective conductances (between metal nodes and fluid nodes) belong to the second group. That information will be used to fill down lumped model with thermal properties (conductive conductances and capacitances) and correlations (for convective conductances). Detailed information about turbocharger lumped model and experimental procedure to determine thermal properties can be found in [119].

Summarizing, the lumped model has 14 unknowns to be determined (showed in table 3.2). These are, 4 metal conductance ($K_{T/H1}$, $K_{H1/H2}$, $K_{H2/H3}$, $K_{H3/C}$), 5 metal capacitance (C_T, C_{H1}, C_{H2}, C_{H3}, C_C) and 5 convective conductances ($hA_{Gas/T}$, $hA_{H1/oil}$, $hA_{H2/oil}$, $hA_{H2/W}$, $hA_{C/Air}$). Finally, in order to close turbocharger power balance a mechanical losses model is needed. This model has been introduced as an energy source into the lumped model ($\dot{W}_m$). That model will take into account the increase in lube oil temperature due to friction losses only [153, 154].

3.3 Metal Properties

Turbocharger heat transfer properties, depending only on the internal geometry and material (metal conductances and thermal capacitances), have been

Table 3.2: Model unknowns

Thermal Properties			
Independent of operative conditions		Dependent on the operative conditions	
Conductive Conductances	$K_{T/H1}$	Convective Correlations	$hA_{Gas/T}$
	$K_{H1/H2}$		$hA_{H1/Oil}$
	$K_{H2/H3}$		$hA_{H2/Oil}$
	$K_{H3/C}$		$hA_{H2/W}$
			$hA_{C/Air}$
Thermal Capacitances	C_T	Energy Source	$\dot{W}_m$
	C_{H1}		
	C_{H2}		
	C_{H3}		
	C_C		

obtained on a specific test bench [129, 171] following the methodology described by Serrano et al. [152].

3.3.1 Thermohydraulic Test Rig Description

A schematic view of the test rig is presented in figure 3.3, as it is observed the turbocharger unit was placed in the center of the installation and it was connected to two different flow circuits. There was a high temperature circuit (connected to a heating system) and a low to medium temperature circuit (connected to a cooling system). Fluid temperature and mass flows in both circuits could be varied in a wide range of operative conditions using PID controllers, heat exchangers and manual valves.

Heat in the high temperature circuit was provided by three electrical resistances (12.5 kW of nominal power each of them) to a heat transmitter incompressible fluid. The selection of that fluid was made attending to not changing its temperature with pressure variations inside the turbomachinery and two other main parameters, on the one hand, its thermal properties (specific heat and working temperatures). On the other hand, the simplicity to measure its flow and to detect possible leakages. So thermal oil was used, since

it fitted accurately with previous requirements. That hot oil was delivered by an external system which included an expansion tank, an electrical oil pump, temperature and pressure control and different valves to allow changes in mass flow rates. The system could deliver thermal oil up to a temperature of 300°C and a volumetric flow up to 6.5 m^3h^{-1} That heat system was able to be used to feed any element under study with a controlled thermal energy. Oil temperature leaving the system was controlled by a PID controller that switched on or off the different electrical resistances. Flow was controlled manually by adjusting valves until the desired oil mass flow value was reached.

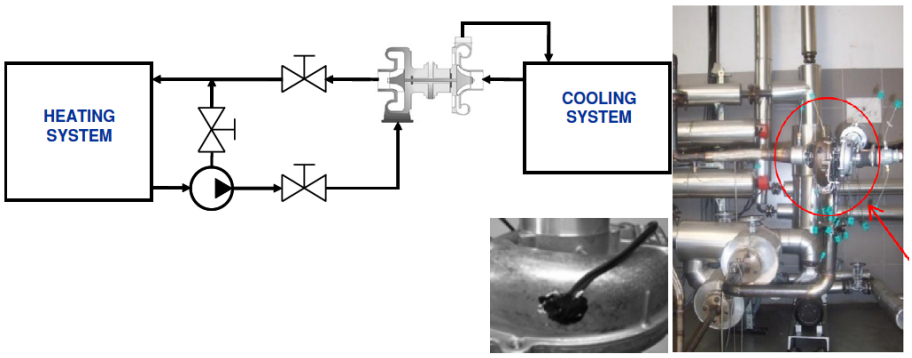

Figure 3.3: Schematic view of the test bench

On the other hand, a heat drain system was necessary, this system was designed, manufactured and mounted attending to the requirements of the specific tests to be performed. The drain system consisted of a low to medium temperature oil circuit whose temperature was controlled by means of an external heat exchanger. Inside such an exchanger, cool oil delivered its energy to a glycol-based coolant solution; a specific PID acted over HVAC equipment and an automatic valve for the coolant that allowed getting a constant temperature for the cool oil. More details about this particular test bench can be found in [171].

In order to carry out turbocharger thermal characterization, wall temperatures along the turbocharger unit were recorded by means of K-type thermocouples placed at different system positions. It was decided to divide turbocharger unit into the five measurement planes showed in lumped model of figure 3.1 (*T, H1, H2, H3, C*).Three thermocouples were installed on each plane at several azimuthal locations in order to validate axial heat transfer assumption. That assumption ensured that circumferential dispersion of tem-

peratures was negligible compared with axial temperature distribution.

For fluid temperatures, measurements were accomplished using RTD due to their higher precision, which was an important factor for heat fluxes determination. Oil flow was measured using two Coriolis flow meters (one for the highest oil temperature circuit and the other for the lowest temperature circuit). Information from different measurement devices (mass flow and temperatures) was acquired with a data acquisition system. Details about measurement probes mentioned above are summarized in table 3.3.

Table 3.3: Thermo-Hydraulic sensors instrumentation

Parameter	**Equipment**	**Range**	**Error**
Oil mass flow (high temperature side)	Coriolis flow meter	0 to 2720 kgh^{-1}	±0.1%
Oil mass flow (low temperature side)	Coriolis flow meter	0 to 100 kgh^{-1}	±0.1%
Fluid temperature	RTD	-75 °C to 350 °C	0.01 °C
Metal temperature	K Thermocouples	0 to 1260 °C	±0.75%

3.3.2 Experimental Methodology

Experimental methodology for turbocharger metal properties determination consisted of the installation of turbocharger unit into the thermo-hydraulic test bench. In order to avoid expansion or compression processes in the machine, turbine and compressor cases were filled out with thermal oil, remaining the axis physically blocked. Hot oil was passed through one of the turbocharger cases (turbine or compressor) meanwhile cold oil was passed through the other case in order to create a heat flux inside the turbocharger by means of temperature differences. During the whole experiment, the turbocharger was fully insulated to minimize heat transfer to the ambient meanwhile housing cavities for oil and water remained empty. This experiment ensured that the whole heat flux was transmitted from the hot side (one of the cases) to the cold side (the other case) by pure metal conduction. Several tests under steady and transient conditions were carried out to determine conductive conductances ($K's$) and thermal capacitances ($C's$) respectively.

Due to the fact that turbine and compressor cases were fed with thermal oil

during the experiments, some modifications were necessary to ensure a good sealing. Turbocharger original seals were replaced by Teflon^{TM}ones to avoid fluid leakages through turbocharger axis. Besides, the shaft was blocked to avoid internal turbulence in case wheels will rotate. Finally small drills at the top part of compressor and turbine cases were performed to drain air from cases. Those modifications improved heat fluxes determination.

3.3.2.1 Steady state tests

Steady tests were performed passing hot thermal oil through the turbine case while cold oil passed through the compressor case. Inlet conditions were kept as constant as possible by means of PID controllers. In order to maximize the heat transfer from the hot turbine to the cold compressor, for the hot oil (turbine side), a constant temperature near 300°C with three levels of mass flows were chosen to test the hot turbine. At the same time compressor conditions were fitted to a minimum temperature of 20°C with three levels in mass flow as it is observed on the left side of figure 3.4. Those flows were chosen as low as possible in order to increase residence time inside turbine and compressor cases. A criteria of a lower variation than 0.1°C per minute in turbocharger wall temperature was used to ensure that steady state conditions had been achieved. Measurements repeatability was verified by checking the averaged dimensionless temperatures. Those were calculated using equation 3.7, results have been showed against turbocharger axial position on the right side of figure 3.4.

$$\theta_i = \frac{T_i - T_{min}}{T_{max} - T_{min}} \tag{3.7}$$

Where T_i is the temperature that is going to be transformed into dimensionless units and T_{max} and T_{min} are the highest and lowest temperatures in the system, corresponding to turbine and compressor inlet flows respectively. As it is observed on the right side of figure 3.4 all tests collapsed into a single line what confirmed that conductive conductances between model nodes were independent from turbine and compressor inlet conditions. That ensured the described experimental methodology was robust and metal conductances calculated with presented procedure was invariant for a given turbocharger. Higher temperature differences in the axial direction (among metal nodes) than the circumferential dispersion were observed, which confirmed the axial

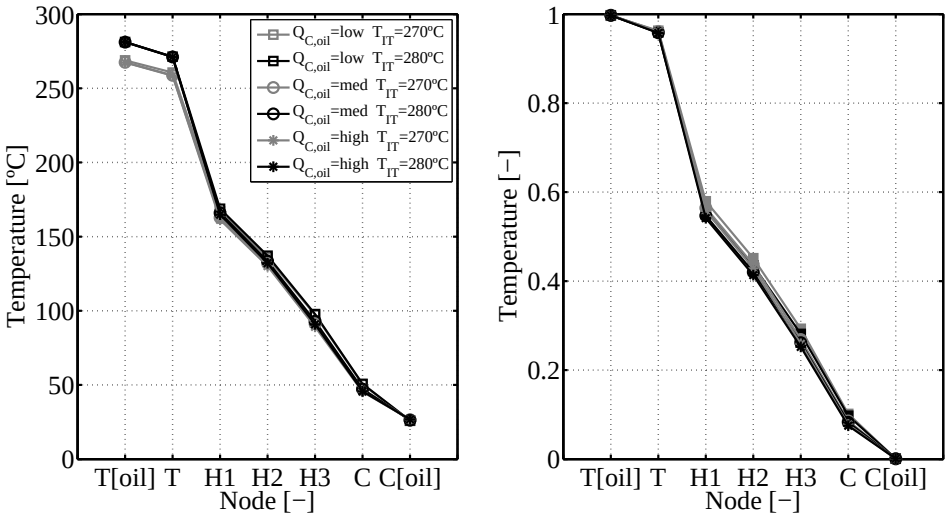

Figure 3.4: Nodes temperatures from steady tests, Left: Temperatures in ºC, Right: Dimensionless temperatures

one-dimensional heat transfer hypothesis. Previous hypothesis simplifies conductive conductances calculation since all heat fed in the turbine side travels axially across the whole turbocharger.

3.3.2.2 Transient state tests

Several testing experiments have been developed to quantify the storage of energy by turbocharger metal nodes during transient conditions. A thermal charge experiment was defined where hot oil was heated up to the desired temperature level in a closed loop. Once desired testing conditions were achieved, valves were operated in order to send hot oil towards the turbine case. During that time, cold oil at constant conditions had been passing through the compressor case. All temperatures were recorded along the transient until their stabilization. In order to validate transient performance the opposite testing procedure was carried out. The discharge test consisted of the sudden removal of the hot oil feeding turbine case operating over installation valves, meanwhile cold oil continued passing at constant conditions through compressor case. Equivalent test on the compressor side was also performed;

discharging it from hot oil while cold oil passed through the turbine case. Whole temperature evolution during charge and discharge thermal transient tests passing hot oil through the turbine case is shown in figure 3.5. First state (1^{st} period) corresponds to initial turbocharger conditions (wall temperatures equal to the ambient), a small variation in wall temperature of node C was appreciated. It was due to the stabilization process of the PID controlling its temperature. That state was followed by a sudden increase of wall temperatures (2^{nd} period), except node C that was kept at constant temperature. That temperature increase is due to the sudden release of hot thermal oil to the turbine case. At the end of this transient charge, another stabilization (3^{rd} period) was achieved, those steady conditions were used to determine thermal conductances ($K's$). At that point (end of 3^{rd} period) turbine circuit valves were operated to perform turbine discharge test, turbocharger wall temperature decrease is observed in the last stage (4^{th} period) of figure 3.5.

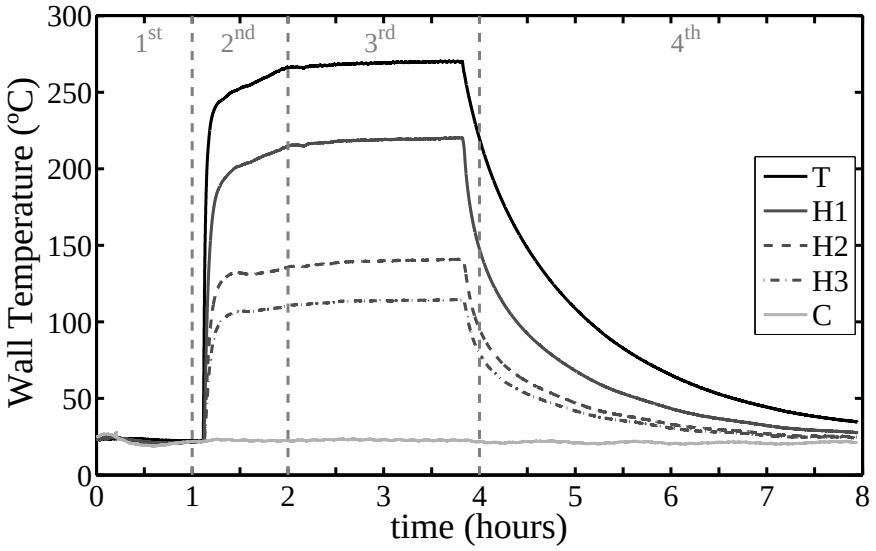

Figure 3.5: Transient evolution from a whole test

3.3.3 Metal Properties Determination

With previous considerations the general lumped model showed in figure 3.1 simplifies to the thermal network presented in figure 3.6. That simplification takes into account turbocharger particular set-up and the high residence times

for oil in both casings. With those considerations heat from hot oil is transferred to the turbine case ($\dot{Q}_{Oil/T}$) but also to the housing plate H_1 ($\dot{Q}_{Oil/H1}$). The same pattern takes place at the compressor side where cold oil recovers heat from two possible branches, one from compressor back-plate H_3 to the oil ($\dot{Q}_{H3/Oil}$) and the other from compressor case C to oil ($\dot{Q}_{C/Oil}$).

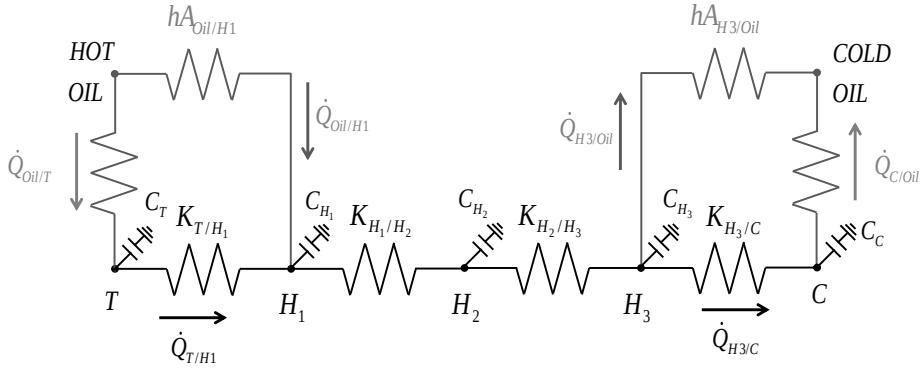

Figure 3.6: Lumped model for tests in thermo-hydraulic test bench

Conductive conductances ($K's$) between adjacent nodes have been determined using Fourier's Law (equation 3.5). Where heat flux entering the system has been calculated as the enthalpy drop of hot oil passing through the turbine case. Conductive conductances of central nodes $K_{H1/H2}$ and $K_{H2/H3}$ have been easily determined since there was only one way for the heat flux. Metal conductances $K_{T/H1}$ and $K_{H3/C}$ determination was not so direct due to the unknown convective branches $hA_{Oil/H1}$ and $hA_{H3/Oil}$. In order to avoid doing any hypothesis for its calculation [152], both the steady and transient tests have been used. When discharge test on the turbine side was performed, convective branch $hA_{Oil/H1}$ (and $hA_{Oil/T}$) disappeared since no oil passed along the turbine being able the direct calculation of metal conductance $K_{T/H1}$. Energy conservation equation applied to metal nodes T and H_1 for transient state (turbine discharge) leads to equation 3.8.

$$T_T^{t+\Delta t} = \frac{\Delta t}{C_T}\left[K_{T/H_1}\cdot\left(T_{H_1}^t - T_T^t\right)\right] + T_T^t \tag{3.8}$$

$$T_{H_1}^{t+\Delta t} = \frac{\Delta t}{C_{H_1}}\left[K_{T/H_1}\cdot\left(T_T^t - T_{H_1}^t\right) + K_{H_1/H_2}\cdot\left(T_{H_2}^t - T_{H_1}^t\right)\right] + T_{H_1}^t \tag{3.9}$$

And to equation 3.9 in the case that temperature of node H_2 was used as a boundary condition to process the discharge test on the turbine side, the equivalent lumped model was simplified including only conductive branches between metal nodes T and H_2. Where $K_{T/H1}$, C_T and C_{H1} were unknowns and $K_{H1/H2}$ was already known from the steady tests. In such conditions two subsets of boundaries could be used to determine the unknowns. Imposing temperatures at nodes T and $H2$ allows the determination of $K_{T/H1}$ and C_{H1} using equation 3.9. Since that expression can be set out for each time step of the discharge evolution, a least square method has been used to determine $K_{T/H1}$ and C_{H1} minimizing the sum of the squares of errors made in the prediction of every single equation. Imposing temperature at node H_1 allowed $K_{T/H1}$ and C_T determination using equation 3.8. Good agreement predicting those parameters together is shown in figure 3.7 for the turbocharger named #1. A single value for those parameters has been chosen in order to minimize error predicting instantaneous temperatures of nodes T (showed in the top part of figure 3.7) and H_1 (the bottom part of figure 3.7) for several turbine discharge tests.

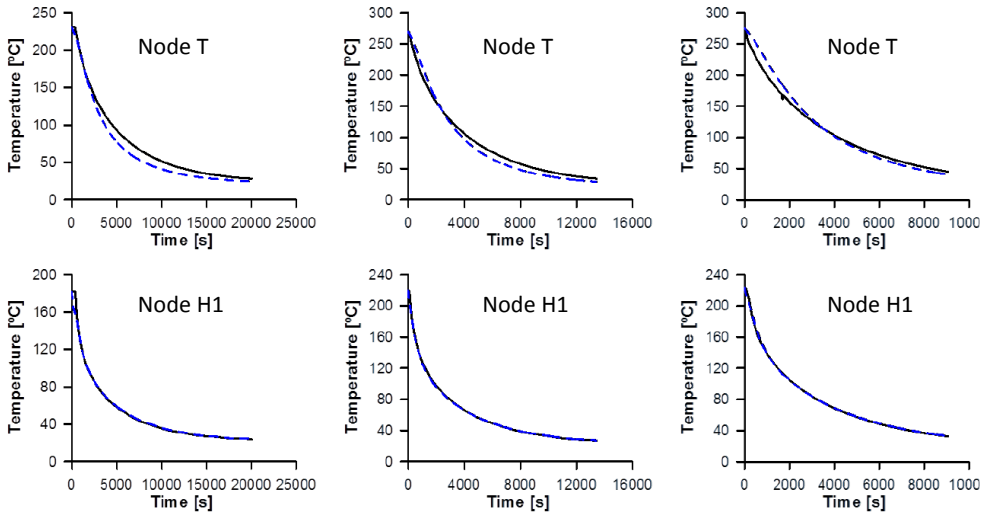

Figure 3.7: Fitting of thermal capacitances C_T, C_{H1} and metal conductance $K_{T/H1}$ together. Measurement in solid, prediction in dashed. Top: Temperature prediction of node T prediction. Bottom: Temperature prediction of node H_1 prediction.

The equivalent procedure has been applied to the convective oil branch at

compressor side. In this case a discharge experiment of the thermally loaded compressor has been done in order to remove convective branch $hA_{H3/Oil}$. If temperatures of nodes H_2 and C are used as boundary conditions, equivalent lumped model includes conductive branches between metal nodes H_2 and C (equation 3.10). Where $K_{H3/C}$, C_{H3}, C_C were unknown and $K_{H2/H3}$ was already known from the steady tests. In order to determine those unknowns, two subsets of boundaries could be chosen. Imposing temperature at node C allowed determining $K_{H3/C}$ and C_{H3} using equation 3.10. When temperature of node H_3 was imposed, $K_{H3/C}$ and C_C will be determined using equation 3.11.

$$T_{H_3}^{t+\Delta t} = \frac{\Delta t}{C_{H_3}} \left[K_{H_2/H_3} \cdot \left(T_{H_2}^t - T_{H_3}^t \right) + K_{H_3/C} \cdot \left(T_C^t - T_{H_3}^t \right) \right] + T_{H_3}^t \quad (3.10)$$

$$T_C^{t+\Delta t} = \frac{\Delta t}{C_C} \left[K_{H_3/C} \cdot \left(T_{H_3}^t - T_C^t \right) \right] + T_C^t \quad (3.11)$$

Good agreement modelling instantaneous temperature of nodes H_3 and C, is observed in figure 3.8 where a single value for thermal capacitances C_{H3} and C_C and the metal conductance $K_{H3/C}$ was chosen as it was described above. Due to the limitations of the compressor oil circuit, oil temperature to perform compressor discharge test was set to 110°C.

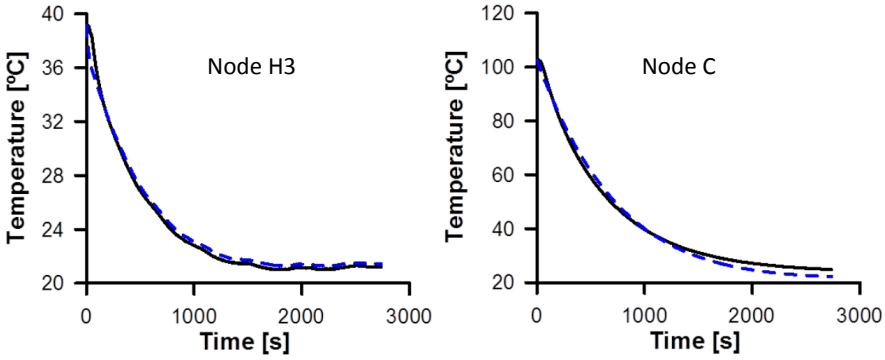

Figure 3.8: Fitting of thermal capacitance C_{H3}, C_C and metal conductance $K_{H3/C}$. Left: Prediction of node's H_3 temperature. Right: Prediction of node's C temperature. Measurement in solid, prediction in dashed.

Thermal capacitance calculation of central node C_{H2}, was obtained from previously determined conductances and some boundary conditions. In this case nodes H_1 and H_3 have been used as boundary conditions to avoid convective fluxes from H_1 or H_3 to the oil. Mathematical expression to calculate housing capacitances (equation 3.12) is based on the finite difference technique commented before.

$$T_{H_2}^{t+\Delta t} = \frac{\Delta t}{C_{H_2}} \left[K_{H_1/H_2} \cdot \left(T_{H_1}^t - T_{H_2}^t \right) + K_{H_2/H_3} \cdot \left(T_{H_3}^t - T_{H_2}^t \right) \right] + T_{H_2}^t \quad (3.12)$$

Where metal conductances $K_{H1/H2}$ and $K_{H2/H3}$ were determined from steady tests, and temperatures from nodes H_1 and H_3 were imposed as boundary conditions. Good agreement modelling thermal capacitance of node H_2 is shown in figure 3.9 for turbocharger named #1, a single value for that capacitance has been found for the different transient tests (two charges and two discharges).

Terms within brackets in equations 3.8, 3.9, 3.10, 3.11 and 3.12 represent the energy balance of the node under consideration. Under transient conditions, that balance is not zero, so those terms allow calculating temperature increase for successive instants. Steady temperature values, reached after the transient evolution, allow validation of results found for conductive conductances since they resulted from a different kind of test.

3.3.3.1 Summary of Metal Properties

Table 3.4 shows averaged values for metal thermal properties, i.e. conductances and capacitances for the studied turbochargers. Results assessed were satisfactory considering the good agreement between measured values and modelled ones along transient evolution, nevertheless small differences were observed between measured and modelled temperature results. Those differences could arise from the inherent simplification of the heat transfer problem. Following that methodology and with that test bench configuration it was possible to study only pure conduction problem between turbine and compressor, without the coexistence of expansion in turbine, compression in compressor, mechanical losses, internal convection to the lubricant oil port and external

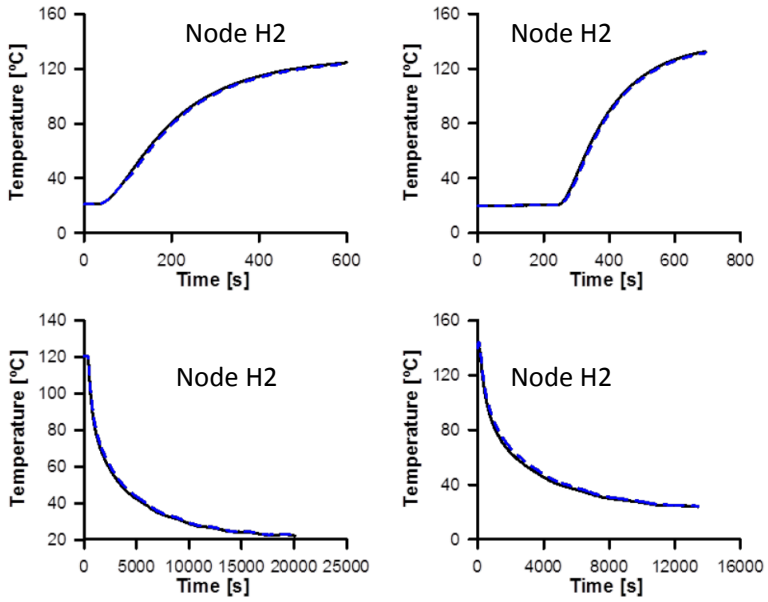

Figure 3.9: Fitting of thermal capacitance. Prediction of node's temperature H_2. Measurement in solid, prediction in dashed.

convection and radiation that are normally present during turbocharger normal operation.

3.4 Convective properties

Convective conductances depend on turbocharger geometry (wetted surface) but also on turbocharger operative conditions (fluid velocity and temperature). Thermal correlations for those heat transfer paths have been wisely determined from turbocharger measurements under steady hot flow conditions [119]. Those correlations are based on Nusselt' number definition assuming that turbocharger internal cases (turbine and compressor volutes, lubricating and cooling ports) can be modelled as single pipes. With that assumption Nusselt number correlations can be expressed in the form of Dittus-Boelter (equation 3.13) and Sieder-Tate (equation 3.14) correlations [88]. Nusselt num-

Table 3.4: Metal properties results for different turbochargers ($K's$ and $C's$)

TURBO	**#1**	**#2**	**#3**
Conductances $\left[\mathrm{WK}^{-1}\right]$			
$K_{T/H1}$	2.96	3.5	1.97
$K_{H1/H2}$	5.86	5.9	7.36
$K_{H2/H3}$	13.63	9.8	4.93
$K_{H3/C}$	2	14.55	1.63
Capacitances $\left[\mathrm{JK}^{-1}\right]$			
C_T	4261	4223	4377
C_{H1}	902	1642	525
C_{H2}	197	450	219
C_{H3}	218	1076	320
C_C	1143	1796	339

ber correlations for convective branches account for fluid operative conditions; i.e. mass flow and length scale in the Reynolds number and fluid state in the Prandtl number.

$$\mathrm{Nu_D} = 0.023 \cdot \mathrm{Re_D}^{4/5} \cdot \mathrm{Pr^n} \tag{3.13}$$

$$\mathrm{Nu_D} = 0.027 \cdot \mathrm{Re_D}^{4/5} \cdot \mathrm{Pr}^{1/3} \cdot \left(\frac{\mu}{\mu_\mathrm{w}}\right)^{0.14} \tag{3.14}$$

Those expressions are based on the simplicity of forced convection inside smooth and long pipes, but these assumptions cannot be confirmed studying turbocharger internal heat transfer phenomena due to its complex geometry, not smoothy ports and the short length of pipes. For that reason the aforementioned expressions could not be used in their original fashion. However it has been desired keeping generality in the study and so only constant coefficients and exponents of these correlations have been recalculated for any convective branch. Those parameters have been fitted using experimental data from hot steady flow tests performed in a turbocharger test bench [119]. In some cases extra dimensionless numbers have been introduced to account for turbocharger complex geometry. Once Nusselt number correlations have been determined, heat fluxes between fluids and wetted metal nodes have been calculated us-

ing Newton's cooling law (equation 3.6). Taking into account Nusselt number definition (equation 3.15).

$$\mathrm{Nu_D} = \frac{\mathrm{h} \cdot \mathrm{D_h}}{\kappa_\mathrm{l}} \tag{3.15}$$

Where h represents convective heat transfer coefficient, D_h hydraulic diameter and κ_l thermal conductivity of the fluid. Isolating h from that equation and introducing into equation 3.6 leads to.

$$\dot{Q}_{li}^{conv} = \frac{\mathrm{Nu_D} \cdot \kappa_\mathrm{l}}{D_h} \cdot A \cdot (T_l - T_i) \tag{3.16}$$

Being A wetted surface of the equivalent straight pipe (calculated as $\pi \cdot D_h \cdot L_{eff}$, rearranging equation 3.16 it is obtained.

$$\dot{Q}_{l,i}^{conv} = \mathrm{Nu_D} \cdot \kappa_\mathrm{l} \cdot \pi \cdot \mathrm{L_{eff}} \cdot (\mathrm{T_l} - \mathrm{T_i}) \tag{3.17}$$

3.4.1 Test Rig Description

A basic diagram of the turbocharger test rig used for convective heat transfer characterization can be seen in figure 3.10. This test rig has been designed by CMT-Motores Térmicos and has the following capabilities,

- Maximum temperature at turbine inlet: 600ºC
- Maximum absolute pressure at turbine inlet: 3.5 bars
- Maximum mass flow: 0.2 kg/s

3.4.1.1 Turbine side

The internal combustion engine has been replaced by a 55kW screw compressor pumping air into the turbine side, it can be heated up to a maximum temperature of 600ºC using a set of 5 electrical heaters. Heating is optional depending on the type of test being carried out. In case very low temperatures

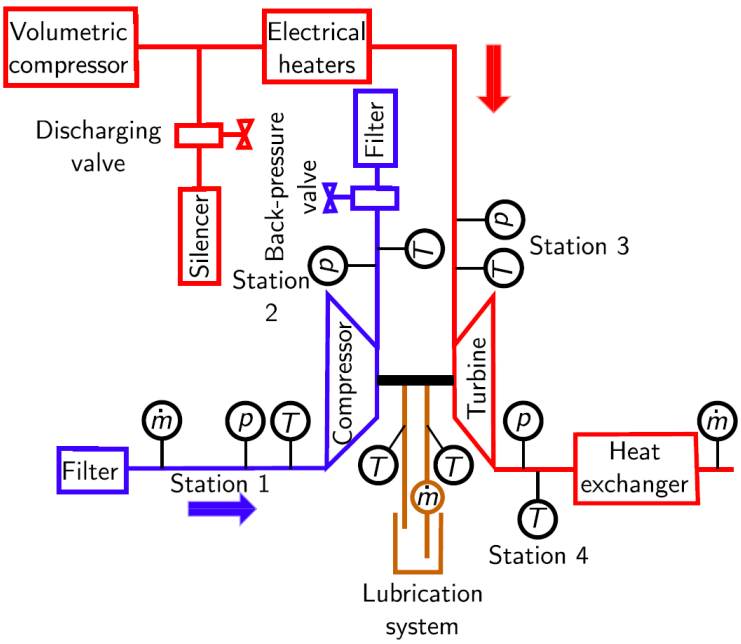

Figure 3.10: Schematic view of the turbocharger test rig

at turbine inlet are required, a heat exchanger is also available. In case it is desired to test turbine (or compressor) under pulsating flow conditions, a rotary valve can be installed to generate pulses; frequency, shape and amplitude can be controlled as desired. An intercooler has been installed at the turbine exit, to cool down the air before releasing it to the atmosphere doing so possible the mass flow measurement.

3.4.1.2 Compressor side

An air filter has been installed at compressor inlet line to avoid dust or foreign objects enter to the system. A back-pressure valve has been used at compressor outlet to control its load, simulating what would be the intake valves and cylinders of the engine. A silencer and oil catch tank have been also used at the compressor exit line before releasing air to the atmosphere.

3.4.1.3 Sensors

A series of sensors have been also installed to record measured parameters allowing turbocharger characterization.

Average pressure sensors are used to record the average flow static pressure. Eight KISTLER sensors have been installed with a measuring range of 0-5 bar; two at the compressor inlet, two at the compressor outlet two at the turbine inlet and two at the turbine outlet.

Temperature sensors Type K thermocouples have been used to record flow temperature. Sixteen thermocouples are used, four at each inlet and outlet of the turbocharger unit. They have been installed according to the SAE J1723 supercharging testing standard [142]; two thermocouples on 1/3 depth of the pipe diameter, one thermocouple on 1/4 of the diameter and one thermocouple in the middle of the tube.

Mass flow sensors ABB hot wire air flow meters have been used to record air mass flow in both the turbine and compressor machines. Turbine mass flow sensor has been installed after the intercooler due to temperature limitations (it must work with temperatures below 50^{o}C). At compressor side it has been installed at the inlet to prevent from high temperatures. An extra compressor mass flow meter has been installed at the compressor outlet whose operation was based on vorticity measurements and had no temperature restrictions for the operative conditions tested on compressor side.

Speed sensor A PICOTURN sensor with a range of 0-300,000 rpm has been installed at compressor case to record turbocharger speed.

3.4.1.4 Lubrication system

The auxiliary lubrication system showed in figure 3.11 was installed to provide lubricating oil to the turbocharger at controlled pressure, mass flow and temperatures. Capabilities from that lubricating system are,

- Maximum oil flow: 80 l/h
- Maximum working pressure: 6 bars
- Maximum oil temperature: 150 ºC
- Minimum oil temperature: 25 ºC

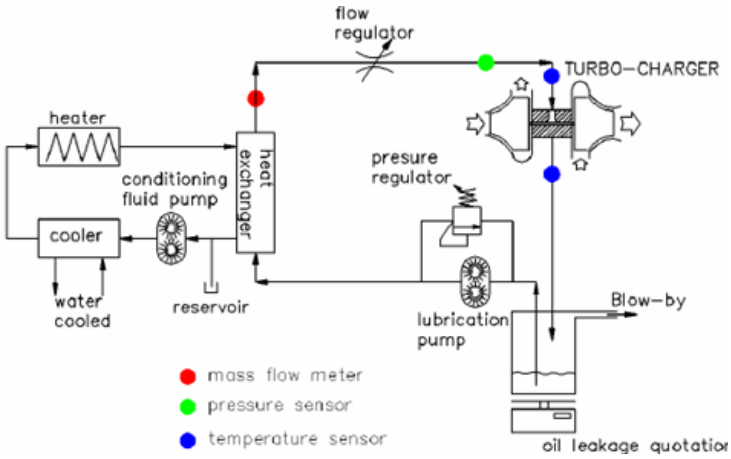

Figure 3.11: Auxiliary lubrication system

3.4.2 Experimental Methodology

Turbochargers presented in table 3.1 have been tested in the gas stand showed in figure 3.10 under steady hot flow conditions. Operative conditions were chosen in order to obtain turbocharger performance maps at highest possible turbine inlet temperature as it is observed in figure 3.12. Measurements at different turbine openings have been carried out for the biggest turbocharger (#1). Meanwhile medium size turbocharger (T.#2) was studied only for the highest turbine efficiency opening (60% VGT opening). Steady measurements were carried out with the turbocharger fully insulated and they have been used as the data basis to determine convective correlations of the turbocharger proposed model in figure 3.1.

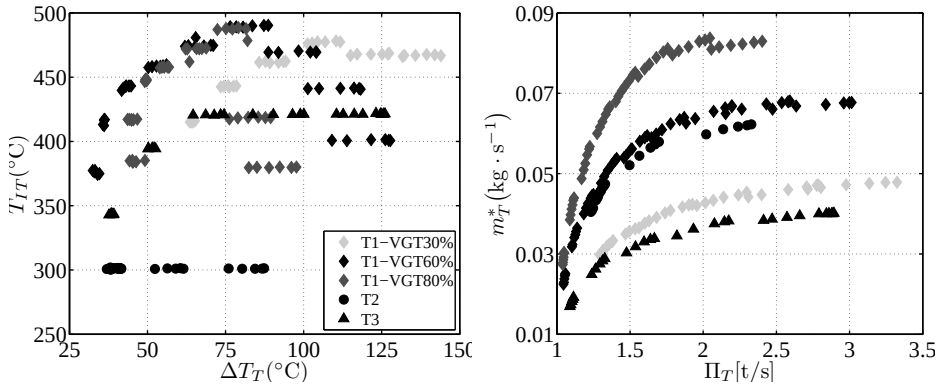

Figure 3.12: Experimental hot test campaign. Left: turbine inlet temperature vs. total temperature drop, Rigth: Turbine performance maps.

3.4.3 Convective Properties Determination

3.4.3.1 Gas/T

Convective heat flux in the turbine side ($\dot{Q}_{Gas/T}$ in figure 3.1), (assuming there are no heat losses to the ambient), is equal to conductive heat flux $\dot{Q}_{T/H1}$, according to nodal model proposed in figure 3.1. This heat flux has been obtained by means of measured temperatures at nodes T and H_1 and previously determined conductive conductance between both nodes using equation 3.18 [152]. One can say that after previous characterization, whole turbocharger (with instrumented thermocouples) behaves as a heat flow sensor).

$$\dot{Q}_{Gas/T} = \dot{Q}_{T/H1} = K_{T/H1} \cdot (T_T - T_{H1}) \tag{3.18}$$

Figure 3.13 shows the energy transmitted from the exhaust gases to the turbine case ($\dot{Q}_{Gas/T}$), as it is observed the higher is the turbine power the higher is the transmitted heat flux up to a given point. That is observed for turbochargers T.#2 and T.#3 that were measured under constant turbine inlet temperature as it is observed on the left side of figure 3.12. That was due to the reduction in residence time (turbine mass flow increased and so it did gases velocity) what made thermal process more adiabatic. Nevertheless for turbocharger T.#1 that was measured increasing turbine inlet temperature

as load increases (as it occurs in an engine), heat flux to the turbine case ($\dot{Q}_{Gas/T}$) grew up as turbine power increased. That was due to turbine inlet temperature increment compensated the reduction in residence time. If that heat is rated to the total enthalpy drop across the turbine ($\Delta\dot{H}_T$) relative importance of heat fluxes inside the turbine becomes lower than 5% of total energy. However that relative effect becomes important from operative points corresponding to low loads conditions (in some cases reaches the 70% of the total turbine enthalpy drop for turbocharger #1). Similar results have been found for the other tested turbochargers as it is showed in figure 3.14. These results are similar to those found by Baines et al. [14].

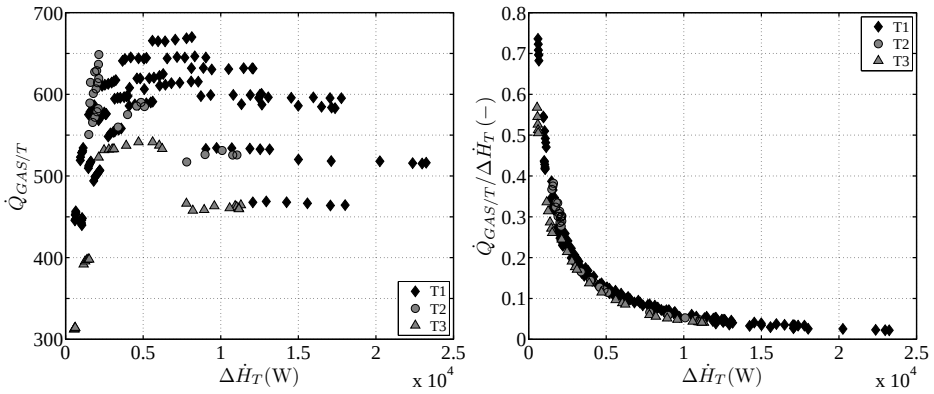

Figure 3.13: Heat transfer flux $\dot{Q}_{GAS/T}$

Turbine heat losses are assumed to occur at turbine inlet, i.e. the processes followed by the gases are a heat transfer and a polytropic expansion in the turbine, as several authors have proposed.

Nusselt number inside the turbine has been calculated using equation 3.17 where heat flux has been calculated using equation 3.18 and measured temperatures. Plotting that parameter versus Reynolds number, a trend with the VGT opening has been observed as it is shown in figure 3.15 for turbocharger T.#1. Correlation for Nusselt number governing heat transfer process between exhaust gases and the turbine case is in the original fashion of Sieder-Tate (equation 3.14) but including corrector term F [19] that will account for the observed VGT effect.

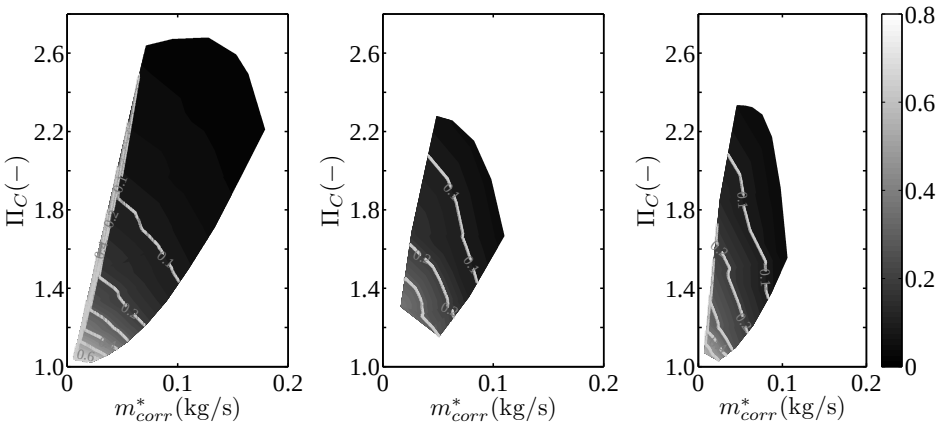

Figure 3.14: Heat flux $\dot{Q}_{Gas/T}$ from the studied turbochargers plotted in compressor map. Left:Big size, Center: Medium size, Right: Small size

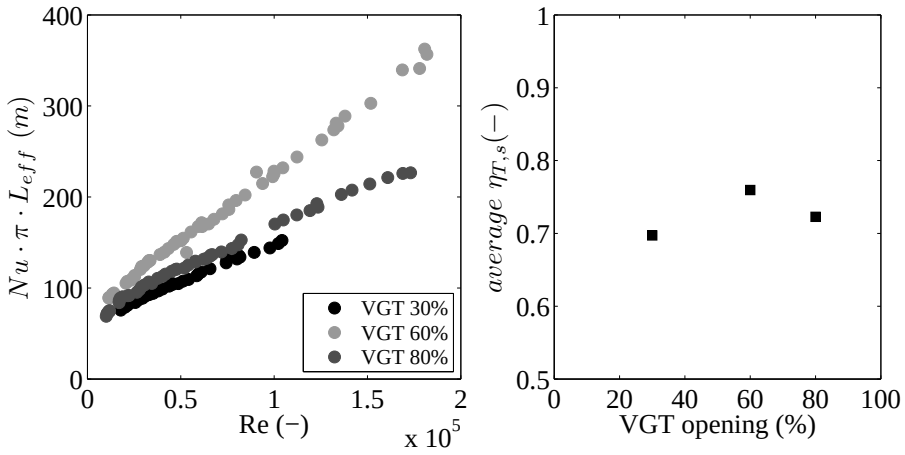

Figure 3.15: Nusselt number from convection Gas/T for T.#1.

$$\mathrm{Nu_{Gas/T}} = \mathrm{a} \cdot \mathrm{Re_{mT}^{b}} \cdot \mathrm{Pr}^{1/3} \cdot \left(\frac{\mu}{\mu_{\mathrm{w}}}\right)^{0.14} \cdot \mathrm{F} \tag{3.19}$$

As it is observed in figure 3.15, the existing trend in Nusselt number with the VGT opening is similar than the observed for turbine maximum isentropic

efficiency with VGT opening. For that reason it has been decided to include the effect of turbine efficiency in corrector term since that parameter gives an idea about turbine internal turbulence what what affects heat transfer.

$$F = 1 + 0.9756 \cdot \left(\frac{\frac{D_p}{\eta_{\max}}}{L_{eff}} \right)^{0.76} \tag{3.20}$$

Where an effective diameter has been defined using turbine inlet port diameter (D_p) and turbine maximum isentropic efficiency ($\eta_{\max}$). Scale length for Reynolds' number definition and the equivalent length (L_{eff}) of equation 3.17 have been defined from turbine geometrical parameters as equation 3.21 shows. Where L_t denotes turbine volute length.

$$L_{eff} = \frac{L_t^2}{4 \cdot D_p} \tag{3.21}$$

Parameters a and b from equation 3.19 have been fitted for each VGT position and turbocharger unit. In addition, a global fitting has been performed in order to get a unique solution for internal convective problem using whole testing data from the three tested turbochargers. Both fittings have been carried out by minimising mean square root value between measured heat flux from node Gas to metal node T using equation 3.18 and modelled heat flux using equation 3.22.

$$\dot{Q}_{Gas/T} = \mathrm{Nu_{Gas/T}} \cdot \kappa \cdot \pi \cdot \mathrm{L_{eff}} \cdot (\mathrm{T_{IT}} - \mathrm{T_T}) \tag{3.22}$$

Fitting parameters for convective correlation are shown in table 3.5 and figure 3.16 that shows those modelled versus measured heat fluxes using expression 3.22. As it is observed in figure 3.16 good prediction is obtained for most measured points and turbochargers, big dispersion is observed for the third turbocharger mainly for the intermediate range of heat fluxes since it is the smallest tested turbocharger and temperature measurements were more complicated.

Table 3.5: Fitting coefficients for correlation $\dot{Q}_{Gas/T}$

Gas/T	$\mathrm{Nu_{Gas/T}} = \mathrm{a} \cdot \mathrm{Re_{mT}^{b}} \cdot \mathrm{Pr}^{1/3} \cdot \left(\frac{\mu}{\mu_{\mathrm{w}}}\right)^{0.14} \cdot \mathrm{F}$				
	T1	**T1**	**T1**	**T2**	**T3**
VGT (%)	**30**	**60**	**80**	**60**	**-**
measured					
$\eta_{max}(-)$	0.6972	0.7596	0.7228	0.7509	0.7363
$L_{eff}(m)$	0.086	0.086	0.086	0.106	0.052
fitted					
a	1.07	1.07	1.07	5.34	0.101
b	0.57	0.57	0.57	0.48	0.84
$RMS(-)$	0.044	0.044	0.044	0.009	0.010

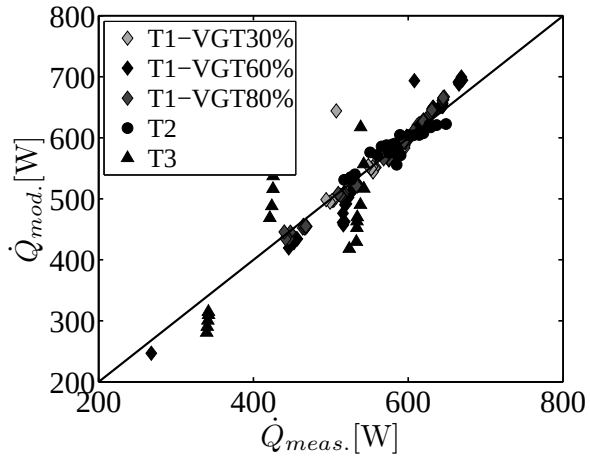

Figure 3.16: Heat fluxes modelling from node *Gas* to node T.

3.4.3.2 H2/W

Turbocharger coolant circuit works as an energy sink and so the heat flux recovered by node W can be directly determined from operative conditions. Doing so enthalpy drop through the coolant circuit is calculated using equation 3.23.

$$\dot{Q}_{H2/W} = \dot{m} \cdot c_p \cdot \Delta T_W \tag{3.23}$$

For low load conditions, heat removed by the cooling port can reach 40% of turbine total enthalpy drop. It is observed how an important amount of heat from the exhaust gases are recovered by the cooling port, since both heat fluxes $\dot{Q}_{T/Gas}$ (figure 3.13) and $\dot{Q}_{H2/W}$ (figure 3.17) are similar in magnitude. Even bigger in some cases due to heat recovering from oil coming from friction losses power. That effect will be observed later in oil branches, as in case of a water-cooled turbocharger heat recovered by lubricating oil drastically reduces compared with the recovered by a non-cooled turbocharger.

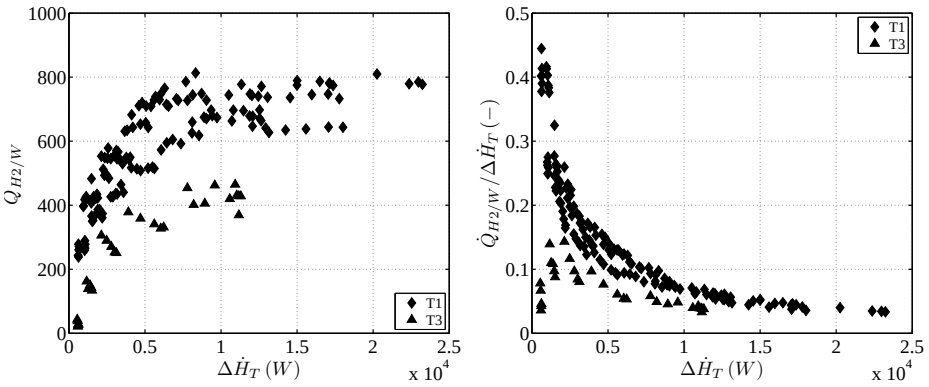

Figure 3.17: Importance of heat flux $\dot{Q}_{H2/W}$. Left: absolute value, Right: relative importance compared to turbine enthalpy drop

Table 3.6: Heat transfer modelling from node H_2 to node W

H2/W	$\mathrm{Nu_{H2/W}} = \mathrm{a} \cdot \mathrm{Re_{mW}^{0.8}} \cdot \mathrm{Pr^{0.4}}$	
	T1	**T3**
measured		
$L_{eff}(m)$	0.03	0.035
fitted		
a	0.1134	0.1562
$RMS(-)$	0.241	0.322

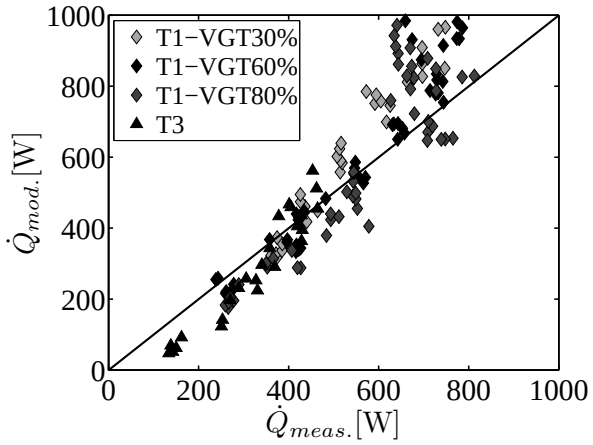

Figure 3.18: Heat fluxes modelling from node H_2 to node W.

Proposed correlation for Nusselt number (equation 3.24) in that circuit is in the original fashion of Dittus-Boelter correlation 3.13 but using exponent 0.4 (since water heats under normal operative conditions). Cooling port diameter has been used as the scale length for Reynolds' number calculation. Cooling liquid properties (Prandtl, viscosity and specific heat at constant pressure) have been estimated at inlet conditions.

$$\mathrm{Nu_{H2/W}} = \mathrm{a} \cdot \mathrm{Re_{mW}^{0.8}} \cdot \mathrm{Pr^{0.4}} \tag{3.24}$$

Where heat transfer from node H_2 to node W has been modelled using Nusselt number correlation proposal and equation 3.25.

$$\dot{Q}_{H2/W} = \mathrm{Nu_{H2/W}} \cdot \kappa \cdot \pi \cdot \mathrm{L_{eff}} \cdot (\mathrm{T_{H2}} - \mathrm{T_{WI}}) \tag{3.25}$$

Being T_{WI} coolant inlet temperature. Heat transfer validation for proposed correlation is observed in figure 3.18. That figure shows a good agreement modelling heat flux compared to the measured one. Fitting coefficients are shown in table 3.6, where housing length has been chosen as the effective length.

3.4.3.3 C/Air

Heat transfer from compressor case to the air moving inside the diffuser is equal to the heat coming from node H_3 to node C according to the proposed lumped model (figure 3.1). That assumption is true when no heat losses to the ambient through the insulated turbocharger are considered. In those conditions, $\dot{Q}_{C/Air}$ modelling can be performed from measured wall temperatures and previously determined conductance as equation 3.26 shows.

$$\dot{Q}_{C/Air} = \dot{Q}_{H3/C} = K_{H3/C} \cdot (T_{H3} - T_C) \tag{3.26}$$

Moving air can absorb energy from compressor case (node C) from medium to low loads as it is showed in figure 3.19 (positive values of $\dot{Q}_{C/Air}$). At those conditions lubricating is hotter than compressed air and heat transfer mechanism moves to increase compressor outlet temperature. As compressor load increases (higher compression ratio and mass flows) compressor outlet temperature will be higher than lubricating oil and the mechanism will be reversed. In that case the heat flux will move from node C to H_3 represented as negative fluxes in figure 3.19.

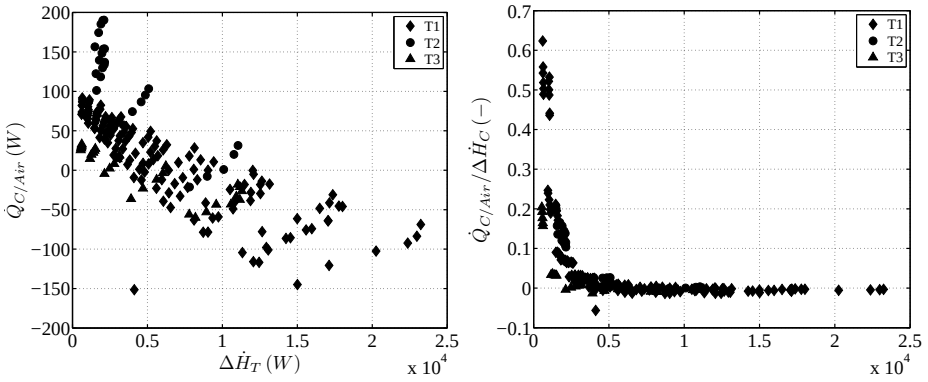

Figure 3.19: Importance of heat flux $\dot{Q}_{C/Air}$. Left: absolute value, Right: relative importance compared to compressor enthalpy drop.

The same information can be showed in a contour map (figure 3.20) where the relative importance of heat flux $\dot{Q}_{C/Air}$ has been plotted versus the whole enthalpy gain across the compressor. That representation shows clearly in

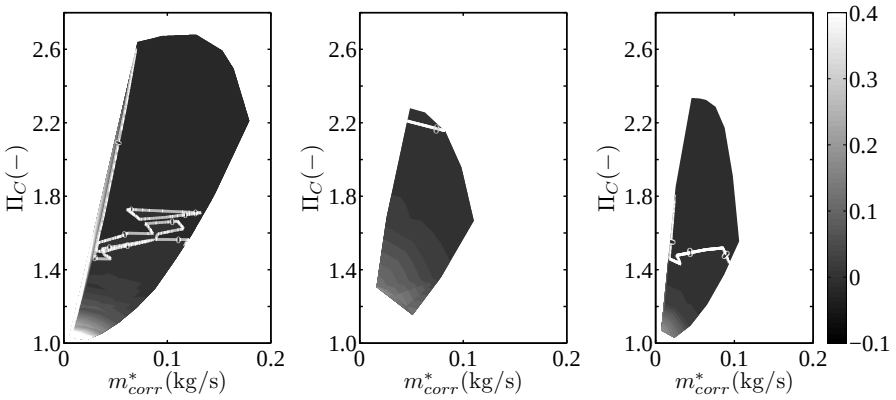

Figure 3.20: Importance of heat flux $\dot{Q}_{C/Air}$ compared to compressor enthalpy gain over compressor performance. Left: Big size turbocharger (water cooled), Center: Medium size turbocharger (non-water cooled), Right: Small size turbocharger (water cooled).

which region of the turbocharger maps change in the heat path occurs represented with a white solid line. As figure 3.20 shows, boundary between positive and negative heat fluxes from compressor casing to compressed air (zero line represented in white line) occurs at higher compression ratios for no water-cooled turbochargers than for the water-cooled turbo (medium size). For turbocharger T.#1 some islands appear predicting the boundary between compressor receiving or losing heat. That is due to several measurements were performed in order to obtain turbine map and so that compressor map was repeated three times (one for each turbine measured opening). Nevertheless, it is observed how the boundary between positive and negative heat fluxes to the compressed air occur at a compression ratio below 1.8 for that water-cooled turbocharger and below 1.5 for gasoline turbocharger T.#3. That is due to the fact that in water-cooled turbochargers housing temperature remains practically constant (around 85°C to 90°C). That temperature can be achieved at compressor side for a relatively low pressure level (around 1.6). For instance, isentropic outlet temperature for those conditions is around 70°C meanwhile adiabatic outlet temperature (considering a typical efficiency of 0.7) leads to a compressed air temperature around 90°C. Nevertheless for the no water-cooled turbocharger (turbo #2) housing remains at higher temperatures, due to no water can be used to cool down its temperature and boundary between

positive and negative heat fluxes will occur at higher compression ratios.

It has been assumed that heat transferred to the air in the compressor occurs at compressor diffuser (after adiabatic compression) due to the higher exposed area. Proposed correlation for Nusselt number governing heat transfer phenomena from node C to node Air has been chosen in the original fashion of Dittus-Boelter correlation (equation 3.13). Exponent 0.4 for Prandtl has been used when air cools while passing through compressor case and 0.3 in case it heats. Constants for that correlation also depend whether the air heats or cools as equation 3.27 shows.

$$\mathrm{Nu_{C/Air}} = \begin{cases} a_1 \cdot \mathrm{Re}_{mC}^{0.8} \cdot \mathrm{Pr}^{0.3} & \text{if} \quad \mathrm{T_{air}} < \mathrm{T_{wall}} \,(\, \mathrm{Q} > 0) \\ a_2 \cdot \mathrm{Re}_{mC}^{0.8} \cdot \mathrm{Pr}^{0.4} & \text{if} \quad \mathrm{T_{air}} > \mathrm{T_{wall}} \,(\, \mathrm{Q} < 0) \end{cases} \tag{3.27}$$

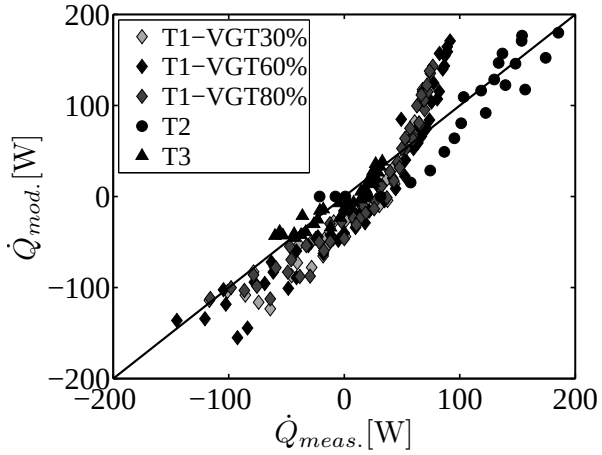

Figure 3.21: Heat fluxes modelling from node C to node Air.

Heat transfer has been modelled using the expression above for Nusselt and an average temperature between compressor adiabatic outlet (node Air in figure 3.1) and compressor outlet temperature (T_{OC}) as equation 3.28 shows. Compressor case diameter has been chosen as the effective length (L_{eff}).

$$\dot{Q}_{C/Air} = \mathrm{Nu_{C/Air}} \cdot \kappa \cdot \pi \cdot \mathrm{L_{eff}} \cdot \left(\mathrm{T_C} - \frac{\mathrm{T_{Air}} + \mathrm{T_{OC}}}{2} \right) \tag{3.28}$$

Table 3.7: Heat transfer modelling from node C to node Air

C/Air $\mathrm{Nu_{C/Air}} = \begin{cases} a_1 \cdot \mathrm{Re}_{mC}^{0.8} \cdot \mathrm{Pr}^{0.3} & (\mathrm{Q} > 0) \\ a_2 \cdot \mathrm{Re}_{mC}^{0.8} \cdot \mathrm{Pr}^{0.4} & (\mathrm{Q} < 0) \end{cases}$			
	T1	**T2**	**T3**
measured			
$L_{eff}(m)$	0.125	0.123	0.104
fitted			
a_1	0.276	0.254	0.081
a_2	0.127	0.035	0.047
$RMS(-)$	0.337	0.181	0.51

Validation of proposed correlation to account for the heat flux between nodes C and Air has been presented in figure 3.21 for particular fitting parameters of each studied turbocharger. As it is observed, good agreement modelling that heat flux has been obtained for all tested turbochargers and operative conditions. Table 3.7 shows obtained fitting parameters.

3.4.3.4 H2/Oil

Heat transfer to the oil in the central housing ($\dot{Q}_{H2/Oil}$) can be calculated using measured wall temperatures and previously determined metal conductances as equation 3.29 shows for a non-water cooled turbocharger.

$$\dot{Q}_{H2/Oil} = \dot{Q}_{H1/H2} - \dot{Q}_{H2/H3} = K_{H1/H2} \cdot (T_{H1} - T_{H2}) - K_{H2/H3} \cdot (T_{H2} - T_{H3}) \tag{3.29}$$

In case of a water-cooled turbocharger would be studied, the energy balance at central node H_2 should include the heat flux transmitted to the cooling liquid ($\dot{Q}_{H2/W}$).

Figure 3.22 shows measured heat flux from housing central node (H_2) to the lubricating oil ($\dot{Q}_{H2/Oil}$) in both absolute and relative value (compared to turbine enthalpy drop). As it is observed for the non-water cooled turbocharger (T.#2), heat fluxes to the oil in that branch are higher than for

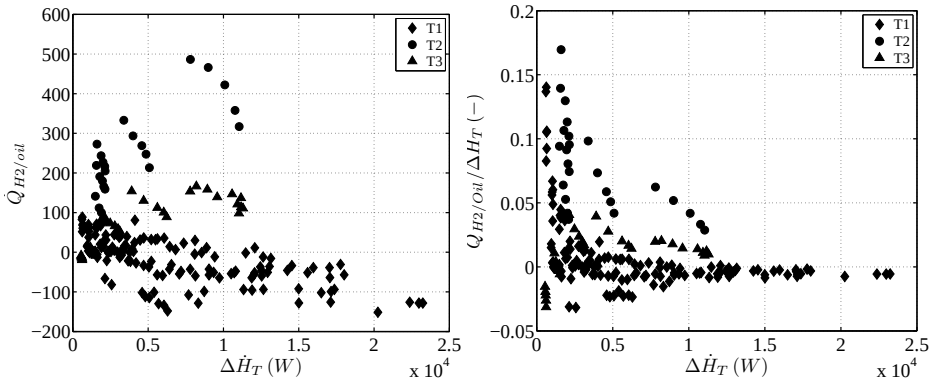

Figure 3.22: Importance of heat flux $\dot{Q}_{H2/Oil}$. Left: absolute value, Right: relative importance compared to the enthalpy drop at turbine side.

the rest of turbochargers. Being its relative importance also higher for most tested points since lube oil purposes were twofold in that configuration, first lubricating (increasing its temperature by means of frictional losses). Secondly isolating compressor from hot turbine (increasing its temperature due to heat transfer effects). As it is observed, for some operative conditions of turbocharger T.#1 heat flux to the oil ($\dot{Q}_{H2/Oil}$) was negative. That was due to the water cooling effect making temperature of metal node H_2 lower than oil temperature.

Nusselt number correlation has been chosen in the original fashion of Sieder-Tate (expression 3.14), but fitting constant for each analysed turbocharger. Oil port diameter has been chosen as the scale length for Reynolds' number calculation. Housing diameter has been chosen as characteristic length in equation 3.17.

$$\mathrm{Nu_{H2/Oil}} = \begin{cases} a_1 \cdot \mathrm{Re_{mO}^{0.8}} \cdot \mathrm{Pr^{0.3}} \cdot \left(\frac{\mu}{\mu_\mathrm{w}}\right)^{0.14} & \text{if} \quad \mathrm{T_{oil}} < \mathrm{T_{wall}} \\ a_2 \cdot \mathrm{Re_{mO}^{0.8}} \cdot \mathrm{Pr^{0.4}} \cdot \left(\frac{\mu}{\mu_\mathrm{w}}\right)^{0.14} & \text{if} \quad \mathrm{T_{oil}} > \mathrm{T_{wall}} \end{cases} \tag{3.30}$$

Where constants a_1 and a_2 have been determined from experimental measurements making distinction between operative conditions where oil receives heat from node H_2 (condition if oil heats) or heat is released to the central

housing (condition if oil cools). First situation is typical from no water-cooled turbochargers, where lubricating oil is heated up due to mechanical friction losses but also due to the heat flux coming from the turbine side. The latter situation is common in water-cooled turbochargers where heat transferred from the hot turbine is recovered by the cooling liquid and lubricating oil is mainly heated up due to mechanical losses. That configuration occurs for high load operative conditions (high turbocharger speeds) where oil temperature, due to pure friction losses, can be higher than central housing temperature and heat transfer moves from oil to the housing. Heat flux to the oil can be calculated using proposed correlation for Nusselt number (equation 3.30) and an averaged oil temperature as showed by equation 3.31. Where housing length has been chosen as the effective length.

$$\dot{Q}_{H2/Oil} = \mathrm{Nu_{H2/Oil}} \cdot \kappa \cdot \pi \cdot \mathrm{L_{eff}} \cdot \left(\mathrm{T_{H2}} - \frac{\mathrm{T_{OO}} + \mathrm{T_{OO/H2}}}{2} \right) \tag{3.31}$$

Modelling heat fluxes effects from node H_2 to node Oil have been evaluated once oil has received some heat from its inlet conditions (OI, right side of figure 3.2). That is due to the heat transfer phenomena at node H_1 ($\dot{Q}_{H1/Oil}$) and the temperature increase due to mechanical friction losses. Both effects lead lubricating oil temperature rise up to conditions named $OO/H2$ as denoted on the right side of figure 3.2. At those conditions, oil exchanges heat with central housing node H_2. Figure 3.23 shows the good agreement modelling heat flux between node H_2 and Oil, where two possibilities have been considered. Oil is heated receiving some heat from metal node H_2 or it is cooled down. As the figure shows, for water-cooled turbochargers (T.#1 and T.#3) most of operative conditions correspond to situations where lubricating oil cools down ($T_{OH2} > T_{H2}$) that is due to the fact that central node H_2 remains cool due to the coolant liquid. Nevertheless for the no water-cooled turbocharger (turbo T.#2) all operative points correspond to situation where lubricating oil increases its temperature due to the heat fluxes.

Table 3.8 shows fitting parameters for the modelled heat flux $\dot{Q}_{H2/Oil}$. Since that correlation has been fitted for both possibilities (whether the oil heats or cools down) but only one of those operative conditions happened during some experiments from turbochargers, it was decided to use all experimental information in order to fit correlation parameters for a global correlation.

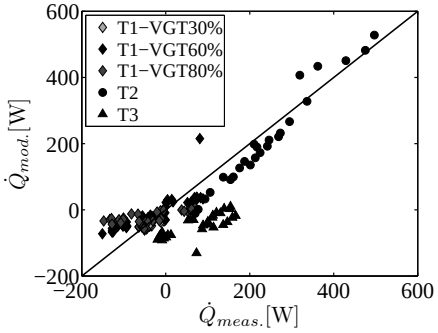

Figure 3.23: Modelling heat fluxes from node $H2$ to node Oil.

Table 3.8: Fitting parameters for heat flux between node H_2 and node Oil.

H2/Oil	$\mathrm{Nu}_{\mathrm{H2/oil}} = \begin{cases} a_1 \cdot \mathrm{Re}_D^{0.8} \cdot \mathrm{Pr}^{0.3} \cdot \left(\frac{\mu}{\mu_\mathrm{w}}\right)^{0.14} & (\mathrm{Q} > 0) \\ a_2 \cdot \mathrm{Re}_D^{0.8} \cdot \mathrm{Pr}^{0.4} \cdot \left(\frac{\mu}{\mu_\mathrm{w}}\right)^{0.14} & (\mathrm{Q} < 0) \end{cases}$			
	T1	**T2**	**T3**	**ALL**
measured				
$L_{eff}(m)$	0.03	0.031	0.035	-
fitted				
a_1	-	-	-	2.235
a_2	-	-	-	0.908
$RMS(W)$	-	-	-	59

3.4.3.5 H1/Oil

Heat transfer to the oil passing near the turbine side ($\dot{Q}_{H1/Oil}$) can be calculated from temperature measurements and previously known conductances, as equation 3.32 shows.

$$\dot{Q}_{H1/Oil} = \dot{Q}_{T/H1} - \dot{Q}_{H1/H2} = K_{T/H1} \cdot (T_T - T_{H1}) - K_{H1/H2} \cdot (T_{H1} - T_{H2}) \tag{3.32}$$

Figure 3.24 shows the heat flux to the lubricating oil near the turbine side

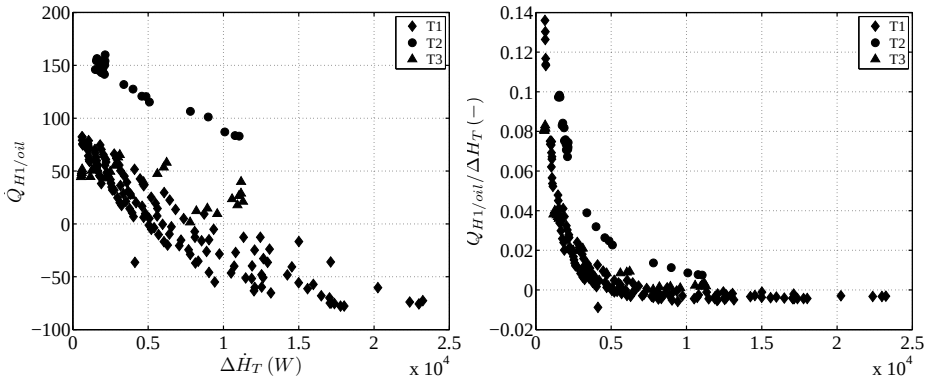

Figure 3.24: Importance of heat flux $\dot{Q}_{H1/Oil}$, Left: absolute heat flux, Right: relative importance compared to the turbine enthalpy drop.

($\dot{Q}_{H1/Oil}$). As it is observed for turbochargers T.#1 and T.#2 (containing most of the experimental information) heat fluxes through that branch were small and centred around zero (below 5% of turbine power for most of operative conditions). For turbocharger T.#3 there was no heat transfer to oil branch at node H_1, according to proposed thermal model and performed experiments. Being the highest heat transfer towards the cooling liquid, being that a plausible situation since that small turbocharger was designed for gasoline applications. Due to the small effect of model branch *H1 to Oil* it was decided to correlate heat transfer to the oil using measurement data from all turbochargers.

$$\mathrm{Nu_{H1/Oil}} = \mathrm{a} \cdot \mathrm{Re_{mO}^{0.8}} \cdot \mathrm{Pr}^{1/3} \cdot \left(\frac{\mu}{\mu_\mathrm{w}}\right)^{0.14} \cdot \mathrm{Re_s^{-0.5}} \tag{3.33}$$

This correlation (equation 3.33) is in the original fashion of Sieder-Tate (expression 3.14), but fitting constant using analysed turbochargers. An extra Reynolds' number associated to the turbocharger shaft speed has been introduced (defined in equation 3.34). Oil film thickness (h) has been chosen as the characteristic length to that expresion.

$$\mathrm{Re_s} = \frac{\rho \cdot \pi \cdot \frac{\mathrm{N}}{60} \cdot \mathrm{D_s} \cdot \mathrm{h}}{\mu} \tag{3.34}$$

Housing length has been chosen as the characteristic length to calculate heat flux to the oil from metal node H_1 according to Newton's cooling law using equation 3.35.

$$\dot{Q}_{H1/Oil} = \mathrm{Nu_{H1/Oil}} \cdot \kappa \cdot \pi \cdot \mathrm{L_{eff}} \cdot \left(\mathrm{T_{H1}} - \left(\frac{\mathrm{T_{OI}} + \mathrm{T_{OI/H1}}}{2} \right) \right) \tag{3.35}$$

Heat fluxes modelling to the oil from metal node H_1 only takes into account the possibility than oil heats due to the fact that neighbouring nodes T and H_1 are at higher temperatures and so oil is always receiving heat. Nevertheless that heat flux ($\dot{Q}_{H1/Oil}$ is small since its value has been calculated indirectly as a difference of heat fluxes between two similar magnitudes ($\dot{Q}_{T/H1}$ and $\dot{Q}_{H1/H2}$). So that, measured heat flux ($\dot{Q}_{H1/Oil}$) was strongly affected by the accuracy in wall temperature measurements (T_T, T_{H1} and T_{H2}), conductive conductance determination ($K_{T/H1}$ and $K_{H1/H2}$) and simplification of heat transfer problem using proposed 1-D lumped model. As it is observed in figure 3.25, proposed correlation to account for heat fluxes between node $H1$ and Oil was predicting a nearly constant value of that flux for turbocharger # 1 (around 40 W) situation that was far from real measurement, but its value was limited what ensured that lubricating oil temperature (after receiving that heat) will not be exaggerated. Nevertheless it was preferred having a rough estimation of that heat flux than neglecting that heat path. Table 3.9 shows parameters fitting heat transfer correlation to account for $\dot{Q}_{H1/Oil}$.

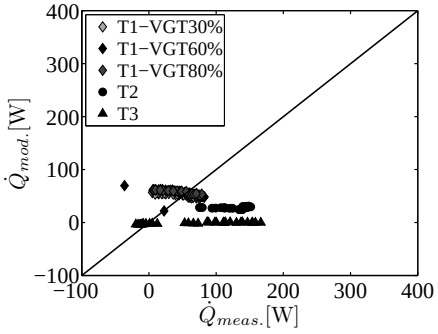

Figure 3.25: Modelling heat flux from node H_1 to Oil (before introducing mechanical losses)

Table 3.9: Fitting parameters modelling heat flux from node H_1 to node Oil

H1/Oil	$\mathrm{Nu_{H1/Oil}} = \mathrm{a} \cdot \mathrm{Re_m^{0.8}} \cdot \mathrm{Pr^{1/3}} \cdot \left(\frac{\mu}{\mu_w}\right)^{0.14} \cdot \mathrm{Re_s^{-0.5}}$			
	T1	**T2**	**T3**	**ALL**
measured				
$L_{eff}(m)$	0.03	0.031	0.035	-
fitted				
a	-	-	-	0.855
$RMS(W)$	-	-	-	205

Regarding the power to the oil due to the internal heat fluxes ($\dot{Q}_{H1/Oil}$, $\dot{Q}_{H2/Oil}$) compared with the experimental oil enthalpy drop (figures 3.24 and 3.22), it was observed how the relative importance of heat fluxes to the oil increased as turbine power reduced. In other words, power to the oil due to mechanical losses at low loads is less important than internal heat fluxes. Nevertheless, as turbine load increases, the importance of internal heat fluxes to the oil decreases compared with global oil enthalpy drop (that includes power due to mechanical losses but also heat transfer effects). It is also observed how for a non-cooled turbocharger heat fluxes to the oil are more important than for a cooled turbocharger, what confirms that water is acting as a sink.

Summary of Convective Properties

Table 3.10 summarizes convective properties needed to model convective heat fluxes inside the turbocharger.

3.5 Adiabatic Maps Calculation

Turbocharger adiabatic maps are a key modelling tool since they only contain information about pure aerodynamic behaviour (internal irreversibilities). Nevertheless manufacturers maps include heat transfer and friction losses effects for the particular experiment performed when those maps were measured. For that reason, computational simulations using those maps only provide accurate results when similar testing conditions than those occurring when turbocharger map was measured are reproduced. Nevertheless, that condition is

Table 3.10: Convective correlations summary

Heat Flux	Equation	parameters
$\dot{Q}_{Gas/T}$	$\dot{Q}_{Gas/T} = \mathrm{Nu_{Gas/T}} \cdot \kappa \cdot \pi \cdot \mathrm{L_{eff}} \cdot \Delta \mathrm{T}$ $\mathrm{Nu_{Gas/T}} = \mathrm{a} \cdot {\mathrm{Re_{mT}}}^{\mathrm{b}} \cdot \mathrm{Pr}^{1/3} \cdot \left(\frac{\mu}{\mu_{\mathrm{w}}}\right)^{0.14} \cdot \mathrm{F}$	$\Delta T = (T_{IT} - T_T)$ $L_{eff} = \frac{D_i^2}{4 \cdot D_p}$ $F = 1 + 0.9756 \cdot \left(\frac{D_{eff}}{L_{eff}}\right)^{0.76}$ $D_{eff} = \frac{D_p}{\eta_{max}}$ $\mathrm{Re}_{mT} = \frac{4 \cdot \dot{m}_T}{\pi \cdot \mu \cdot D_{eff}}$
$\dot{Q}_{H2/W}$	$\dot{Q}_{H2/W} = \mathrm{Nu_{H2/W}} \cdot \kappa \cdot \pi \cdot \mathrm{L_{eff}} \cdot \Delta \mathrm{T}$ $\mathrm{Nu_{mW}} = \mathrm{a} \cdot \mathrm{Re_{mW}^{0.8}} \cdot \mathrm{Pr}^{0.4}$	$\Delta T = (T_{H2} - T_{WI})$ $L_{eff} = L_h$ $\mathrm{Re}_{mW} = \frac{4 \cdot \dot{m}_W}{\pi \cdot \mu \cdot D_{eff}}$ $D_{eff} = D_{IW}$
$\dot{Q}_{C/Air}$	$\dot{Q}_{C/Air} = \mathrm{Nu_{C/Air}} \cdot \kappa \cdot \pi \cdot \mathrm{L_{eff}} \cdot \Delta \mathrm{T}$ $\mathrm{Nu_{C/Air}} = \begin{cases} a_1 \cdot \mathrm{Re_{mC}^{0.8}} \cdot \mathrm{Pr}^{0.3} & (\mathrm{Q} > 0) \\ a_2 \cdot \mathrm{Re_{mC}^{0.8}} \cdot \mathrm{Pr}^{0.4} & (\mathrm{Q} < 0) \end{cases}$	$\Delta T = \left(T_C - \frac{T_{OC} + T_{Air}}{2}\right)$ $L_{eff} = D_{C,ext}$ $\mathrm{Re}_{mC} = \frac{4 \cdot \dot{m}_C}{\pi \cdot \mu \cdot D_{eff}}$ $D_{eff} = D_{C,out}$
$\dot{Q}_{H2/Oil}$	$\dot{Q}_{H2/Oil} = \mathrm{Nu_{H2/Oil}} \cdot \kappa \cdot \pi \cdot \mathrm{L_{eff}} \cdot \Delta \mathrm{T}$ $\mathrm{Nu_{mO}} = \begin{cases} a_1 \cdot \mathrm{Re_{mO}^{0.8}} \cdot \mathrm{Pr}^{0.3} \cdot \left(\frac{\mu}{\mu_{\mathrm{w}}}\right)^{0.14} & (\mathrm{Q} > 0) \\ a_2 \cdot \mathrm{Re_{mO}^{0.8}} \cdot \mathrm{Pr}^{0.4} \cdot \left(\frac{\mu}{\mu_{\mathrm{w}}}\right)^{0.14} & (\mathrm{Q} < 0) \end{cases}$	$\Delta T = T_{H2} - \frac{T_{OO} + T_{OO/H2}}{2}$ $L_{eff} = L_h$ $\mathrm{Re}_{mO} = \frac{4 \cdot \dot{m}_O}{\pi \cdot \mu \cdot D_{eff}}$ $D_{eff} = D_{O,in}$
$\dot{Q}_{H1/Oil}$	$\dot{Q}_{H1/Oil} = \mathrm{Nu_{H1/Oil}} \cdot \kappa \cdot \pi \cdot \mathrm{L_{eff}} \cdot \Delta \mathrm{T}$ $\mathrm{Nu_{H1/Oil}} = \mathrm{a} \cdot \mathrm{Re_{mO}^{0.8}} \cdot \mathrm{Pr}^{1/3} \cdot \left(\frac{\mu}{\mu_{\mathrm{w}}}\right)^{0.14} \cdot \mathrm{Re_s^{-0.5}}$	$\Delta T = T_{H1} - \left(\frac{T_{OI} + T_{OI/H1}}{2}\right)$ $L_{eff} = L_h$ $\mathrm{Re}_{mO} = \frac{4 \cdot \dot{m}_O}{\pi \cdot \mu \cdot D_{eff}}$ $\mathrm{Re}_s = \frac{\rho \cdot \pi \cdot \frac{N}{60} \cdot D_s \cdot h}{\mu}$ $D_{eff} = D_{O,in}$

hard to ensure since manufacturers usually do not provide much details about how those maps were measured. Besides, those maps will also provide reasonable results for turbocharger conditions where heat transfer and friction losses effects will be negligible compared to turbocharger power (map points corresponding to high loads). Nevertheless those points are out of the region of engine homologation cycles. Being main area of interest in turbocharger modelling points from engine partial load conditions, where heat transfer and friction losses effects are important compared to the turbocharger power. For that reason in this Thesis it has been proposed using turbocharger heat transfer and friction losses models to subtract both effects from a turbocharger manufacturer map to obtain its adiabatic performance. This is a kind of direct advantage of having available a heat transfer model for turbochargers.

3.5.1 Calculation Procedure

In order to obtain compressor and turbine adiabatic maps using manufacturer maps, the following procedure has been proposed. It has been based on the main assumption that compressor (and turbine) maps were measured together. That is a common practice in turbocharger division, but justifies also the introduction of some plausible assumptions. Those assumptions are necessary since turbocharger manufacturers usually provide few information about how those maps were measured. Enthalpy diagrams for turbine and compressor processes are showed in figure 3.26.

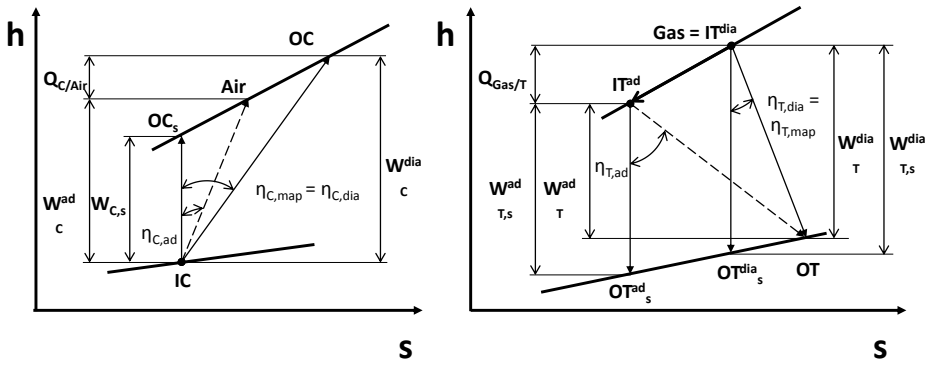

Figure 3.26: Adiabatic and diabatic working processes. Left: Compressor, Right: Turbine.

Input data (Using turbine manufacturer map):

- Turbine reduced mass flow ($\dot{m}_T^{red} = \dot{m}_T \cdot \sqrt{T_{00}}/p_{00}$)
- Total-to-static expansion ratio (Π_T)
- Diabatic efficiency (η_T^{map}), defined as the ratio between compressor absorbed power ($\dot{W}_C$) and turbine isentropic power ($\dot{W}_{T,s}^{dia}$)
- Turbine reduced speed ($N_T^{red} = N/\sqrt{T_{00}}$)
- Reference conditions (T_{ref} and p_{ref})

Main assumptions:

- Turbine inlet temperature (T_{Gas}) is assumed (typical practice is measuring turbine whole map with 600 ^{o}C at the inlet). In case the exact value will be known, that value should be used instead of the proposed approximation.
- Compressor and turbine mass flow are assumed to be equal (what will be a plausible assumption since this is the case on an engine test cell, and is usual practice to avoid high thrust loads).
- Turbine outlet pressure is assumed to be the ambient pressure (typical practice). Doing so turbine inlet pressure can be considered equal to the expansion ratio (Π_T) times the ambient pressure.
- Ambient conditions are assumed for compressor inlet temperature (T_{IC}) and pressure (p_{IC}). Doing so compressor outlet pressure can be considered equal to the pressure ratio times the ambient pressure.
- Lubricant and coolant inlet conditions (temperature and mass flow) must be assumed (typical engine values can be used).
- External heat transfer has not been considered in this procedure. Turbocharger heat transfer model can be adapted to include heat transfer correlations for external radiation and convection, that work has not been carried out in this Thesis since turbochargers were tested with thermal insulation from the outside.

Objective: Obtaining turbine and compressor adiabatic efficiency using manufacturer maps (measured under turbine hot inlet conditions).

Calculation procedure:

Obtaining turbocharger operative point

Assuming operative point is known in turbine map,

1. Turbine real mass flow ($\dot{m}_T$) is obtained using reduced mass flow parameter (from map) and the aforementioned assumptions ($p_{IT} = \Pi_T \cdot p_{amb}$ and $\dot{m}_C = \dot{m}_T$).

$$\dot{m}_T = \frac{\dot{m}_T^{red} \cdot p_{00}}{\sqrt{T_{00}}} \tag{3.36}$$

2. In case operative point will be known in compressor map, equation 3.37 will be used to calculate turbine and compressor real flows (assumption $\dot{m}_C = \dot{m}_T$).

$$\dot{m}_C = \dot{m}_T = \frac{\dot{m}_C^* \cdot \dot{p}_{IC}}{\sqrt{T_{IC}}} \cdot \frac{\sqrt{T_{ref}}}{p_{ref}} \tag{3.37}$$

3. Turbocharger speed is calculated using turbine reduced speed and turbine inlet temperature (T_{IT}). Compressor corrected speed is calculated using turbocharger speed, compressor inlet conditions (assumed) and given references. That turbocharger speed can be used to interpolate in compressor manufacturer map to determine compressor efficiency corresponding to the analysed working conditions. It could be used a typical value of compressor efficiency ($\eta_C = 0.6$) instead of interpolating at compressor map.

$$\begin{aligned} N &= N_T^{red} \cdot \sqrt{T_{IT}} \\ N_C^* &= \frac{N \cdot \sqrt{T_{ref}}}{\sqrt{T_{IC}}} \end{aligned} \tag{3.38}$$

4. In case compressor operative point will be known, a typical value of turbine efficiency should be assumed ($\eta_T = 0.6$) since turbine opening cannot be known from compressor map.

5. Compression ratio (Π_C) and compressor efficiency (η_C^{map}) are obtained from manufacturer map entering with corrected mass flow ($\dot{m}_C^*$) and corrected speed.

6. Once compressor (and turbine) operative conditions have been obtained (from maps), isentropic powers can be calculated using isentropic outlet temperatures. Equations 3.39 and 3.40 are used for compressor calculations meanwhile equations 3.41 and 3.42 are needed for turbine calculations.

$$T_{OC,s} = T_{IC} \cdot \Pi_C^{\frac{\gamma-1}{\gamma}} \tag{3.39}$$

$$\dot{W}_{C,s} = \dot{m}_C \cdot c_p \cdot (T_{OC,s} - T_{IC}) \tag{3.40}$$

$$T_{OT,s}^{dia} = T_{Gas} \cdot \left(\frac{1}{\Pi_T}\right)^{\frac{\gamma-1}{\gamma}} \tag{3.41}$$

$$\dot{W}_{T,s}^{dia} = \dot{m}_T \cdot c_p \cdot \left(T_{Gas} - T_{OT,s}^{dia}\right) \tag{3.42}$$

7. Compressor power ($\dot{W}_C$) can be calculated using compressor map efficiency (η_C^{map}) and calculated isentropic power ($W_{C,s}$) as equation 3.43 indicates. Compressor power includes heat transfer effects since diabatic map efficiency has been used.

$$\dot{W}_C = \frac{\dot{W}_{C,s}}{\eta_C^{map}} \tag{3.43}$$

8. Compressor outlet temperature (T_{OC}) is calculated using equation 3.44 once compressor power ($\dot{W}_C$) has been determined.

$$T_{OC} = T_{IC} + \frac{\dot{W}_C}{\dot{m}_C \cdot c_p} \tag{3.44}$$

Initial Values Assumption

9. Initial value for air temperature after the adiabatic compression process has been assumed (compressor diffuser temperature T_{OD}). That parameter cannot be obtained directly from compressor map since compressor efficiency also includes heat transfer effects. A $\pm$ 10ºC variation around compressor outlet temperature (T_{OC}) criterion has been chosen to initialize the calculation. For high load points, compressed air will be at higher temperature than compressor case and so air will cool down from compressor diffuser to compressor outlet. For low load points it will occur the opposite.

10. Initial mechanical losses ($\dot{W}_m$) are estimated using model proposed by Serrano et al. [153, 154]. Apart from geometrical data from turbocharger shaft and bearings, oil conditions (inlet temperature and mass flow) and also turbocharger speed are needed to apply that model. In addition turbine and compressor pressure ratios are also necessary to calculate friction on the axial thrust. Oil inlet temperature in mechanical losses model has been considered after adding some heat transfer from metal node $H1$ ($\dot{Q}_{H1/Oil}$) as it was shown in Chapter 3. Nevertheless oil inlet port temperature has been assumed here instead as an initial value.

11. Lubricating outlet temperature (T_{OO}) has been calculated in a first approximation considering mechanical losses power only ($\dot{W}_m$) obtained from previous step as it is showed in equation 3.45.

$$T_{OO} = T_{OI} + \frac{\dot{W}_m}{\dot{m}_O \cdot c} \tag{3.45}$$

12. An initial set of nodes temperatures has been chosen (n=0). As it was discussed in Chapter 3, there are four working fluid nodes named as Gas, Air, Oil and W. Node Gas referrers to the exhaust gases entering the turbine, being characterized that node by turbine measured inlet temperature (T_{IT}). Node Air referrers to compressed air at compressor outlet diffuser (T_{OD}) meanwhile nodes Oil and W are characterized by lube oil and coolant liquid inlet conditions (T_{IO} and T_{IW}). In addition there are five metal nodes named as T, $H1$, $H2$, $H3$ and C and two nodes introduced to account for mechanical losses and heat transfer effects inside the lubricating oil. They have been named as $OH1$ and $OH2$ according to the diagram on the right side of figure 3.2. Values showed in table 3.11 have been chosen as initial values for nodes temperature.

Criteria for initial wall temperature estimation has been chosen according to wall temperature distribution observed in figure 3.4. Lubricating oil outlet temperature (T_{OO}) estimated in item 11 has been chosen as the initial temperature for nodes $OH1$ and $OH2$.

Table 3.11: Initial nodes temperatura (n=0)

Fluid Nodes		Metal Nodes	
node	initial value	node	initial value
T_{Gas}	T_{IT}	T_T	$0.8 \cdot (T_{IT} - T_{IC}) + T_{IC}$
T_{Air}	T_{OD}	T_{H1}	$0.5 \cdot (T_{IT} - T_{IC}) + T_{IC}$
T_{Oil}	T_{IO}	T_{H2}	$0.3 \cdot (T_{IT} - T_{IC}) + T_{IC}$
T_{OH1}	T_{OO}	T_{H3}	$0.2 \cdot (T_{IT} - T_{IC}) + T_{IC}$
T_{OH2}	T_{OO}	T_C	$0.1 \cdot (T_{IT} - T_{IC}) + T_{IC}$
T_W	T_{IW}		

Iterative Procedure Begins

13. Vector of nodes temperatures shown on equation 3.46 is built using initial values from item 12. Conductances matrix K_s shown in equation 3.47 has been built using heat transfer correlations developed in this chapter.

$$\mathbf{T}_N^n = \begin{bmatrix} T_{Gas} & T_{Air} & T_{OI} & T_W & T_T & T_{H1} & T_{H2} & T_{H3} & T_C & T_{OH2} & T_{OH1} \end{bmatrix}^t \tag{3.46}$$

$$\mathbf{K_s} = \begin{pmatrix} 1 & 0 & 0 & 0 & 0 & 0 & 0 & 0 & 0 & 0 & 0 \\ 0 & 1 & 0 & 0 & 0 & 0 & 0 & 0 & 0 & 0 & 0 \\ 0 & 0 & 1 & 0 & 0 & 0 & 0 & 0 & 0 & 0 & 0 \\ 0 & 0 & 0 & 1 & 0 & 0 & 0 & 0 & 0 & 0 & 0 \\ K_{T/Gas} & 0 & 0 & 0 & K_{T/T} & K_{T/H1} & 0 & 0 & 0 & 0 & 0 \\ 0 & 0 & K_{H1/OH1} & 0 & K_{H1/T} & K_{H1/H1} & K_{H1/H2} & 0 & 0 & 0 & 0 \\ 0 & 0 & 0 & K_{H2/W} & 0 & K_{H2/H1} & K_{H2/H2} & K_{H2/H3} & 0 & K_{H2/OH2} & 0 \end{pmatrix} \tag{3.47}$$

14. Nodes temperatures are calculated applying heat transfer model, what means solving equation 3.48 where vector of inputs temperatures is defined in equation 3.49.

$$\mathbf{T}_N^{n+1} = \mathbf{K}_s^{-1} \cdot \mathbf{T}_l \tag{3.48}$$

$$\mathbf{T}_l = \begin{bmatrix} T_{IT} & T_{OD} & T_{OI} & T_W & 0 & 0 & 0 & 0 & 0 & T_{OH2} & T_{OH1} \end{bmatrix}^t \tag{3.49}$$

15. Temperature differences between model nodes are calculated using expression 3.50 and heat fluxes using equation 3.51.

$$\mathbf{\Delta T(i,j)} = \mathbf{T}_N^{n+1}(i) - \mathbf{T}_N^{n+1}(j) \tag{3.50}$$

$$\boldsymbol{\dot{Q}} = \mathbf{K_s} \cdot \mathbf{\Delta T} \tag{3.51}$$

16. Turbine adiabatic inlet temperature after subtracting heat transfer on the turbine side (T_{IT}^{ad}) can be determined from expression 3.52.

$$T_{IT}^{ad} = T_{Gas} - \frac{\dot{Q}_{Gas/T}}{\dot{m}_T \cdot c_p} \tag{3.52}$$

17. Turbine isentropic temperature for new turbine isentropic expansion (after removing heat transfer $\dot{Q}_{Gas/T}$), can be calculated using equation 3.41. Once that temperature ($T_{OT,s}$) has been determined turbine new isentropic power is calculated using equation 3.53.

$$\dot{W}_{T,s}^{ad} = \dot{m}_T \cdot c_p \left(T_{IT}^{ad} - T_{OTs}^{ad} \right) \tag{3.53}$$

18. Compressor real power, after the adiabatic compression process ($\dot{W}_{C,ad}$) can be determined by subtracting heat flux ($\dot{Q}_{C/Air}$) to compressor diabatic power obtained in step 7 as equation 3.54 shows. Once compressor adiabatic power has been determined, outlet temperature after adiabatic compression (T_{Air}) can be determined using expression 3.55.

$$\dot{W}_{C,ad} = \dot{W}_C - \dot{Q}_{C/Air} \tag{3.54}$$

$$T_{Air} = T_{IC} + \frac{\dot{W}_{C,ad}}{\dot{m}_C \cdot c_p} \tag{3.55}$$

19. Temperatures for oil nodes can be calculated using heat fluxes obtained in step 15, oil inlet temperature (T_{OI}) and mechanical losses model ($\dot{W}_m$). Temperature for oil node $OH1$ is calculated from inlet conditions (T_{OI}) after adding $\dot{Q}_{H1/OH1}$ flux as equation 3.56 shows. Once that temperature has been determined, mechanical losses model is applied to determine mechanical power due to friction losses only ($\dot{W}_m$). That power is translated into an increase in oil temperature from conditions T_{OH1} to conditions T_{OH2} as equation 3.57 indicates. According to proposed thermal model, lubricating oil is receiving heat flux $\dot{Q}_{H2/OH2}$ what increased its temperature from conditions T_{OH2} up to outlet oil port temperature (T_{OO}) as equation 3.58 shows.

$$T_{OH1} = T_{OI} + \frac{\frac{\dot{Q}_{H1/OH1}}{2}}{\dot{m}_O \cdot c} \tag{3.56}$$

$$T_{OH2} = T_{OH1} + \frac{\dot{W}_m + \frac{\dot{Q}_{H2/OH2}}{2} + \frac{\dot{Q}_{H1/OH1}}{2}}{\dot{m}_O \cdot c} \tag{3.57}$$

$$T_{OO} = T_{OH2} + \frac{\frac{\dot{Q}_{H2/OH2}}{2}}{\dot{m}_O \cdot c} \tag{3.58}$$

20. Turbine adiabatic power ($\dot{W}_{T,ad}$) can be determined using compressor adiabatic power ($\dot{W}_{C,ad}$) (from step 18) and mechanical friction losses ($\dot{W}_m$), as it is shown in equation 3.59.

$$\dot{W}_{T,ad} = \dot{W}_{C,ad} + \dot{W}_m \tag{3.59}$$

21. Turbine outlet temperature after the adiabatic expansion ($T_{OT,ad}$) can be calculated using calculated turbine adiabatic power ($\dot{W}_{T,ad}$) as equation 3.60 shows.

$$T_{OT} = T_{IT}^{ad} - \frac{\dot{W}_{T,ad}}{\dot{m}_T \cdot c_p} \tag{3.60}$$

22. New temperatures for compressor outlet diffuser (T_{Air}), turbine outlet (T_{OT}) and lubricating outlet oil (T_{OO}) are compared with calculations

from previous iteration. In case a bigger difference than a defined tolerance is obtained, solver is feed back to step 13.

Iterative Procedure ends

23. Once compressor and turbine isentropic and adiabatic powers have been determined, adiabatic efficiencies can be described, what was the objective of this solver. $W_{C,s}$, $W_{C,ad}$, $W_{T,s}$ and $W_{T,ad}$ have been determined from step calculations 6, 18, 17 and 20 respectively as showed in equation 3.61.

$$\begin{aligned} \eta_{C,ad} &= \frac{W_{C,s}}{W_C^{ad}} \\ \eta_{T,ad} &= \frac{W_{T,ad}}{W_{T,s}^{ad}} \end{aligned} \tag{3.61}$$

3.5.2 Application Example

In this section proposed methodology to obtain adiabatic maps from manufacturer ones has been applied to hot measured maps of turbocharger #1 used in this Thesis. In this case, since lubricating and coolant conditions were recorded during turbocharger characterization some assumption were not necessary. In addition compressor and turbine parameters were recorded at the same time so no mass flow or pressure assumptions were needed.

3.5.2.1 Compressor Adiabatic Maps

Compressor efficiency for steady hot flow tests performed on turbocharger #1 (with cooled housing) have been showed in figure 3.27. Compressor efficiency showed in that figure has been defined according to its typical definition; this is the power ratio between isentropic compression process ($\dot{W}_{C,s}$) and real process ($\dot{W}_C$). The latter can be influenced by heat transfer (for hot tests) or can only account pure aerodynamic effects (for almost-adiabatic tests). Heat transfer and mechanical losses models have been applied to the hot measurements in order to discount heat transfer effects from compressor measured power. Doing so power for the adiabatic compression process ($\dot{W}_{C,ad}$) has been determined using equation 3.54 being adiabatic compression efficiency defined in equation 3.61. Adiabatic efficiency obtained using the procedure presented in previous section using hot tests has been named as "adiabatized". That efficiency

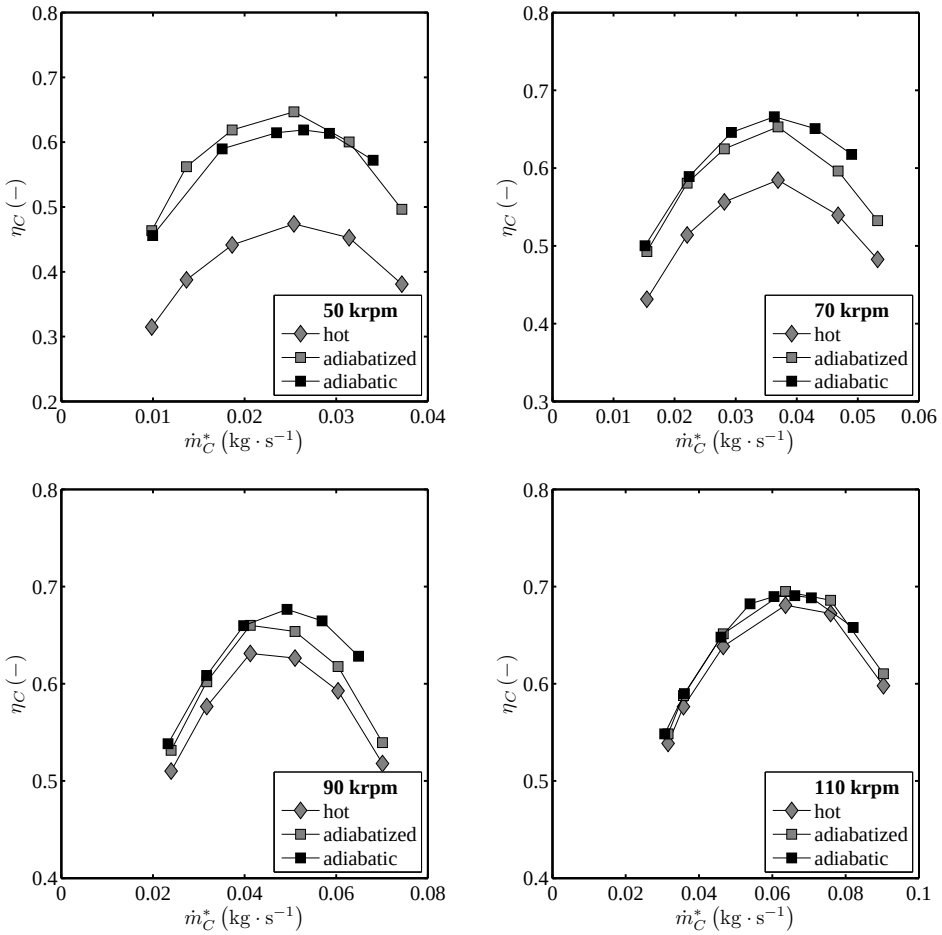

Figure 3.27: Compressor efficiency from almost-adiabatic tests, hot tests and "adiabatized" efficiency

should agree with compressor efficiency from almost-adiabatic tests. Even the results are quite good and small differences appear between both magnitudes since "adiabatized" efficiency has been determined using model correlations. Therefore intrinsic errors in heat transfer and mechanical losses prediction have been translated into compressor calculation efficiency. The best results are at lower turbospeeds where heat transfer effects are more important.

As figure 3.27 shows, those differences in compressor efficiency prediction

comparing "adiabatized" compressor efficiency (from hot tests) with compressor efficiency calculated from almost-adiabatic tests are much lower than the differences between compressor efficiency defined from hot tests and almost-adiabatic efficiency. As compressor speed (and load) increases, discrepancies between adiabatic and hot defined efficiency decreases. That is due to heat transfer and mechanical losses power become less important as load increases compared to turbocharger power as it was showed in Chapter 3. As it is observed in figure 3.27 for turbocharger speeds of 110 krpm (and above), compressor efficiency defined from hot tests could be used instead of using adiabatic efficiency. In other words, compressor efficiency showed in manufacturers maps (defined with hot tests on the turbine side) provide accurate results only for high turbocharger speeds, but at low speeds (and loads) heat transfer models should be used to discount heat transfer effects from hot measurements since compressor efficiency defined in that way highly differs from adiabatic compressor efficiency.

3.5.2.2 Turbine Adiabatic Maps

Figure 3.28 shows turbine efficiency calculated from hot steady tests and almost-adiabatic tests versus blade speed ratio. Turbine efficiency from almost-adiabatic tests has been used to extrapolate performance maps into the whole operative range. Turbine diabatic efficiency calculated from hot steady tests has been defined using equation 3.62, it is represented with the entry "hot" in figure 3.28.

$$\eta_{Tmap} = \frac{(T_{OC} - T_{IC}) \cdot c_{p,C} \cdot \dot{m}_C}{(T_{Gas} - T_{OTs,dia}) \cdot c_{p,T} \cdot \dot{m}_T} = \frac{\dot{W}_{C,ad} + \dot{Q}_C}{\dot{W}_{Ts,dia}} \tag{3.62}$$

Calculation procedure presented in this section has been used to discount heat transfer and mechanical losses effects. Turbine efficiency after applying those models takes only into account internal irreversibilities, it has been named in that figure as "adiabatized". As it is observed that efficiency lies over turbine extrapolated efficiency curve determined from almost-adiabatic tests (procedure needed to extrapolate those maps will be explained in the next section). Those results show that hot steady tests can be used in turbocharger simulations using proposed methodology to obtain adiabatic maps from hot steady measurements. As it is observed, this model can be used to obtain

extra information for extrapolation purposes, since "adiabatized" hot steady measurements cover turbine peak efficiency region. And those measurements continue the available region using almost-adiabatic information.

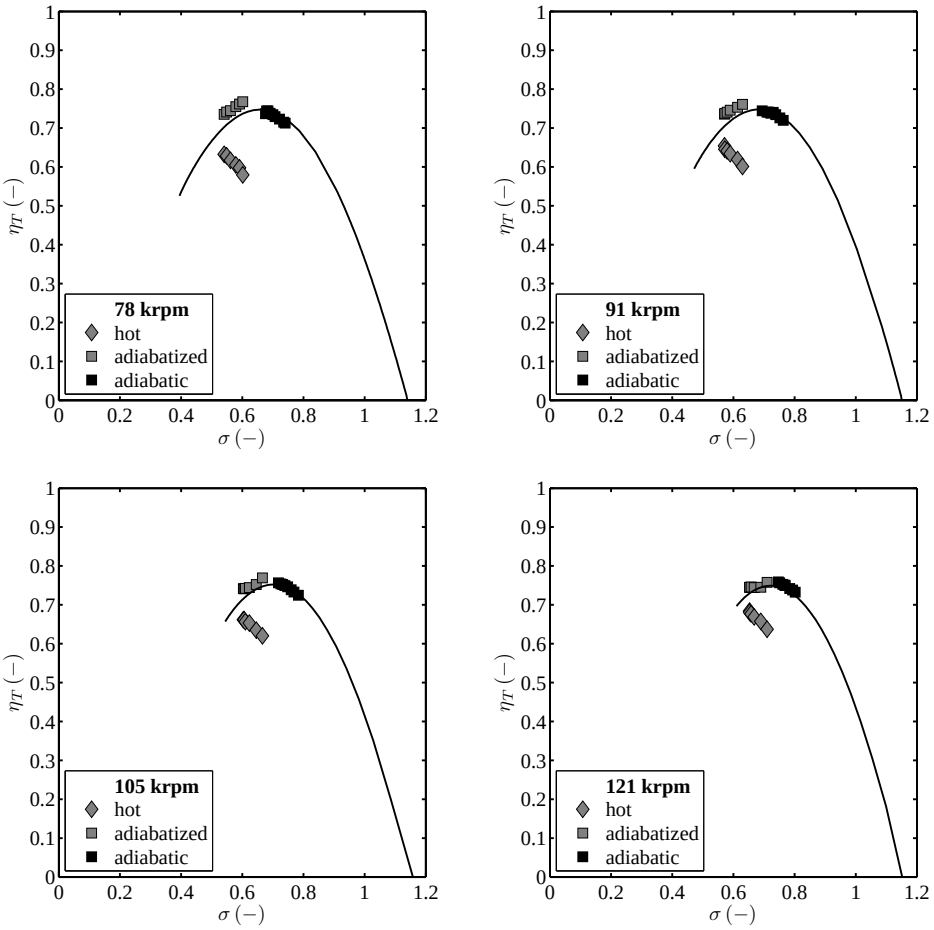

Figure 3.28: Turbine efficiency from almost-adiabatic tests, hot tests and "adiabatized" efficiency (for turbocharger #1)

3.6 Summary

In the present chapter a Heat Transfer Model (HTM) to account for internal heat fluxes in a turbocharger has been presented. That model has been based on the electrical analogy, where 5 metal nodes have been introduced representing turbocharger cases components. Those nodes have been named as T, H1, H2, H3 and C. Heat transfer mechanism among those nodes occurred by means of pure metal conduction according to Fourier's law. Conductive conductance properties governing that mechanism have been determined among metal nodes. Those metal nodes have been connected to 4 fluid nodes corresponding to the exhaust gases moving the turbine (Gas), the fresh air coming into the compressor (Air), the lubricant oil (Oil) and the cooling liquid in case it exists (W). Heat transfer mechanism between a metal node and a fluid node occurs according to Newton's cooling law. In addition thermal capacitances have been introduced to account for thermal inertia during transient processes. Eventually a mechanical losses model has been introduced as a source term into turbocharger model connected to the oil node to introduce the amount of heat flux corresponding to the friction losses model. Three automotive turbocharger models from different sizes have been analysed in order to validate proposed model.

Two sets of experiments on different facilities have been designed in order to determine conductive conductances and convective conductances. Where firsts only depended on turbocharger geometry and materials, depending the latter on turbocharger operative conditions. First of all, turbocharger unit was installed into a thermo-hydraulic test bench where conductive conductances and thermal capacitances were determined. In order to do so, hot thermal oil was introduced by the turbine case whilst cold oil passed along compressor case, remaining dry its housing and being the turbocharger fully insulated. That procedure allowed the direct characterization of conductive properties by measuring temperature drops along turbocharger planes. In order to characterize thermal inertia from turbocharger cases a transient experiment on the same facility was designed. It consisted of the sudden release or discharge of hot oil to the turbine/compressor case while instantaneous wall temperature variations were recorded. Energy conservation equations were applied to each metal node to calculate its associated thermal inertia. Despite the simplification of proposed internal conduction model, good agreement reproducing the steady and transient response was obtained.

Once conductive conductances and thermal capacitances have been validated, turbocharger unit was installed into a gas stand facility where internal convective conductances were characterized by passing hot steady flow through the turbine side. Turbocharger flow parameters (mass flow, pressure ratio and rotational speed) were changed in order to modify Reynolds and Prandtl dimensionless numbers inside turbocharger cases. Correlations in the fashion of Sieder-Tate and Dittus-Boelter equations have been chosen to characterize turbocharger internal heat transfer problem. Constant and exponents from those equations have been fitted to well reproduce convection inside the turbocharger, accurate results were observed for convective heat transfer modelling.

Adiabatic maps are an useful tool to determine accurately turbine and compressor outlet temperatures. In addition they can be used for later extrapolation purposes. Nevertheless that information is not usually provided by turbomachinery manufacturers since they measure performance maps under hot flow conditions. For that reason, in this chapter a calculation procedure to determine turbocharger adiabatic maps using hot measured maps has been proposed. As it has been observed, turbine and compressor adiabatic efficiencies could be calculated using hot steady measurements, and those results agreed with adiabatic efficiencies obtained from almost-adiabatic tests.

References

[14] N. Baines, K. Wygant, and A. Dris. "The analysis of Heat Transfer in Automotive Turbochargers". In: *Proceedings of ASME Turbo Expo 2009, GT2009-59618*. 2009 (cit. on pp. 24, 26, 27, 29, 37, 44, 111).

[19] M.S. Bhatti and R.K. Shah. *Turbulent and transition flow convective heat transfer in ducts*. Ed. by S. Kakaç, R.K. Shah, and W. Aung. Vol. Handbook of Single-Phase Convective Heat Transfer, chapter 4. Wiley-Interscience, 1987 (cit. on p. 111).

[88] F.P. Incropera and D.P. De Witt. *Fundamentos de transferencia de calor*. Prentice Hall, 1999 (cit. on p. 104).

[119] P. Olmeda, V. Dolz, F.J. Arnau, and M.A. Reyes-Belmonte. "Determination of heat flows inside turbochargers by means of a one dimensional lumped model". In: *Mathematical and Computer Modelling* 57.7-8 (2013), pp. 1847 –1852. ISSN: 0895-7177. DOI: 10.1016/j.mcm.2011.11.078. URL: http://www.sciencedirect.com/science/article/pii/S0895717711007631 (cit. on pp. 93, 104, 105, 233).

[129] F. Payri, J. Galindo, J.R. Serrano, and M.A. Reyes-Belmonte. "Experimental methodologies for a comprehensive characterization of automotive turbochargers". In: *13th EAEC European Congress, Valencia, Spain*. 2011 (cit. on p. 94).

[142] J1723 SAE Standards. *Supercharger Testing Standard*. Engine Power Test Code Committee. 1995-08-01 (cit. on p. 108).

[152] J.R. Serrano, P. Olmeda, A. Páez, and F. Vidal. "An Experimental Procedure to Determine Heat Transfer Properties of Turbochargers". In: *Measurement Science and Technology* 21 (2010), 14pp (cit. on pp. 89, 94, 100, 110).

[153] J.R. Serrano, P. Olmeda, A. Tiseira, L.M. García-Cuevas, and A. Lefebvre. "Importance of mechanical losses modeling in the performance prediction of radial turbochargers under pulsating flow conditions". In: *SAE Int. J. Engines 6(2)* 6(2) (2013), pp. 729–738. DOI: 10.4271/2013-01-0577 (cit. on pp. 8, 46, 48, 49, 93, 132, 157, 189, 216, 217, 255).

[154] J.R. Serrano, P. Olmeda, A. Tiseira, L.M. García-Cuevas, and A. Lefebvre. "Theoretical and experimental study of mechanical losses in automotive turbochargers". In: *Energy* 55 (2013), pp. 888 –898 (cit. on pp. 8, 46, 48, 49, 93, 132, 157, 189, 216, 217, 223, 233, 255, 271).

[159] S. Shaaban, J. Seume, R. Berndt, H. Pucher, and H.J. Linnhoff. "Part-load performance prediction of turbocharged engines". In: *C647/019. Proceedings of 8th International Conference on Turbochargers and Turbocharging. Woodhead Publishing and CRC Press LLC. London*. 2006 (cit. on pp. 20, 89).

[171] A. Torregrosa, A. Broatch, P. Olmeda, and J. Martín. "A Contribution to Film Coefficient Estimation in Piston Cooling Galleries". In: *Experimental Thermal and Fluid Science* 34 (2010), pp. 142–151 (cit. on pp. 94, 95).

[173] A. Torregrosa, P. Olmeda, J. Martín, and C. Romero. "A Tool for Predicting the Thermal Performance of a Diesel Engine". In: *Heat Transfer Engineering* 32 (2011), pp. 891–904 (cit. on p. 87).

Chapter 4

Turbocharger Primary Flows Modelling

Contents

4.1 Introduction

When turbocharged reciprocating internal combustion engines are modelled using 1-D gas dynamics codes, normally, the calculation of the turbine performance is not satisfactory, even using a lot of information from experiments like turbine characteristics maps. These maps provide reduced mass flow and turbine efficiency as a function of total to static expansion ratio and they are standard source of information from turbocharger manufacturers [13].

Simple mean value models that interpolate average thermodynamic variables in these maps, which consider the turbine as adiabatic, do not provide good results. The highly unsteady and usually high temperature flow that moves the turbine in passenger car engines makes this kind of models too simple to predict accurately turbine operation in such environment. A new generation of simple models keeping turbine maps as the main source of information is needed. Those models should be 1-D where the Strouhal number is high enough (relation between frequency of pulses and characteristic frequency of the element) like the turbine scroll and stator, and 0-D with mass accumulation capabilities where the Strouhal number is low. Therefore, the quasi-steady behaviour of the turbine efficiency can be kept and well used by interpolating in turbine maps. It can be done using instantaneous thermodynamic conditions of the flow upstream of the stator inlet, instead of the mean variables. In addition, those models should take into account heat transfer phenomena associated with high gas temperatures at turbine inlet and heat transfer from turbine to compressor and from both elements to the surroundings (lubricating oil, coolant and the ambient). Nevertheless, this will be the objective of the following chapter. It is the interest of the turbocharger model presented in this section that turbocharger maps continue being the main source of input data for turbocharger modelling.

4.2 Non-Steady Compressor Characterization

4.2.1 Introduction

Turbocharger compressor in engine simulation codes is usually represented by a node or a boundary condition where the information contained in the

compressor chart is imposed. In these kinds of models, and under pulsating flow conditions, instantaneous mass flow at compressor inlet and outlet is the same, which means that the cumulative mass flow effects are not considered. As a consequence of this simplification, the model distorts the pressure wave that is transmitted from the engine to the intake orifice and the same in the reverse direction. Therefore, such a model has big limitations predicting radiated noise. Some authors have proposed compressor models represented by several pipes simulating the different flow paths. These models provide good results even at high frequencies but the calculation of a high number of short pipes can increase considerably the computation time.

Model presented here is based on compressor map information and it is able to predict how pressure waves are transmitted and reflected by compressor. Compressor fluid-dynamic behaviour has been reproduced by simplifying its real geometry into 0-D and 1-D elements with acoustic purposes. These elements are responsible for attenuating or reflecting the pressure pulses generated by the engine. Compressor model has been validated using experimental results obtained in a turbocharger test bench under pulsating flow conditions. Characteristics of pressure waves (amplitude, frequency and mean flow) are similar to those of the pulses that compressor undergoes when it is working coupled to a reciprocating internal combustion engine. Pressure pulses generated by engine intake valves, which travel through the intake ducts and arrive at the compressor, can also change compressor performance and cause problems of low frequency radiated noise. That noise in compressors is becoming an important issue for both vehicle and turbocharger manufacturers [34]. On the other hand, unsteady flow can be used to improve engine performance by means of tuned manifolds.

Due to the effects and limitations commented above, the proper selection of the turbocharger is a key point affecting engine efficiency and performance. In order to help turbocharger selection, most engine manufacturers use computer codes to simulate turbocharger matching. Those codes predict quite accurately fluid dynamic phenomena in the intake and exhaust systems but they need a good characterization of the different elements involved such as the turbocharger [184, 182, 16, 130, 125, 66]. More details about experimental facility and compressor modelling presented here can be found in [170].

4.2.2 Experimental Methodology

4.2.2.1 Turbocharger Test Rig

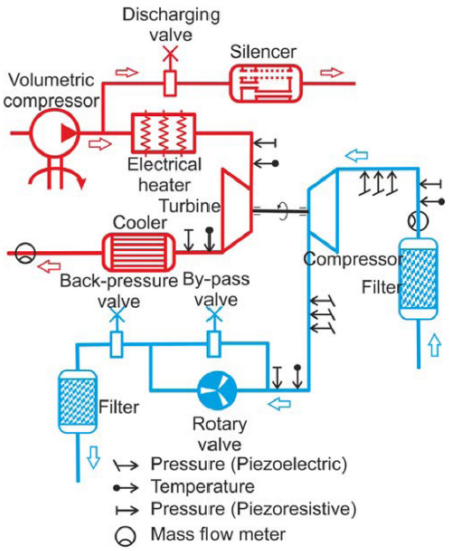

Figure 4.1: Layout of the test

Figure 4.1 shows schematically the layout of the continuous air mass flow test bench adapted to test turbocharger compressor under pulsating flow conditions. Temperature and pressure sensors were installed on the inlet and outlet pipes of compressor and turbine according to SAE J1826 standards [175]. In order to measure actual pressure wave transmission and reflection in compressor and turbine, a beamforming-based methodology decomposing pressure signals into incident and reflected pressure waves has been applied [133]. Beamforming is a spatial processing technique for estimating the signal waveform arriving at an array of sensors from a given direction by means of the definition of a suitable filter from the pressure measured by the different sensors in the array. The procedure is based on three main assumptions;

- Linear superposition of the forward and backward flow velocities.
- Linear propagation of the pressure and sound speed, assuming that the array aperture (total length) is small compared with the wavelength.

- Opposite angles of incidence of the forward and the backward waves onto the array of sensors.

This method requires at least pressure measurements at three different axial positions of the pipe. Arrays of three "Kistler 7031" piezoelectric transducers with water cooled adaptors have been used at each measurement position (upstream and downstream of compressor). Distance between two consecutive sensors was set to 0.05 m, in order to get a suitable compromise between the measurement precision and the assumption of linear propagation between transducers. On the one hand, very small distances between sensors can cause that observed differences between measurement signals would be lower than sensor precision. On the other hand, excessively large distances do not allow for the assumption of linear propagation between transducers. In addition, four piezoresistive KISTLER sensors have been installed with a measuring range of 0-5 bar; two at the turbine inlet, one at the turbine outlet and one at the compressor outlet. These sensors were installed since they provided the mean value of the pressure wave (piezoelectric sensors only detected pressure oscillations around 0). Finally, the test bench has been equipped with a robust data acquisition system registering data from all sensors at the different measurement points. At the same time, acquisition system allowed monitoring and controlling the main variables necessary to accomplish with the tests requirements.

Rotary valve A rotary valve was built and fitted in the turbocharger test rig to generate the pulsating flow required for the experiments. This rotary valve was controlled by an electric motor and in order to withstand the high flow temperatures, a turbocharger shaft and housing was used instead of regular ball bearings since they could not withstand temperatures above 150°C. With this configuration, the rotary valve could deal with temperatures over 600°C. Test rig lubrication system was also used to supply oil to the rotary valve. The rotary valve had the capability of changing the following parameters independently:

- Pulse frequency: By changing rotational speed of the rotary valve, pulse frequency could be changed. Due to the fact that the rotary valve was controlled by an electric motor, the speed change could be easily done. Frequency range was from 0 Hz to 150 Hz, implying that it was able of

simulating 4 cylinder engines up to 4500 rpm, 3 cylinder engines up to 6000 rpm and 2 cylinder engines up to 9000 rpm.

- Pulse shape: In order to simulate better engine exhaust pressure pulses shape, rotary disks could be changed, for that reason several disks were designed and they were easily swapped.

- Pulse amplitude: Amplitude of the pressure pulses could be modified using a bypass circuit, controlled by a bypass valve (figure 4.1), around the rotary valve in a way that peak pressure could be decreased at will. Pulse amplitudes peak to peak up to 1 bar could be obtained, although it greatly depended on the inlet pressure and mass flow being tested.

4.2.2.2 Test Planning

Facility described in the previous section provided the data needed to validate 1-D compressor model able to account for acoustic effects. A typical compressor used in automotive engines of about 2 litres size was tested in the turbocharger test bench. A test matrix, changing turbocharger speed and compression ratio and adapting frequency and amplitude of the pulses was performed. Frequency was varied from 33.3 Hz up to 150 Hz, which was equivalent to engine speeds ranging from 1000 rpm to 4500 rpm for a four cylinder engine. Different values of peak to peak amplitude were considered reaching the maximum value of 250 mbar. Table 4.1 shows the test matrix performed, where temperature at compressor outlet and turbine inlet have been also indicated. Cases denoted by (1) were not measured since disk holes were too big for the desired peak to peak amplitude. For the highest engine speed, the lowest amplitude operative point (2) was not affordable since rotary disk holes were too small. Cases denoted by (3) in table 4.1 were unmeasured since flow limitations (holes too small with by-pass valve closed and back-pressure valve opened). Experimental information provided by the piezoelectric sensors was processed using beamforming technique, as commented above.

Figure 4.2 shows the nomenclature used to identify different pressure waves depending on its direction and location. The convention says that incident pressure (i) is the wave coming from the engine. This signal can be reflected (r) in the compressor or transmitted (t). Finally the pressure wave can also be reflected (r2) in the filter or other elements upstream of the compressor.

Table 4.1: Compressor test matrix

Engine (rpm)	Turbocharger speed (krpm)	Frequency (Hz)	Peak to peak amplitude 50 100 150 200 250
1000	52	33.3	COT: 45°C TIT: 150°C
1500	92	50	COT: 70°C TIT: 170°C
1750	114	58.3	COT: 101°C TIT: 170°C
2000	112	66.7	COT: 88°C TIT: 170°C
2500	113	83.3	COT: 85°C TIT: 170°C
3000	119	100	COT: 88°C TIT: 170°C
3500	121	116.6	COT: 90°C TIT: 170°C
4000	127	133.3	COT: 92°C TIT: 180°C
4500	139	150	(2) COT: 110°C TIT: 250°C

(1)

(3)

4.2.3 Compressor Model Development

Compressor real geometry has been simplified into a combination of 1-D and 0-D elements, and boundary conditions, as it is shown in Figure 4.3. Mass, momentum and energy equations have been solved numerically for 1-D elements applying finite difference schemes meanwhile 0-D elements have been solved by means of a filling and emptying model. Finally, boundary conditions have been solved using the Method of Characteristics assuming quasi-steady behaviour. Geometrical simplifications of that model were described in [172] where the effect of different geometries was analysed. Optimum results were obtained using the following settings as described in [170].

- Equivalent length was set equal to 1/3 of the largest run of a particle from the rotor outlet to the volute outlet (tongue), which meant $L = L_{volute}/3$

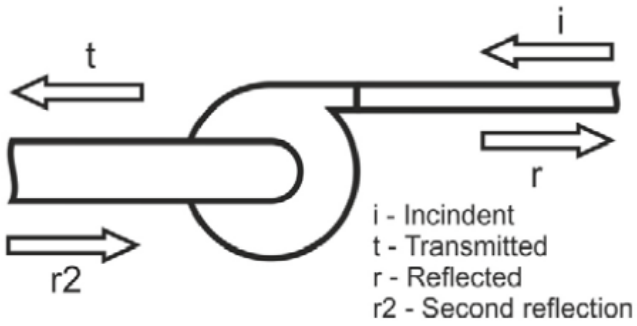

Figure 4.2: Compressor pressure components nomenclature

in Figure 4.4.

- Inlet and outlet diameters of that pipe (placed between volumes) took the value of the diameter corresponding to a circular section equivalent to the exhaust section at compressor tongue (D_t).
- Optimum discharge coefficient was set to 0.7.
- Rotor equivalent volume (V_1) represented volume of the rotor wheel.
- Stator equivalent volume (V_2) represented the volume of the stator and volute. Volume of the pipe placed between volumes must be discounted.
- Two small pipes representing compressor inlet and outlet ports have been included. Lengths and diameters of those pipes are pointed out in figure 4.4, but both were real geometry.
- Compressor map used at the boundary must be corrected to account for pressure losses of the introduced elements.

That correction is needed since compression ratio given in a manufacturer map or measured in a gas stand is calculated between nodes 1 (compressor inlet port) and node 2 (compressor outlet port) of figure 4.3. Nevertheless compressor model to account for accoustic non-linear must be calculated between nodes 1' and 2' showed in figure 4.3. To get that internal compression ratio it is neccesary to discount friction losses on compressor model elements (inlet port, volumes, diffuser and outlet port). That procedure can be describe as equation 4.1 shows.

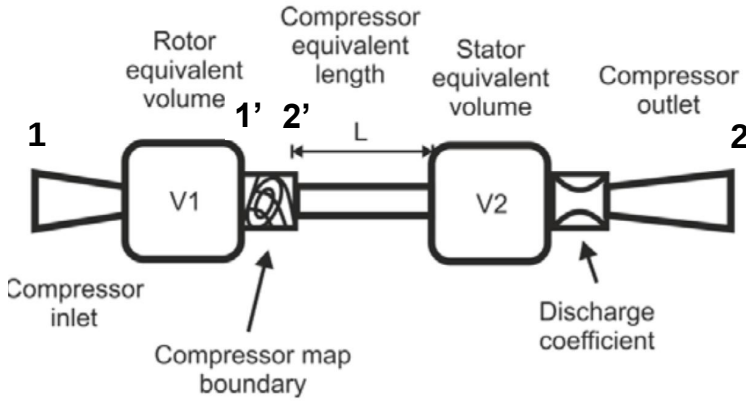

Figure 4.3: Compressor model simplification

$$\Pi_{map} = \frac{p_{02}}{p_{01}} = \frac{p_{01'}}{p_{01}} \cdot \frac{p_{02'}}{p_{01'}} \cdot \frac{p_{02}}{p_{02'}} \tag{4.1}$$

Where pressure losses at compressor inlet ($\frac{p_{01'}}{p_{01}}$) and compressor outlet ($\frac{p_{02}}{p_{02'}}$) will be determined each time step in fluid-dynamic code OpenWAM^{TM} in order to discount from manufacturer compressor map (Π_{map}) pressure losses at model elements obtaining so pressure ratio at compressor boundary map ($\frac{p_{02'}}{p_{01'}}$). Isolating compression ratio from boundary map from equation 4.1 it is obtained:

$$\frac{p_{02'}}{p_{01'}} = \frac{\Pi_{map}}{\frac{p_{01'}}{p_{01}} \cdot \frac{p_{02}}{p_{02'}}} = \Pi_{map} \cdot K \tag{4.2}$$

Due to the fact that $p_{01'} < p_{01}$ and $p_{02'} < p_{02}$ bottom part of equation 4.2 will be lower than unity and so corrector term (K) will be higher than one as it is observed on the right side of figure 4.4. As it is observed that factor depended of corrected air mass flow and turbocharger speed. With that correction and with a similar correction for compressor efficiency, a new compressor map can be obtained and introduced into the compressor map boundary. At the end, compression ratio between inlet and outlet nodes of the

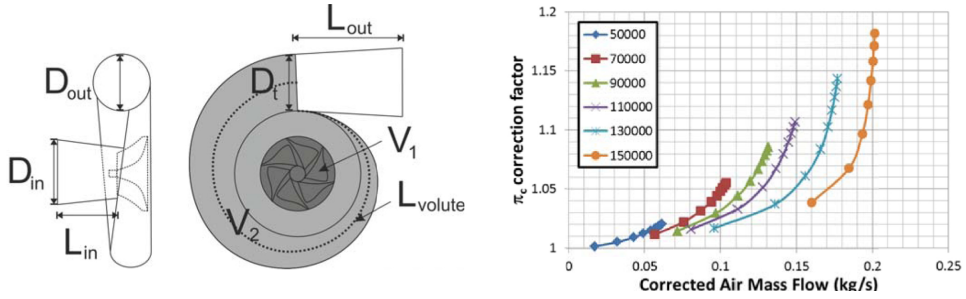

Figure 4.4: Compressor acoustic model. Left: Compressor geometry, Right: Corrector term on the compression ratio.

proposed compressor model (for a given corrected mass flow and turbocharger speed) must be the same as the provided by the original map. Compressor efficiency must be corrected too since compression ratio for boundary map is bigger than compressor map, and so efficiency must be corrected to get the same compressor outlet temperature with different compression ratio.

4.2.4 Compressor Model Validation

Tests have been simulated using gas-dynamic simulation code OpenWAM^{TM} [189]. Only the part of the facility between the two piezoelectric sensor arrays has been modelled to avoid external interferences. Pressure waves moving towards the compressor (incident and second reflected) and also turbocharger speed were imposed from the experimental data, so that the turbine did not need to be calculated. Instantaneous temperature was imposed at compressor inlet pipe since flow moved from the boundary to the pipe. However, only average temperatures could be measured in the test bench and thus the assumption of isentropic compression at the boundaries was adopted, so that the instantaneous temperature was calculated from the average temperature and the instantaneous pressure variation.

Model calculated reflected and transmitted pressure waves upstream and downstream of the compressor. Figure 4.5 (left side) represents the good agreement between modelled and measured pressure waves in time domain (corresponding to 66.7 Hz and 100 mbar in peak-to-peak amplitude). As it can be observed, second reflection and incident wave have been imposed (r2

and i in figure 4.2). Accuracy of compressor acoustic model was determined by comparing transmitted and reflected pressure waves (t and r in figure 4.2), since those signals were calculated by the model.

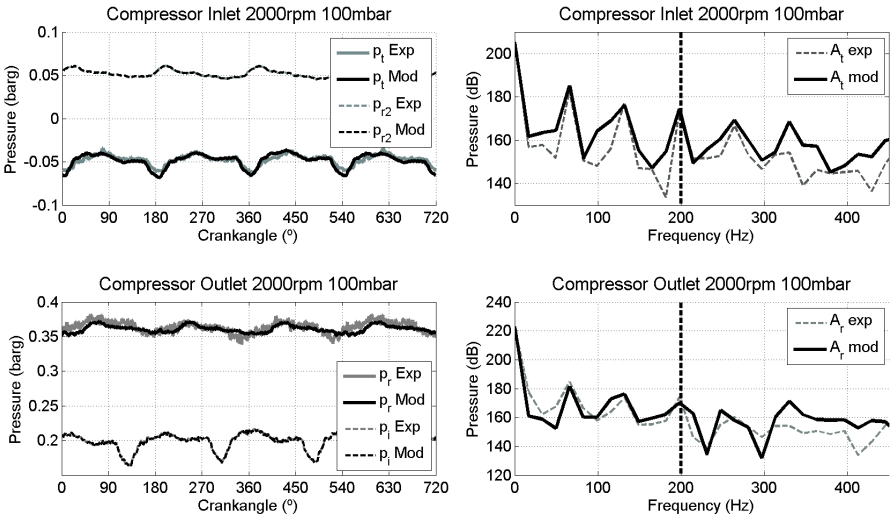

Figure 4.5: Upstream and downstream pressure waves. Left: time domain, Right: frequency domain

Modelled pressure waves have been represented in the frequency domain (right side of figure 4.5), to carry out an analysis of model acoustic response. Assuming a four cylinder and four stroke engine, relevant frequencies are 2nd engine order and its multiples. At these frequencies wave amplitude has a local maxima. Therefore, acoustic compressor model should be able to reproduce those peaks (as the right side of figure 4.5 shows). In that case, only sound pressure level of the outgoing waves (t and r) has been plotted. Vertical line marks the 6th engine order which limits the frequency range of interest. Up to this limit difference in decibels between modelled and measured signals was quite small.

Beamforming technique also allowed the estimation of instantaneous mass flow, providing another parameter to assess the model by comparing instantaneous calculated mass flow to that obtained from experimental data (using beamforming technique). That comparison can be observed on the left side of figure 4.6, where very good agreement between modelled and experimentally estimated instantaneous mass flow upstream and downstream of the compres-

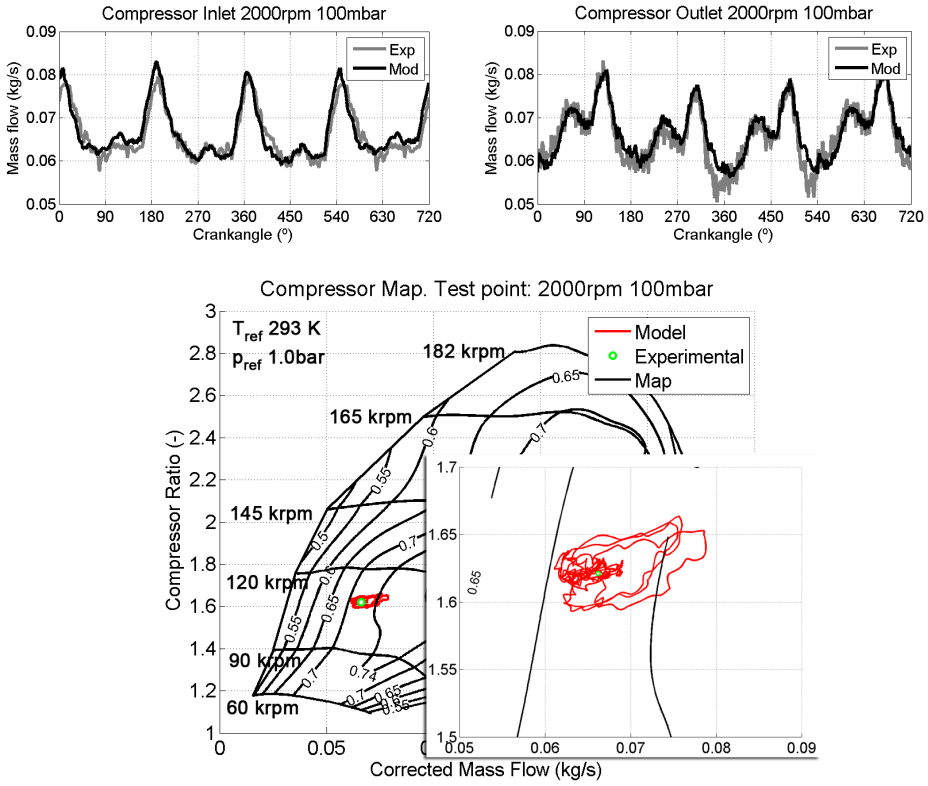

Figure 4.6: Top: Upstream and downstream instantaneous mass flow, Down: Operating point on the compressor map

sor is observed. It was also possible to represent instantaneous operating point on the compressor map, this capability allowed detecting whether instantaneously compressor passed through an undesirable zone of operation (surge, low efficiency, choke ...). Right side of figure 4.6 shows instantaneous evolution on the compressor map.

Analysis shown above for one of the experimental points of the test matrix, was repeated for the whole test campaign. Differences in decibels were obtained for the 2nd, the 4th and the 6th engine order. That information gave a global view on compressor model accuracy. Figure 4.7 shows errors for both the transmitted and reflected wave amplitudes. Horizontal lines have been drawn in the figures to indicate the ± 5 dB range, points located inside that

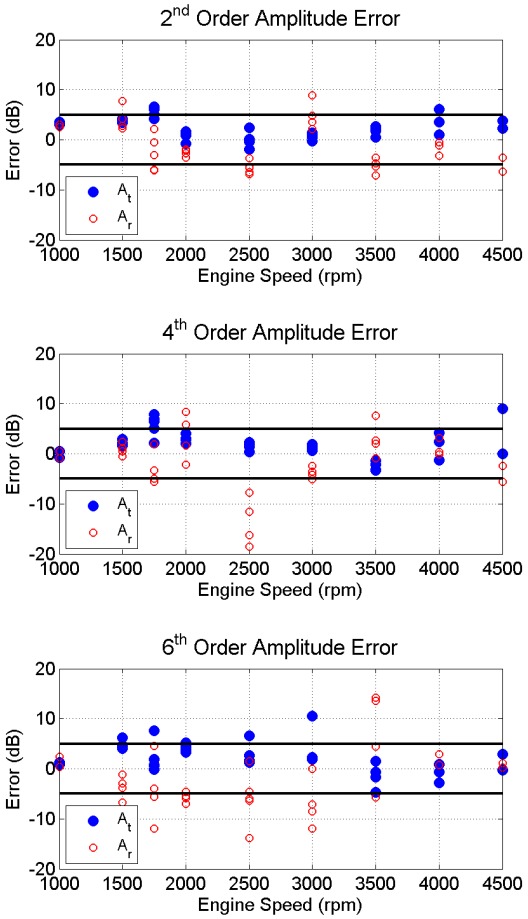

Figure 4.7: Comparison between modelled and measured data applying OpenWAM^{TM}

range are considered to have good accuracy. As it can be observed most of the points for the transmitted wave lied between both limits. Regarding the reflected wave, the presented model was able to predict it for the second engine order but for higher engine orders and medium engine speeds some problems appear, since the model underestimated wave amplitude.

From the point of view of radiated noise, the most important wave is the transmitted one, for that case, the model was able to predict accurately low frequency noise generated by flow pulsations. Additionally, reflected waves

affected volumetric efficiency of the engine due to the influence on the intake processes of the cylinders. Second engine order frequencies were the most important in this case.

4.3 Non-Steady Turbine Characterization

4.3.1 Introduction

Turbine modelling using conventional 1-D gas dynamics codes based on manufacturer maps interpolation is not accurate enough for most of real operative conditions due to for example the highly pulsating flow on the turbine. That phenomenon is produced by the opening and closing of cylinder's exhaust valves what causes an instantaneous variation of the gas pressure inside the exhaust manifold that is translated into a variation in the expansion ratio and mass flow across the turbine. Those variations affect turbine efficiency too due to the associated variation of the instantaneous temperature inside the exhaust manifold. Those variations cause turbine parameters (mass flow and efficiency) move instantaneously far from the narrow region supplied by steady state measurements.

4.3.2 Experimental Methodology

Taking into account the aforesaid considerations, testing procedure to characterize turbine behaviour should include steady flow characterization, off-design characterization and pulsating flow characterization.

4.3.2.1 Steady Flow Characterization

Performance maps for the turbine (and the compressor) have been obtained carrying out a series of tests in the gas stand presented in section 4.2.2.1. It was desired decoupling heat transfer effects (in the turbocharger) from its aerodynamic behaviour (isentropic performance). With that aim, a series of almost-adiabatic steady flow tests were performed in both turbine and compressor obtaining so the adiabatic maps. That methodology consisted of testing the turbocharger at the same temperature at turbine inlet, at lubrication

inlet port and at compressor outlet. That value was chosen as the average temperature between compressor choke and surge limits at every turbo speed. Those limits were determined modifying position of the counter-pressure valve installed at compressor outlet. That procedure ensured that turbocharger internal heat fluxes were small compared to its mechanical power. Nevertheless some heat transfer effects were expected since those tests were not truly adiabatic, for that reason the appearing small heat fluxes were discounted using proposed thermal model. Additionally, the turbocharger unit was fully insulated to avoid the external heat transfer effects. That technique was limited by the maximum temperature reachable at lubricating inlet oil. Oil temperature measurements were used too as the data source to validate mechanical losses model [153, 154] but gas temperature measurements have been also used to extrapolate turbine perforrmance maps.

4.3.2.2 Pulsating Flow Characterization

Pulsating flow effects on the turbine side have been studied reproducing several engine conditions using the gas stand presented before. Those tests have been performed installing the rotary valve at turbine inlet to simulate what would be cylinders and exhaust valves of the engine. Pulses amplitude and frequency have been modified as desired to cover a wide operative range. Compressor has been tested under continuous flow conditions to isolate it from pulsating phenomena occurring on the turbine side. Testing campaign has been carried out under almost-adiabatic conditions to avoid heat transfer effects. Testing points have been chosen to be representative from the engine mounting the studied turbochargers. Table 4.2 shows engine operative points for the different turbochargers (pulses amplitude in mbar).

Instantaneous pressure at turbine inlet and outlet has been recorded by means of six piezoelectric pressure transducers, three at turbine inlet pipe and the other three at turbine outlet. Those sensors provide only information about pressure fluctuations inside pipes. Two instantaneous piezoresistive transducers have been installed at turbine inlet and outlet to obtain the absolute pressure. Piezoelectric pressure transducers have been installed in a smooth and straight pipe with the same diameter than turbine entry to ensure that the internal flow would be completely developed being negligible turbulence effects. A minimum distance of 10 times pipe diameter has been chosen. Piezoelectric transducers from the sensor array have been separated

Table 4.2: Engine simulated points with quasy-adiabatic flow (amplitude pressure in mbar)

Load → **Engine Speed ↓**	**12%**	**25%**	**50%**	**75%**	**100%**
1500	T1(150) T2 (220) T3 (200)	T1 (260) T2 (220) T3 (250)	T1 (495) T2 (500) T3 (500)	T1 (670) T2 (600) T3 (700)	T1 (600) - T3 (700)
2000	T1 (200) T2 (210) -	T1 (330) T2 (280) -	- - T3 (500)	- - T3 (700)	T1 (520) T2 (700) T3 (700)
3000			T1 (550)	T1 (700)	T1 (600)
3500					T1 (566)

the distance of one pipe diameter to decompose pressure fluctuations into its basic components using a beam forming technique [133].

Figure 4.8 shows the nomenclature used in the turbine side for decomposed pressure waves. Pressure wave generated by the cylinder head and exhaust valves and moving from the engine to the turbine entry has been named as "incident wave". Once that pressure wave has reached the turbine, a reflection wave moving backwards from the turbine inlet to the engine appears and it has been named as "reflected wave". The information travelling with the incident pressure wave traversing the turbine and that continues travelling along the outlet pipe up to the aftertreatment devices has been named "transmitted wave". Once that pressure wave (moving downstream the turbine) reachs the aftertreatment devices (or silencer) part of that information is reflected backwards to the turbine and has been named as "2nd reflected wave". Sum of both decomposed pressure signals is known as composed pressure and is equal to the instantaneous measured pressure wave (original wave).

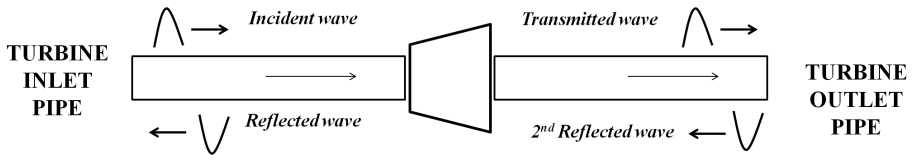

Figure 4.8: Turbine pressure component nomenclature

4.3.3 Turbine Model Development

Several turbine models have been proposed over the last few decades being the main difference between them the way in which fluid-dynamic behaviour has been characterized. Watson and Janota [183] proposed a simple model where the turbine was replaced by a single nozzle whose equivalent area was that producing the same pressure drop for the same steady mass flow. That model provided good results modelling axial turbines with moderate expansion ratios. Nevertheless this model did not predict successfully radial turbines with higher expansion ratios due to the fact that choking conditions were predicted earlier than the obtained from measurements. Payri et al. [126, 127] proposed a turbine model based on a filling and emptying model where turbine was represented by two nozzles in series to characterize stator and rotor with an intermediate reservoir.

Turbine model presented here is based on Payri's proposal using turbine map information and including some elements in order to predict how pressure waves are transmitted and reflected by the turbine. Its fluid-dynamic behaviour has been reproduced by simplifying its real geometry using 0-D and 1-D elements with acoustics purposes. It has been decided to keep 0-D model from Payri proposal to account for compressibility effects. In addition a series of pipes (1-D elements) have been connected to the 0-D element in order to account for acoustic effects. Those pipes will reproduce turbine volute and diffuser with a simplified geometry.

Turbine volute in the proposed model has been split into two pipes in series as figure 4.9 shows. First stage comprised from turbine inlet port to volute tongue (pipe A) and the second pipe representing turbine volute (pipe B). Geometry of the first stage (A in figure 4.9) has been modelled as a tapered pipe with real measured geometry (as proposed by Chen et al. [32]). Geometry of the second pipe (B in figure 4.9), representing turbine volute has been simplified to a straight pipe (similar to the proposal of Costall et al. [37]) with the same diameter than the real measured at the tongue section, being pipe length arbitrary but keeping the same volume than turbine volute. Turbine volute volume (region B on Figure 4.9) has been calculated subtracting to the total measured volume the calculated volume from the first stage (region A). Intermediate volume from turbine model proposed by Payri et al. [127] has been considered as the sum of the stator blades region but subtracting blades volume (region C), the intermediate volume between stator and rotor (region

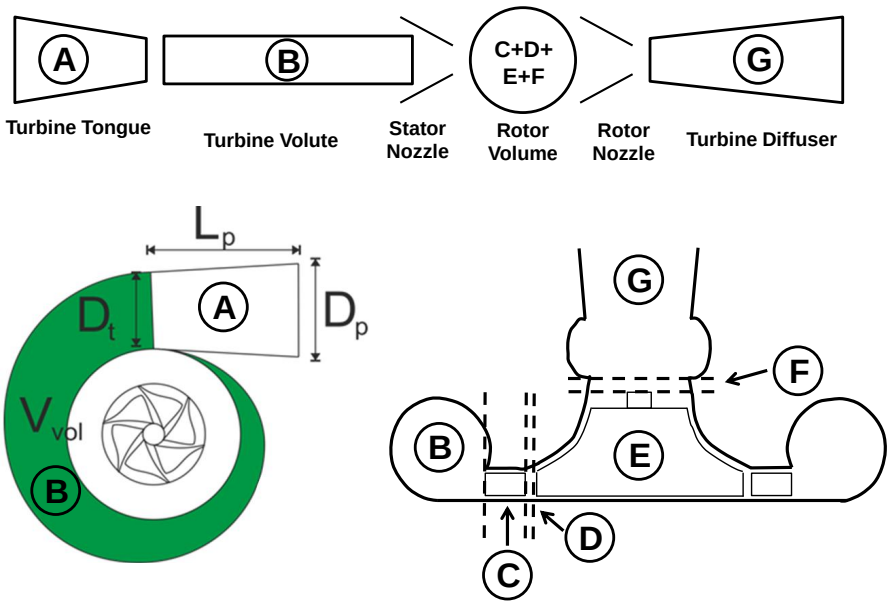

Figure 4.9: Top: Turbine geometry to account for acoustics non-linear. Bottom-left: Turbine volute geometry, Bottom-right: Turbine rotor and diffuser geometry.

D), rotor volume until end of nut subtracting blade and nut volumes (region E) and the intermediate volume between rotor and diffuser (region F). Turbine outlet has been modelled as a tapered duct keeping the same volume than the measured one, and with the same inlet and outlet diameters (region G).

4.3.4 Turbine Performance Maps Extrapolation

New advances in engine technologies are pushing the limits of operation for turbochargers to low expansion ratios, which in turn brings the analysis of turbine phenomena to higher blade speed ratios. In that region having estimations of turbine efficiency gives the possibility to run reliable full engine simulations. That is one of the main reasons to look for techniques to extrapolate turbochargers maps [105]. Extrapolation is necessary even when specific turbine models - such as those developed by Benson [17], Payri et al. [127] and Serrano et al. [148] - are used for solving the turbocharger as a boundary condition in 1-D simulation codes of reciprocating ICE. Since that kind of

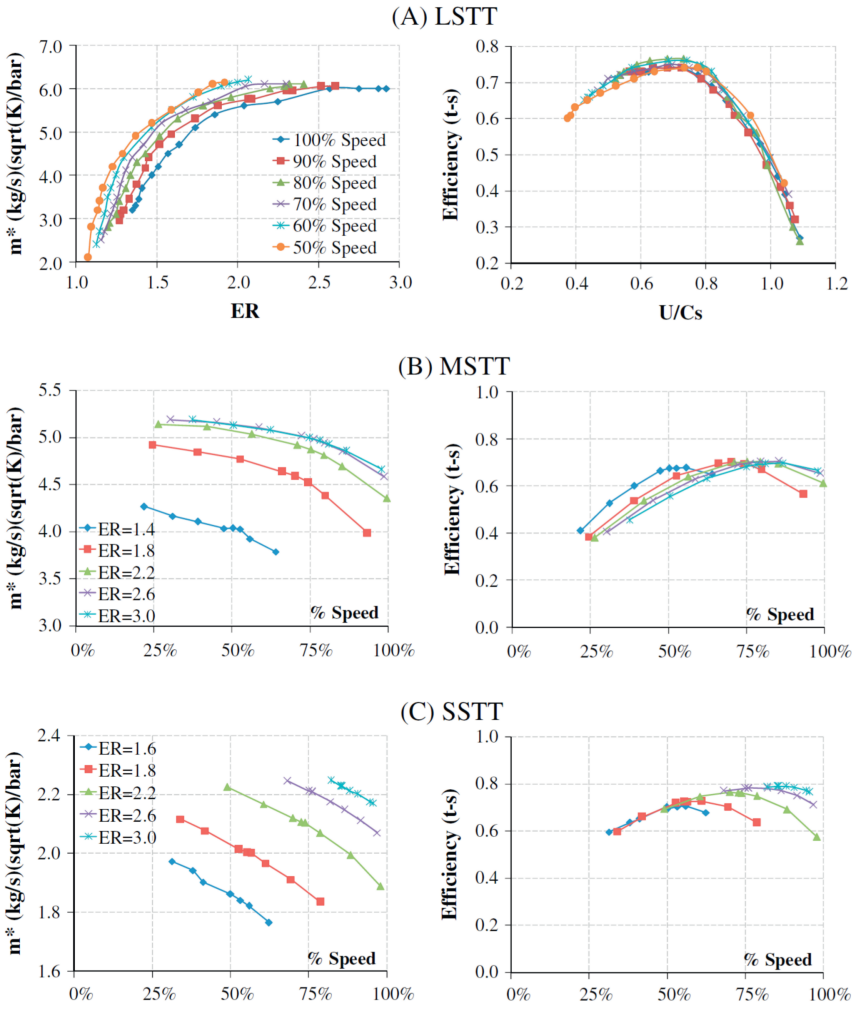

Figure 4.10: Vaneless example turbines (turbine maps). (A) LSTT [106]. (B) MSTT. (C) SSTT

turbine models need to be calibrated against a complete set of experimental information.

The objective of the proposed methodology is to extrapolate turbine efficiency and mass flow curves from the range of available experimental data which is usually obtained for a narrow mass flow range. The present method-

ology will allow estimating efficiency in regions where there is no experimental data available. That tool would help improving engines analyses and prediction of their operational characteristics. As deduced from the works of Katrasnik [93, 94], in advanced engine concepts like hybrids, the available 1-D models will benefit from more robust physical based methodologies for turbine map extrapolation. Since proposed methodology for turbine maps interpolation and extrapolation is based on physical concepts, this will make it sufficiently robust to solve for the lack of turbine data at off-design operative conditions. The aim of this methodology is not to be predictive with a base on geometrical data (only one measured point is not enough); but strictly to extrapolate turbine behaviour from experimental data. Typical radial turbine maps taken as examples for the application of this methodology are shown in figure 4.10 for three vaneless stator radial turbines. Data from the large size truck turbine (LSTT) was taken from Martinez-Botas [106] (figure 4.10-A) and it was tested in the rig developed by Szymko [167]. Medium and Small Size Truck Turbines (MSTT) and (SSTT) were also radial, vaneless stator turbines used as low and high pressure turbines in a two stage system. Maps for these turbines (shown in figures 4.10-B and C) were obtained from the turbocharger manufacturer who tested them in a hydraulic brake test rig for turbine characterisation, similar to those of Winterbone et al. [187] and Nikpour [118]. Data from figure 4.10-A was measured at constant turbine reduced speed, while 4.10-B and C were measured at constant turbine expansion ratio. Another turbine data used in present work, comes from a single radial inflow stage Commercial Vaned Turbine (CVT) used for an analysis carried out by Futral and Wasserbauer [63]. Finally data from four turbines from passenger car applications were tested at Universitat Politécnica de València turbochargers test rig [70] and have been also used to validate turbine extrapolation technique. They have been named henceforth turbocharger T.#0, T.#1, T.#2 and T.#3 . All of them were variable geometry turbines (VGT) with nozzles in the stator unless the last one (T.#3) that was a small fixed turbine with waste-gate valve.

All turbines used to validate the proposed extrapolation technique were tested with air and with low turbine inlet temperature. Doing so heat transfer effects were negligible allowing measuring directly turbine adiabatic efficiency. But at the same time high enough to avoid freezing the air moisture at the turbine outlet. Experimental procedure to measure experimental data in a radial turbine is deeply presented on [41, 188, 118, 12, 167], where different types of gas stands for turbocharger testing are identified. Nevertheless, the

most common source of data are the gas stands using turbocharger's compressor as a brake, which unfortunately does not produce information in a range of turbine operative conditions wide enough. Therefore, although the proposed methodology is likely to work with data from any type of gas stand, it is more useful in the case where the turbine data has been obtained with the compressor as the turbine brake [70].

4.3.4.1 Extension of turbines mass flow parameter map

Procedure for turbine mass flow map extension is based mainly on the definition of the sub-critical mass flow parameter through the orifice of a single isentropic nozzle given by equation 4.3 [82].

$$\frac{\dot{m} \cdot \sqrt{T_{00}}}{p_{00}} = A_{eff} \cdot \sqrt{\frac{\gamma}{R}} \cdot \left(\frac{1}{\Pi_T}\right)^{\frac{1}{\gamma}} \cdot \sqrt{\frac{2}{\gamma - 1} \cdot \left[1 - \left(\frac{1}{\Pi_T}\right)^{\frac{\gamma-1}{\gamma}}\right]} \tag{4.3}$$

Some authors have attempted to model the turbine as a single nozzle with some success, for example Watson and Janota [183] and Benson [17]. The same basic approach has been followed here, but taking into account the possibility for the equivalent nozzle flow area (A_{eff}) to be variable instead of a constant value. Considering mass flow parameter charts presented in figure 4.10, it is possible to say that equation 4.3 would represent the physical relationship between mass flow parameter ($\dot{m}^{red}$) and the expansion ratio (Π_T) if the turbine behaved like a nozzle with an equivalent area of A_{eff}. Once variations of A_{eff} have been known for every Π_T, it would be possible to plot the entire mass flow curve. Therefore, the objective will be to estimate A_{eff} as a function of turbine operative conditions, these are expansion ratio (Π_T) and reduced speed (u^*) or blade speed ratio (σ). Taking into account the definition of blade speed ratio given in equation 4.4 and turbine experimental data, which in this case are: mass flow parameter ($\dot{m}^{red}$), reduced blade tip velocity (u^*), the expansion ratio (Π_T) and the gas properties (i.e. γ and c_p); it is possible to calculate blade speed ratio for every tested point.

$$\sigma = \frac{u_1}{c_s} = \frac{\pi \cdot D_T \cdot N}{\sqrt{2 \cdot c_p \cdot T_{30} \cdot \left(1 - \Pi_T^{\frac{1-\gamma}{\gamma}}\right)}} \tag{4.4}$$

In case of turbines tested at constant U^* lines (like the results shown in 4.10-A, for the LSTT, or for the turbochargers tested at UPV gas test rig), it is quite convenient to plot the equivalent area A_{eff} as a function of the blade speed ratio (σ) since an almost linear trend is observed. For that reason some authors, Zinner [193] and Muñoz et al. [112] proposed a linear approximation between effective area and blade speed ratio. Nevertheless some deviations of that linear trend at lower speeds and at small values of σ appeared (figure 4.12). That was due to the intrinsic simplification of the linear trend, which introduced high errors at the lowest turbo speeds and when the mass flow approached to choke conditions. Sanchez et al. [143] deduced that the relationship between the area of a nozzle equivalent to the turbine (A_{eff}) and blade speed ratio was also affected by turbine reaction degree and isentropic efficiency. And that such influence became more important as turbine speed was reduced and the expansion ratio was increased. On the other hand, when turbines were characterised at constant expansion ratio, such as the medium and small size truck turbines (figures 4.10-B and C), this trend changed and became quadratic, as it is shown in figure 4.12 (middle and bottom). That is not surprising since due to the different testing procedure (at constant Π_T instead of at constant u^*) operative conditions in the turbine were intrinsically different. Indeed, figure 4.12 (middle and bottom) shows that A_{eff} decreases at constant expansion ratio (according to equation 4.4 c_s would be constant in those conditions) when turbocharger speed increases. This behaviour was a consequence of the centrifugal force field created by the rotor of the radial turbine [183] that reduced the mass flow for a given expansion ratio (figure 4.10), therefore the equivalent nozzle reproducing turbine mass flow behaviour should show a decreasing trend in A_{eff} to A_0 ratio. That decreasing trend should be proportional to the square of the reduced speed [13] due to centrifugal force field. Nevertheless, it would be expected that independently on which variable was fixed during turbine testing (U^* or Π_T) the same type of function could relate A_{eff} to A_0 ratio with turbine operative variables. In addition it seemed that A_{eff} to A_0 ratio should be a function not only of σ but also of Π_T and/or U^*. The relation proposed is based on equation 4.5, deducted by Sanchez et al. [143] for the area of a nozzle equivalent to the

turbine (A_{eff}), and on the diagrams of figure 4.11.

$$A_{eff} = \frac{A_R^{'} \cdot \sqrt{1 + \left(\frac{c_0}{c_s}\right)^2 + \left(\frac{w_1}{c_s}\right)^2 + \sigma^2 \cdot \left[\left(\frac{D_2}{D_1}\right)^2 - 1\right]}}{\sqrt{1 + \left(\frac{A_R^{'}}{A_S^{'}}\right)^2 \cdot \left(\frac{\rho_2}{\rho_1}\right)^2}} \tag{4.5}$$

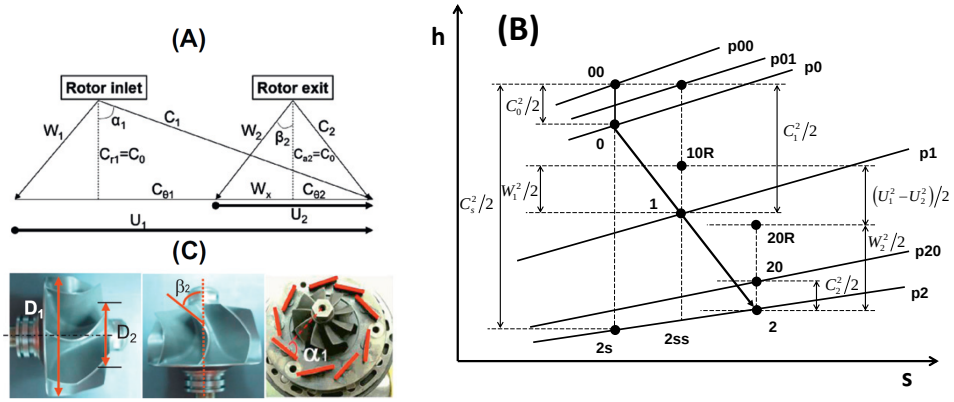

Figure 4.11: (A) Velocity triangles for constant meridional component velocity in a radial turbine. (B) Enthalpy versus entropy diagram for the turbine stage. (C) Definition of dimensions and metal angles in the turbine rotor and stator.

Equation 4.5 was obtained from kinetic energy balance (figure 4.11-B) and mass conservation equation [143]. Mass conservation was applied to the mass flow through A_{eff}, which should be equal to the mass flow through two nozzles in series, first one with stator throat as throat area (A_S) and second one with rotor available area at rotor outlet as throat area (A_R). Fitting coefficients (μ_S and μ_R), correcting stator and rotor geometrical areas were introduced. Such mass conservation equation and both areas can be expressed as,

$$\begin{aligned} \dot{m} &= A_S^{'} \cdot \rho_1 \cdot c_1 = A_R^{'} \cdot \rho_2 \cdot w_2 = A_{eff} \cdot \rho_2 \cdot c_s \\ A_S^{'} &= \mu_S \cdot A_S \\ A_R^{'} &= \mu_R \cdot A_R \end{aligned} \tag{4.6}$$

Density ratio from equation 4.5 is a very complex function of turbine ex-

pansion ratio (Π_T), turbine reaction degree and turbine efficiency. In order to simplify equation 4.5 making it operative for extrapolation objectives, two major assumptions have been used [131]. First one was that polytropic expansion in stator and rotor had the same index (γ); second one was that p_1 was an average of p_{00} and p_2 (see figure 4.11-B for nomenclature). Using these two simplifications equation 4.5 can be written as,

$$A_{eff} = \frac{(\mu_R \cdot A_R) \cdot \sqrt{1 + k_1 + \sigma^2 \cdot \left[\left(\frac{D_2}{D_1}\right)^2 - 1\right]}}{\sqrt{1 + \left(\frac{\mu_R}{\mu_S}\right)^2 \cdot \left(\frac{A_R}{A_S}\right)^2 \cdot \frac{(k_2 \cdot IER)^2}{\left(1 - \eta_{TS} \cdot \left[1 - (k_2 \cdot IER)^{\frac{\gamma-1}{\gamma}}\right]\right)^2}}} \tag{4.7}$$

Where,

$$\begin{aligned} IER &= \frac{2}{\Pi_T + 1} \\ k_1 &= \left(\frac{c_0}{c_s}\right)^2 + \left(\frac{w_1}{c_s}\right)^2 \end{aligned} \tag{4.8}$$

Fitting factor k_2 (constant for every turbine opening) was introduced to correct big deviations from previous two assumptions. Fitting parameters μ_S and μ_R have been introduced to compensate errors measuring geometrical area of turbine stator and rotor throat. Equation 4.7 provides an intermediate level of complexity between the too simple linear assumption proposed by Muñoz et al. [112] and the too complex detailed resolution in the approach proposed by Sanchez et al. [143] with equation 4.5. This approach needs knowing extrapolated turbine efficiency (η_{TS}) to extrapolate effective area as it is observed in equation 4.7. It will be explained in the next section how that extrapolated efficiency has been obtained for the results showed in the following figures.

Unknown values from equation 4.7 that have been used as fitting coefficients for a whole turbine map (or an opening for a VGT turbine) are: μ_R, μ_S, k_1 and k_2. Parameter k_1 (equation 4.8) takes into account velocity terms according to the nomenclature shown in figure 4.11-(A) and so that value should not be constant with turbine operative conditions. Nevertheless a constant fitting value has been used since its relative variations are small with respect to 1 (in the range of $\pm$ 0.02). Charts in figure 4.12 show graphically extrapo-

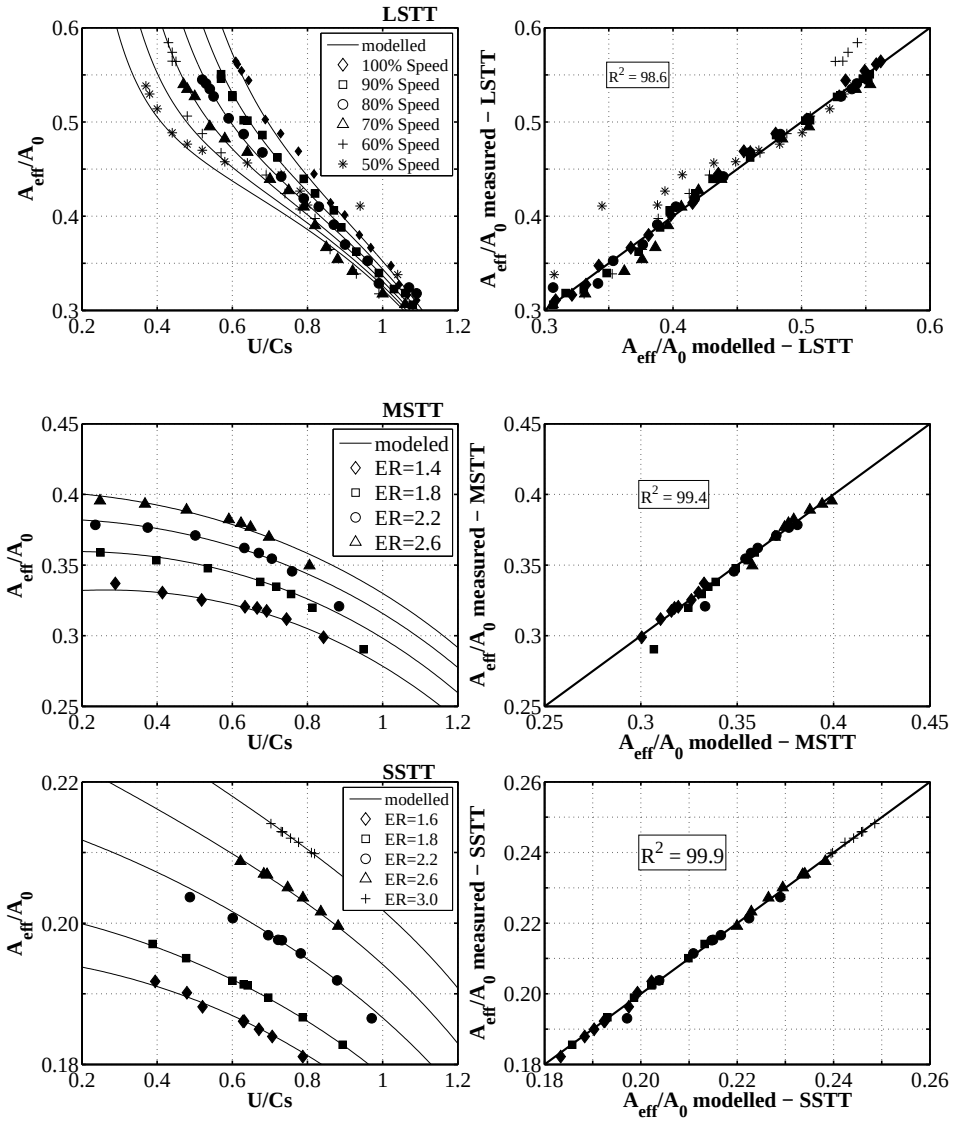

Figure 4.12: A_{eff} to A_0 ratio versus blade to jet velocity ratio for stator vaneless turbines. Top: Data measured at constant u^* (LSTT [106]). Center and Bottom: Data measured at constant Π_T (MSTT and SSTT).

lation results for A_{eff} to A_0 ratio for the three vaneless stator truck turbines, being A_0 turbine inlet port area.

At the same time figure 4.12 shows the level of accuracy obtained when

equation 4.7 was used to reproduce experimental data. On the left side charts of figure 4.12, experimental values have been plotted as points while equation 4.7 has been represented with a continuous line, both versus blade speed ratio (σ). Constant speed lines in the case of the LSTT are observed but also deviations from linear behaviour of A_{eff} to A_0 ratio with σ for the case of LSTT are clearly shown. In the case of the MSTT and SSTT, figure 4.12 (middle and bottom) left charts show fitting and extrapolation results of constant Π_T lines to the experimental results (from figures 4.10-B and C). Experimental data have been plotted versus predicted values using equation 4.7 on the right side charts of figure 4.12. R^2 factor presented in figure 4.12 indicates the high level of correlation between A_{eff} to A_0 ratio and the two independent variables (Π_T and σ). Figure 4.13 shows the results of fitting equation 4.7 to the data from turbines with vaned stators. That is the CVT data measured by Futral [63] in figure 4.13-A and the T.#0 (VGT) data in figure 4.13-B. The narrower operative range tested for the T.#0 (VGT) was a drawback, since very few points were available for the fitting procedure.

Equation 4.7 in conjunction with equations 4.3 and 4.4 have been used to perform an extrapolation of the mass flow map using the following procedure,

1. Using the data available in turbine map and equations 4.3 and 4.4, experimental (A_{eff}) can be calculated and plotted versus the independent variables (σ, Π_T and U^*).
2. Equation 4.7 is then used to fit values for μ_R, μ_S, k_1 and k_2 coefficients for the whole turbine map.
3. Evaluating equations 4.3, 4.4 and 4.7 for a wide range of Π_T and/or U^*, extrapolation of the sub critical nozzle equation 4.3 can be carried out.

Because of the intrinsically sub-critical condition of the nozzle equation 4.3, mass flow never chokes [193]. Indeed, if A_{eff}/A_0 is hold constant the value of equation 4.3 increases with Π_T up to a certain value (Π_T^c) and further results provided by equation 4.3 decrease, (for Π_T values higher than Π_T^c). That effect is compensated in equation 4.7 by the exponentially increasing of A_{eff}/A_0 when σ decreases (i.e. when Π_T increases) as it is shown in figures 4.12-A and 4.13. In spite of this, at very high Π_T values, it can happen that the first derivative of equation 4.3 will be zero and mass flow shows a slight decreasing trend (grey dotted line in figure 4.14). Once that point has been

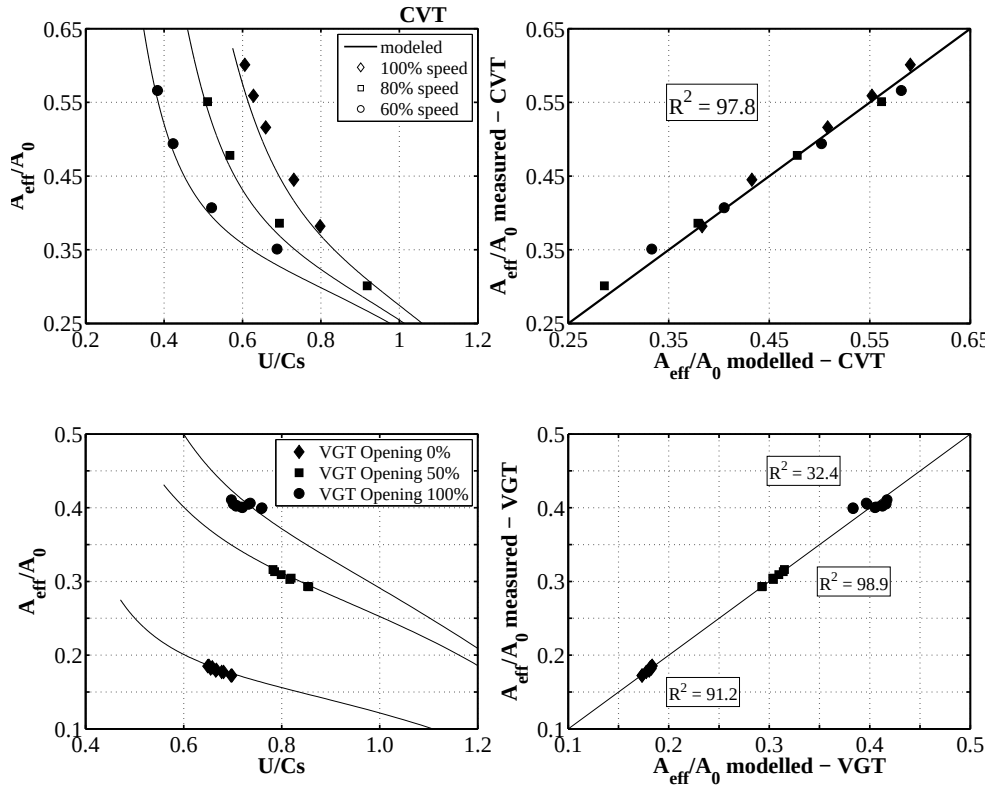

Figure 4.13: A_{eff} to A_0 ratio versus blade to jet velocity ratio for the CVT and the VGT. Top: CVT [63]. Bottom: T.#0 (VGT). Data measured at constant turbocharger speed.

reached, the corresponding Π_T^c can be considered the critical expansion ratio for which choked flow is achieved. Therefore, an extra step can be added to previous procedure,

- When the first derivative of the sub-critical nozzle expression, equation 4.3, is zero turbine flow is choked and, from this point on (Π_T^c), the corresponding value of mass flow parameter is kept constant as the Π_T is increased.

Results of such extrapolation procedure for five of the eight studied turbines are shown in figures 4.14, 4.15 and 4.16. Figure 4.14 shows for the

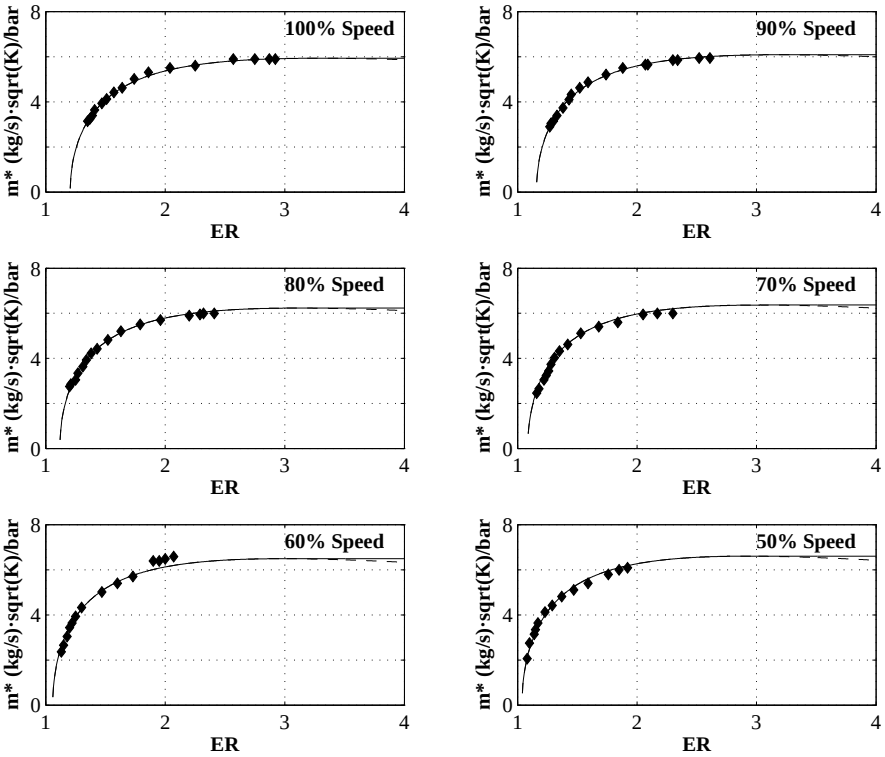

Figure 4.14: Mass flow parameter charts versus expansion ratio for the LSTT. Rhombic dots are measured points [106].

LSTT experimental points and in continuous line results from the extrapolation. A dotted line has been plotted just to show the non-physical behaviour of equation 4.3 after critical conditions are reached. It is worth highlighting that critical conditions of an isentropic nozzle differs from those guessed from figures 4.14, 4.15 and 4.16 for two reasons: flow expansion in the turbine is non-isentropic and due to the turbine chocking situation is similar to what would happen with two nozzles in series, one equivalent to the stator and another to the rotor [127, 148]. In this equivalent case the critical pressure ratio in the whole assembly would be much higher than the critical pressure ratio in only one isentropic nozzle since it is the individual pressure ratio in every nozzle what controls chocking flow conditions. It is worth clarifying that some experimental values taken from the CVT analysis (figure 4.16 left side) correspond to mass flows values extracted directly from Futral's prediction [63]

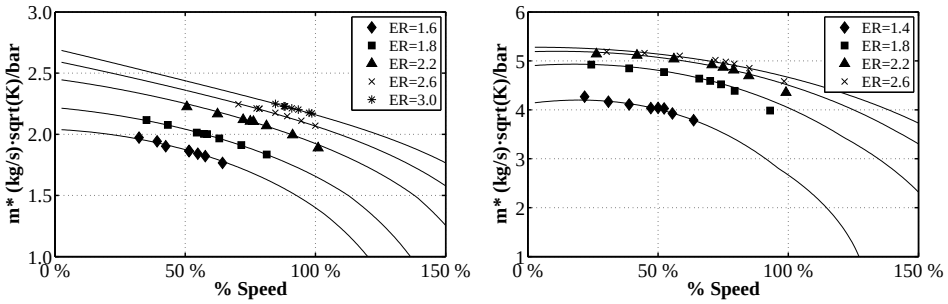

Figure 4.15: Mass flow parameter charts versus turbocharger speed. Left: MSTT. Right: SSTT. Dots are measured points.

because of the absence of more experimental information in this reference. In the right side of figure 4.16 the advantages presented by this extrapolation technique can be observed, taking into account the reduced amount of Π_T values available in the experimental points.

4.3.4.2 Extension of turbines total-to-static efficiency map

Extension of turbine efficiency map needs an efficiency equation based on the definition of total-to-static efficiency for turbines expanding ideal gas with constant heat capacity (equation 4.9).

$$\eta_{ts} = \frac{h_{00} - h_{02}}{h_{00} - h_{2s}} = \frac{T_{00} - T_{02}}{T_{00} - T_{2s}} \tag{4.9}$$

Triangle for constant meridional component velocities (c_0) is presented in figure 4.11-A and the enthalpy-entropy diagram for the turbine stage is presented in figure 4.11-B. Figure 4.11-B shows stagnation enthalpy and rothalpy points and it is also possible to observe the term corresponding to the rotor centrifugal force field (i.e.: $u_1^2 - u_2^2)/2$). That term is proportional to the square of turbocharger speed, as discussed previously. Taking into account velocity triangles, it can be said that;

$$\tan \alpha_1 = \frac{c_{\theta 1}}{c_0} \Rightarrow c_{\theta 1} = c_0 \cdot \tan \alpha_1 \tag{4.10}$$

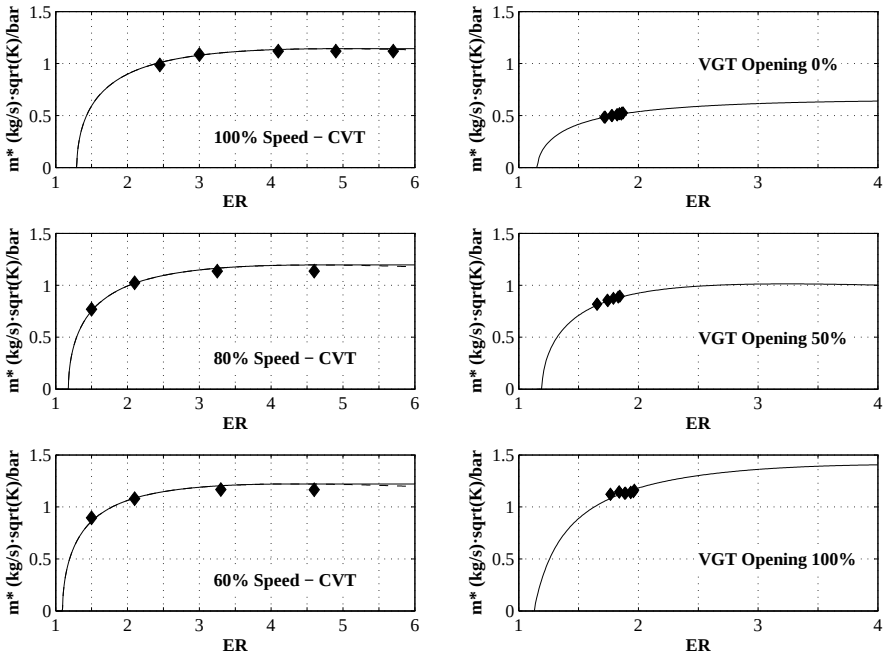

Figure 4.16: Mass flow parameter charts versus expansion ratio for vaned stator turbines. Left: CVT [63]. Right: T.#0 (VGT) Rhombic dots are measured points.

$$\tan \beta_2 = \frac{w_\chi}{c_0} \Rightarrow w_\chi = c_0 \cdot \tan \beta_2 \tag{4.11}$$

$$u_2 = w_\chi + c_{\theta 2} \Rightarrow c_{\theta 2} = u_2 - w_\chi \tag{4.12}$$

Where α_1 and β_2 denote flow angle at turbine rotor inlet and outlet respectively. As usually done in radial machinery r_2 (rotor outlet radius) has been defined as the root mean square radius between $r_{2,hub}$ and $r_{2,shroud}$. Figure 4.11-C shows a scheme of turbine wheel diameters and metal angles definitions.

$$\frac{u_1}{r_1} = \frac{u_2}{r_2} \Rightarrow u_2 = u_1 \cdot \left(\frac{r_2}{r_1} \right) \tag{4.13}$$

Combining equations 4.11 and 4.13 into equation 4.12, equation 4.14 is obtained.

$$c_{\theta 2} = u_1 \cdot \left(\frac{r_2}{r_1}\right) - c_0 \cdot \tan \beta_2 \tag{4.14}$$

Combining turbine power definition (equation 4.15), with Euler's equation of turbomachinery for radial gas turbines (equation 4.16) [13, 143], equation 4.17 is obtained;

$$\dot{W} = \dot{m} \cdot c_p \cdot (T_{00} - T_{02}) \tag{4.15}$$

$$\dot{W} = \dot{m} \cdot (u_1 \cdot c_{\theta 1} - u_2 \cdot c_{\theta 2}) \tag{4.16}$$

$$T_{00} - T_{02} = \frac{u_1 \cdot c_{\theta 1} - u_2 \cdot c_{\theta 2}}{c_p} \tag{4.17}$$

Inserting equations 4.10, 4.13, 4.14, and 4.17 into 4.9 and arranging terms;

$$\eta_{ts} = \frac{u_1 \cdot c_0 \cdot \tan \alpha_1 - u_1 \cdot \left(\frac{r_2}{r_1}\right) \cdot \left[u_1 \cdot \left(\frac{r_2}{r_1}\right) - c_0 \cdot \tan \beta_2\right]}{c_p \cdot T_{00} \cdot \left(1 - \left[\frac{1}{\Pi_T}\right]^{\frac{\gamma-1}{\gamma}}\right)} \tag{4.18}$$

Defining c_s as proposed by Watson and Janota [183], i.e.: the velocity which would be attained if the turbine working fluid was expanded in an ideal nozzle over the same expansion ratio as that of the turbine (figure 4.11)-B, then it can be written;

$$c_s^2 = 2 \cdot c_p \cdot T_{00} \cdot \left(1 - \left[\frac{1}{\Pi_T}\right]^{\frac{\gamma-1}{\gamma}}\right) \tag{4.19}$$

Using equation 4.19, then equation 4.18 can be written as;

$$\eta_{ts} = \frac{-2 \cdot u_1^2 \cdot \left(\frac{r_2}{r_1}\right)^2 + 2 \cdot u_1 \cdot c_0 \cdot \left(\tan \alpha_1 + \left(\frac{r_2}{r_1}\right) \cdot \tan \beta_2\right)}{c_s^2} \tag{4.20}$$

Recalling equation 4.4 and grouping into K_i coefficients;

$$\eta_{ts} = -K_1 \cdot \sigma^2 + K_2 \cdot \sigma \cdot \frac{c_0}{c_s} \tag{4.21}$$

Where

$$K_1 = 2 \cdot \left(\frac{r_2}{r_1}\right)^2 \qquad K_2 = 2 \cdot \left(\tan\alpha_1 + \left(\frac{r_2}{r_1}\right) \cdot \tan\beta_2\right) \tag{4.22}$$

Due to the fact that flow angles at rotor inlet (α_1) and rotor outlet (β_2) are unknown, in a first approximation metal angles have been considered instead. It has been assumed that rotor inlet metal angle will be equal to rotor inlet flow angle (α_1). Also rotor wheel outlet metal angle will be considered equal to rotor outlet flow angle (β_2). Nevertheless, in real both angles will not be equal and a deviation should appear. That will be a function of throat width/blade pitch ratio and the local curvature of the nozzle blade between throat and trailing edge. Watson [183] showed that the deviation between metal blade angle and the actual gas angle (α_1) varied with stator exit velocity, rotor speed and the blade angle. A linear trend for the flow angle at rotor inlet (α_1) with turbine blade speed ratio (σ) has been considered as equation 4.23 shows.

$$\alpha_1 = k' \cdot \sigma + k'' \tag{4.23}$$

Where k' and k'' are fitting constants. Nevertheless that variation was expected to be smooth with σ [183] and so constant k' should tend to small values near to zero and k'' should tend to values near the geometric value of stator blades angle. However for some operative conditions (guide vanes quite closed), mathematical instabilities appear in K_2 factor prediction (due to the tangent function in α_1). In order to avoid that difficulty, it has been decided to calculate rotor inlet angle (α_1) as a function of stator outlet flow angle (α_0) according to Watson's proposal [183].

$$\tan\alpha_1 = \frac{r_0 \cdot 2\pi \cdot b_1}{b_0 \cdot l_{th0} \cdot z_0} \cdot \sin(\alpha_0) \tag{4.24}$$

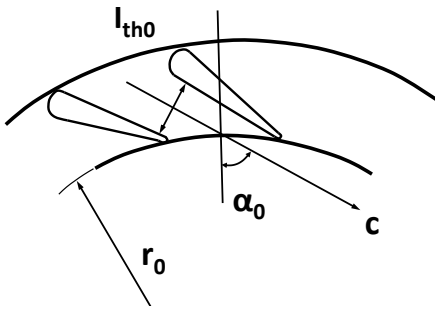

Figure 4.17: Turbine stator vanes geometry according to Watson proposal [183].

Where r_0 is the radius at the exit of stator nozzles, b_1 is the rotor tip width (at rotor inlet), b_0 is the width of the flow passage (at the stator vanes), l_{th0} is the length of the throat formed by two adjacent nozzle stator blades and z_0 is the number of stator vanes as figure 4.17 shows. Parameters l_{th0} and α_0 depend on turbine operative conditions (position of the guide vanes) meanwhile rest of geometrical parameters do not depend on such conditions. Introducing equation 4.24 into 4.22, equation 4.25 is obtained, were again α_0 is assumed to change linearly with blade speed ratio (σ).

$$K_2 = 2 \cdot \left(\left[\frac{r_0 \cdot 2\pi \cdot b_1}{b_0 \cdot l_{th0} \cdot z_0} \cdot \sin\left(c' \cdot \sigma + c''\right) \right] + \sqrt{\frac{K_1}{2}} \cdot \tan \beta_3 \right) \tag{4.25}$$

Using equation 4.25 into equation 4.21, factor K_2, has been fitted to experimental results using metal angle at rotor outlet (β_3), instead of using flow angle at rotor outlet (β_2). From here on, equation 4.21 will be used in a different way if turbine tests were performed at constant Π_T or at constant u^*.

Constant expansion ratio tests

It was necessary to find a relation between σ and term c_0/c_s in equation 4.21 in order to make it functional. c_0 is the circulation velocity (figure 4.11-B) and can be deducted from continuity equation 4.26, where A_0 is the cross area at volute inlet, i.e. at the same azimuthal angle than the tongue;

$$c_0 = \frac{\dot{m} \cdot R \cdot T_0}{p_0 \cdot A_0} \tag{4.26}$$

Inserting equations 4.19 and 4.26 into c_0/c_s and solving for the mass flow;

$$\dot{m} = \left(\frac{c_0}{c_s}\right) \cdot \frac{p_0 \cdot A_0}{R \cdot T_0} \cdot \sqrt{\gamma \cdot R \cdot T_{00}} \cdot \sqrt{\frac{2}{\gamma - 1} \cdot \left(1 - \left[\frac{1}{\Pi_T}\right]^{\frac{\gamma-1}{\gamma}}\right)} \tag{4.27}$$

Remembering equation 4.3 again, equating with equation 4.27 and solving for c_0/c_s;

$$\frac{c_0}{c_s} = \frac{A_{eff} \cdot p_{00} \cdot \gamma \cdot \left[\frac{1}{\Pi_T}\right]^{\frac{1}{\gamma}} \cdot R \cdot T_0}{p_0 \cdot A_0 \cdot \gamma \cdot R \cdot T_{00}} = \frac{A_{eff}}{A_0} \cdot \left(\frac{1}{\Pi_T}\right)^{\frac{1}{\gamma}} \cdot \left(\frac{T_0}{T_{00}}\right)^{\frac{1}{\gamma}} \tag{4.28}$$

Usually the ratio of static to total temperatures is very close to one mainly for high temperatures, so assuming this simplification and substituting equations 4.28 into 4.21, equation 4.29 is obtained;

$$\eta_{ts} = -K_1 \cdot \sigma^2 + K_2 \cdot \sigma \cdot \frac{A_{eff}}{A_0} \cdot \left(\frac{1}{\Pi_T}\right)^{\frac{1}{\gamma}} \tag{4.29}$$

A_{eff} is further expanded as a function of σ and Π_T considering that it comes from equation 4.7. In equation 4.29 is interesting noting that extrapolated efficiency is zero at blade speed ratio (σ) equal to zero and that situation is only possible if rotor tip velocity (u_1) is zero. This results in a turbine efficiency map crossing through the origin at zero blade speed ratio for every constant Π_T curve, as it would be expected. Therefore, equation 4.29 can be used for extrapolating and analysing data measured at constant expansion ratio (SSTT and MSTT). Results obtained from fitting equation 4.29 to measured data and extrapolating are shown in figure 4.19 for the MSTT and figure 4.18 for the SSTT. As it is observed, good accuracy between measured and calculated efficiency is obtained. It is also observed the expected values of σ when extrapolating to zero efficiency values have been obtained.

Figure 4.20 shows fitted stator outlet flow angle ($\alpha 0$) versus blade speed ratio (σ) for turbine MSTT. As it is observed, a smooth variation of flow angle ($\alpha 0$) with turbine operative conditions has been observed.

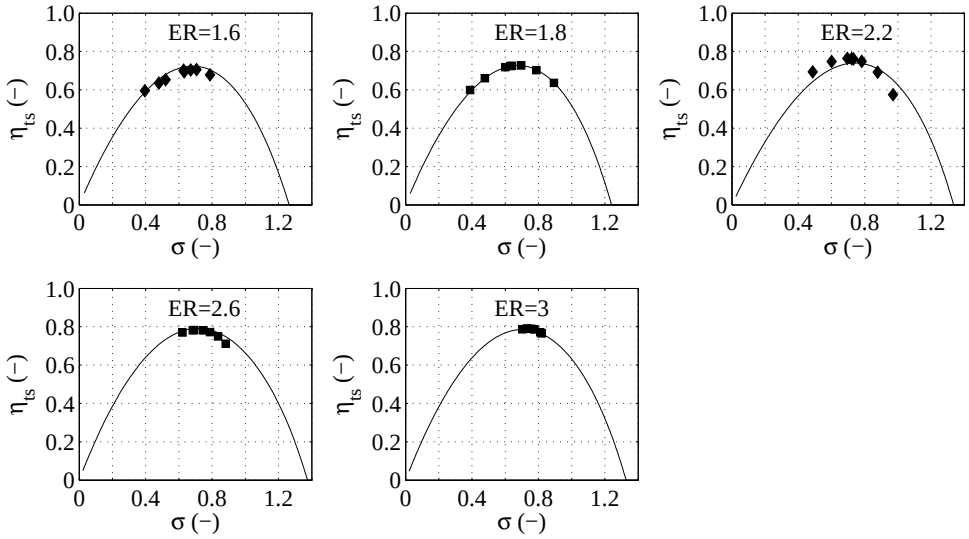

Figure 4.18: Extrapolated efficiency for turbine SSTT.

Constant corrected rotor tip speed tests

It is a frequent practice measuring turbocharger characteristics at constant corrected rotor tip speed rather than at constant Π_T (indeed, it is easier if a turbine brake is not available). Therefore, an expression with that variable as a constant has been also developed. Corrected rotor tip velocity of the turbine is defined as;

$$u_1^* = \frac{u_1}{\sqrt{T_{00}}} \tag{4.30}$$

Combining equation 4.30 with equations 4.4 and 4.19 and solving for $1/\Pi_T$;

$$\left(\frac{1}{\Pi_T}\right) = \left[1 - \frac{u_1^{*2}}{2 \cdot c_p \cdot \sigma^2}\right]^{\frac{\gamma}{\gamma-1}} \tag{4.31}$$

Inserting equation 4.31 into equation 4.28;

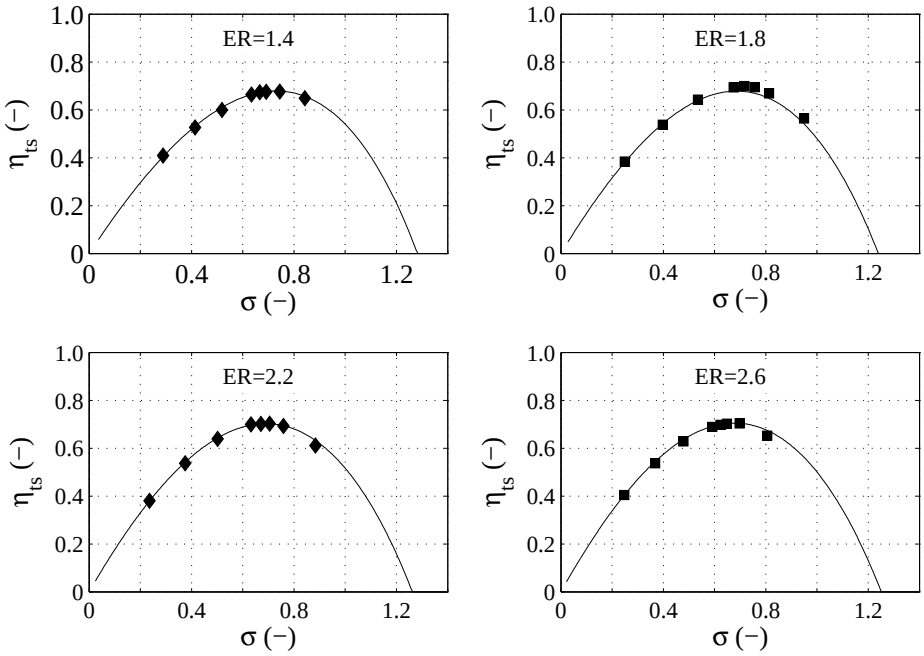

Figure 4.19: Extrapolated efficiency for turbine MSTT.

$$\frac{c_0}{c_s} = \frac{A_{eff}}{A_0} \cdot \left[1 - \frac{(\gamma - 1) \cdot u_1^{*2}}{2 \cdot \gamma \cdot R \cdot \sigma^2}\right]^{\frac{1}{\gamma - 1}} \cdot \left(\frac{T_0}{T_{00}}\right)^{\frac{1}{\gamma}} \tag{4.32}$$

For turbine operative points located in a constant rotational speed line, u_1^* is constant and for cold tests usually T_0/T_{00} exponential expression is very close to one. Therefore, inserting 4.32 in 4.21, turbine efficiency can be expressed just as a function of σ as equation 4.33 shows;

$$\eta_{ts} = -K_1 \cdot \sigma^2 + K_2^* \cdot \left[1 - \frac{K^3}{\sigma^2}\right]^{\frac{1}{\gamma - 1}} \cdot \sigma \tag{4.33}$$

Where K_1 has been already defined in equation 4.22 being K_2^* and K_3 defined as;

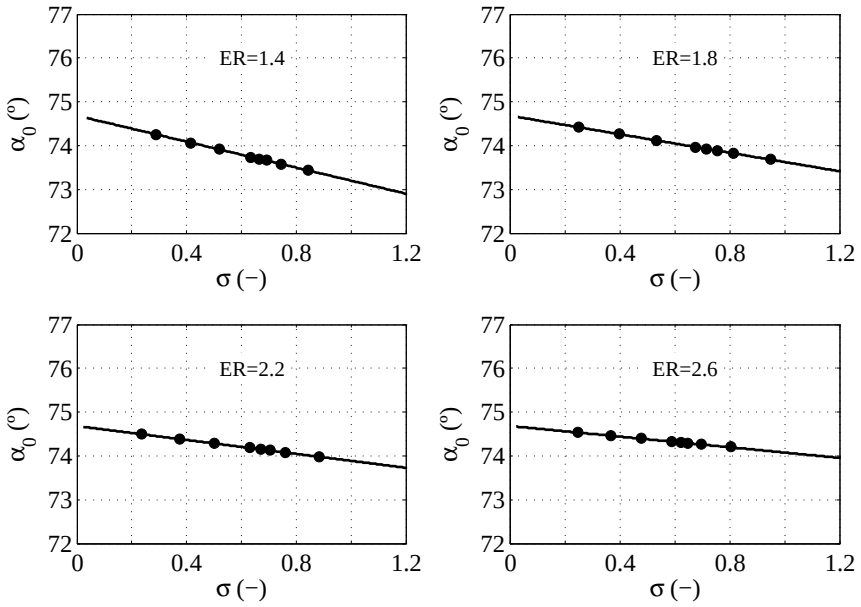

Figure 4.20: Extrapolated stator flow outlet angle (α_0) for turbine MSTT.

$$K_2^* = 2 \cdot \frac{A_{eff}}{A_0} \cdot K_2 \tag{4.34}$$

$$K_3 = \frac{(\gamma - 1) \cdot u_1^{*2}}{2 \cdot \gamma \cdot R} = \frac{u_1^{*2}}{2 \cdot c_p} \tag{4.35}$$

K_2^* expression is further expanded as a function of σ and Π_T considering that A_{eff} comes from equation 4.7 and K_2 from equation 4.25. Equation 4.33 has been applied to turbine data measured at constant u^* and described in previous sections in order to get the efficiency extended map. Results for the extension of these curves are shown (independently for every u_i^*) in figure 4.21 for the LSTT with vaneless stator and in figure 4.22 for the different openings of the T.#1 VGT with nozzles in the stator. Figure 4.23 shows turbine efficiency extrapolation for T.#2 (VGT) and T.#3 (FGT). Good accuracy between measured efficiency and predicted values using equation 4.33 has been observed. In order to get a general view of the entire turbine behaviour, curves

were extrapolated up to efficiency values near zero at both low and high σ limits. As figures 4.21, 4.22 and 4.23 show, zero efficiency (at low σ values) will be obtained at values of σ higher than zero. This is due to u^* is constant and therefore σ zero can only be obtained if c_s becomes infinity i.e. Π_T becomes infinity. The same conclusion can be obtained from the mathematical structure of equation 4.33, i.e. at σ zero it is an undetermined equation.

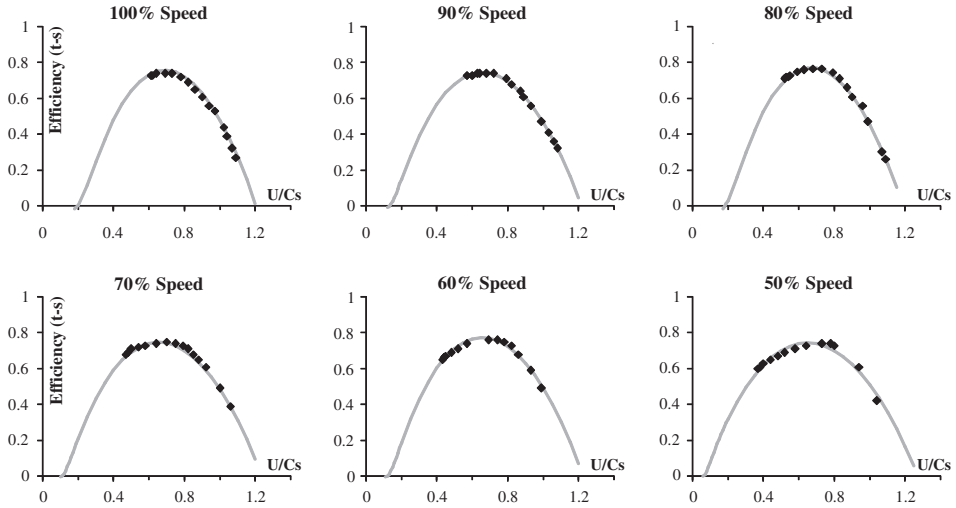

Figure 4.21: Extrapolated efficiency for turbine LSTT

4.3.4.2.1 Chocked flow conditions Equations 4.29 and 4.33 have been based on A_{eff} to A_0 ratio from equation 4.7, for that reason they are only valid for not choked flow in the turbine. Therefore, a new expression has been needed dealing with chocked mass flow parameter ($\dot{m}^*_{crit}$). Indeed c_0 for choked flow conditions can be written as;

$$c_0 = \frac{\dot{m} \cdot R \cdot T_0}{p_0 \cdot A_0} = \frac{\dot{m}^*_{crit} \cdot R \cdot \sqrt{T_0}}{A_0} \cdot \left(\frac{T_0}{T_{00}}\right)^{-\frac{\gamma+1}{2\cdot(\gamma-1)}} \tag{4.36}$$

Where reduced mass flow ($\dot{m}^*_{crit}$) is defined according to stagnation inlet conditions ($\sqrt{T_{00}}$ and p_{00}).

Considering equation 4.36, blade speed ratio definition (equation 4.4) and

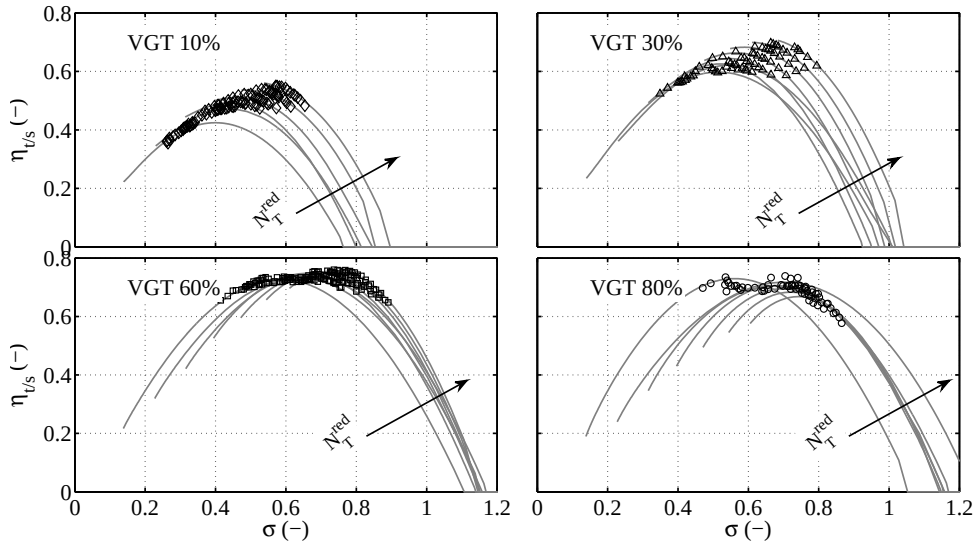

Figure 4.22: Extrapolated efficiency for turbine #1 for different VGT openings

corrected tip speed definition (equation 4.30) and solving for c_0/c_s it is possible to obtain such velocity ratio for choked flow conditions, as equation 4.37 shows.

$$\left(\frac{c_0}{c_s}\right)_{crit} = \frac{\sigma}{u_1} \cdot \frac{\dot{m}^*_{crit} \cdot R \cdot \sqrt{T_0}}{A_0} \cdot \left(\frac{T_0}{T_{00}}\right)^{-\frac{\gamma+1}{2\cdot(\gamma-1)}} = \frac{\dot{m}^*_{crit}}{u_1^*} \cdot \frac{R \cdot \sigma}{A_0} \cdot \left(\frac{T_0}{T_{00}}\right)^{\frac{-1}{\gamma+1}} \tag{4.37}$$

Assuming that usually T_0/T_{00} exponential is close to one, turbine efficiency for choked conditions can be expressed as:

$$(\eta_{ts})_{crit} = -K_1 \cdot \sigma^2 + K_2 \cdot \sigma^2 \cdot \frac{\dot{m}^*_{crit}}{u_1^*} \cdot \frac{R}{A_0} = \sigma^2 \cdot \left(K_2 \cdot \frac{\dot{m}^*_{crit}}{u_1^*} \cdot \frac{R}{A_0} - K_1\right) \tag{4.38}$$

Equation 4.38 has been used to predict and extrapolate decreasing efficiency at σ values beyond choked flow conditions and no discontinuity with equation 4.33 is shown at initial choked flow point.

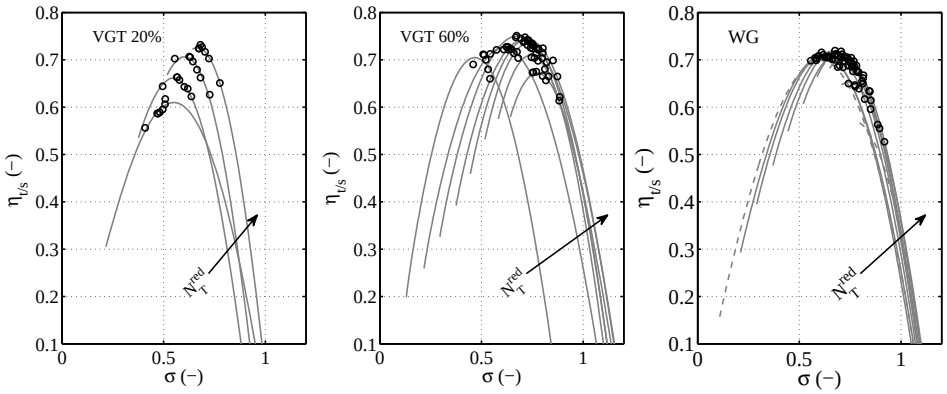

Figure 4.23: Extrapolated efficiency for several turbines. Left: Turbine #2 (VGT 60%), Medium: Turbine #2 (VGT 20%) and Right: Turbine #3

4.3.4.3 Solving procedure

As it was observed before, to calculate turbine extrapolated isentropic efficiency (η_{TS}), extrapolated effective area (A_{eff}) is needed (equations 4.29 and 4.33). Nevertheless that effective area also depends of the extrapolated efficiency (4.7). To solve that difficulty, the iterative procedure shown in figure 4.24 has been proposed.

First of all turbine characteristics (mass flow, expansion ratio and temperatures) are obtained whether from gas stand measurements or a manufacturer chart. Derived parameters like turbine equivalent area (A_{eff}) and blade speed ratio (σ) can be determined from equations 4.3 and 4.4. Geometrical parameters shown in figure 4.11-(c) and in figure 4.17 are measured too since that information will be used to calculate K_1 and K_2 factors (equations 4.22 and 4.25).

Using that information fitting parameters for effective area equation 4.7 are determined for the whole turbine map (in case of a FGT, or for each stator vanes opening in case of a VGT). Fitting parameters k' and k'' are determined using experimental information, those constants take into account flow angle variation at rotor inlet due to turbine operative conditions. Once fitting parameters for the equivalent area expression 4.7 and isentropic efficiency (equations 4.29 and 4.33 via factor K_2 shown in equation 4.25) have been obtained, the iterative procedure begins. It will provide both extended

efficiency and equivalent area, since that information is necessary to simulate turbine instantaneous performance under pulsating flow conditions. It has been proposed assuming a constant initial value of 0.5 for turbine extended efficiency in the whole range of variation for expansion ratio (or blade speed ratio). That extended efficiency (η_{Ts}) is introduced into equation 4.7 to determine extended equivalent area in that range (A_{eff}). That vector of values is introduced now into equation 4.29 or 4.33 to determine new extrapolated efficiency and that information will be sent back to equivalent area function 4.7. Solving loop is repeated until convergence is achieved. Converged solution for turbine equivalent area will be used to calculate extrapolated mass flow.

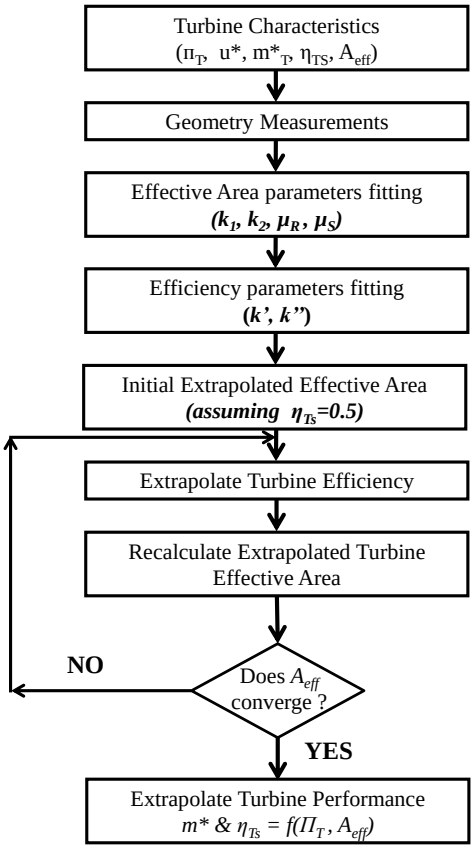

Figure 4.24: Iterative procedure to obtain extrapolated turbine performance maps

4.3.4.4 Extrapolation comparisons

Comparisson with GT-Power extrapolation

Turbocharger almost-adiabatic measurements for turbocharger #2 (obtained with the extended range methodology) have been used to extrapolate turbine performance maps using commercial engine simulation software GT-Power^{TM}. Those results have been compared with extrapolation performed using the methodology presented above. Two stator blades openings have been analysed (one quite closed near to 20% of opening and the other quite opened near to 60% of opening). Figure 4.25 shows mass flow map extrapolation to the same measurements but using GT-Power^{TM} code (on the left) and using the proposed methodology (on the right). As it is observed both methodologies provide accurate results for turbine mass flow inside the range of the experimental measurements. Main discrepancies appear for the most opened turbine position at higher expansion ratios, where extrapolation using GT-Power^{TM} provides an outrageous trend since the reduced mass flow decreases steeply near an expansion ratio of 2.5.

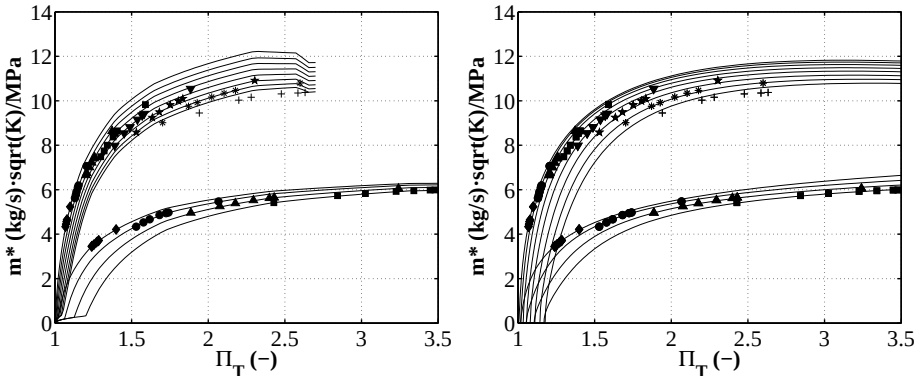

Figure 4.25: Turbine #2 mass flow map extrapolation. Left: using GT-Power^{TM} to extrapolate, Right: using the proposed methodology.

Figure 4.26 shows results for turbine efficiency extrapolations for the 20% opening (top) and 60% opening (bottom) using proposed methodology (black lines) and extrapolation results provided by GT-Power^{TM} (grey lines). As it is observed big discrepancies using GT-Power^{TM} extrapolation method appear mainly for the lowest turbine power point of each iso-speed line. Predicted efficiency is lower than measured and for some cases differences over 10 points

in efficiency have been observed. Proposed methodology provides more accurate results, with negligible differences predicting turbine efficiency as can be observed in figure 4.26 bottom side.

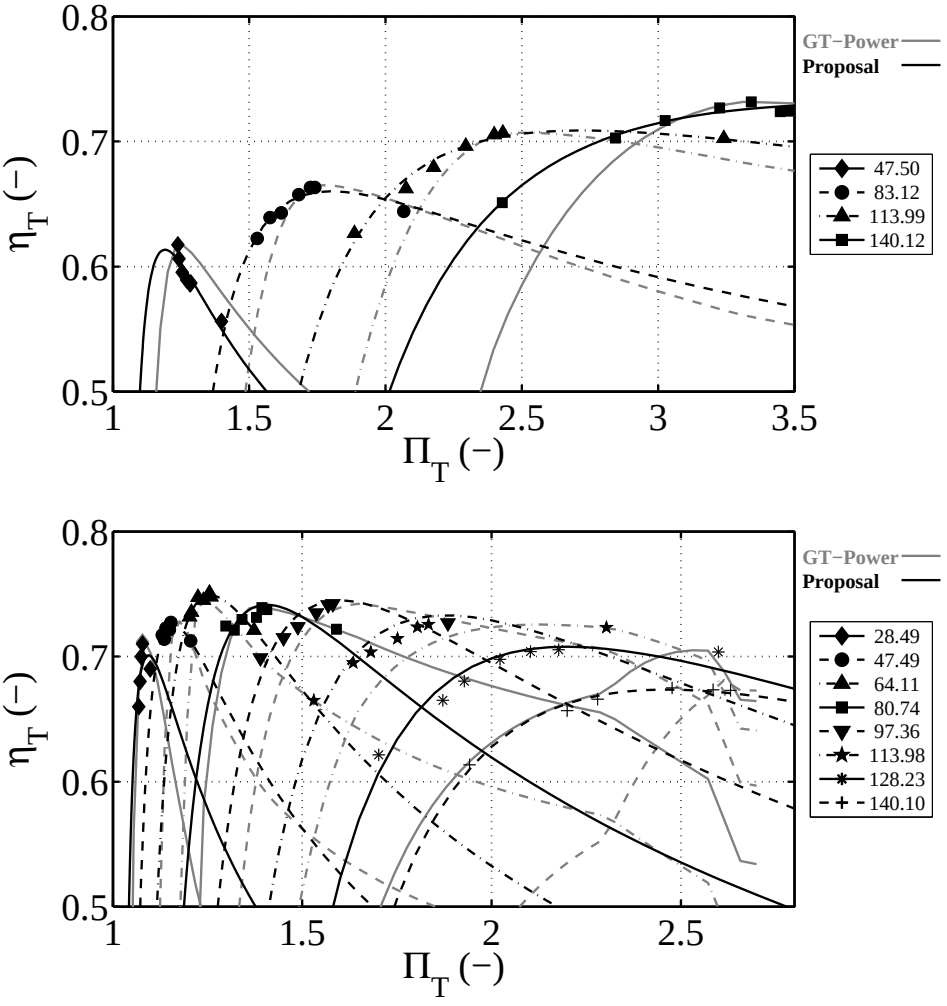

Figure 4.26: Turbine #2 efficiency extrapolation using GT-Power^{TM} and physically based proposed methodology. Top: 20% VGT opening, Bottom: 70% VGT opening. Grey: GT-Power results, Black: Thesis proposal.

Extrapolations using extra data

Due to the fact that compressor wheel acted as a brake for the turbine in

such methodology, information obtained for the turbine only covered a narrow region of the performance map as it is observed in figure 4.27-(left). In this section, importance of getting extra information (in a wider operative range) for turbine extrapolation purposes has been studied. The following off-design testing procedure has been developed.

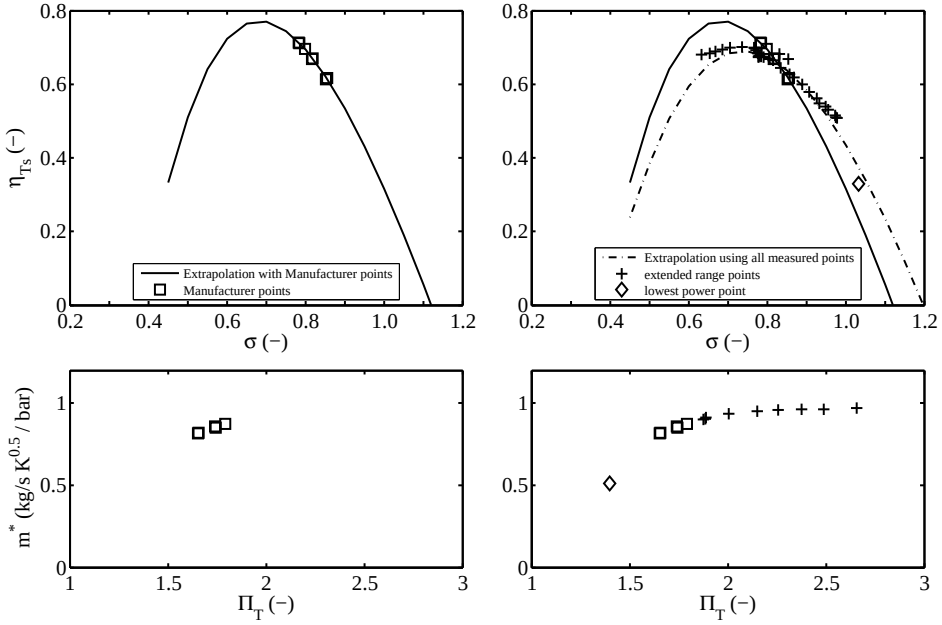

Figure 4.27: Characterization of turbine efficiency and mass flow when it is working under off-design conditions. Left: Manufacturer information. Right: Extended range

Extended Range (Varying compressor inlet pressure)

In order to extend turbine performance maps, compressor line was connected into a closed loop according to the diagram shown in figure 4.28. Compressor inlet and outlet were connected through a pressure pump regulator which allowed for compressor inlet pressure modification. Using that technique turbine map can then be extended to the low power regions (low expansion ratio and mass flow), by testing compressor near the surge limit and once there, reducing inlet pressure below ambient conditions. Using that procedure several testing points can be obtained keeping the same pressure ratio, corrected velocity, and corrected mass flow at the surge limit while turbine points moved to the left on the mass flow map as it is shown in figure 4.27-rigth. In terms of

blade speed ratio, new set of points was placed on the right hand side of manufacturer measured points. In order to cover the other side of turbine efficiency map (points with lower blade speed ratio than those given by manufacturer) the pressure regulator was used to increase compressor inlet pressure. Using that procedure, compressor demanded power substantially increased and turbine was forced to operate with higher expansion ratios (or lower blade speed ratios) and slightly higher mass flows. According to figure 4.27-rigth turbine extrapolated efficiency, when all testing points were available, showed a significant decrease in its maximum efficiency value compared to the prediction given with the narrow range given in manufacturer information.

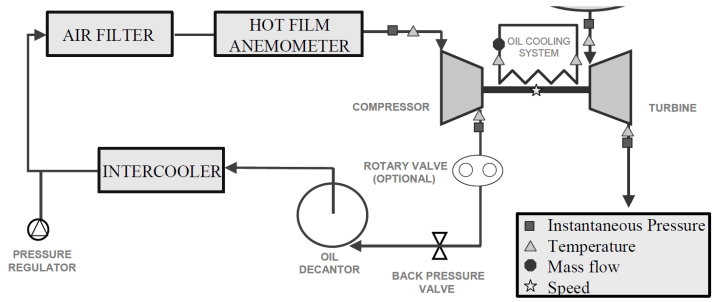

Figure 4.28: Test Rig Scheme for the extended range tests

Extended Range (High Frequency surge)

Another testing methodology allowing getting more information in the low power region consisted of several calibrated orifices placed just at compressor outlet to characterize turbine behaviour while compressor works beyond its surge limit. Due to the small distance between compressor outlet and the calibrated orifice, the appearing high frequency surge allows stabilizing compressor operative conditions and then more testing data in the low power region was obtained.

Lowest Power Point

The latest methodology to characterize turbine behaviour in the off-design region consisted of the measurement of turbine's lowest power point. For that purpose it was necessary removing the physical brake of turbocharger turbine. Compressor wheel and its case were removed, as it is shown in figure 4.29. With that kind of test, expansion ratio and mass flow in the turbine were drastically reduced (as it is observed in the rhombic point of figure 4.27-right). Although

the new point was placed far from conventional turbine points, extrapolation obtained with extended range methodology was enough to well predict so low power conditions.

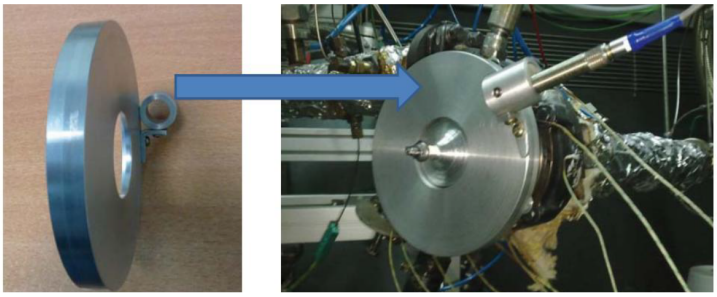

Figure 4.29: Removal of compressor wheel and case

Extrapolation using hot measurements Along this section extrapolation methodology is validated using different kind of almost-adiabatic measurements. For that purpose measurements from turbocharger hot steady characterization (data used in chapter 3 for convective properties determination) have been "adiabatized" and used. The procedure to obtain adiabatic maps presented in section 3.5.1 has been applied to discount heat transfer effects from turbine efficiency. As it is observed in figure 3.28 that has been calculated using only adiabatic points (black squares), "adiabatized" efficiency (grey squares) lied over turbine extrapolated curve what confirms the accuracy of proposed methodology.

4.3.5 Turbine Model Validation

One-dimensional simulation code OpenWAM^{TM} [189] has been used to create the turbocharger model and simulate almost-adiabatic pulsating flow test campaign presented in table 4.2. That model has been presented in figure 4.30, elements composing the turbocharger model are the compressor model (upper line in figure 4.30), the turbine model (bottom line of figure 4.30) and turbocharger shaft connecting turbine and compressor (box in the middle). These are the basic components of an automotive turbocharger. Each one of those elements on the model must be defined with accuracy, since experimental results will be compared to computational ones. Steady flow conditions have been imposed at compressor inlet and also the steady map information

given by the manufacturer. A back-pressure valve has been introduced at compressor outlet to represent the same conditions as it would be in the gas stand. While pulsating flow conditions from test campaign have been imposed at turbine, i.e. instantaneous pressure and temperature at the inlet and just pressure at the outlet. Finally mechanical losses model proposed by Serrano et al. [153, 154] has been introduced at turbocharger shaft. Turbine model in OpenWAM^{TM} has been based on Serrano proposal [148], where turbine has been represented by two nozzles in series with an intermediate reservoir. That model has been connected to pipe elements accounting for acoustic effects. Turbine geometry has been determined according to section 4.3.3.

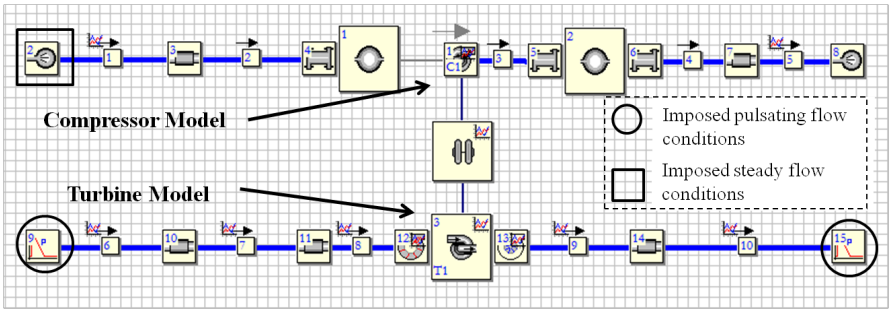

Figure 4.30: OpenWAM^{TM} turbocharger model

Almost-adiabatic pulsating flow tests on the turbine side have been used to validate turbine model described above. In order to do so, experimental incident pressure wave at turbine inlet pipe has been imposed. At turbine outlet pipe, experimental 2nd reflected pressure wave has been imposed (representing what would be reflected from the aftertreatment device). Apart from those data, associated entropy level to both signals has been imposed. Table 4.3 shows imposed parameters needed in turbine model.

Table 4.3: Turbine Model parameters (imposed)

Turbine Inlet Pipe	**Turbine Outlet Pipe**	**Turbine Model**
Incident Pressure Wave	2nd Reflected Pressure Wave	Geometry for acoustics
Entropy Level	Entropy Level	Performance Map

4.3.5.1 Time Domain Validation

Once incident pressure wave (at turbine inlet) and 2nd reflected pressure wave (at turbine outlet) have been imposed to the turbine model, this calculates other pressure components, instantaneous temperatures and mass flows. Three engine operative conditions corresponding to turbocharger #1 have been shown in detail in this section. They correspond to engine conditions of 2000, 3000 and 3500 rpm. In **Annex A**, all tested engine conditions shown on table 4.2 for turbochargers #1, #2 and #3 have been sorted.

Experimental decomposed signal for reflected pressure (at turbine inlet) is compared with the calculated by the turbine model observing good agreement between both signals as it is showed on the left side of figure 4.31. Measured and modelled waves are in phase what ensures that proposed turbine geometrical model is valid for the studied frequencies. In addition good prediction comparing their average values has been observed in figure 4.32 what confirms the accurate results predicting turbine mean parameters that can be observed on figure 4.40.

Accurate estimation in peak and trough values between measured and modelled pulses is observed (for most testing points). Good prediction in peak to peak amplitude has been checked in frequency domain analysis too. Due to the fact that composed pressure wave at turbine inlet is the sum of the incident wave (imposed) and the calculated reflected wave (what showed a good agreement to experimental information), accurate results in composed wave have been observed (right side of figure 4.31). Instantaneous mass flow at turbine inlet pipe has been calculated for the experimental measurements by means of pressure decomposition using continuity equation 4.39.

$$\dot{m}_T^{in} = \rho_T^{in} \cdot u_T^{in} \cdot S_T^{in} \tag{4.39}$$

Where instantaneous density at turbine inlet conditions is evaluated using ideal gas law (equation 4.40) and experimental composed pressure wave and instantaneous temperature.

$$\rho_T^{in} = \frac{p_T^{in}}{R \cdot T_T^{in}} \tag{4.40}$$

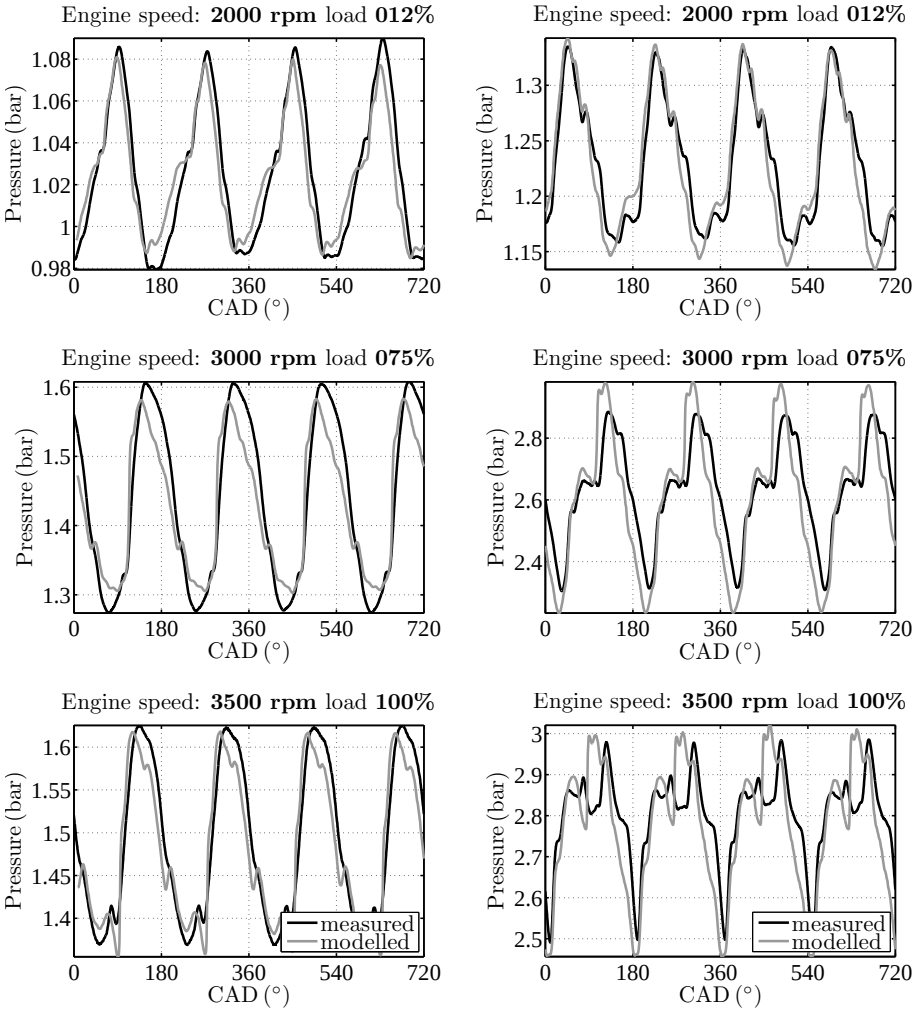

Figure 4.31: Calculated pressure waves at turbine inlet (from turbocharger #1). Left: Reflected wave, Right: Composed wave.

Due to the fact that a rotary valve has been used to generate pulses at the turbine inlet, an isentropic expansion process from the average level of composed pressure and temperature can be assumed to calculate turbine instantaneous temperature.

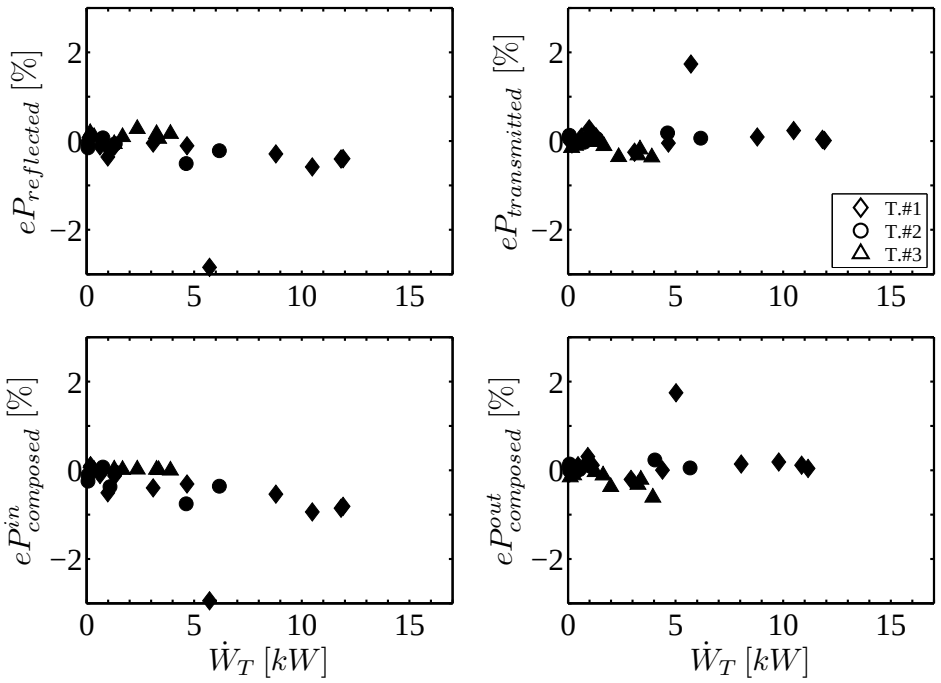

Figure 4.32: Errors predicting turbine waves components for all turbochargers (in average values).

$$T_T^{in} = \bar{T}_T^{in} \cdot \left(\frac{p_T^{in}}{\bar{p}_T^{in}} \right)^{\frac{\gamma-1}{\gamma}} \tag{4.41}$$

Instantaneous velocity at turbine inlet needed in equation 4.39 can be calculated using the entropy level (A_A^{in}), composed pressure wave and incident pressure signals at turbine inlet as it is showed by equation 4.42.

$$u_T^{in} = \frac{2 \cdot A_A^{in}}{\gamma - 1} \cdot \left({p_{comp}^{in}}^{\frac{1-\gamma}{2 \cdot \gamma}} \cdot \left[2 \cdot {p_{inc}^{in}}^{\frac{\gamma-1}{2 \cdot \gamma}} - 1 \right] - 1 \right) \tag{4.42}$$

Where incident pressure at turbine inlet is given by decomposition pressure wave signals technique and entropy level at turbine inlet has been calculated using its definition (equation 4.43).

$$A_A^{in} = \sqrt{\gamma \cdot R \cdot T_T^{in}} \tag{4.43}$$

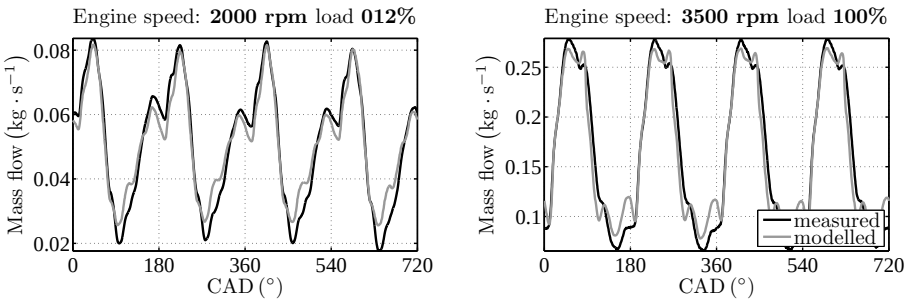

Figure 4.33: Instantaneous mass flow at turbine inlet (calculated) for turbocharger #1. Left: 2000 rpm load 12%. Right: 3500 rpm load 100%.

According to previous equations, modelled instantaneous mass flow at turbine inlet depends on the incident pressure wave (imposed), instantaneous temperature (imposed via entropy level) and composed pressure wave that has been calculated by the model. Differences predicting instantaneous mass flow at turbine inlet are a consequence of errors predicting composed inlet pressure. For example for turbocharger #1, the modelled operative point for 3500 rpm at 100 % load shows a lower composed pressure at turbine inlet in the trough region (as it is observed on the right side of figure 4.31). According to equation 4.42 the lower is the pressure the higher will be flow velocity at turbine inlet and consequently mass flow at the trough region will be higher as it is observed on the right side of figure 4.33. At turbine outlet, experimental second reflected wave has been imposed. Transmitted pressure wave modelling depends on modelled reflected pressure wave (at turbine inlet), turbine geometrical model and turbine map. Composed pressure wave (modelled) at turbine outlet depends on transmitted pressure wave prediction. Accurate composed pressure wave prediction at turbine outlet has been observed in average value. As figure 4.32 shows, errors below 1% for most operative points have been observed, what ensured good prediction in turbine mass flow.

Instantaneous temperature at turbine outlet cannot be determined from the experimental data and the isentropic compression hypothesis as it was done before due to the fact that power has been extracted in the turbine rotor. From the gas stand only an average value for that temperature will

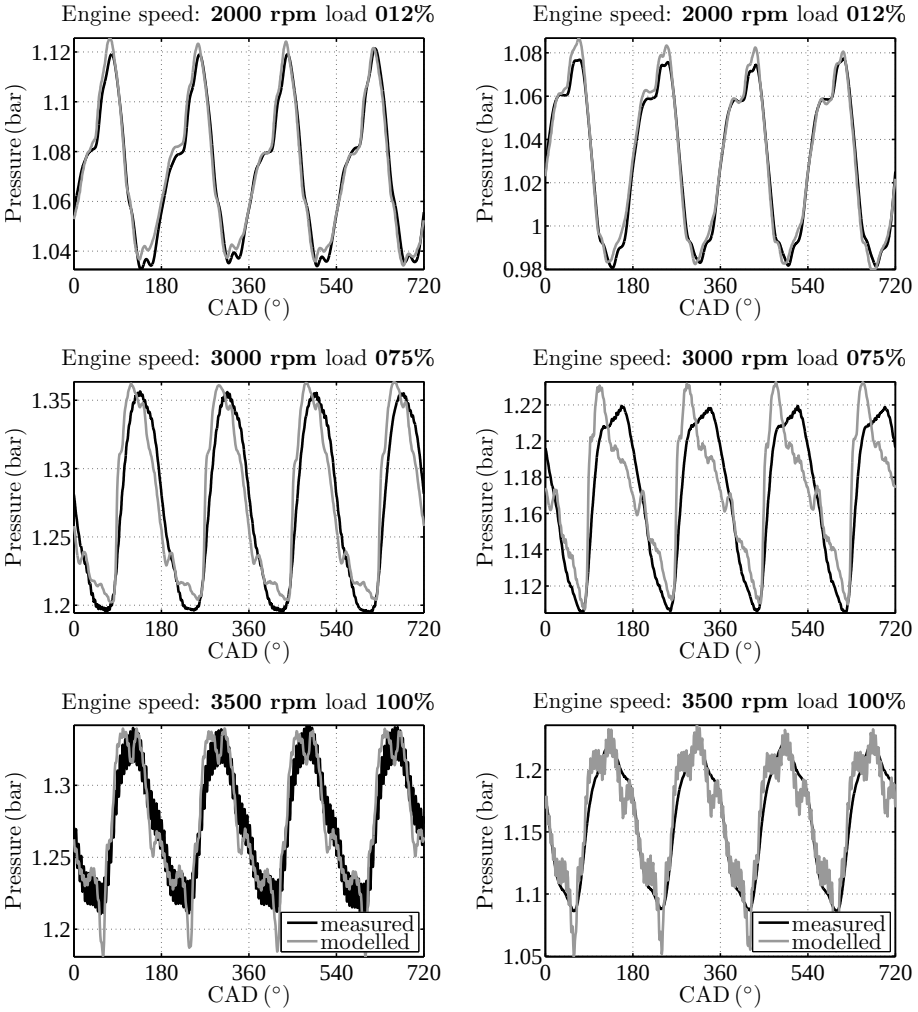

Figure 4.34: Calculated pressure waves at turbine outlet (from turbocharger #1). Left:Transmitted wave, Right: Composed wave.

be available. The average value from the instantaneous modelling has been compared with measured temperatures showing that error in figure 4.40.

Experimentally determined parameters

Errors predicting average values of turbocharger performance are going to be analysed. But first, a description of how those parameters were measured

has been carried out, turbine stages definition is shown on figure 4.35.

Expansion Ratio Its instantaneous value has been determined as the pressure ratio between total conditions at turbine inlet pipe (stage B) and static conditions at turbine outlet pipe (stage G), using piezo-electric instantaneous pressure recording and the average pressure level provided by piezo-resistive pressure sensor (stages A and H).

Reduced Mass Flow This average parameter has been determined as equation 4.44 shows, where mass flow measurement has been performed at turbine outlet pipe (after passing through an intercooler due to temperature restrictions, stage I). Total inlet pressure and temperature have been measured at turbine inlet pipe (stage A), at a distance higher than 10 times turbine inlet diameter to ensure fully developed flow at the measurement node.

$$\dot{m}_T^{red} = \frac{\dot{m}_T \cdot \sqrt{T_{00}}}{P_{00}} \tag{4.44}$$

Efficiency It has been determined as the enthalpy drop between real expansion evolution and the isentropic one. Since specific heat capacity can be considered as the average value from the expansion process, efficiency definition can be done in terms of temperatures as showed by equation 4.9. Those temperatures have been measured experimentally at turbine inlet and outlet pipes (stages A and I).

Modelled parameters

Expansion ratio It has been determined taking pressures between inlet and outlet of the turbine model, corresponding to the first node of turbine inlet port (stage C) and the last node of turbine diffuser (stage F). Nevertheless those values match up with the experimental ones since straight connection pipes with no pressure losses have been considered for modelling purposes. Mean values match up between experimental and modelled results but differences in phase have been observed due to pipe length.

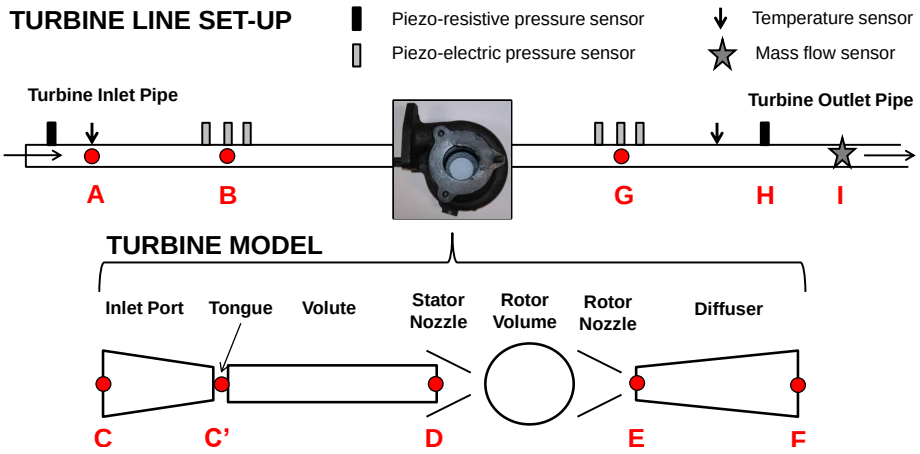

Figure 4.35: Turbine set-up and stages definition.

Reduced mass flow Modelled turbine mass flow can be considered at any position of turbine line set-up or turbine model (figure 4.35). It has been decided to take that value at stator nozzle (stage D) to avoid mass flow accumulations due to pipes volume. Figure 4.36 shows the effect of mass flow accumulation in case other nodes would be used for turbine reduced mass flow and expansion ratio calculations.

- Figure 4.36-(a): Expansion ratio is considered between turbine inlet and outlet pipes (stages B and G), and mass flow at station B.
- Figure 4.36-(b): Expansion ratio is calculated between turbine model inlet/outlet ports (C and F) and mass flow at first node of turbine tongue (stage C') what shows volute mass accumulation.
- Figure 4.36-(c): Expansion ratio between stator/rotor nozzles (stages D and E) and mass flow at last node of turbine volute pipe (stage D), only mass accumulation at turbine rotor is appreciated.

As it is observed in figure 4.36, when inlet/outlet installation pipes are considered (case a), big accumulation effects are observed due to the big volume of the whole system. When only turbine model is considered (case b), accumulation effects are still observed due to inlet port, volute and diffuser volumes. When turbine parameters between stator and rotor nozzles are con-

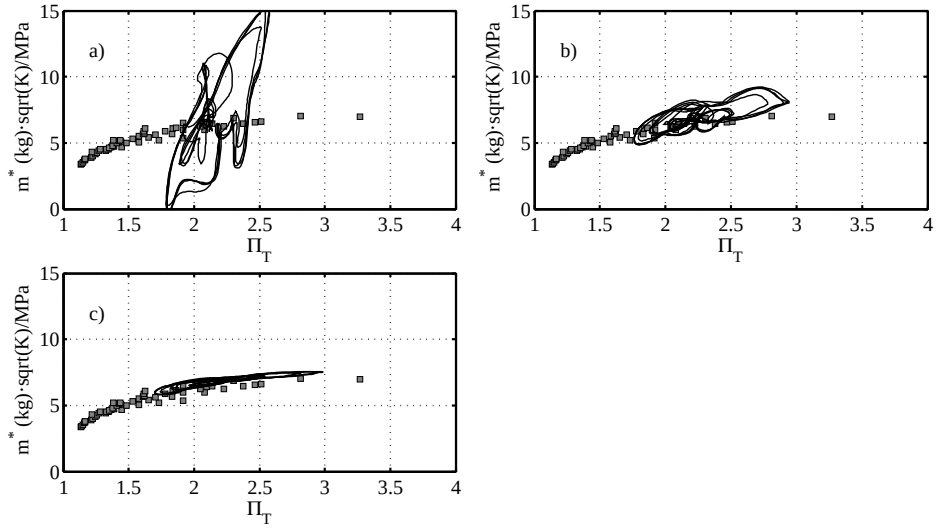

Figure 4.36: Effect of turbine mass flow accumulation (Turbine from turbocharger #3, 2000 rpm, 100% load) calculated between different stages. a) Stages B-G. b) Stages C-F. c) Stages D-E.

sidered (case c), small accumulation effect appears due to the emptying/filling process in rotor volume.

Efficiency It has been determined according to equation 4.9, taking temperatures between inlet/outlet ports of the turbine model (between stages C and F). Turbine efficiency can be also determined interpolating directly into turbine efficiency map using blade speed ratio as it is showed in figure 4.37. Although both methods provide the same average value (figure 4.37-left), instantaneous efficiency changes if it is calculated using inlet/outlet temperatures than interpolating in map. That is due to the phase shift between instantaneous temperatures (figure 4.37-right), caused by pipe lengths. Mean value for efficiency has been averaged with instantaneous mass flow as equation 4.45 shows.

$$\bar{\eta}_T = \frac{\sum \left(\eta_T^{ins} \cdot \dot{m}_T^{ins}\right)}{\sum \dot{m}_T^{ins}} \tag{4.45}$$

Compressor performance

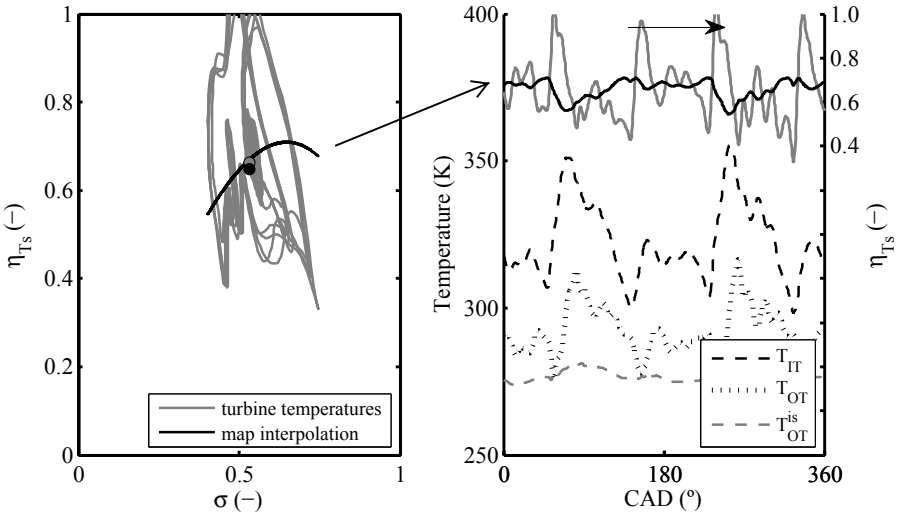

Figure 4.37: Turbine efficiency determination (for turbocharger #3)

Albeit turbine was tested under pulsating inlet flow conditions, compressor (which acted like a brake) worked under steady flow assumption. That was due to oscillations in turbocharger speed caused by pulsating flow on the turbine side were not enough to modify compressor operative point. That can be observed in the small ripple appearing in compressor corrected speed showed in figure 4.38-(a,b). That fluctuation produced small changes in compressor performance (corrected mass flow, compression ratio and outlet temperature prediction) as it is shown in figure 4.38 for turbocharger #3 (engine speed 1500 rpm, load 12%). As it is observed, the small variation in compressor corrected speed (around 200 rpm) produced a negligible variation in compressor corrected mass flow and pressure ratio (figure 4.38-(a)-(b)). Observing compressor performance map, such instantaneous variation was not translated into a locus (black point observed in performance map zoom).

As it is observed in figure 4.39 small differences predicting compressor average parameters, when turbine was modelled under almost-adiabatic pulsating flow conditions, have been observed. That ensured accuracy of compressor and turbine sub-models, as well as the introduced performance maps and mechanical losses model. Errors have been defined according to equation 4.46 for

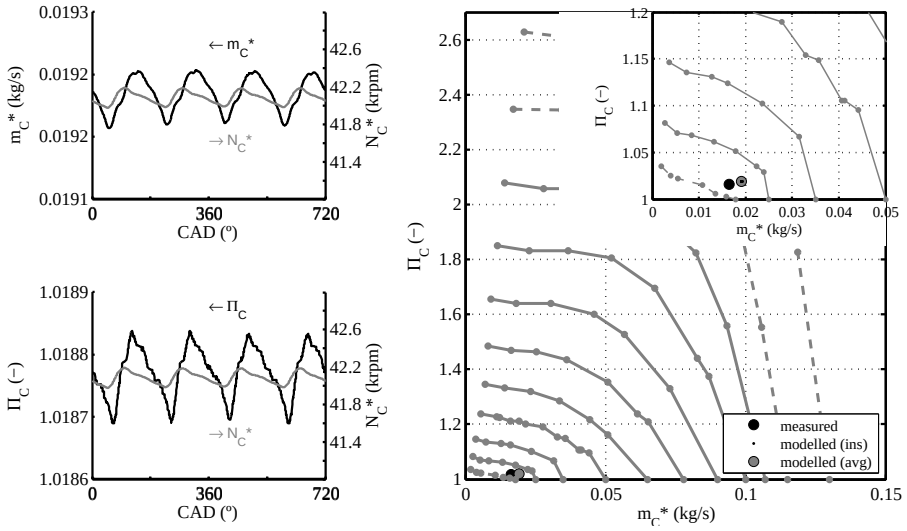

Figure 4.38: Quasi-Steady flow at compressor side (turbocharger #3)

performance parameters and using equation 4.47 for temperature prediction.

$$error = \frac{X^{mod.} - X^{meas.}}{X^{meas.}} \tag{4.46}$$

$$error = X^{mod.} - X^{meas.} \tag{4.47}$$

As it is observed on figure 4.39, turbocharger model predicted compressor main parameters with an error below $\pm 5\%$ for the three turbocharger in most of tested operative conditions with pulsating flow at turbine inlet. Biggest differences were observed for the lowest compressor powers, where errors over 5% in turbocharger speed and mass flow were observed. Those big errors appeared for compressor powers below 500 W , where small differences predicting mechanical losses or turbine mass flow lead to big relative errors in compressor performance.

Nevertheless those errors were not translated into pressure ratio and outlet temperature prediction. In case of compressor outlet temperature differences below ± 2°C for most operative points were observed. Although those

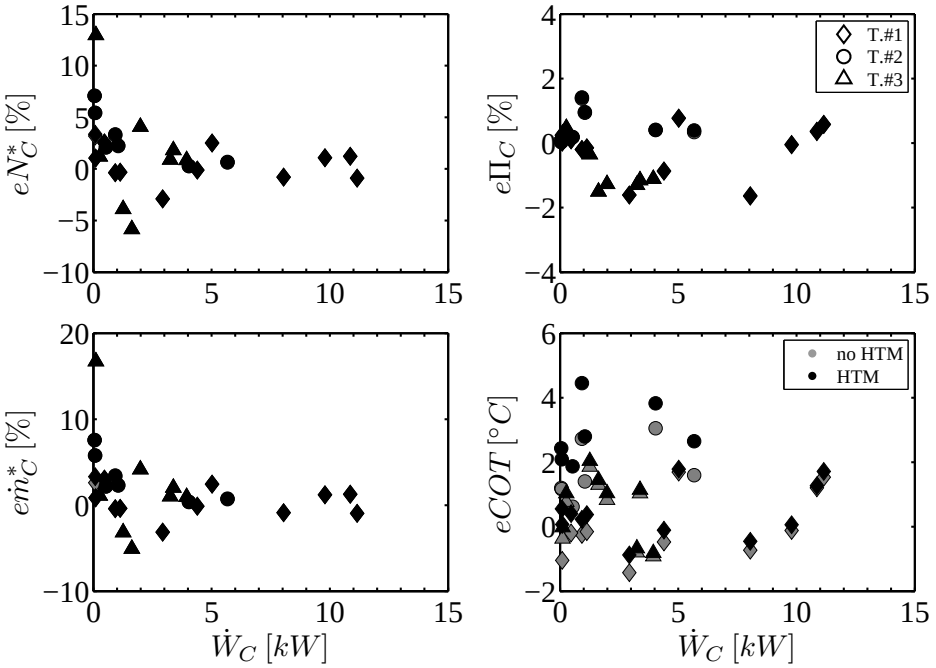

Figure 4.39: Errors in compressor average parameters (for all turbochargers).

measurements were carried out under almost-adiabatic conditions, simulations using HTM were performed too in order to take into account the small heat fluxes between turbocharger components. As it is observed in figure 4.39 turbocharger speed was over-predicted for most of low load operating conditions, what lead to higher prediction in compressor mass flow and compression ratio prediction. That effect was translated into an over-estimation of compressor outlet temperature only due to the modification in compressor operative conditions. When HTM was introduced, compressor received heat fluxes from housing nodes (for low load operative conditions) and so COT was slightly over-predicted compared to results provided without considering heat fluxes. Nevertheless differences between both possibilities were nearly negligible (below 1°C).

Turbine Performance

Figure 4.40 shows error of turbine proposed model predicting main performance parameters. As it is observed ,small errors below the threshold of ±5%

were obtained for most of the operative conditions, from low to high loads and for the three studied turbochargers. Nevertheless errors over 5% appeared for engine operative conditions with a corresponding turbine power below 500 W. Those points corresponded to the lowest turbocharger speeds, expansion ratios and VGT openings. In that region small differences in turbine pressure ratio and VGT position prediction could lead to big errors in mass flow prediction due to the steep slope of turbine mass flow lines in that region.

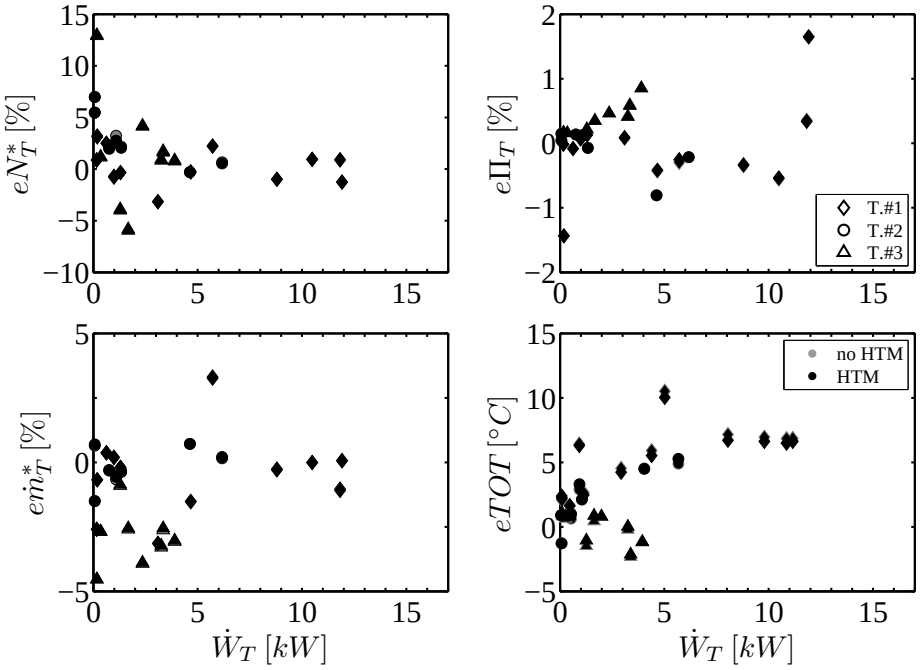

Figure 4.40: Errors in turbine average parameters for all turbochargers.

Average turbine outlet temperature calculated from modelled instantaneous signal showed a good agreement with the experimental measured value as it is observed in figure 4.40 for tested campaign presented in section 4.3.2.2. Although tests were carried out under almost-adiabatic flow conditions, simulations using HTM were performed in order to discount the small heat fluxes. Nevertheless no differences were observed predicting turbine performance parameters using or not HTM as figure 4.40 shows due to the small appearing heat fluxes.

Instantaneous performance over turbine mass flow versus expansion ratio

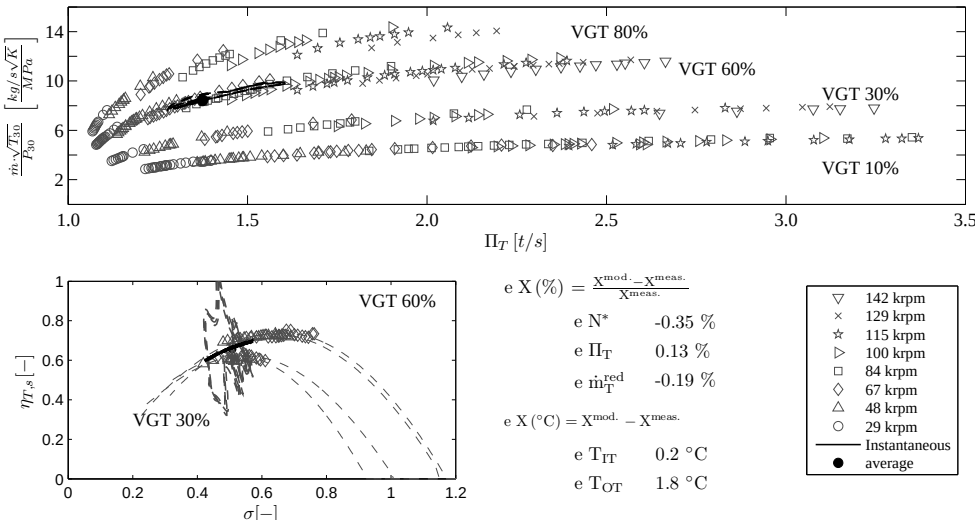

Figure 4.41: Turbine instantaneous performance from turbocharger #1 (engine speed 2000 rpm, load 25%)

map and efficiency versus blade speed ratio map has been represented in figure 4.41 for turbocharger #1. Those conditions correspond to an engine speed of 1500 rpm and a 25% of load, measured under almost-adiabatic pulsating flow conditions. In that figure each symbol represents a different turbine corrected speed. Averaged values for main turbine parameters have been showed for the experimental and modelled signals and the corresponding modelling error, as it is observed small errors (below 1%) were obtained for most of the analysed parameters. In order to make that representation clearer only almost-adiabatic measurements were shown in turbine mass flow map, although computational simulations used extrapolations presented in figure 4.22. Instantaneous variations of reduced mass flow and expansion ratio were calculated between stator and rotor nozzles (stages D and E in figure 4.35) and they are observed in the loop showed over turbine mass flow map. As it is observed there was practically no error between the experimentally measured reduced mass flow and the average value from instantaneously modelled parameters. Turbine efficiency map contains steady-flow adiabatic measurements and corresponding extrapolation curves for the nearest turbine VGT openings and corrected speeds. Instantaneous modelling for turbine adiabatic efficiency (interpolations inside characteristic charts) was showed in figure 4.41 (in solid black line) as well as the instantaneous turbine diabatic efficiency (in dashed grey) calculated by

means of instantaneous temperatures between turbine inlet and outlet. Big oscillations in turbine diabatic efficiency (calculated using tempeatures between stages C and F of figure 4.35) appeared due to the phase shift between both temperature signals.

4.3.5.2 Frequency Domain Validation

Besides the time domain analysis presented above for the turbine, an analysis in the frequency domain has been also done for the experimental and modelling pressure signals on the turbine side. Reflected pressure wave (at turbine inlet) and transmitted pressure wave (at turbine outlet) have been analysed in the frequency domain since those signals are calculated by turbine model. Fast Fourier Transform (FFT) has been applied to those signals to analyse their sound pressure levels (SPL) according to equation 4.48.

$$\mathrm{SPL} = 20 \cdot \log_{10}\left(\frac{\tilde{p}}{p_{\mathrm{ref}}}\right) \tag{4.48}$$

Where 20 μPa has been chosen as the reference pressure (p_{ref}) since it is the threshold of human hearing, meanwhile $\tilde{p}$ is the FFT of the analysed pressure signal. Sound pressure level spectrum signal for both experimentally measured and modelled signals have been shown versus the frequency axis. Frequencies corresponding to the 2nd, 4th, 6th, 8th, 10th and 12th engine orders have been marked with vertical dashed lines in figure 4.42. Those harmonics have been determined using equation 4.49.

$$f = \frac{n}{60} \cdot Z \tag{4.49}$$

Where n denotes engine speed (in rpm) and Z the engine order.

Left side of figure 4.42 shows comparison between SPL from measured reflected pressure wave (turbine inlet) of turbocharger #1 and that signal calculated using turbine model introduced in OpenWAM$^{\mathrm{TM}}$. As it is observed best prediction is obtained for the 2nd engine order for reflected pressure wave, where small differences, below the threshold of $\pm$ 5 dB have been obtained for the three operative conditions showed. Figure 4.43 shows errors in SPL prediction for the three tested turbochargers (T#1, T#2 and T#3) in several

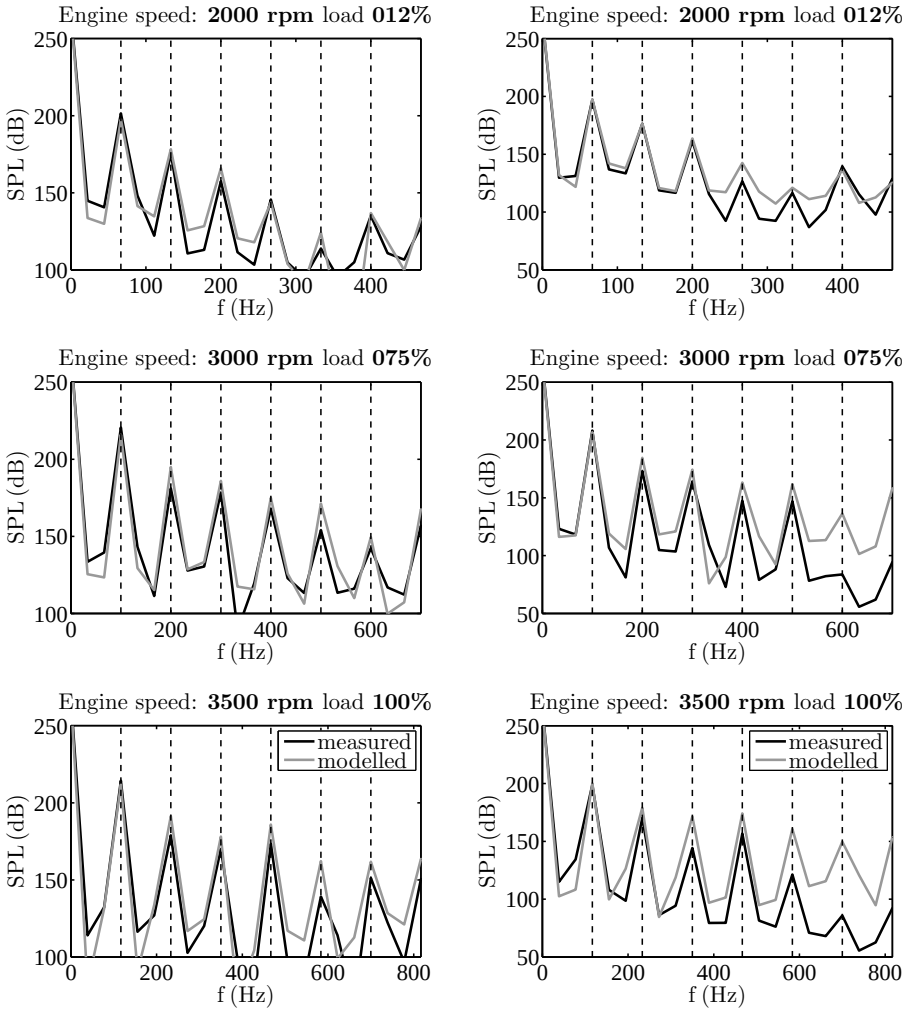

Figure 4.42: Frequency analysis of calculated pressure waves (from turbocharger #1). Left:Reflected wave, Right: Transmitted wave.

operative conditions, ranging from low to high loads. Peak differences between measured and predicted SPL for the engine frequencies corresponding to the 2nd, 4th and 6th engine orders have been computed. Errors in peaks have been defined according to expresion 4.50.

$$eSPL = SPL^{meas.} - SPL^{mod.} \tag{4.50}$$

As it is observed on the right side of figure 4.43, most of tested points (80%) are predicted with an error below ± 2.5% in SPL for 2nd engine order. For the 4th engine order, best results are obtained for the lowest engine speeds (1500 rpm and 2000rpm), where all tested points lied in the ± 5dB threshold corresponding to 75% of tested points showed an error below the ± 2.5% in SPL prediction. For highest engine speeds (3000 rpm and 3500 rpm) model over-predicts sound pressure level. For higher engine orders (6th, 8th,10th and 12th) bigger errors and dispersion in SPL prediction have been observed. Nevertheless those differences are not critical for engine air management prediction, being the lowest orders (2nd and 4th) the most relevant with the noise radiated from the engine.

Right side of figure 4.42 shows frequency analysis for same testing points but for transmitted pressure wave. As it is observed, best results are obtained for 2nd engine speed order for three operative conditions in figure 4.42 and for most testing points as it is showed in figure 4.43. Turbocharger T#3 shows worst results for 2nd engine order in transmitted pressure wave, but that turbine was the smallest one and with a large diffuser at turbine outlet (due to the waste-gate valve). As the right side of figure 4.43 shows, best results are observed for the 2nd and 4th engine orders, mainly for the lowest engine speeds (1500 rpm and 2000 rpm), where 75% of tested operative conditions are reproduced with an error lower than ± 2.5% in SPL for transmitted pressure wave.

Results provided by turbine acoustic model are satisfactory for most tested operative conditions, taking into account that turbine proposed geometrical model is purely 0-D and 1-D. And it tries to reproduce the complex problem of pulsating flow through the radial turbine, which is clearly 3-D.

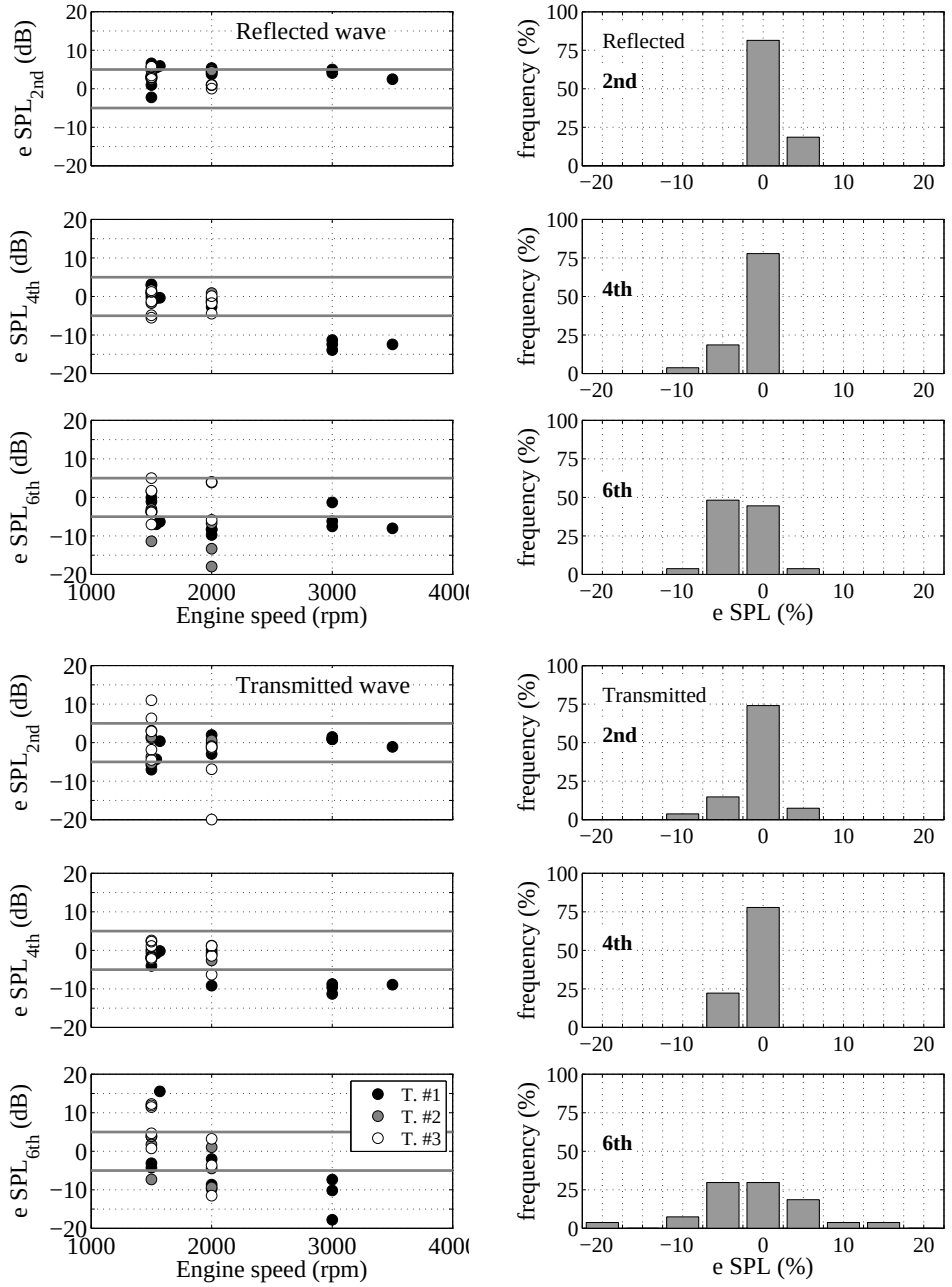

Figure 4.43: Turbine Sound Pressure Level modelling prediction. Top part: Reflected wave, Bottom part: Transmitted wave

4.4 Summary

In the present chapter compressor and turbine models accounting for acoustic effects have been presented. Both models have been designed using 0-D and 1-D elements such as volumes, straight and tapered pipes in order to be used coupled to any engine commercial code. In this Thesis 1-D gas-dynamic simulation code OpenWAM^{TM} has been used to validate turbocharger model. Turbocharger isentropic performance maps have been also provided to both models to be used in a quasi-steady way. In order to validate both models, a series of pulsating flow tests on the compressor side first and later on the turbine side have been carried out. Turbochargers have been tested under almost-adiabatic flow conditions to isolate pulsating phenomena from heat transfer problem. Several engine operative conditions have been reproduced in the turbocharger test rig from CMT-Motores Térmicos. Turbocharger characterization under a wide range of operative conditions was able using such experimental facility. A rotary valve was installed at the compressor outlet to reproduce what would be engine intake valves. Those tests have been used in compressor acoustic model validation under pulsating flow conditions. Later the rotary valve was mounted on the turbine inlet line to reproduce what would be engine exhaust valves. That information has been used in turbine acoustic model validation. That procedure allowed decoupling pulsating phenomena from turbine and compressor being only one of turbocharger elements tested under pulsating flow conditions at the same time, meanwhile the other worked under steady flow conditions. Long straight pipes were installed at compressor and turbine inlet and outlet ports to ensure completely-developed flow on the measurement section. An array of three piezo-electric pressure sensors was installed at inlet/outlet pipes of the element working under pulsating flow conditions allowing pressure wave decomposition using a beam-forming technique.

On the first section, compressor model has been validated imposing measured signals for the 2nd reflected pressure wave (at compressor inlet) and incident pressure wave (at compressor outlet). Transmitted and reflected pressure waves have been calculated using compressor model integrated in OpenWAM^{TM} software. Good agreement with corresponding measured signals was observed in both time and frequency domain. Sound pressure level (SPL) prediction at compressor inlet and outlet was satisfactory showing most tested points an error in the threshold of ± 5 dB.

On the second section, turbine geometrical model accounting for acoustic effects has been proposed and validated. But first an extrapolation methodology has been presented allowing turbine operative maps extension for any given pressure ratio. Turbine extrapolated maps are necessary to carry out pulsating flow simulations, since turbine operative point moves instantaneously far from the steady state measurement range.

Extension of turbine mass flow parameter has been based on the definition of sub-critical mass flow through a single isentropic nozzle. A function to extend turbine effective area has been needed to extrapolate mass flow parameter. That equation has been obtained from kinetic energy balance and mass conservation equations. That expression depended on turbine geometry (stator and rotor areas, wheel diameters and metal angles). But also was dependent on turbine operative parameters (expansion ratio, blade speed ratio and isentropic efficiency). Some fitting parameters have been introduced to compensate main flow assumptions. Extension of turbine isentropic efficiency has been based on Euler's turbomachinery equation, that depended on turbine operative conditions (blade speed ratio and effective area). Due to the fact that mass flow parameter and turbine isentropic efficiency equations depended on each other, an iterative process to get turbine extrapolated performance has been necessary. Several turbines from the largest ones used in truck applications to the smallest ones used in downsized engines have been extrapolated using the proposed model. Good results in turbine extrapolated maps have been obtained for all tested turbines, both for the externally measured turbines and for the three analysed turbines for heat transfer model validation. Proposed model showed better results extending turbine maps than obtained using GT-Power^{TM} software that is the most widespread engine simulation code. Biggest differences were observed mainly for the lowest turbocharger speeds and for turbine efficiency extrapolation. The narrow measurement region on turbine performance maps is due to manufacturer experimental techniques, since turbine maps have been traditionally measured coupled to the compressor which acts like a brake. In those arrangements, measurements inside compressor stable region (from surge to choke) are only available. Several experiments on the gas stand have been described in order to measure turbine performance far from that traditional region. It has been showed how the closed loop technique on the compressor line provided the widest operative range, mainly on the top peak efficiency region where that data showed to be useful obtaining reasonable values for turbine extrapolated efficiency.

Turbine geometrical model to account for acoustics has been validated using pulsating flow measurements on the turbine side for the three studied turbochargers. Validation has been carried out imposing incident pressure wave (at turbine inlet) and 2nd reflected wave (at turbine outlet) calculating OpenWAM^{TM} code the other two components. Calculated reflected and transmitted pressure waves have been compared to the experimentally measured, showing good agreement in shape, shift, peak and trough values. Nevertheless small differences in shift have been observed for the highest engine speed mainly due to the main assumption than turbine volute behaved like a pipe with no mass losses. Mass flow accumulation effects on the turbine rotor have been analysed too, as well as the validation of the quasi-steady approach for turbine efficiency and mass flow maps.

References

[12] C. Arcoumanis, I. Hakeem, L. Khezzar, R.F. Martinez-Botas, and N. Baines. "Performance of a mixed flow turbocharger turbine under pulsating flow conditions". In: *ASME International gas turbine and aeroengine congress and exposition* 95-GT-210 (1995) (cit. on p. 162).

[13] N. Baines, H. Mousthapa, M. Zelesky, and D. Japikse. *Axial and Radial Turbines*. ISBN 0 933283 12 0. Concepts NREC, Vermont, 2003 (cit. on pp. 144, 164, 173).

[16] J. Benajes, E. Reyes, and J.M. Luján. "Modelling study of the scavenging process in a turbocharged diesel engine with modified valve operation". In: *Proc. IMechE, Part C: Journal of Mechanical Engineering Science* 210(4) (1996), pp. 383–393. DOI: 10.1243/PIME_PROC_1996_210_210_02 (cit. on p. 145).

[17] R.S. Benson. *The thermodynamics and gas dynamics of internal-combustion engines*. Vol. 1. Clarendon Press Oxford, 1982 (cit. on pp. 160, 163).

[32] H. Chen and D. Winterbone. "A method to predict performance of vaneless radial turbine under steady and unsteady flow conditions". In: *Proceedings of the Institution of Mechanical Engineers, Turbocharging and Turbochargers* (1990), pp. 13–22 (cit. on pp. 59, 61, 159).

[34] D.C. Clay and S.W. Moch. "Development of a new test facility for evaluation of turbocharger noise emissions". In: *IMechE Conference Transactions*. 7th International Conference on Turbochargers and Turbocharging C602/032/2002. 2002, pp 129–141 (cit. on p. 145).

[37] A.W. Costall, R.M. McDavid, R.F. Martinez-Botas, and N.C. Baines. "Pulse performance modelling of a twin-entry turbocharger turbine under full and unequal admission". In: *ASME paper* GT2009-59406 (2009) (cit. on pp. 59, 61–63, 159).

[41] A. Dale. "Radial Vaneless Turbocharger Turbine Performance". PhD thesis. Imperial College, London, 1990 (cit. on pp. 59, 64, 162).

[63] S.M. Futral and C.A. Wasserbauer. *Off-design performance prediction with experimental verification for a radial-inflow turbine.* Tech. rep. TN D-2621. NASA, 1965 (cit. on pp. 162, 168–170, 172).

[66] J. Galindo, J.M. Luján, J.R. Serrano, V. Dolz, and S. Guilain. "Design of an exhaust manifold to improve transient performance of a high-speed turbocharged Diesel engine". In: *Experimental Thermal and Fluid Science* 28.8 (2004), pp. 863–875 (cit. on p. 145).

[70] J. Galindo, J.R. Serrano, C. Guardiola, and C. Cervelló. "Surge limit definition in a specific test bench for the characterization of automotive turbochargers". In: *Experimental Thermal and Fluid Science* 30 (2006), pp. 449–462 (cit. on pp. 57, 162, 163).

[82] J. Heywood. *Internal Combustion Engine Fundamentals.* Ed. by ISBN 007 028637 X. McGraw-Hill Science/Engineering/Math, 1988 (cit. on pp. 66, 163).

[93] T. Katrasnik. "Hybridization of powertrain and downsizing of IC engine - a way to reduce fuel consumption and pollutant emissions - Part 1". In: *Energy Conversion and Management* 48 (2007), pp. 1411–23 (cit. on p. 162).

[94] T. Katrasnik. "Hybridization of powertrain and downsizing of IC engine - analysis and parametric study - Part 2". In: *Energy Conversion and Management* 48 (2007), pp. 1424–34 (cit. on p. 162).

[105] G. Martin, V. Talon, P. Higelin, A. Charlet, and C. Caillol. "Implementing Turbomachinery Physics into Data Map-Based Turbocharger Models". In: *SAE Technical Paper* 2009-01-0310 (2009) (cit. on pp. 50, 51, 160).

[106] R. Martinez-Botas. "Opportunities and challenges. Turbocharger trends and requirements forum". In: *Annex in the proceedings of the 8th International conference on turbochargers and turbocharging, London 15-18 May.* 2006 (cit. on pp. 69, 161, 162, 167, 170).

[112] M. Muñoz and F Payri. *Motores de Combustión Interna Alternativos.* ISBN 84 86043 01 9. Madrid: Sección de Publicaciones de la E.T.S. de Ingenieros Industriales Fundación General - U.P.M, 1989 (cit. on pp. 68, 164, 166).

[118] B. Nikpour. "Measurement of the performance of a radial inflow turbine". PhD thesis. Manchester, UK: UMIST, 1990 (cit. on p. 162).

[125] F. Payri, J. Benajes, J. Galindo, and J.R. Serrano. "Modelling of turbocharged diesel engines in transient operation: Part 2: wave action models for calculating the transient operation in a high speed direct injection engine". In: *Proceedings of the Institution of Mechanical Engineers, Part D: Jour* 216 (2002), pp. 479–493 (cit. on pp. 72, 145).

[126] F Payri, J. Benajes, J. Jullien, and Q. Duan. "Non-steady flow behaviour of a supercharger turbine". In: *Proceedings of the Third EAEC International Conference, pp. 347-351, Strassbourg.* 1991 (cit. on pp. 59, 159).

[127] F. Payri, J. Benajes, and M. Reyes. "Modelling of supercharger turbines in internal-combustion engines". In: *Journal of Mechanical Science* 38.8-9 (1996), pp. 835–869 (cit. on pp. 59, 60, 159, 160, 170).

[130] F. Payri, E. Reyes, and J. Galindo. "Analysis and modelling of the fluid-dynamic effects in branched exhaust junctions of ICE". In: *International Journal for Gas Turbine and Power: Transactions of the ASME* 123 (2001), pp. 197–203. DOI: 10.1115/1.1339988 (cit. on p. 145).

[131] F. Payri, J.R. Serrano, P. Fajardo, M.A. Reyes-Belmonte, and R. Gonzalo-Belles. "A physically based methodology to extrapolate performance maps of radial turbines". In: *Energy Conversion and Management* 55 (2012), pp. 149–163 (cit. on pp. 166, 233, 234, 260).

[133] G. Piñero, L. Vergara, and J.M. Desantes. "Estimation of velocity fluctuation in internal combustion engine exhaust systems through beam forming techniques". In: *Measurement Science and Technology* 11 (2000), pp. 1585–1595 (cit. on pp. 146, 158).

[143] T. Sanchez, A. Muñoz, and F. Jiménez-Espadafor. *Turbomáquinas Térmicas.* Chapter 11, Section 7.4. ISBN 84-9756-185-6. Editorial Síntesis, 2004 (cit. on pp. 164–166, 173).

[148] J.R. Serrano, F.J. Arnau, V. Dolz, A. Tiseira, and C. Cervelló. "A model of turbocharger radial turbines appropriate to be used in zero- and one-dimensional gas dynamics codes for internal combustion engines modelling". In: *Energy Conversion and Management* 49 (2008), pp. 3729–3745 (cit. on pp. 59, 63, 160, 170, 189, 215, 216, 231, 234, 271, 275).

[153] J.R. Serrano, P. Olmeda, A. Tiseira, L.M. García-Cuevas, and A. Lefebvre. "Importance of mechanical losses modeling in the performance prediction of radial turbochargers under pulsating flow conditions". In: *SAE Int. J. Engines 6(2)* 6(2) (2013), pp. 729–738. DOI: 10.4271/2013-01-0577 (cit. on pp. 8, 46, 48, 49, 93, 132, 157, 189, 216, 217, 255).

[154] J.R. Serrano, P. Olmeda, A. Tiseira, L.M. García-Cuevas, and A. Lefebvre. "Theoretical and experimental study of mechanical losses in automotive turbochargers". In: *Energy* 55 (2013), pp. 888 –898 (cit. on pp. 8, 46, 48, 49, 93, 132, 157, 189, 216, 217, 223, 233, 255, 271).

[167] S. Szymko. "The development of an eddy current dynamometer for evaluation of steady and pulsating turbocharger turbine performance". PhD thesis. Imperial College, London, UK, 2006 (cit. on p. 162).

[170] A. Torregrosa, F.J. Arnau, P. Piqueras, and M.A. Reyes-Belmonte. "Acoustic One-Dimensional Compressor Model for Integration in a Gas-Dynamic Code". In: *SAE Technical Paper* 2012-01-0834 (2012) (cit. on pp. 145, 149).

[172] A. Torregrosa, J. Galindo, J.R. Serrano, and A. Tiseira. "A procedure for the unsteady characterization of turbochargers in reciprocating internal combustion engines". In: *The 4th International Symposium on Fluid Machinery and Fluid Engineering, November 24-27, 2008, Beijing, China*. 2008 (cit. on pp. 55, 56, 72, 149, 274).

[175] *Turbocharger Gas Stand Test Code (J1826)*. SAE International Surface Vehicle Recommended Practice, 1995-03-01 (cit. on p. 146).

[182] N. Watson. "Transient performance simulation and analysis of turbocharged Diesel engines". In: *SAE Technical Paper 810338*. 1981. DOI: 10.4271/810338 (cit. on p. 145).

[183] N. Watson and S. Janota. *Turbocharging the internal combustion engine*. London: MacMillan Publishers Ltd, 1982 (cit. on pp. 23, 30, 58, 59, 69, 159, 163, 164, 173–175).

[184] N. Watson and M. Marzouk. "A Non-Linear Digital Simulation of Turbocharged Diesel Engines Under Transient Conditions". In: *SAE Technical Paper* 770123 (1977). DOI: 10.4271/770123 (cit. on p. 145).

[187] D.E. Winterbone, B. Nikpour, and G.I. Alexander. "Measurement of the performance of a radial inflow turbine in conditional steady and unsteady flow". In: *Proceedings of the 4th international conference on turbocharging and turbochargers. IMechE* C405/015 (1990), pp. 153–62 (cit. on p. 162).

[188] D.E. Winterbone and M. Yoshitomi. "The accuracy of calculating wave action in engine intake manifolds". In: *SAE Technical Paper 900677*. 1990 (cit. on p. 162).

[189] *www.Openwam.org*. OpenWAM, CMT-Motores Térmicos; Universitat Politècnica de València (UPV). 2012 (cit. on pp. 7, 152, 188, 214, 218, 228, 253).

[193] K. Zinner. *Supercharging of Internal Combustion Engines*. ISBN 3 540 085440. Springer-Verlag New York, 1978 (cit. on pp. 68, 164, 168).

Chapter 5

Turbocharger Global Model Integration and Analysis

Contents

5.1 Introduction

In previous sections, physical phenomena appearing during turbocharger working operation have been studied. In order to simplify the complex problem of turbocharger simulation's, modelling problem was split into several sub-models. Those sub-models were developed and validated using ad-hoc designed experiments, and they showed good accuracy reproducing gas stand measurements. In the present chapter, those turbocharger sub-models will be used instantaneously in a quasi-steady way to reproduce conditions of hot pulsating flow on the turbine side. Those conditions are more likely to occur when the turbocharger is connected to the ICE. To demonstrate the robustness of the turbocharger proposed model, no corrector terms have been used to account for heat transfer, mechanical losses or pulsating flow [103] although it has been the usual trend in turbocharger modelling. Importance of those sub-models will be studied modelling turbocharger performance under pulsating hot flow tests.

5.2 Integration into a Global Model

Turbocharger sub-models accounting for heat transfer, mechanical losses and turbine extrapolation maps have been developed and validated using steady flow information. Nevertheless they will be applied instantaneously in a quasi-steady way coupled to 0-D and 1-D engine simulation code OpenWAM [189]. Those models will interact among them in the following way.

5.2.1 Heat transfer integration

In this section it is explained how heat transfer model presented in Chapter 3 is integrated into turbocharger global model. Heat transfer is introduced or removed from compressor fluid-dynamic model at node Air of figure 3.1 what represents temperature after adiabatic compression. Physically that node corresponds with compressor diffuser outlet and compressor volute inlet (components with larger exposed areas) so heat will be injected/extracted to/from volume *V2* of figure 4.3.

On the turbine side heat transfer is removed from fluid-dynamic model at

turbine volute (since it is that component the one with larger exposed area). To simplify its integration into 1-D fluid-dynamic codes (such as OpenWAM^{TM}) it has been decided taking out that heat at intermediate volume represented in figure 4.9. Due to the fact that heat is removed from turbine rotor volume before rotor expansion, rotor effective area ($A^{map}_{eff,R}$) calculated using Serrano's model [148] must be compensated to take into account volume temperature (temperature of point e of figure 5.1). In order to so, and calculate rotor effective area with its inlet temperature corrector factor shown in equation 5.1 has been introduced.

$$A^{*}_{eff,R} = \frac{A^{map}_{eff,R}}{\sqrt{T_{10R}} \cdot T00} \cdot \sqrt{\frac{T_e}{T_0}} \tag{5.1}$$

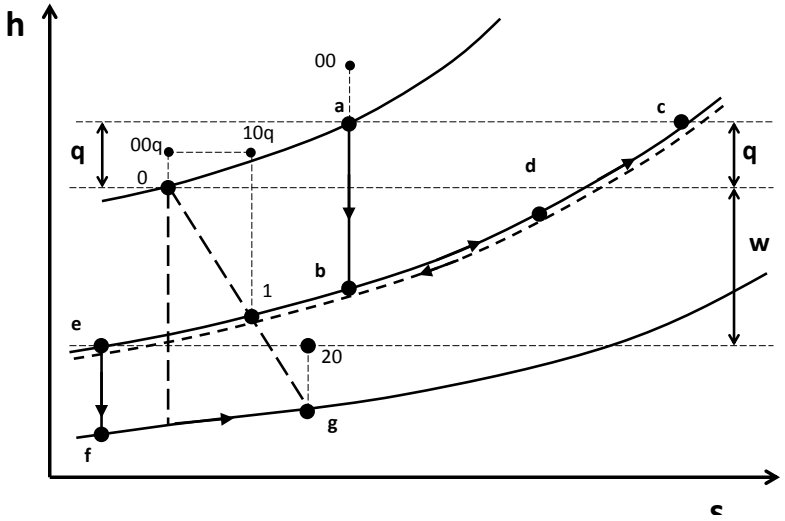

Figure 5.1: Turbine expansion process

Where point *10R* refers to rotor relative stagnation conditions (point *1* after adding relative rotor velocity). Turbine expansion process shown in figure 5.1 can be split into the following stages.

- Process *a*-*b* represents the expansion process in the stator.
- Process *b*-*c* kinetic energy losses at intermediate volume.

- Process *c*-*d* turbine heat transfer is substracted at intermediate volume to simplify its programming into 1-D fluid-dynamic codes.

- Process *d*-*e* work extraction. In that point it is necessary to correct rotor effective area using equation 5.1.

- Process *e*-*f* rotor adiabatic expansion.

- Process *f*-*g* represents discharge at pipe and energy balance up to turbine outlet conditions (*20*).

5.2.2 Mechanical losses interactions

Turbocharger mechanical losses model introduced into OpenWAM [153, 154] has been coupled to heat transfer model since lube oil temperature needed in friction losses model depends on the internal heat fluxes to the oil. Mechanical losses have been considered to occur in turbocharger model after adding heat flux $\dot{Q}_{H1/Oil}$ as it was observed in figure 3.2. That makes temperature governing friction losses is affected in some way by the heat released by the turbine.

On the other hand turbine and compressor fluid-dynamic models are affecting mechanical losses calculation since instantaneous pressure variations at compressor and turbine side affect friction losses determination at the axial thrust bearing [153, 154]. Pressure at compressor back-plate and turbine stator outlet are needed each time step to determine turbocharger axial thrust. That pressure at compressor side has been considered as the average between its inlet and outlet. Meanwhile at turbine side, stator outlet pressure has been instantaneously determined in terms of turbine geometry, operative conditions (expansion ratio and efficiency) and reaction degree as proposed by Serrano et al. [148].

5.2.3 Pulsating flow interactions

Pulsating flow at turbine (and compressor side) must be taken into account in heat fluxes determination since those fluxes are calculated instantaneously using correlations proposed in chapter 3. Although heat transfer correlations

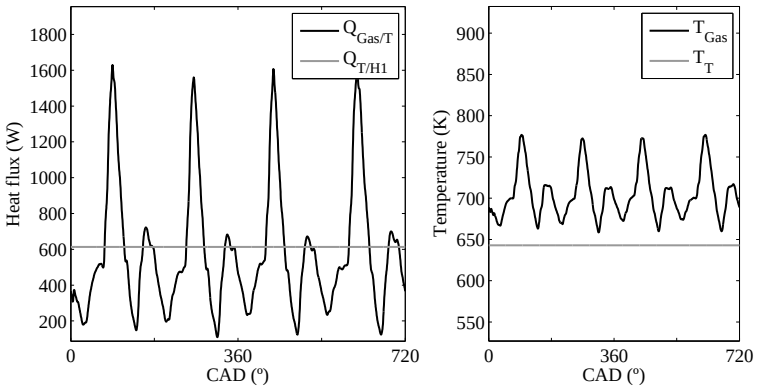

Figure 5.2: Instantaneous heat fluxes modelling under pulsating flow conditions for turbocharger #1 (1570 rpm 100% load). Left: Heat fluxes, Right: Temperature

were obtained and validated under steady flow conditions, instantaneous pulsating flow characteristics will be used in a quasi-steady way in heat fluxes calculations. Since modifications of turbine mass flow and its inlet temperature (due to pulsating flow), lead to instantaneous variations in Reynolds and Prandtl numbers and so in heat transfer calculations. Figure 5.2 shows turbine instantaneous temperature and modelled heat flux from the hot air moving through the turbine to its case. As it is observed, instantaneous variations in air temperature and heat flux are not transmitted to the turbine case due to the intrinsic high thermal capacitance of turbine casing material.

5.3 Global Model Validation

5.3.1 Steady Flow Model Validation

In order to close thermal analysis of the turbocharger, a source term has been used to take into account the energy transmitted to the lubricating oil due to friction losses only (figures 3.1 and 3.2). Mechanical losses model description and results are further discussed in [153, 154]. Oil temperature increases due to friction losses but also due to internal convection between lubricating oil and housing nodes. Once conductive and convective conductances, nodes capacitances and mechanical losses have been determined, Heat Transfer Model

(HTM) is already prepared to perform turbocharger simulations. In this case the 1-D gas dynamic open code for engine simulations, OpenWAM^{TM} [189, 67, 68] has been used. Besides, performance maps for both turbine and compressor (measured under adiabatic conditions) have been introduced into the turbocharger model to be used coupled with HTM. Those maps are necessary to calculate turbine and compressor outlet temperatures. Hot steady tests showed in figure 3.12 have been simulated using turbocharger model integrated into OpenWAM^{TM}. Heat Transfer Model validation has been done comparing prediction of the following parameters, when HTM was included or not, detailed information about results showed in this section have been presented in [151] .

5.3.1.1 Turbine outlet temperature

When no Heat Transfer Model (HTM) was activated to perform 1-D simulations, temperature governing the expansion process (named IT at diagram of figure 3.1) was the same than turbine inlet temperature (named as Gas). It was due to the fact that no heat was released to the turbine case and later to the housing. For that reason inlet temperature to the expansion process for no HTM cases was bigger than for HTM cases. Due to the fact that turbine expansion ratio was not affected by the HTM, turbine outlet temperature (TOT) results bigger in simulations without HTM. Error in turbine outlet temperature prediction ($eTOT$) has been computed as the difference between modelled and measured outlet temperature according to equation 5.2.

$$eTOT = T_{OT}^{mod.} - T_{OT}^{meas.} \tag{5.2}$$

Biggest errors have been observed at the low load area (corresponding to the NEDC conditions; i.e. low loads) for simulations without HTM as it is observed in figure 5.3 for turbocharger #1. In such conditions errors predicting TOT were above 20ºC for all analysed VGT positions of turbocharger T.#1 and for some operative conditions turbine outlet temperature could be overpredicted in 50ºC. When HTM was introduced, $eTOT$ drastically reduced and most simulated points lied in a threshold of $\pm$10ºC.

As it is observed in figure 5.3 for really low load points (that is the smallest turbine temperature drop across the turbine), errors predicting TOT were in

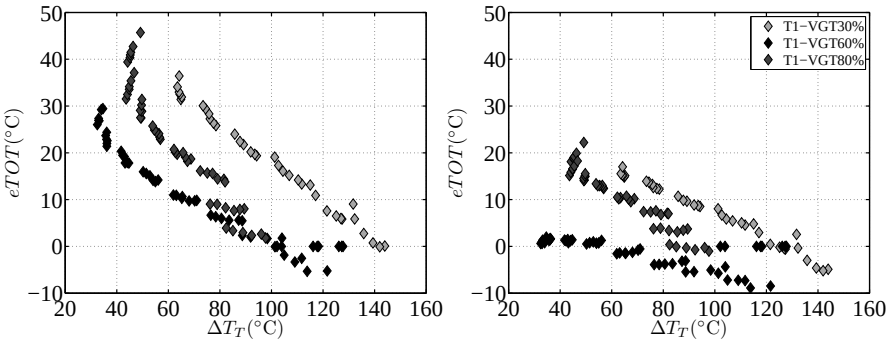

Figure 5.3: Errors predicting Turbine Outlet Temperature (eTOT) for turbocharger # 1 vs. measured turbine temperature drop. Left: with no HTM, Rigth: with HTM.

the same magnitude than measured temperature drop (x axis in that figure) what ensured that temperature decrease along the turbine was conducted by heat transfer effects and not by work exchange (low expansion ratios). It was in that area where HTM showed its potential since errors were drastically reduced (practically no error for the VGT opening of 60% and below the half of that error for the rest of openings). The same analysis has been done in a histogram fashion where information from three tested turbochargers has been showed together. A criteria of $\Delta T_C = 60$°C in compression process has been chosen as the boundary between load loads $\Delta T_C < 60$°C and high turbocharger loads $\Delta T_C > 60$°C. Height of that bars represent the number of simulated operative points having an error in $eTOT$ in the range covered by the basis of that bar. For the case shown, frequency bars cover a width of 5°C in the threshold of ± 2.5°C around vertical grid lines, being those bars centred at 0°C. As it is shown in the histogram of figure 5.4, when HTM was used (column on the right) error drastically reduced since there were less simulated points deviated from 0°C line and most of them were concentrated around zero. It is also observed that simulations using HTM showed a distribution centred in zero both for the high and low powers. Good prediction for low load points ensured the accuracy of HTM model, as it was in that region where heat fluxes became more important to engine overall prediction.

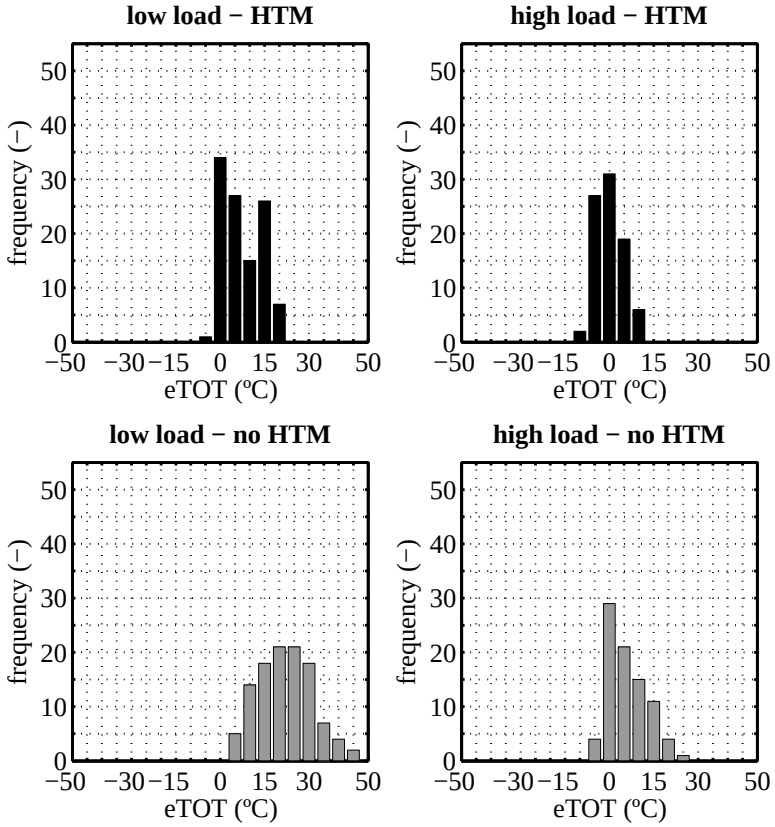

Figure 5.4: Turbine outlet temperature error distribution (all turbochargers).

5.3.1.2 Compressor outlet temperature

On the compressor side, heat transfer phenomena is more complex than on the turbine side since exhaust gases could only release heat passing through the turbine. Nevertheless, compressed air can absorb or release energy from neighbouring node C depending on turbocharger operative conditions. The first situation occurs from medium to low loads as it was observed in figure 3.19 for heat flux $\dot{Q}_{C/Air}$.

At those conditions, compressor case is at higher temperature than moving air due to the reduced compression ratio but the high heat transfer from

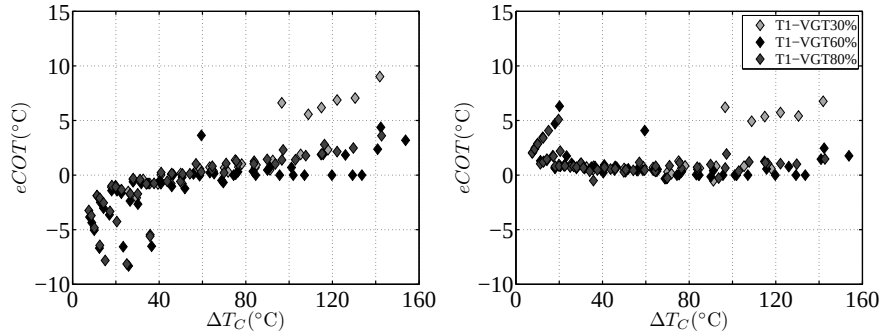

Figure 5.5: Error predicting Compressor Outlet Temperature ($eCOT$) in turbocharger #1. Left: no HTM, Rigth: HTM

the turbine side. Part of that heat can achieve compressor case worsening its efficiency. Nevertheless, as load increases, temperature associated to the compression process increases too. Under those conditions temperature at central housing is lower than compressed air temperature due to the lubrication (and coolant in case it exists). For that reason heat fluxes move from compressed air (Air node) to compressor case (C node) decreasing so compressor outlet temperature (improving compressor apparent efficiency). When HTM was used in simulations, error predicting compressor outlet temperature ($eCOT$), defined as showed by equation 5.3, reduced, mainly for the low load areas and water-cooled turbochargers. Figure 5.5 shows improvement in compressor outlet temperature prediction when HTM was introduced in calculations for turbocharger #1.

$$eTOC = T_{OC}^{mod.} - T_{OC}^{meas.} \tag{5.3}$$

The same trend was observed in histogram fashion on figure 5.6 where each bar represented an error of 2°C with a threshold of ±1°C around vertical grid line. As it is observed, when HTM was introduced (black bars) errors drastically reduced collapsing around the ±1°C frequency bar. Nevertheless, when HTM was disabled for turbocharger simulations, big errors in compressor outlet temperature prediction appeared (grey bars).

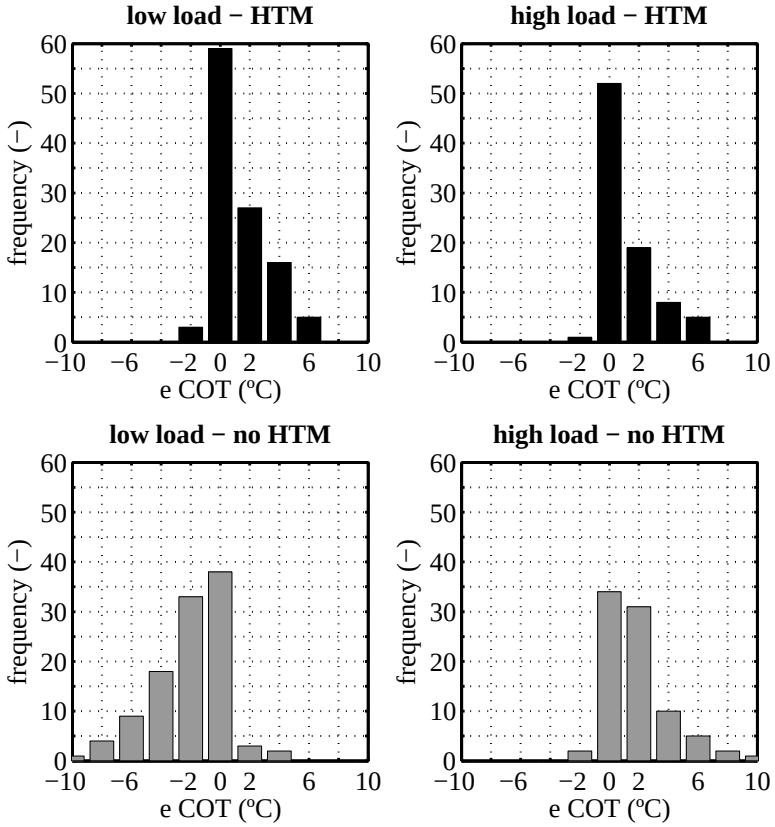

Figure 5.6: Compressor error distribution (all turbochargers).

5.3.1.3 Enthalpy drops

Figure 5.7 shows the agreement between simulated and measured turbocharger enthalpy drops considering or not heat transfer effects. As it is observed when heat transfer effects were not taken into account to perform 1-D simulations (column on the right), turbine modelled enthalpy drop was lower than measured one. That was due to modelled turbine outlet temperature was higher than in case of including HTM. The reason was that no heat flux had been removed before the expansion process of the exhaust gases. With respect to compressor enthalpy gain prediction, effect of taking into account the HTM was not so noticeable for the used scale covering the whole operative range.

Nevertheless, figure 5.5 showed better prediction in compressor outlet temperature and consequently better prediction in compressor enthalpy change.

With respect to the power exchanged to the oil, it included the increase in outlet temperature due to friction losses [154] but also due to heat transfer from metal nodes to the oil according to the lumped model presented in figure 3.1. The latter one was only considered in case HTM was introduced in simulations. Oil enthalpy analysis is described using dimensionless figure 5.8 due to the fact that energy transferred to the oil is quite small compared to turbine and compressor powers, and no differences including or not HTM can be appreciated.

In case no HTM is included in simulations, convective branch to the cooling circuit is deactivated (there is not a graphics on the left side on figures 5.7 and 5.8). As it is observed, when HTM is used (introducing water convection), turbine and compressor enthalpy drops are better predicted. In case of water enthalpy prediction itself is overestimated for turbocharger T.#3. That turbocharger was the smallest one for gasoline applications, were physically cooling cavities will be placed nearer the turbine than central housing node ($H2$) as it has been proposed as general solution for turbocharger lumped model. Despite differences observed in water enthalpy drops that effect is compensated by heat transfer exchanged to lubricating oil, remaining compressor and turbine enthalpy drops accurately predicted (and so air and exhaust gases outlet temperature are well estimated).

The same simulated information has been represented in dimensionless figures, dividing enthalpy values by corresponding maximum experimental value of each analysed turbocharger. Since in absolute values it is not possible to observe anything since same scale of $\Delta\dot{H}_T$ and $\Delta\dot{H}_C$ has been kept in order to highlight relative importance of the different power flows in the turbocharger.

With respect to the energy transmitted to the lubricating oil, column on the right side of figure 5.8 (without including HTM) took into account the energy transmitted to the oil due to mechanical losses only but not due to heat transfer from housing nodes. That graphic shows how modelled power to the oil (considering only friction phenomenon) was generally lower than measured enthalpy drop to the oil (what included intrinsically the contribution due to friction and due to heat transfer effects) for some turbocharger operative conditions. That effect was not so clear at the low load region and for turbocharger #3. For that reason, when HTM was included in simulations,

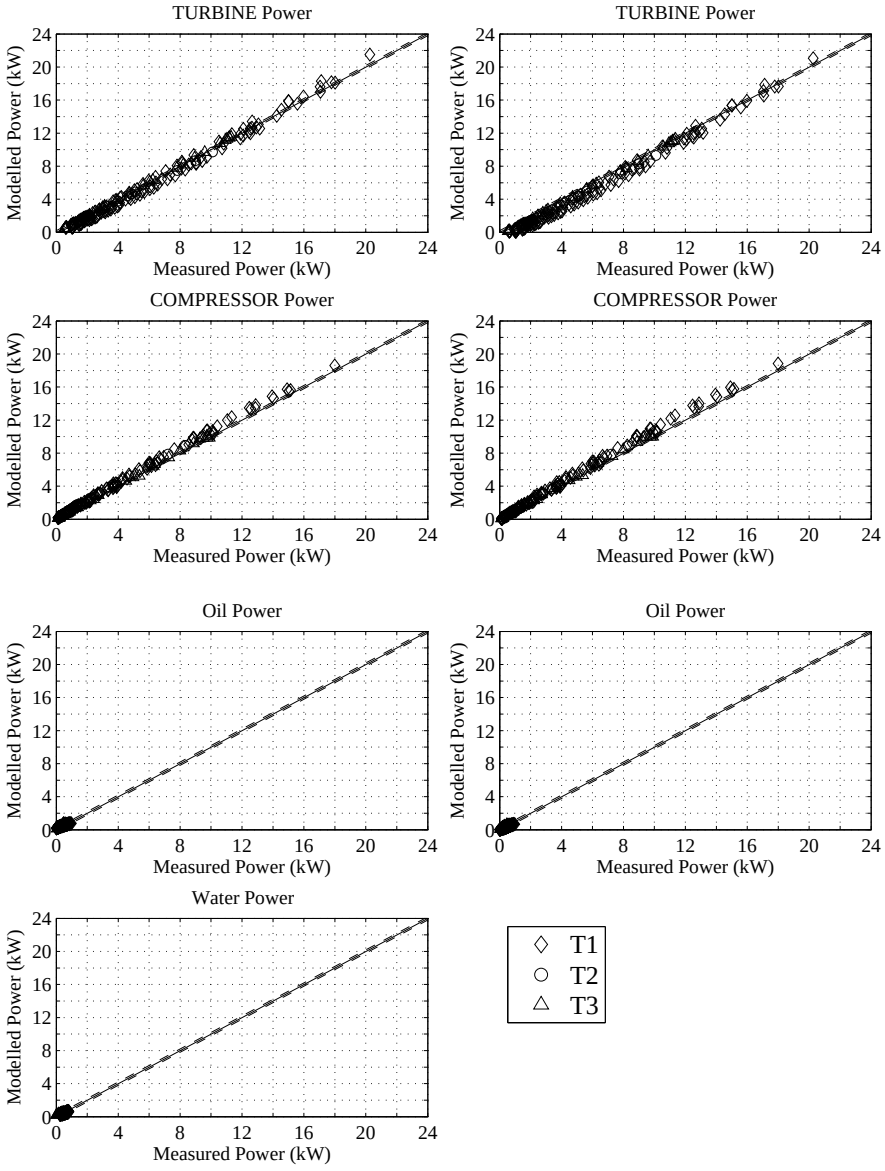

Figure 5.7: Enthalpy drops in turbocharger simulations. Left: with HTM, Right: without HTM

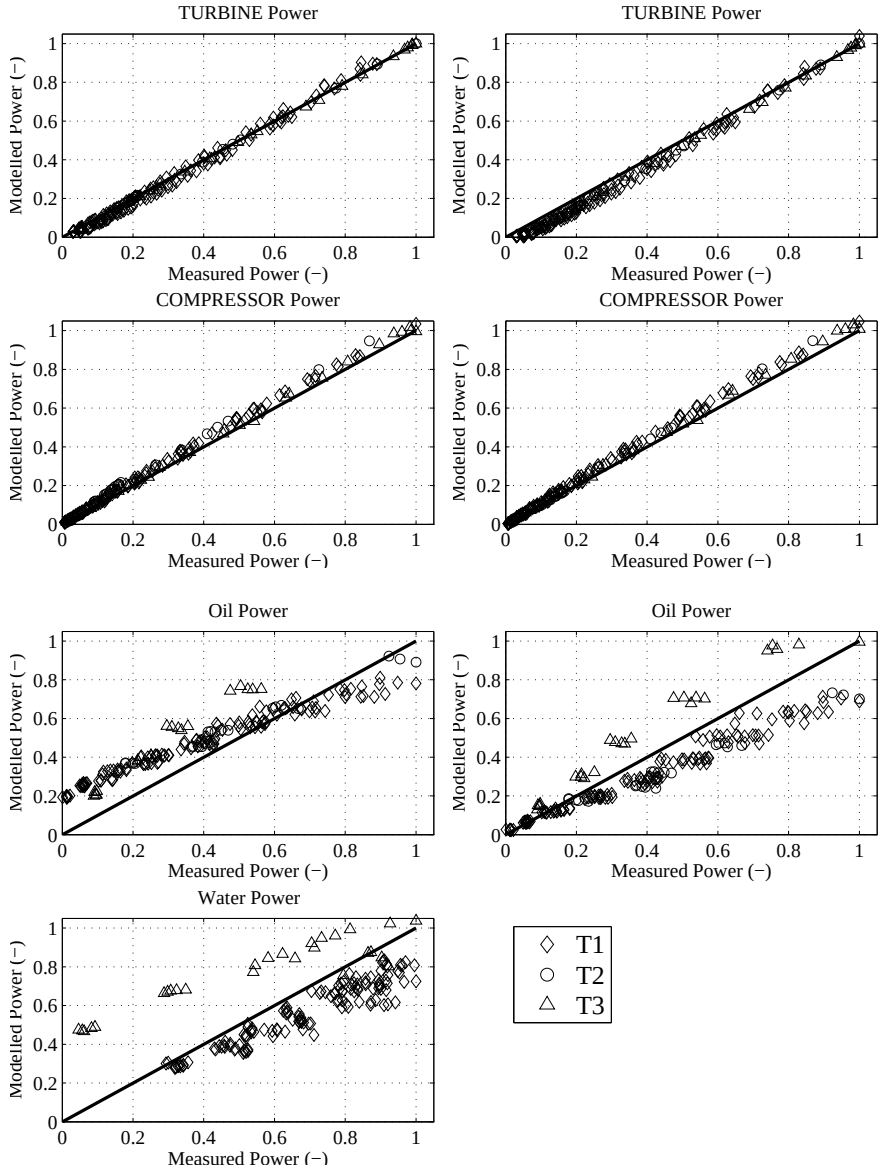

Figure 5.8: Enthalpy drops in turbocharger simulations, dimensionless form. Left: with HTM, Right; without HTM

energy to the oil was even higher since positive heat fluxes to the oil appeared. Nevertheless modelled data including HTM were more grouped and centred to the measurements. In the high load area HTM showed better prediction in lubricating oil enthalpy changes.

5.3.1.4 Turbocharger Speed

Figure 5.9 shows errors in turbocharger speed prediction when HTM was included or not in 1-D computational simulations. As it is observed slightly lower errors in turbocharger speed were obtained when HTM was included. Nevertheless those differences were not very high due to the fact that error in turbocharger speed was computed doing an energy balance between turbine, compressor and shaft mechanical powers. Turbine and compressor powers were not affected by HTM, they remain the same whether heat transfer was considered or not since pressure lines divergence was not very high for the pressure ratios and heat flows the turbocharger was working with. Nevertheless small differences predicting friction losses appear since heat fluxes modified oil temperature and so oil viscosity and friction.

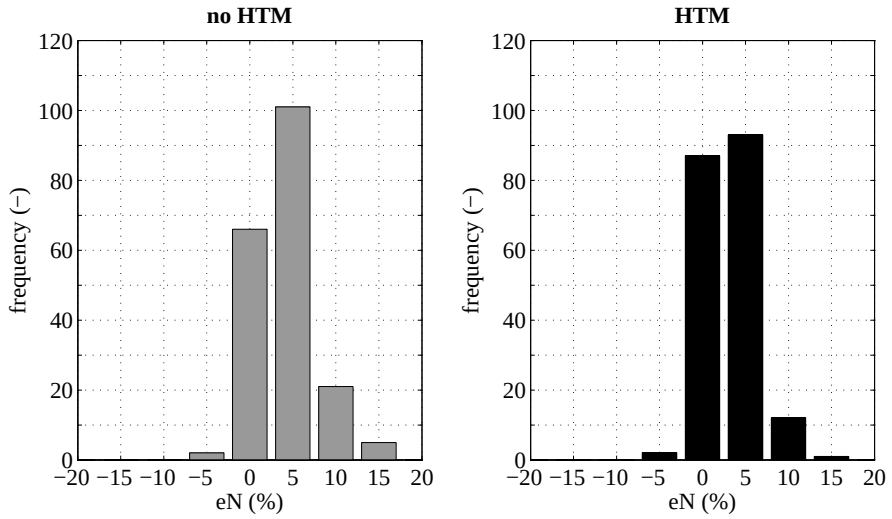

Figure 5.9: Error predicting turbocharger speed (eN). Left: without HTM, Rigth: with HTM

5.3.1.5 Nodes temperature

Proposed thermal model also calculates wall temperatures for turbocharger metal nodes presented in figure 3.1 (T, H_1, H_2, H_3, C). Figure 5.10 shows wall temperature prediction at each metal nodes compared to the measured ones. As it is observed, thermal model provides good results in wall temperature prediction for most of testing points. As it is shown, for the non-water cooled turbocharger (T.2), higher temperatures are observed at housing nodes (H1, H2 H3). That is due to the fact that only lubricating oil is removing heat from the central housing leading to higher wall temperatures.

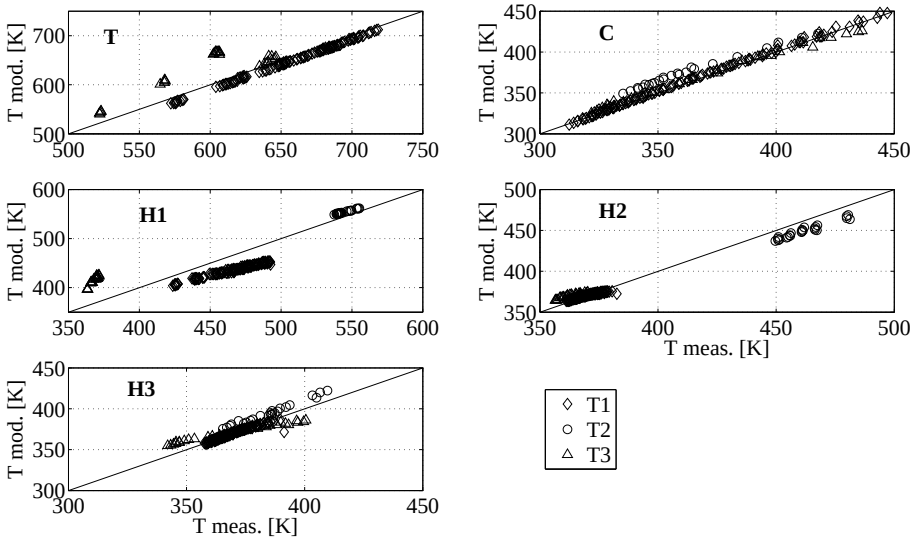

Figure 5.10: Temperature prediction at metal nodes

5.3.2 Pulsating Flow Model Validation

Once turbochargers sub-models have been validated individually, a series of pulsating hot flow tests on the turbine side have been carried out to validate turbocharger sub-models working altogether. Those tests have been performed on the gas stand instead of an engine test bench due to geometry restrictions needed to apply beam-forming technique for wave's decomposition. Nevertheless those tests have been undertaken reproducing pulsating conditions (same

pulses amplitude and frequency) and same turbine average corrected mass flow to several engine operative conditions (speed and load). Table 5.1 shows main characteristics of those tests for turbochargers named #1, #2 and #3.

Table 5.1: Engine simulated points with hot flow (turbine inlet temperature in °C)

Load →	**12%**	**25%**	**50%**	**75%**	**100%**
Engine Speed					
	T1(260)	T1 (300)	T1 (370)	T1 (425)	T1 (430)
1500	T2 (315)	T2 (330)	T2 (365)	T2 (420)	-
	T3 (295)	T3 (290)	T3 (360)	T3 (365)	T3 (370)
	T1 (380)	T1 (385)	-	-	T1 (400)
2000	T2 (370)	T2 (390)	-	-	T2 (430)
	-	-	T3 (355)	T3 (375)	T3 (380)
3000			T1 (400)	T1 (400)	T1 (400)
3500					T1 (400)

Figure 5.11 shows operative engine conditions over turbocharger performance maps for turbocharger #1. As it is observed a wide range of operative conditions have been covered, both in the turbine and compressor maps. Goodness of the global model will be analysed in terms of error predicting turbine and compressor averaged-cycle parameters.

Model validation has been carried out using engine simulation code OpenWAM [189], imposing recorded average pressure and temperature levels at compressor inlet and a likely instantaneous variation of temperature at turbine inlet calculated from the measured average temperature assuming an isentropic compression due to the rotary valve. Incident pressure at turbine inlet and 2nd reflected pressure wave at turbine outlet have been imposed for acoustic response validation as it was explained in chapter 4. In order to well represent test cell characteristics, lube oil and coolant properties at turbocharger inlet have been imposed too. Resistance conditions imposed by the back-pressure valve installed at compressor outlet line have been reproduced as well. Turbocharger modelling have been carried out including or not HTM in order to analyse the importance of heat transfer fluxes in turbocharger global performance.

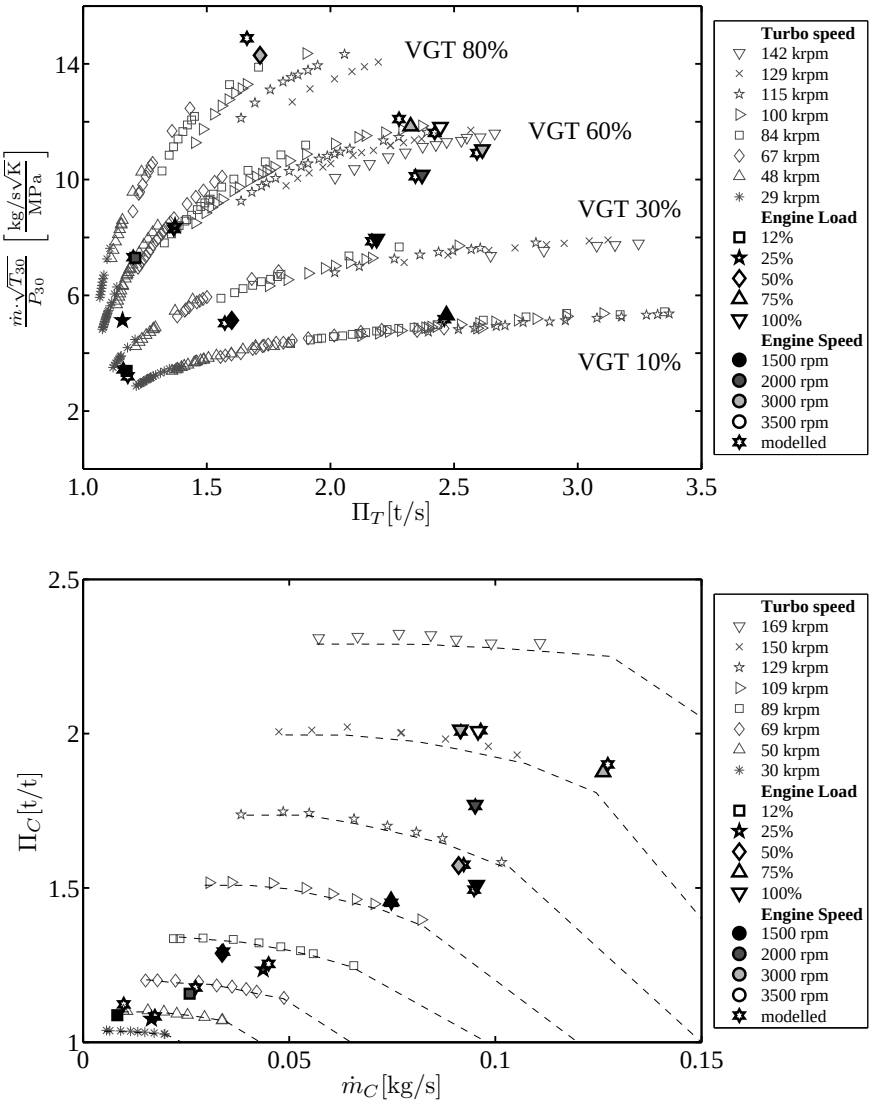

Figure 5.11: Engine operative conditions over turbocharger map (turbo #1). Top: Turbine map, bottom: Compressor map.

5.3.2.1 Compressor performance

Despite flow oscillations on the turbine side, compressor behaved practically at steady flow conditions due to turbo shaft inertia. Oscillations in turbocharger

speed were negligible as it was observed in chapter 4. For those reasons compressor validation have been done in terms of averaged parameters.

Turbocharger Speed

Turbocharger speed in engine simulation codes is updated by computing instantaneously a power balance between mechanical power given by the turbine and mechanical power absorbed by the driven compressor, discounting mechanical losses due to friction in turbocharger shaft as equation 5.4 shows.

$$\Delta N = \left(\frac{60}{\pi}\right)^2 \cdot \frac{\left(\dot{W}_T - \dot{W}_C - \dot{W}_m\right)}{I \cdot N} \tag{5.4}$$

Where $\dot{W}_C$ and $\dot{W}_T$ represent compressor and turbine mechanical power, meanwhile I is the moment of inertia of the turbocharger shaft. Compressor and turbine power are calculated using isentropic power and efficiency definition as equations 5.5 and 5.6 show.

$$\dot{W}_C = \frac{\dot{m}_C \cdot c_p \cdot T_{10}}{\eta_C} \cdot \left(\Pi_C^{\frac{\gamma-1}{\gamma}} - 1\right) \tag{5.5}$$

$$\dot{W}_T = \dot{m}_T \cdot c_p \cdot T_{30} \cdot \eta_T \cdot \left(1 - \left[\frac{1}{\Pi_T}\right]^{\frac{\gamma-1}{\gamma}}\right) \tag{5.6}$$

As equations 5.5 and 5.6 show, compressor and turbine power depend on mass flows, inlet temperatures, pressure ratio across the element and isentropic efficiency. Those parameters are determined in turbocharger model according to the following criteria:

- Inlet temperatures are imposed at boundaries and so their value will be the same whether HTM will be considered or not.
- Compressor mass flow and pressure ratio are determined entering with turbocharger speed from performance map once back-pressure valve at compressor outlet line has been characterized and using turbocharger speed. As it is observed figure 5.12, compressor corrected mass flow prediction does not depend whether HTM is used or not, since heat flux to the compressor is added/subtracted at compressor outlet. So

compressor corrected speed used to interpolate in compressor map is not modified since it is determined before heat fluxes interactions.

- Compressor efficiency is determined from performance map. Turbocharger speed and compressor mass flow are used as inputs, so compressor efficiency is not modified whether HTM will be used or not.
- Turbine pressure ratio is obtained from calculated and imposed pressure components at turbine boundaries, so that parameter does not depend on HTM.
- Turbine mass flow and efficiency are determined from turbine model [148] entering with pressure ratio, turbocharger speed and VGT position. Since heat flux is subtracted at turbine intermediate volume (after the expansion in the stator), turbine corrected mass flow and efficiency appearing in charts are not affected by heat transfer interactions.

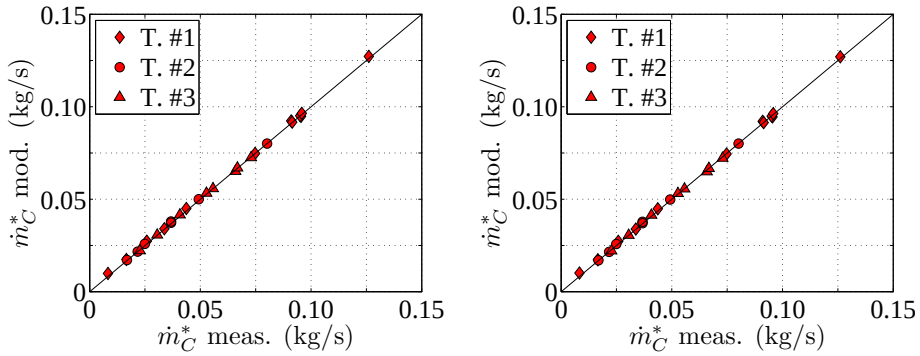

Figure 5.12: Compressor mass flow prediction under pulsating flow conditions. Left: without HTM, Right: with HTM

Those items lead compressor (and turbine) mechanical power remain the same in case heat transfer fluxes are considered or not. On the other hand, mechanical friction losses modification due to lube oil temperature variation when heat transfer model is considered are limited due to the small internal heat fluxes to the lubricating oil.

In summary figure 5.13 shows that there are not noticeable differences predicting turbocharger speed as it was expected. What figure 5.13 shows is

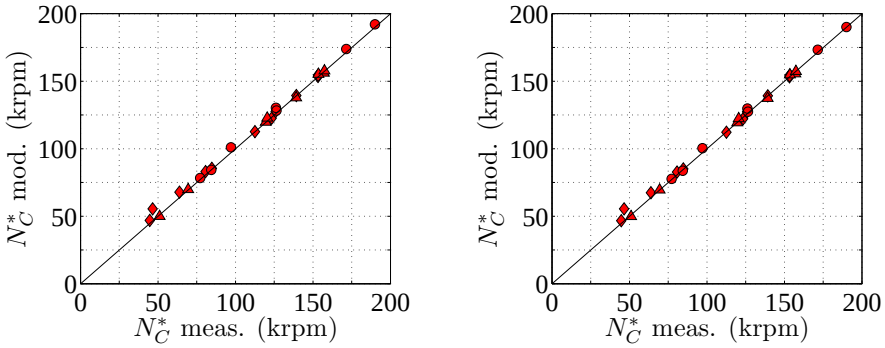

Figure 5.13: Turbocharger speed prediction under pulsating flow conditions. Left: without HTM, Right: with HTM

the accuracy of the used compressor and turbine fluid-dynamics models, as well as the mechanical friction losses model since turbocharger speed prediction is good enough for the wide turbocharger speed studied range.

Compressor Outlet Temperature

As it is observed in figure 5.14 compressor outlet temperature prediction improves when HTM is introduced. Mainly for the lowest compressor powers (intermediate to low compressor temperature drops). Turbocharger #1 shows the higher improvements, mainly for the lowest temperature drops. No differences are observed predicting COT at high loads since heat transfer effects become negligible compared to the turbocharger power as load increases.

Compressor Mass Flow and Pressure Ratio

As it is observed in figure 5.15 most of the simulated turbine hot pulsating flow tests showed a good prediction in compressor average corrected mass flow and compression ratio. More than 75% of tested operative conditions showed an error below the threshold of ± 2.5 %. An outrageous point with an error of 20% in compressor corrected mass flow appeared due to that operative point was placed near surge limit where both mass flow is low and compressor iso-speed lines are quite flat that causes small differences predicting compression ratio will lead to big differences in corrected mass flow prediction.

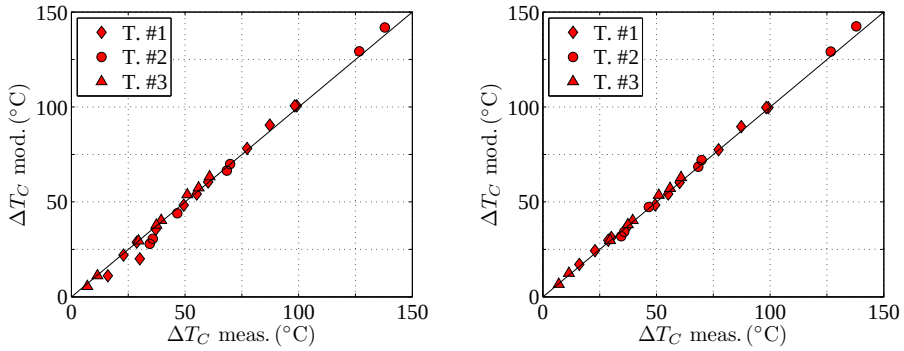

without HTM with HTM

Figure 5.14: Compressor outlet temperature prediction under pulsating flow conditions. Left: without HTM, Right: with HTM

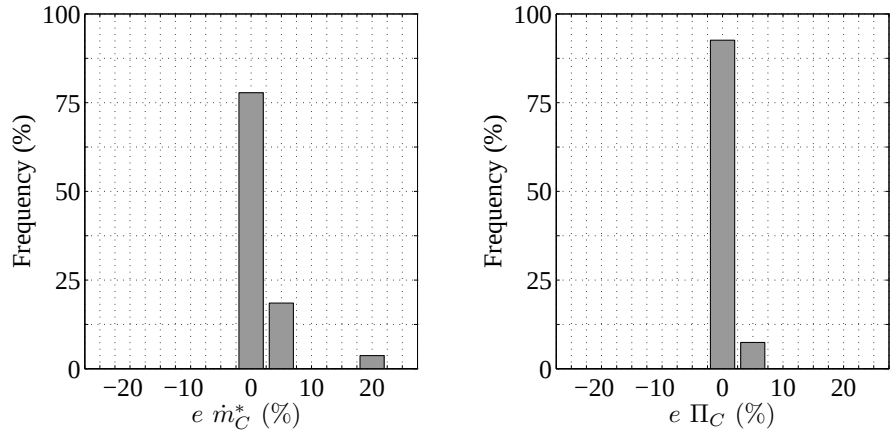

Figure 5.15: Compressor performance prediction. Left: Corrected mass flow, Right: Compression ratio

5.3.2.2 Turbine performance

Turbine model validation under hot pulsating flow conditions has been carried out applying different sub-models in a quasi-steady way (extrapolated efficiency maps [131] in Chapter 4, mechanical losses model [154] and heat transfer model [119]). Instantaneous fluctuations of the calculated inlet/outlet pres-

sures lead to an instantaneous modification on turbine mass flow according to the results of the two serial nozzles, fluid-dynamic model [148], where effective areas are quasi-steadily calculated from the previously extrapolated mass flow maps [131] in Chapter 4. Derived turbine parameter blade speed ratio can be determined instantaneously too what is needed in turbine extrapolated map to obtain turbine instantaneous efficiency. Those variations are observed as a loop in reduced mass flow versus turbine expansion ratio performance maps as well as turbine and efficiency variations observed in figure 5.16 calculated between stages D and E from figure 4.35. Instantaneous turbocharger power balance using equation 5.4 provides current turbocharger speed.

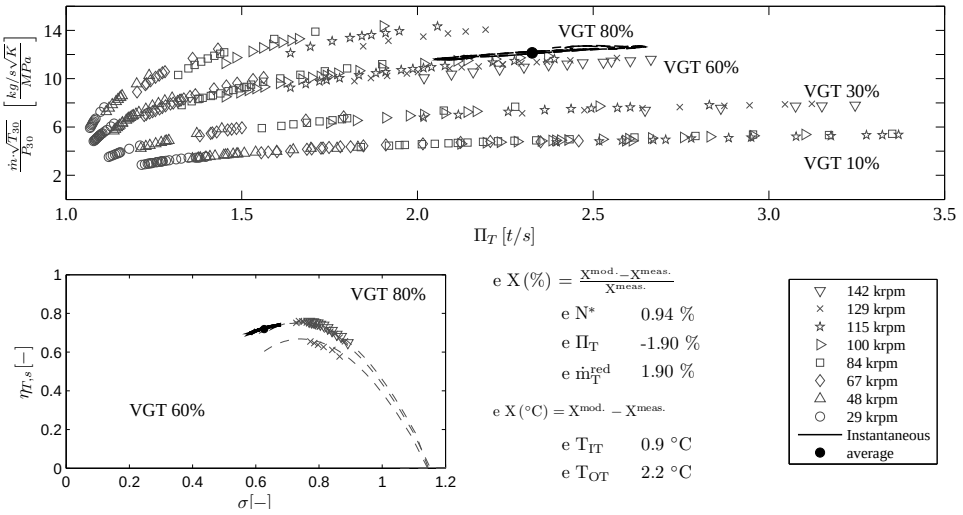

Figure 5.16: Turbine instantaneous performance for pulsating hot flow conditions, turbocharger #1 (3000 rpm - 75%load)

Turbine Outlet Temperature

As it is observed in figure 5.17 turbine outlet temperature prediction improves when HTM is included. Although that model was developed and validated using steady state tests, that figure shows that HTM model is able to accurately predict turbine outlet temperature under pulsating flow conditions. Big differences have been observed without including HTM even for intermediate to high turbine powers. As it is observed for low loads (lowest temperature drops), errors in TOT prediction without HTM are in the same magnitude than measured temperature drop. That is due to heat transfer fluxes at low

loads are very important compared to turbocharger power, as it was shown in Chapter 3.

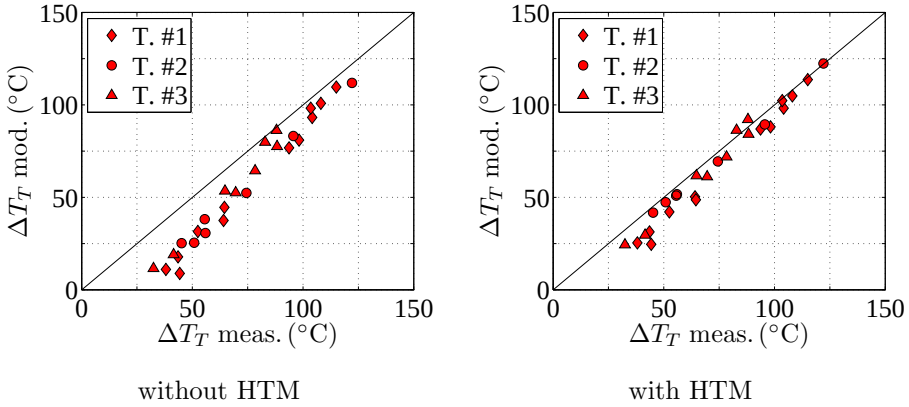

Figure 5.17: Turbine outlet temperature prediction under pulsating flow conditions. Left: without HTM, Right: with HTM

Turbine Mass Flow and Expansion Ratio

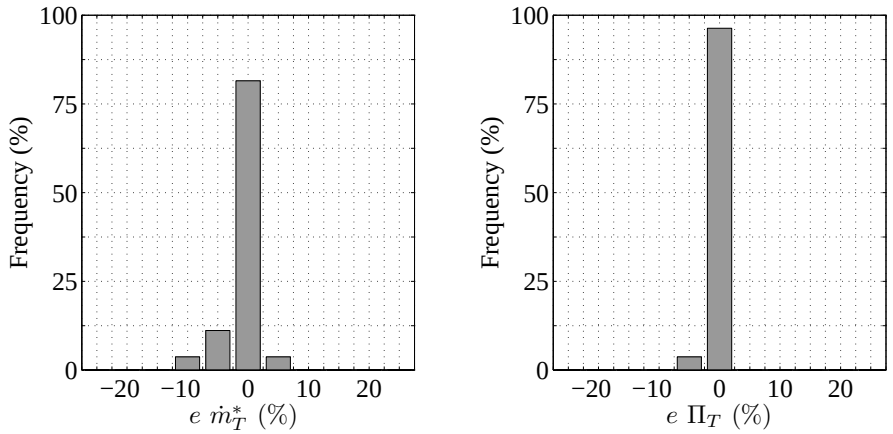

Figure 5.18: Turbine performance prediction. Left: Turbine corrected mass flow, Right: Turbine expansion ratio

As it is observed in figure 5.18 most tested points have an error predicting turbine corrected mass flow in a threshold of ±2.5%. Only one point shows

an error beyond -7.5% of error predicting turbine mass flow but that point was from an operative conditions of 1500 rpm 25% load (turbocharger speed of 44 krpm) where turbine performance lines are quite step what produces big errors predicting mass flow for small differences in expansion ratio.

Instantaneous pressure waves at turbine inlet

Pressure wave components calculated by turbine model have been compared to experimental information to validate turbine fluid-dynamic model under hot pulsating flow conditions.

Figure 5.19 shows measured and modelled reflected pressure wave at turbine inlet for turbocharger #1 under hot pulsating conditions in time and frequency domain. Three engine operative conditions have been presented, those are representative from low power (1500 rpm - 12% load), medium power (2000 rpm - 100% load) and high power (3500 rpm - 100% load). As it is observed in Annex A, good accuracy in shape and mean value has been obtained for most engine operative conditions. A small shifting is appreciated, mainly for the highest speeds, what indicates that the assumptions of proposed 1-D model for the turbine are to simple to account for complex phenomena such as the internal volute geometry and the fact that turbine volute is losing mass through the stator vanes.

Instantaneous pressure waves at turbine outlet

Figure 5.20 shows modelled and measured transmitted pressure wave at turbine outlet in time and frequency domain for same engine conditions. As it is observed, good prediction in shape, mean value and shifting has been obtained due to the good accuracy predicting pressure waves at turbine inlet and modelling turbine outlet diffuser geometry.

5.3.2.3 Frequency analysis

Figure 5.21 shows error predicting SPL for reflected and transmitted pressure waves for all tested turbochargers, that error has been defined as equation 5.7 shows.

$$e\text{SPL (dB)} = \text{SPL}^{\text{meas}} - \text{SPL}^{\text{mod}} \tag{5.7}$$

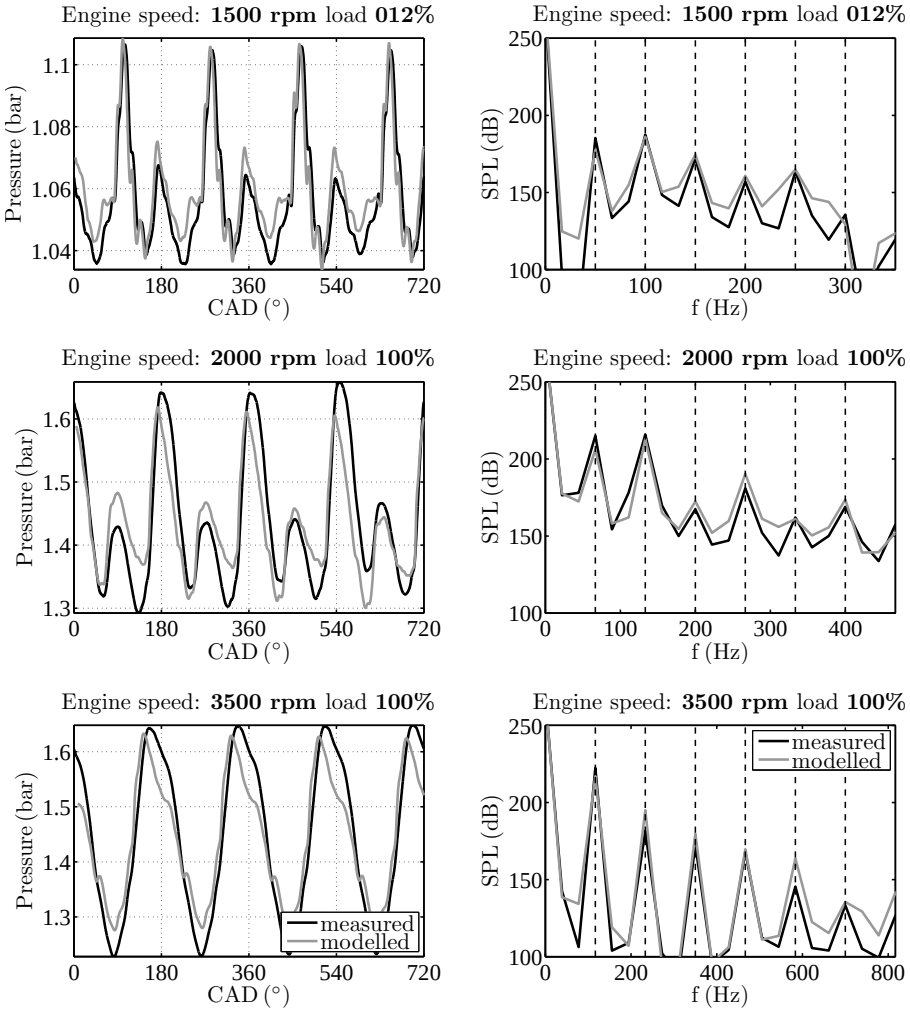

Figure 5.19: Reflected pressure wave at turbine inlet (from turbocharger #1). Left: time domain, Right: frequency domain.

As it is observed, good results are obtained for 2nd and 4th engine order in both reflected and transmitted waves, for most testing cases. Big errors predicting SPL for the 6th have been observed for both the reflected and transmitted pressure waves, big dispersion for all turbochargers and engine speeds has been observed. Right side of figure 5.21 shows relative errors predicting SPL, those are calculated using equation 5.8. As it is shown, 100% of tested

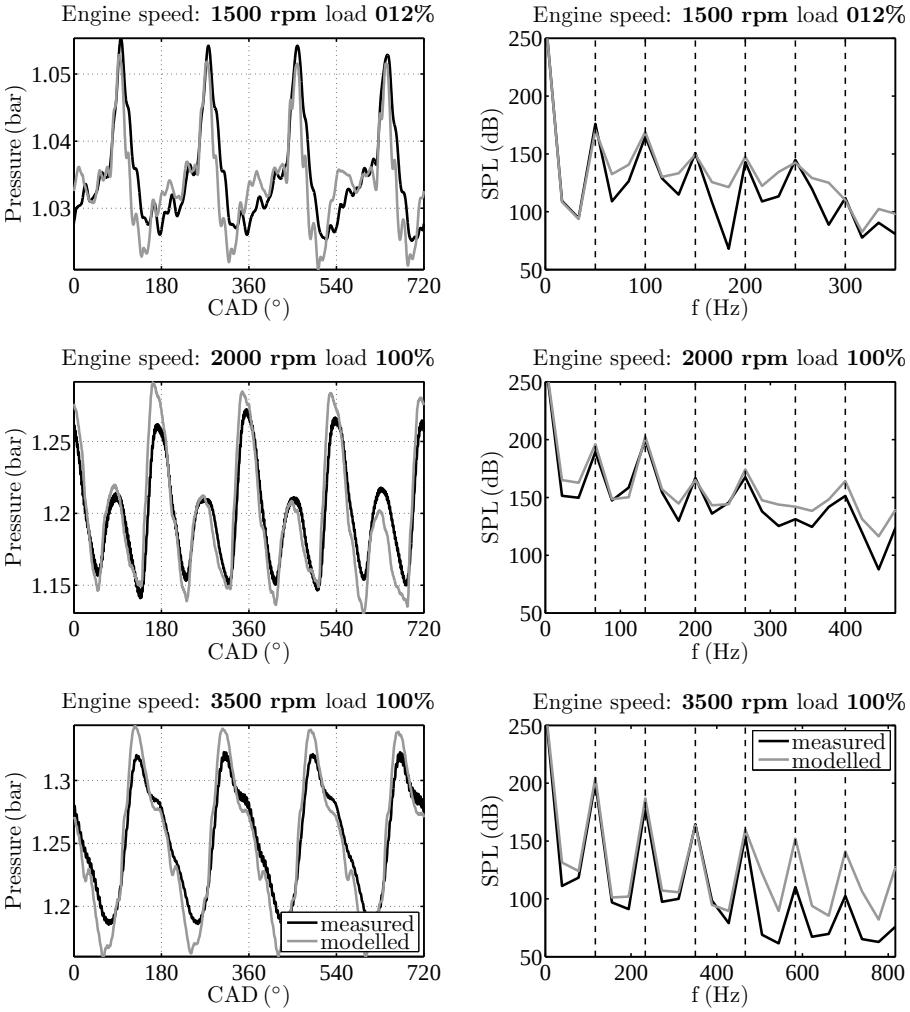

Figure 5.20: Transmitted pressure wave at turbine outlet(from turbocharger #1). Left: time domain, Right: frequency domain.

points are in a threshold of ±7,5% for the second engine order in reflected and transmitted pressure waves. For the fourth engine order, 90% of tested points have an error in the threshold of ±7,5%. For the sixth engine order, 70% of modelled engine conditions show an error in the threshold of ±7,5%.

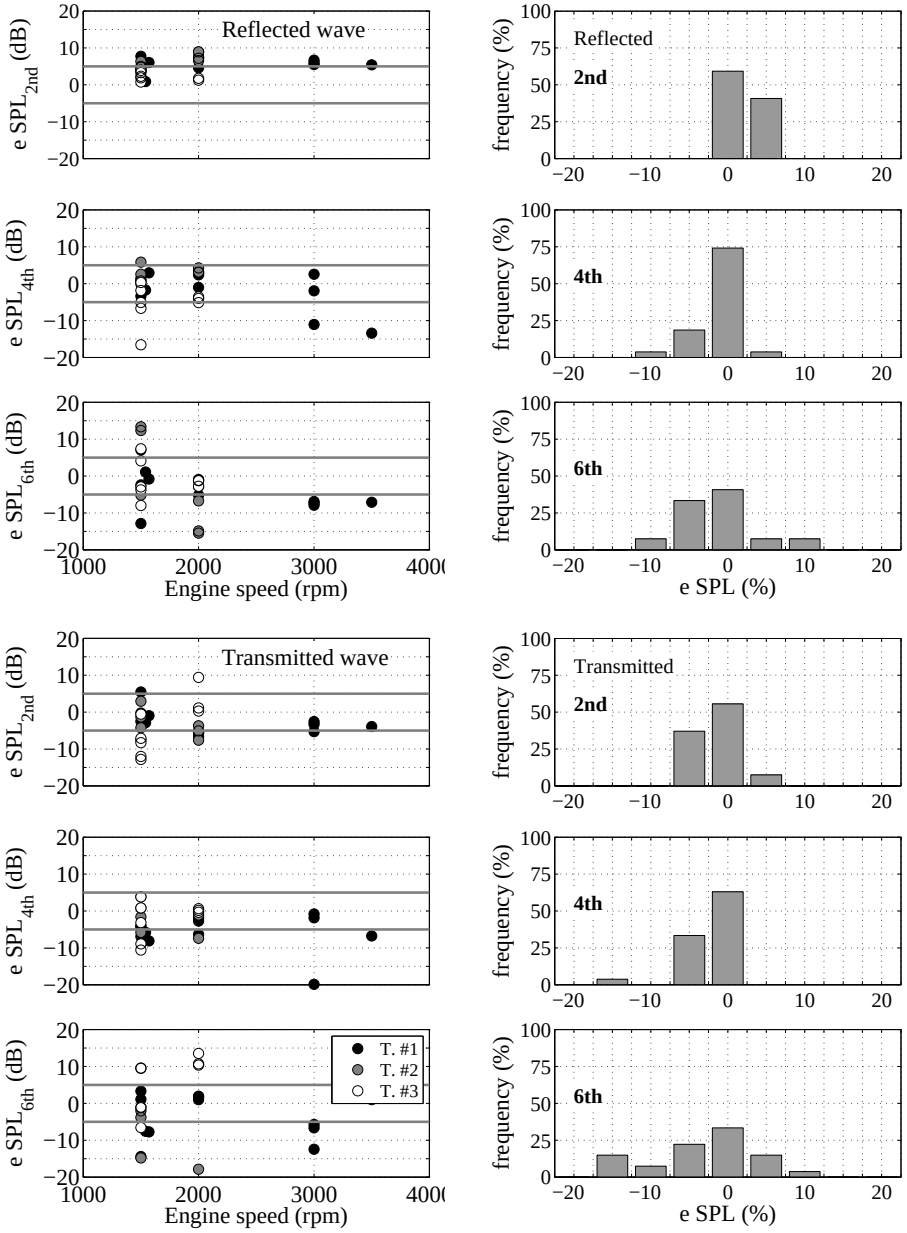

Figure 5.21: Turbine Sound Pressure Level modelling prediction using geometrical model proposed for the turbine. Top part: Reflected wave, Bottom part: Transmitted wave

$$e\text{SPL } (\%) = \frac{\text{SPL}^{\text{meas}} - \text{SPL}^{\text{mod}}}{\text{SPL}^{\text{meas}}} \tag{5.8}$$

5.4 Analysis of proposed model improvements

Improvements with respect to state of the art has been analysed in this section. In order to do so, pulsating hot flow tests on the turbine side have been simulated using the standard source of information provided from manufacturers. That means providing turbocharger maps measured under steady hot flow conditions. Efficiency definition in those maps is a mixture of several phenomena as it is observed in equations 5.9 and 5.15, using nomenclature from figure 5.22.

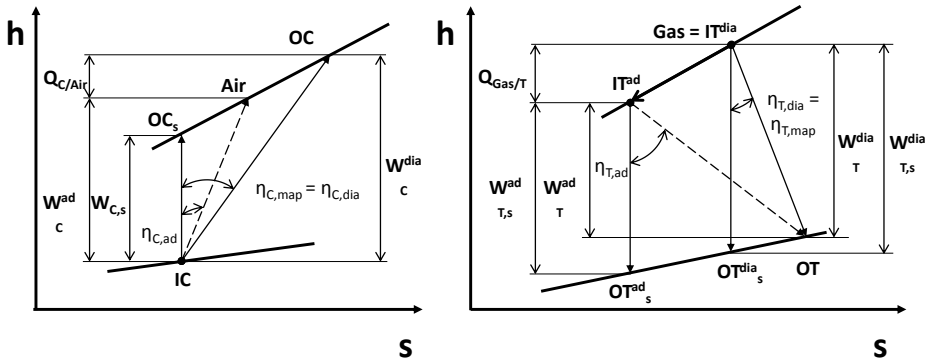

Figure 5.22: Adiabatic and diabatic working processes. Left: Compressor, Right: Turbine.

$$\eta_{Tmap} = \frac{(T_{OC} - T_{IC}) \cdot c_{p,C} \cdot \dot{m}_C}{(T_{Gas} - T_{OTs,dia}) \cdot c_{p,T} \cdot \dot{m}_T} = \frac{\dot{W}_{C,ad} + \dot{Q}_C}{\dot{W}_{Ts,dia}} \tag{5.9}$$

Dividing each term of equation 5.9 by turbine isentropic power (during an adiabatic expansion, $\dot{W}_{Ts,ad}$ according to diagram on right side of figure 5.22), the following expression is obtained. Turbine adiabatic power ($\dot{W}_{T,ad}$) is introduced in that equation in order to make it suitable to introduce later turbocharger efficiency definitions (from equations 5.12 and 5.13).

$$\eta_{Tmap} = \frac{\frac{\dot{W}_{C,ad}}{\dot{W}_{Ts,ad}} + \frac{\dot{Q}_C}{\dot{W}_{Ts,ad}} \cdot \frac{\dot{W}_{T,ad}}{\dot{W}_{T,ad}}}{\frac{\dot{W}_{Ts,dia}}{\dot{W}_{Ts,ad}}} \tag{5.10}$$

Now, relation between diabatic and adiabatic expansions (equation 5.11), mechanical efficiency definition (equation 5.12) and turbine isentropic efficiency definition after an adiabatic expansion (5.13) are considered.

$$\frac{\dot{W}_{Ts,dia}}{\dot{W}_{Ts,ad}} = \frac{T_{Gas}}{T_{IT}} \tag{5.11}$$

$$\eta_m = \frac{\dot{W}_{C,ad}}{\dot{W}_{T,ad}} \tag{5.12}$$

$$\eta_{Ts} = \frac{\dot{W}_{T,ad}}{\dot{W}_{Ts,ad}} \tag{5.13}$$

Introducing expressions 5.11, 5.12 and 5.13 into turbine map efficiency definition (equation 5.10), equation 5.14 is obtained.

$$\eta_{Tmap} = \left(\eta_{Ts} \cdot \eta_m + \eta_{Ts} \cdot \frac{\dot{Q}_C}{\dot{W}_{T,ad}}\right) \cdot \frac{T_{IT}}{T_{Gas}} = \eta_{Ts} \cdot \eta_m \left(1 + \frac{\dot{Q}_C}{\dot{W}_{C,ad}}\right) \cdot \frac{T_{IT}}{T_{Gas}} \tag{5.14}$$

Meanwhile compressor map efficiency is usually defined according to equation 5.15.

$$\eta_{Cmap} = \frac{(T_{20s} - T_{10}) \cdot c_{p,C} \cdot \dot{m}_C}{(T_{20} - T_{10}) \cdot c_{p,C} \cdot \dot{m}_C} = \frac{\dot{W}_{Cs}}{\dot{W}_C + \dot{Q}_C} = \frac{\eta_{Cs}}{1 + \frac{\dot{Q}_C}{\dot{W}_C}} \tag{5.15}$$

Where performance maps efficiency (η_{Tmap} and η_{Cmap}) are affected by isentropic behaviour (η_{Ts} and η_{Cs}), heat fluxes effects ($\dot{Q}_T$ and $\dot{Q}_C$) and mechanical losses (η_m). In addition heat transfer from the turbine $\dot{Q}_T$ can be expressed as equation 5.16 shows.

$$\dot{Q}_T = \dot{m} \cdot c_p \cdot (T_{Gas} - T_{IT}) \tag{5.16}$$

Rearranging equation 5.16, expression 5.17 is obtained.

$$\frac{T_{IT}}{T_{Gas}} = 1 - \frac{\dot{Q}_T}{T_{Gas} \cdot \dot{m} \cdot c_p} \tag{5.17}$$

Introducing equation 5.17 into turbine efficiency map expression 5.14, it is obtained the following equation.

$$\eta_{Tmap} = \eta_{Ts} \cdot \eta_m \left(1 + \frac{\dot{Q}_C}{\dot{W}_{C,ad}}\right) \cdot \left(1 - \frac{\dot{Q}_T}{T_{Gas} \cdot \dot{m} \cdot c_p}\right) \tag{5.18}$$

As it is observed, mechanical efficiency and heat fluxes ocurring when those maps were measured are included in performance map efficiency definitions. For that reason, turbocharger simulations using those maps (from manufacturer) will only provide accurate results reproducing similar testing conditions. In this case, performance maps measured under steady hot flow conditions (with the definitions showed above) have been used as the manufacturer map to simulate hot pulsating flow campaign in order to compare those results with proposed turbocharger model. No heat transfer, mechanical losses or extrapolation models have been introduced to simulate turbocharger performance.

5.4.1 Turbocharger efficiency

A first analysis of heat transfer impact on turbocharger efficiency can be observed in figure 5.23. Where turbocharger adiabatic and diabatic efficiencies have been plotted in logarithmic scale versus turbine expansion ratio for three tested VGT openings under steady hot flow conditions at turbine side for turbocharger #1. Diabatic efficiency (η_T^{dia}) has been defined as the power ratio between diabatic compression (taking into account heat fluxes on the compressor side) and the isentropic expansion in the turbine, as showed in equation 5.9. That is the efficiency definition provided typically on turbocharger maps so it has been named here to as η_{Tmap} . Meanwhile turbocharger adiabatic

efficiency (η_T^{ad}) has been defined as the power ratio between compressor adiabatic process and turbine isentropic process. As it is observed in equation 5.19, that efficiency can be split into two terms, one indicating turbine isentropic efficiency ($\eta_{T,s}$) and the other representing turbocharger mechanical efficiency (η_m). Corrector term K has been defined as the ratio between turbocharger adiabatic and diabatic efficiency. Rearranging that definition it is observed how that term is related with several terms as equation 5.20 shows. That term includes mainly heat transfer effects showed in equation 5.9.

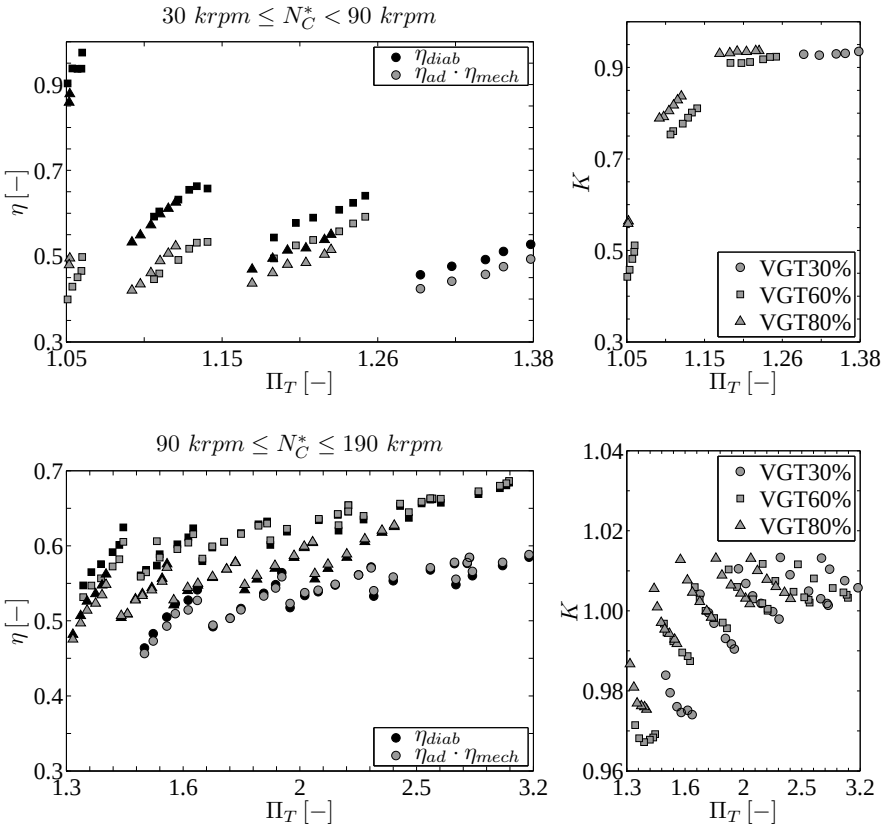

Figure 5.23: Heat transfer and mechanical losses impact on turbocharger efficiency. Top: Low turbocharger speed, bottom: high turbocharger speed.

$$\eta_T^{ad} = \frac{\dot{W}_{C,ad}}{\dot{W}_{T,s}} = \frac{\dot{W}_{C,ad}}{\dot{W}_{T,ad}} \cdot \frac{\dot{W}_{T,ad}}{\dot{W}_{T,s}} = \eta_m \cdot \eta_{T,s} \tag{5.19}$$

$$K = \frac{\eta_T^{ad}}{\eta_T^{dia}} = \frac{\eta_m \cdot \eta_{T,s}}{\eta_T^{dia}} = \frac{1}{\left(1 + \frac{\dot{Q}_C}{\dot{W}_C}\right) \cdot \frac{T_{IT}}{T_{Gas}}} = \frac{T_{Gas}}{T_{IT} \cdot \left(1 + \frac{\dot{Q}_C}{\dot{W}_C}\right)} \tag{5.20}$$

Where turbine adiabatic efficiency has been defined according to equation 5.19 what is a common practice.

As it is observed in figure 5.23, heat transfer influence on turbocharger efficiency becomes important for low turbocharger speed where a corrector term between 0.5 and 0.9 should be used to well represent what occurs on turbine efficiency at low loads corresponding to the NEDC conditions (below 90 krpm). That occurs in case manufacturer maps will be used to predict turbocharger outlet temperatures. Nevertheless, if proposed turbocharger model is used instead no corrector terms will be necessary. That is due to the fact that outlet temperature will be calculated from the isentropic compression hypothesis considering later heat fluxes by means of that sub-model. As turbocharger speed increases heat transfer effects become less critical and no corrector term will be necessary since its value varies between 0.97 and 1.02.

5.4.2 Turbocharger speed

Turbocharger speed is calculated in engine simulation codes using equation 5.4, where rearranging constant terms (Δt and shaft inertia) under parameter K, it can be expressed in the following way in case turbocharger models are used.

$$\Delta N = K \cdot \left(\dot{W}_T^{ad} - \dot{W}_C^{ad} - \dot{W}_m\right) \tag{5.21}$$

As it is observed in equation 5.21 heat fluxes do not take place in turbocharger speed calculation. Using efficiency definitions according to figure 5.22, expression 5.25 is obtained.

$$\eta_m \cdot \dot{W}_T^{ad} = \dot{W}_T^{ad} - \dot{W}_C^{ad} \tag{5.22}$$

$$\dot{W}_T^{ad} = \eta_T^{ad} \cdot W_{Ts}^{ad} \tag{5.23}$$

$$\dot{W}_C^{ad} = \frac{\dot{W}_{C,s}}{\eta_C^{ad}} \tag{5.24}$$

$$\Delta N = K \cdot \left(\eta_m \cdot \eta_T^{ad} \cdot \dot{W}_{T,s}^{ad} - \frac{\dot{W}_{C,s}}{\eta_C^{ad}} \right) \tag{5.25}$$

In case no turbocharger models are used, and only manufacturer maps are introduced in simulations, new turbocharger speed can be calculated using expression 5.26. Using that definition, mechanical losses are already included in performance maps.

$$\Delta N = K \cdot \left(\dot{W}_T^{dia} - \dot{W}_C^{dia} \right) \tag{5.26}$$

Where definitions for diabatic turbine and compressor power are the commonly used by manufacturers using nomenclature from figure 5.22.

$$\dot{W}_T^{dia} = \eta_T^{dia} \cdot \dot{W}_{Ts}^{dia} \tag{5.27}$$

$$\dot{W}_C^{dia} = \frac{\dot{W}_{Cs}}{\eta_C^{dia}} \tag{5.28}$$

Where compressor diabatic efficiency (η_C^{dia}) is defined according to equation 5.29 and taking into account enthalpy diagram from figure 5.22.

$$\eta_C^{dia} = \frac{\dot{W}_{Cs}}{\dot{W}_C^{dia}} = \frac{\dot{W}_{Cs}}{\dot{W}_C^{ad} + \dot{Q}_C} = \frac{1}{\frac{\dot{W}_C^{ad}}{\dot{W}_{Cs}} + \frac{\dot{Q}_C}{\dot{W}_{Cs}}} = \frac{1}{\frac{1}{\eta_C^{ad}} + \frac{\dot{Q}_C}{\dot{W}_{Cs}}} \tag{5.29}$$

Turbine diabatic efficiency (η_T^{dia}) is defined according to expression 5.30.

$$\eta_T^{dia} = \frac{\dot{W}_C^{dia}}{\dot{W}_{Ts}^{dia}} = \frac{\dot{W}_C^{ad} + \dot{Q}_C}{\dot{W}_{Ts}^{dia}} = \frac{\eta_m \cdot \dot{W}_T^{ad} + \dot{Q}_C}{\dot{W}_{Ts}^{dia}} \tag{5.30}$$

Where heat transfer to the compressor ($\dot{Q}_C$) was the occurring when the turbine map was measured. Introducing equations 5.30, 5.29, 5.28 and 5.27 into equation 5.26, the following expression is obtained.

$$\begin{aligned} &\Delta N = K \cdot \left(\frac{\eta_m \cdot \dot{W}_T^{ad} + \dot{Q}_C}{\dot{W}_{Ts}^{dia}} \cdot \dot{W}_{Ts}^{dia} - \frac{\dot{W}_{Cs}}{\eta_C^{dia}} \right) = \\ &K \cdot \left(\eta_m \cdot \dot{W}_T^{ad} + \dot{Q}_C - \left(\frac{\dot{W}_{Cs}}{\eta_C^{ad}} + \dot{Q}_C \right) \right) = K \left(\eta_m \cdot \eta_T^{ad} \cdot \dot{W}_{T,s}^{ad} - \frac{\dot{W}_{Cs}}{\eta_C^{ad}} \right) \end{aligned} \tag{5.31}$$

As it is observed, turbocharger speed is calculated using the same expression whether adiabatic maps and turbocharger maps are used (equation 5.25) or manufacturer maps are used without any model (equation 5.31). And so the same prediction in turbocharger speed will be obtained as also was deducted by the analysis of turbospeed performed in section 5.3.2.1, nevertheless only turbocharger model using adiabatic maps provided accurate prediction for turbine and compressor outlet temperatures and the ratio between isentropic compressor and turbine power.

5.4.3 Analysis of model improvements for a given case

5.4.3.1 Compressor performance

Two operative points from turbochargers #1 and #2 have been showed on compressor performance map showed in figure 5.24. Those points correspond to extreme engine operative conditions, high speed and load for turbocharger #1 represented in the top map corresponding to engine conditions of 3000 rpm and 100% of load. And low engine speed and load for turbocharger #2 represented in bottom map corresponding to 1500 rpm and 12% of load. As it is observed in figure 5.24 for both operative conditions, proposed turbocharger model provides better results in compressor performance prediction since its simulated average value (black star) is over the measured operative point (code of symbols according to figure legend). Nevertheless, when only manufacturer maps are used for turbocharger performance simulations, computational results are showing big errors predicting compressor average values (grey star). It is observed how for the highest engine load, conventional calculation way underestimates turbocharger speed, and so mass flow and compression ratio. However for the lowest engine load, simulation using manufacturer information overestimates turbocharger speed and so the mass flow and pressure ratio.

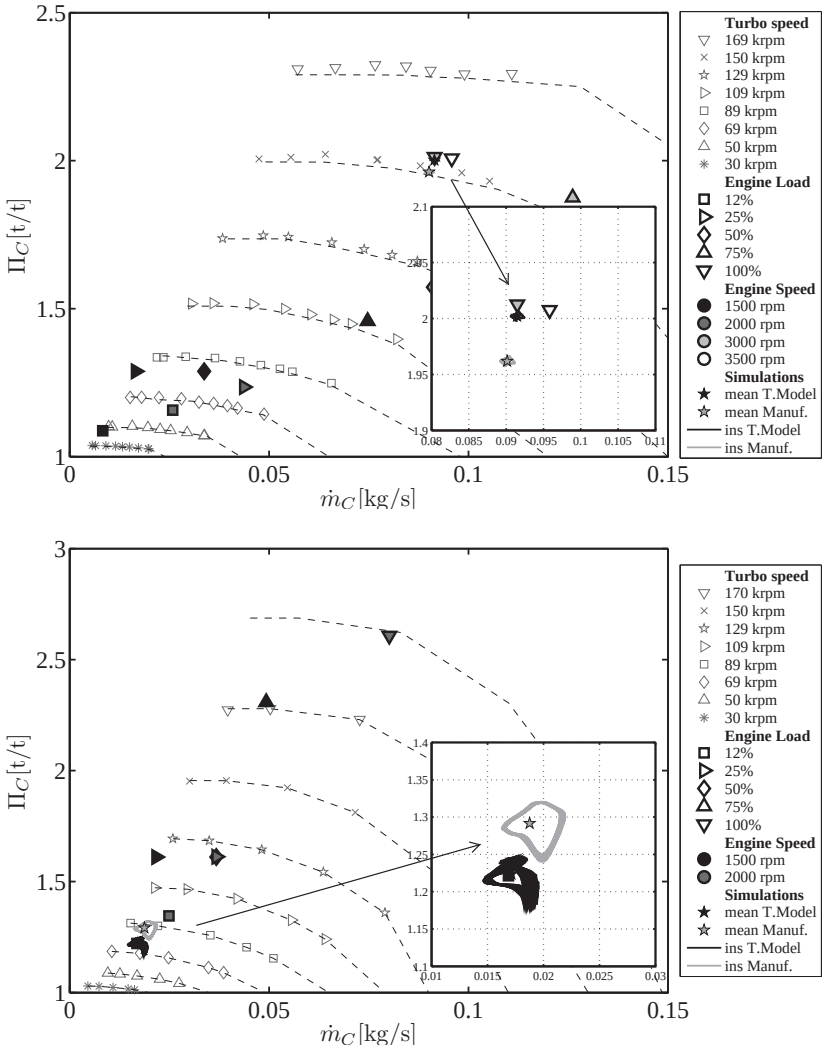

Figure 5.24: Effect of turbocharger submodels on compressor performance prediction. Top: T.#1 Engine speed 3000 rpm, load 100%. Bottom: T.#2 Engine speed 1500 rpm, load 12%.

Figure 5.25 shows errors predicting compressor performance for hot pulsating flow tests on the turbine side for the cases showed in table 5.1 versus measured compressor power. Those errors have been computed as the relative difference between averaged modelled parameters and measured ones. Simu-

lations using manufacturer maps measured under steady hot conditions have been represented with grey series. Any turbocharger model (heat transfer model, mechanical losses model, compressor and turbine geometrical models for acoustics non-linear and extrapolation procedure) have been used for simulations using manufacturer maps information since those effects are mixed within that kind of maps. Results using proposed turbocharger models and adiabatic maps have been represented in black series. Both simulations have been performed imposing compressor inlet conditions (pressure and temperature) and resistance load curve at compressor outlet. Differences in modelled parameters are due to the unbalance predicting compressor and turbine powers.

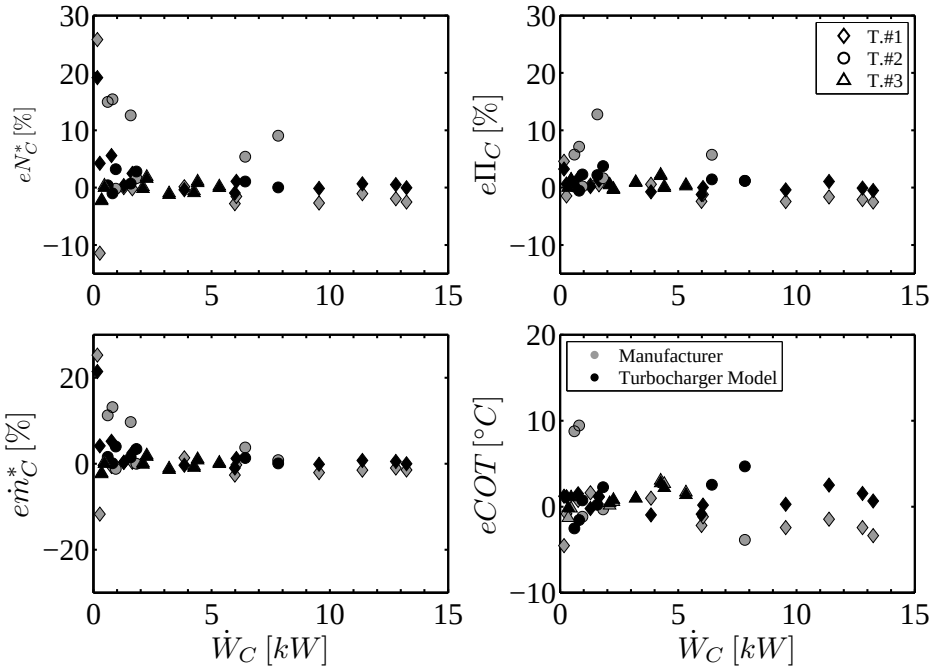

Figure 5.25: Errors comparison predicting compressor performance, using or not turbocharger submodels.

As figure shows, most testing points using proposed turbocharger model are predicted with an accuracy of ±5% even for the low power points (unless the lowest power point for turbocharger #1 which error in speed raises up to 20%). Nevertheless errors predicting compressor performance when manufacturer maps are used with any turbocharger model are considerably bigger.

That is due to the appearing big errors in turbine mass flow prediction observed in figure 5.26 when only the narrow range of information provided for the turbine by the manufacturer is used. In that case no extrapolation methodologies have been included to extend turbine maps when it is working under pulsating flow conditions, biggest differences are observed for turbocharger #2. As it is observed in figure 5.26, when only manufacturer maps are used turbine mass flow is over predicted for most operative conditions. That makes the turbocharger to accelerate what is translated into an over prediction in compressor average parameters (compression ratio, corrected mass flow and outlet temperature) as it is observed in figure 5.25. For the highest turbocharger load conditions, turbo speed slightly decelerates moving compressor operative point to lower operative power consumption, decreasing so its pressure ratio and governing mass flow. That deceleration is produced by an underestimation of turbine mass flow prediction as it is observed in figure 5.26 when no extrapolated maps have been used. Biggest differences have been observed for turbochargers #1 and #2 (both VGT turbochargers), while for the smallest turbocharger both simulations showed similar results for compressor performance. Operative point for turbocharger #1 corresponding to engine conditions 1500 rpm - 12% (the lowest power point) showed the biggest error in turbocharger performance, as it was shown in figure 5.11 that point was at 30,000 rpm and placed in the surge limit what makes its modelling quite complex since small variations in power prediction can lead to big errors in turbocharger speed prediction.

5.4.3.2 Turbine performance

Figure 5.26 shows errors in turbine performance prediction for pulsating hot flow campaign of turbochargers #1, #2 and #3 using performance maps with any proposed turbocharger model and using adiabatic maps coupled to proposed turbocharger model. The former has not included any corrector term neither for the pulsation nor the heat transfer effects, and has directly used those maps in a quasi-steady way to determine turbine characteristics. Second methodology has used adiabatic maps but including proposed sub-models accounting for heat transfer, pulsation effects (instantaneous extrapolation) and mechanical losses in a quasi-steady way. As it is observed, turbine prediction is improved for most operative conditions in all controlled parameters. That improvement is more pronounced from the low to medium turbine power range. Turbine performance prediction using manufacturer maps shows bigger

and more dispersed errors in corrected mass flow and expansion ratio. That is due to no extrapolation techniques have been used for simulations using manufacturer maps and heat transfer effects have not been considered. Turbine outlet temperature prediction is worsened when manufacturer maps are used in simulations. It is due to the fact that heat transfer fluxes occurring when turbine map was measured (those that are included in manufacturer map) were not be the same than those occurring in particular tested points. That uncertainty justifies the importance of having a heat transfer model able to calculate heat fluxes for any engine operative condition.

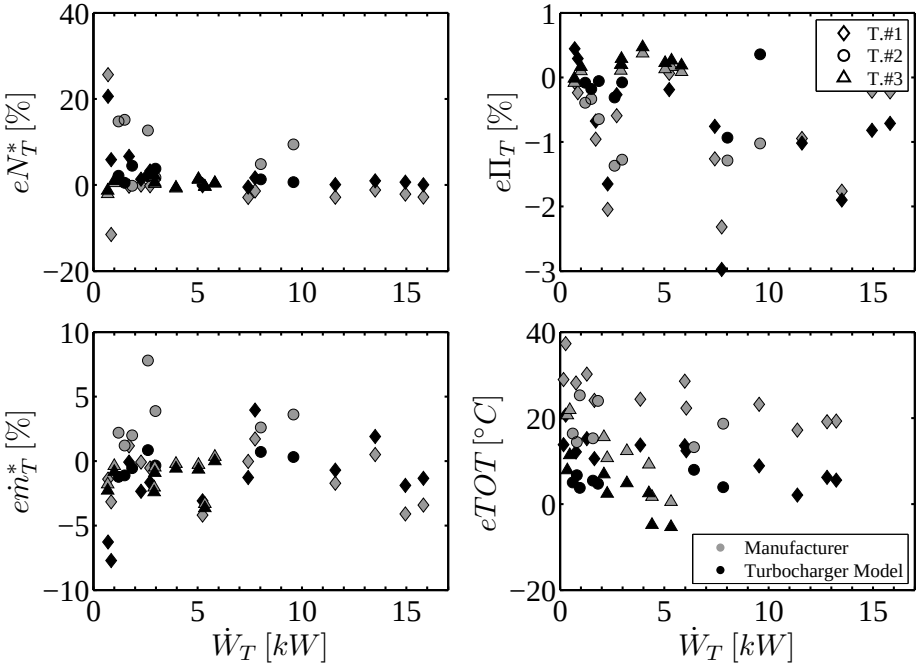

Figure 5.26: Errors comparison predicting turbine performance, using or not turbocharger submodels.

Figure 5.27 shows instantaneous calculation of turbine performance under pulsating flow conditions using proposed turbocharger model and manufacturer map. Two engine operative points corresponding to high load (and high power) have been chosen to show the impact of turbine extrapolation and rest of turbocharger sub-models on turbine performance. Top map corresponds to engine conditions of 3500 rpm and 100% of load for turbocharger #1. That operative point corresponds to the last diamond (the one with highest power)

of figures 5.25 and 5.26. The bottom map corresponds to engine conditions of 2000 rpm and 100% of load for turbocharger #2. Those operative conditions correspond to the last circle (the one with highest power) in figures 5.25 and 5.26.

As it is observed, for high pulses amplitude (both showed points), turbine map provided by the manufacturer and used without any extrapolation of data does not provide enough information to well reproduce the instantaneous mass flow across the turbine. Typical turbine modelling using manufacturer map without extrapolate (grey loop) keeps constant turbine effective area for higher pressure ratios than the measurements in the map. That situation is represented on the top figure 5.27 where mass flow is under predicted both in instantaneous and average value (grey loop and star) when no extrapolated maps are used. Turbine power is under predicted too, what makes turbocharger shaft to decelerate, underestimating so compressor and turbine parameters as it was observed in figures 5.25 and 5.26. Meanwhile the bottom of figure 5.27 shows a pulsating situation where not enough information is provided by manufacturer map on the left side of the occurring turbocharger speed. In that case simulation code provides instantaneously higher mass flow than the one calculated by the proposed turbocharger model. This overestimation in turbine instantaneous mass flow leads to an overestimation in turbine instantaneous power what accelerates turbocharger and overestimating so compressor and turbine modelled parameters (the last grey circle in figures 5.25 and 5.26). Meanwhile proposed turbine extrapolation procedure calculates instantaneously mass flow across turbine although the instantaneous loop moves far from the steady measurements. As it is observed, average value provided for turbine mass flow is quite near to the one measured under pulsating hot flow conditions using turbocharger proposed model. The same tendency has been observed for most of pulsating tested points, where proposed turbocharger model provided better results in turbine pressure ratio and mass flow. That is due to black star (from proposed model) was nearer than the grey star (manufacturer information) to the corresponding symbol according to the plot legend.

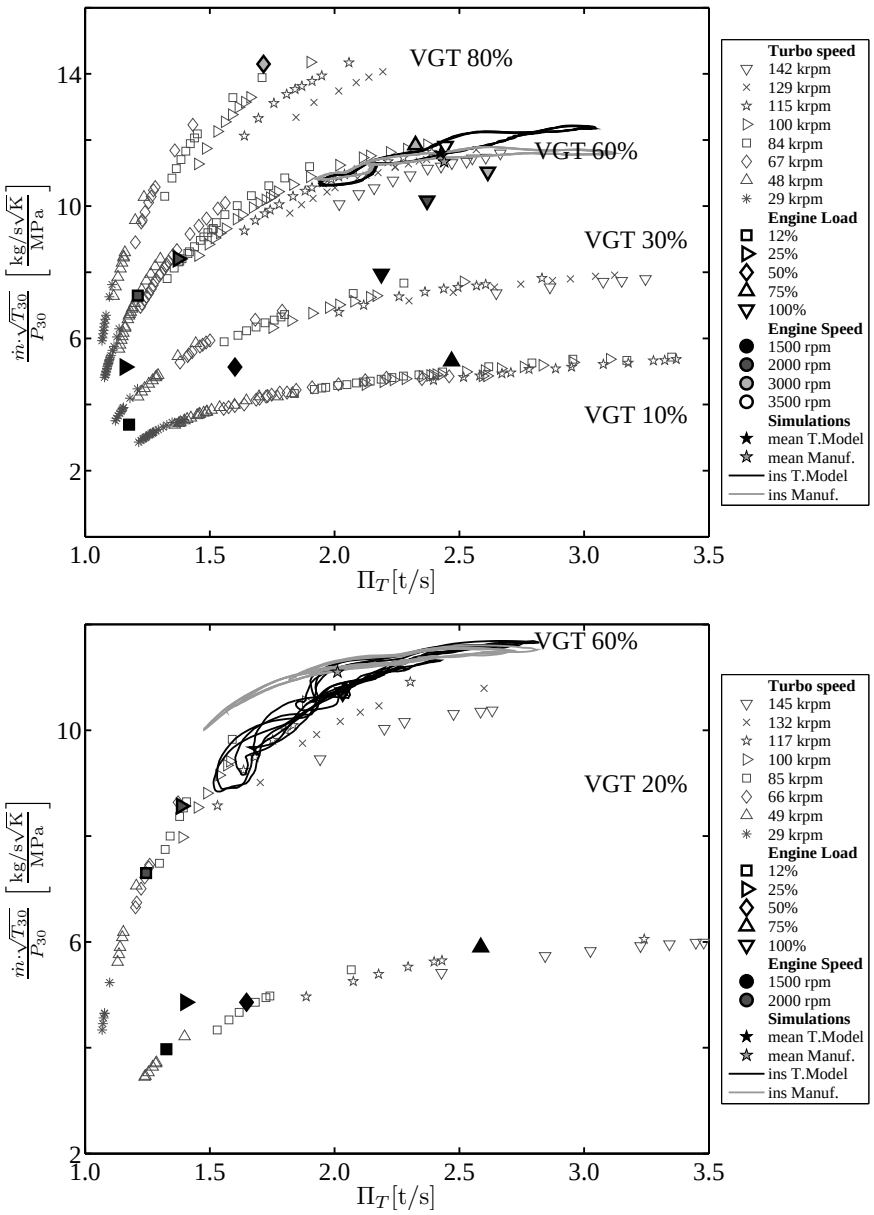

Figure 5.27: Effect of extrapolation procedure on turbine pulsating performance. Top: T.#1 Engine speed 3500 rpm, load 100%. Bottom: T.#2 Engine speed 2000 rpm, load 100%.

5.5 Influence of Pulsating Flow in Turbine Performance

In this section the influence of amplitude and frequency of pulsating flow on the instantaneous and average turbine efficiency has been studied. With that aim, an extensive experimental test campaign of a small radial inflow turbine working under cold pulsating flow has been presented. Turbocharger measured parameters from cold pulsating flow campaign have been compared with the ones obtained from 1-D modelling using turbocharger model introduced into OpenWAM [189] as it was discussed in [147].

5.5.1 Applied Experiment

Methodology followed in this work has been to perform quasi-adiabatic pulsating flow experiments on the turbine side using the test rig presented in this Thesis. Experiments on compressor side have been performed with continuous flow to isolate pulse phenomena of turbine side from compressor side. Table 5.2 summarizes tested frequencies used to simulate effect that engines with different number of cylinders at different rotational speeds have on turbine performance. Engines with 2, 3 and 4 cylinders at different speeds can be simulated. For each selected frequency, three different amplitudes have been tested as it is shown in table 5.3.

Table 5.2: Frequencies of pulsating flow for different number of cylinders and engine speeds. Engine speed in bold font (rpm), pulses frequency in normal font (Hz).

	2 cylinders		**3 cylinders**		**4 cylinders**	
	F6	F5	F4	F3	F2	F1
VGT 0%	**1000**	**1250**	**1000**	**1250**	**1000**	**1250**
	16.67	20.83	25.00	31.25	33.33	41.67
VGT 50%	**1500**	**2000**	**1500**	**2000**	**1500**	**2000**
	25.00	33.33	37.50	50	50	66.67
VGT 100%	**3500**	**4000**	**3500**	**4000**	**3500**	**4000**
	58.33	66.67	87.50	100.00	116.67	133.33

In addition, three different turbine VGT openings have been tested to consider the effect of vanes position in turbine pulsating performance and

Table 5.3: Amplitudes tested for different turbine VGT openings.

Amplitude	**VGT 0%**	**VGT 50%**	**VGT 100%**
A-1	0.40 bar	0.50 bar	0.50 bar
A-2	0.25 bar	0.30 bar	0.35 bar
A-3	0.15 bar	0.15 bar	0.25 bar

covering a region within a given engine operative conditions. Those openings have been named 0% (the closest stator vanes position), 100% (when stator vanes are completely opened) and 50% (an intermediate VGT opening). Those positions are shown on the right chart of figure 5.28. Five operating points have been tested at every turbine corrected speed in order to construct an iso-speed line for each VGT opening (figure 5.28). This procedure allowed making plots of η_{Ts} versus σ. The five points were split evenly in compressor map between choke and surge limits, as it is shown on the left chart of figure 5.28. Frequency and amplitude tests were performed on each turbine operative point. For each point, before and after the unsteady flow tests, two steady flow points were also measured. Average value from those steady tests were used to fit turbine efficiency and mechanical losses models and as base line for comparison. In summary, a matrix of 285 tested points was obtained.

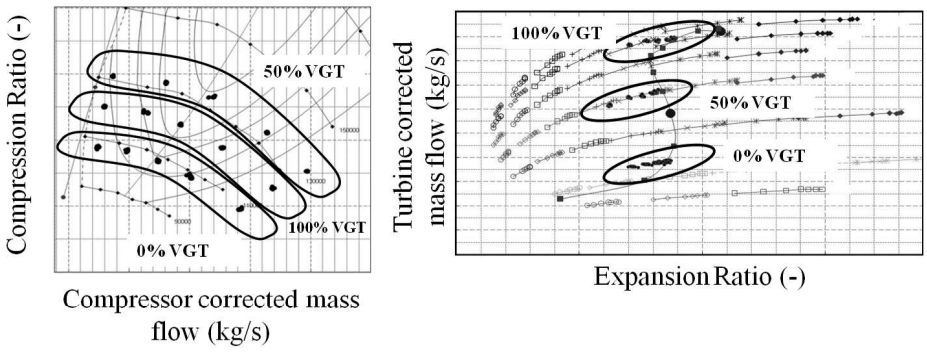

Figure 5.28: Test campaign in compressor and turbine maps.

Effect of pulses in turbine makes the instantaneous isentropic efficiency move along a wide range of proposed turbine efficiency extrapolation equation 4.33. In addition, changes on turbine operation, as variations in the turbine inlet temperature, generate variations on K_3 parameter (equation 4.35) and

so the turbine efficiency curve is updated moving upper and lower from the original fitted equation.

5.5.2 Model Validation

Compressor model works imposing steady flow conditions at its inlet and using manufacturer map information. A back-pressure valve has been introduced at compressor outlet to represent the same conditions as it would be in the gas stand. Turbine model works imposing pulsating flow conditions from test campaign, i.e. incident pressure and entropy level at the inlet and just second reflected pressure at the outlet. Turbocharger shaft is the element where mechanical losses have been taken into account, using the model proposed by Serrano et al. [153, 154]. Turbocharger model described in this section coupled with the steady flow models for turbine efficiency and mechanical efficiency have been used to simulate pulsating test campaign.

First of all, compressor map and its model have been validated imposing and fixing the same turbocharger speed and installation resistance curve measured in the gas stand. Doing so, compressor and turbine behaviours are independent running simulations. Differences between compressor modelled parameters and measured ones are the own errors of turbocharger map used in modelling. Figure 5.29 shows compressor map validation for each VGT position where different symbols have been used according to amplitudes listed in table 5.3. Errors in mass flow parameter and compression ratio have been calculated according to equation 5.32.

$$Error(\%) = \frac{X_i - X_j}{X_j} \cdot 100 \tag{5.32}$$

Where X refers to the studied parameter, being i the modelled case and j the measured one. Modelled parameters are the average result from integrating the instantaneous simulated information, meanwhile test values are directly the mean value given by gas stand sensors. Errors have been represented versus the deviation in blade speed ratio (σ), defined as equation 5.33 shows. This new variable takes into account the blade speed ratio where turbine isentropic efficiency is the maximum and the one where it is zero, on the right side of turbine isentropic efficiency curve (the lowest expansion ratio).

$$\bar{\sigma}\,deviation = \frac{\bar{\sigma} - \sigma\big|_{\text{max efficiency}}}{\sigma\big|_{\text{efficiency}=0} - \sigma\big|_{\text{max efficiency}}} \tag{5.33}$$

Five tested points of compressor map have been shown in graphs grouped by VGT position versus deviation in blade speed ratio. Points near compressor surge are those with the lower expansion ratio in the turbine (the higher blade speed ratio) and so the higher deviation. Meanwhile points near choke in compressor are those with the higher expansion ratio in the turbine (the lower blade speed ratio) and so they are near to the blade speed ratio where the efficiency is the maximum and so the lowest σ deviation or negative σ deviation.

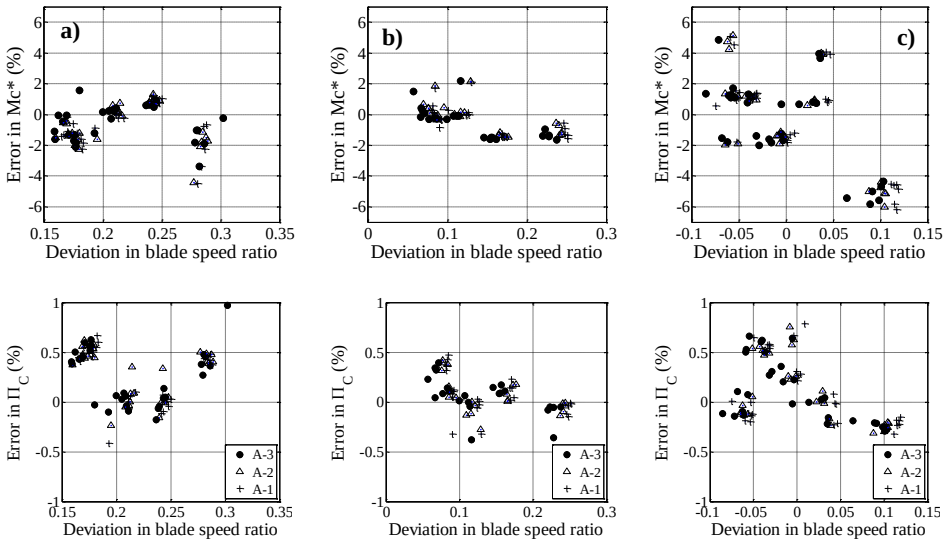

Figure 5.29: Compressor map validation per each VGT opening, a)0%, b) 50%, c) 100% opening. Imposed turbocharger speed.

As it is shown in figure 5.29 errors in compression ratio are below ± 1% for all tested points, differences in mass flow parameter are in a margin of ± 2% for most of the points. The higher is the deviation in blade speed ratio the higher is the error in mass flow parameter since operative points are closer to compressor surge limit. Where by the one hand mass flow is smaller and by the other hand small differences predicting compression ratio are translated into big errors predicting mass flow parameter. The second is due to compressor

lines in that region are considerably flat. This is the case of figure 5.29 for 100% VGT opening and deviation values around 0.1. Once turbocharger model has been checked. Imposing turbocharger speed, computational simulations have been repeated leaving free turbocharger speed, what means updating speed by balancing turbocharger powers. Those simulations have been used to analyse frequency and amplitude effects on turbine performance. Differences between OpenWAM simulations and testing data are shown in figure 5.30, figure 5.31 and figure 5.32 for each turbocharger parameter and VGT openings.

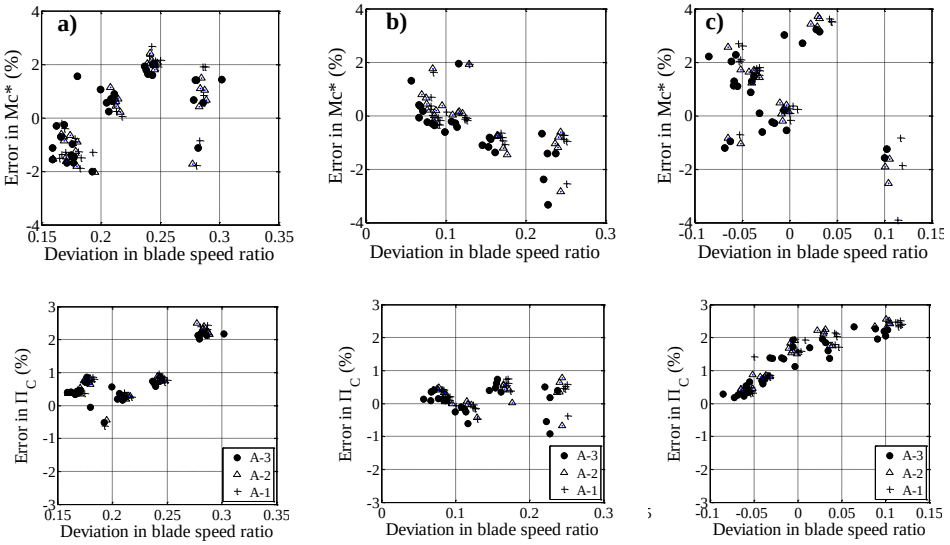

Figure 5.30: Errors in compressor parameters when turbocharger speed is let free, a) 0%, b) 50%, c) 100% VGT opening.

As figure 5.30 shows, errors in compressor mass flow parameter are quite well distributed around 0 when turbocharger speed is let free. In case of 100% and 0% VGT openings compressor mass flow error at the highest deviation in blade speed reduced when turbocharger speed was let free. This phenomena can be observed in figure 5.30 (cases a and c), where errors were in a margin of $\pm$ 2%, meanwhile there were higher negative errors when compressor model was validated, as it is shown in figure 5.29. This compensation in mass flow parameter for 0% and 100% VGT opening is explained by the change in compression ratio shown in figure 5.30 and turbocharger speed in figure 5.31. For the 50% VGT opening, errors in compressor parameters are quite similar to those shown in figure 5.29, although error predicting mass flow parameter

near the surge region (higher deviation in blade speed ratio) slightly increased. Some of the highest errors in figure 5.30 are for compression ratio in case of 100% VGT and maximum σ deviation, probably due to the worst fitting of isentropic turbine efficiency model to experimental data in 100% VGT opening case. Nevertheless the biggest errors are always below 4%. In general it is observed that the higher is the σ deviation the higher are the errors, both in turbine and compressor map. It can be also observed in figure 5.30 that there is not any clear trend predicting compressor error with pulses amplitude.

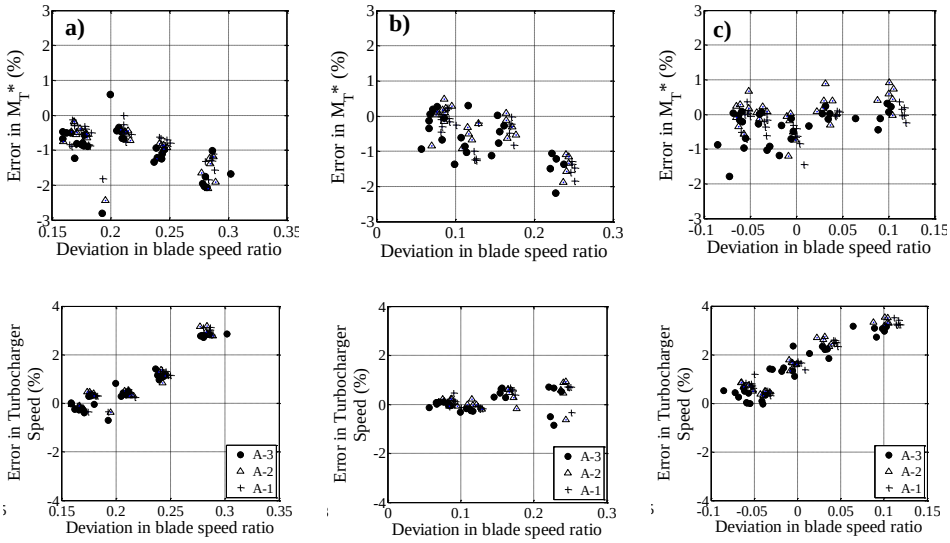

Figure 5.31: Errors in turbine mass flow parameter and turbocharger speed when the second is let free, a) 0%, b) 50%, c) 100% VGT opening.

Figure 5.31 shows error modelling turbine mass flow parameter for different VGT openings. As it is shown, there is not a clear tendency of this error with the σ deviation or the amplitude of the pulse. Most of points are in a region of $\pm$ 2% predicting turbine mass flow parameter. Errors in turbine reduced speed shows similar trend than done in compression ratio. Since it increases positively with σ deviation and the higher are in the 100% VGT case, nevertheless they are contained below 4%. Those errors can be derived from turbine efficiency overestimation since few data was available for turbine extrapolation technique. Other conclusion of turbocharger presented model is the error shown in figure 5.32 predicting turbine outlet temperature. That error has been defined according to equation 5.34 for the absolute error and

equation 5.35 for the relative one.

$$Error(C) = T_{\text{model}} - T_{\text{test}} \tag{5.34}$$

$$Error(\%) = \frac{T_{\text{model}} - T_{\text{test}}^{\text{out}}}{T_{\text{test}}^{\text{in}} - T_{\text{test}}^{\text{out}}} \tag{5.35}$$

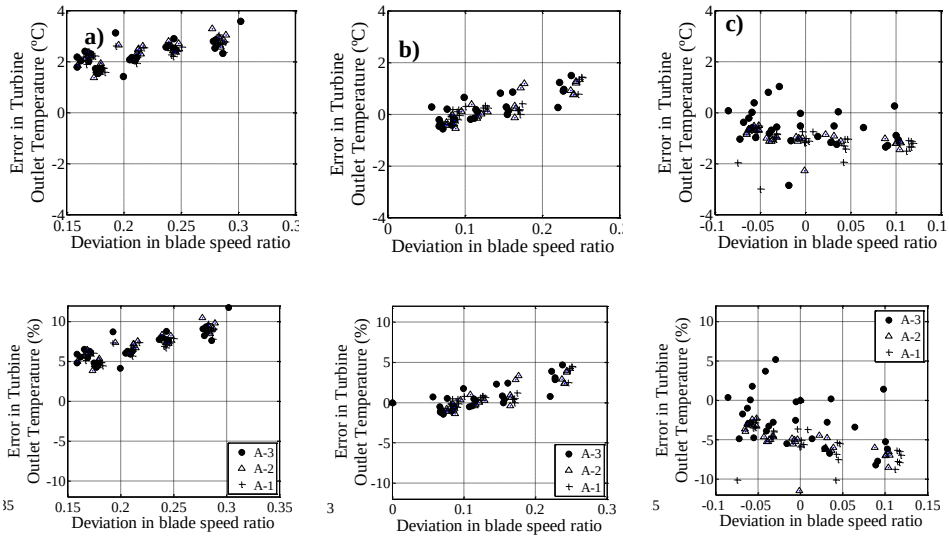

Figure 5.32: Errors in turbine outlet temperature when turbocharger speed is let free, a) 0%, b) 50%, c) 100% VGT opening.

As figure 5.32 shows, errors predicting turbine outlet temperature are below ± 2ºC for the majority of points. Due to test campaign was performed with cold flow (low temperatures), errors in percentage showed high values. Observed differences in turbine outlet temperature are a consequence of all the assumptions and simplifications performed in turbine isentropic efficiency calculation and extrapolation in the proposed quasi-steady way. In summary, like all the errors are below ± 10% for temperature and below ± 5% for the rest of turbocharger variables, they are considered reasonable low. It means, adequate for analysing turbine efficiency variations with pulsating flow conditions from the results calculated by the models used and fitted in present work.

5.5.3 Results Discussion

In this section three examples of instantaneous efficiency excursions (one of each VGT opening) are shown in figure 5.33. Main characteristics of the pulse (VGT opening, frequency and amplitude) are listed in figure 5.33 legends. Differences between modelled and measured compressor parameters (compressor mass flow parameter and compression ratio) are also shown in left part of figure 5.33. Good agreement in compressor behaviour is shown in those examples modelling pulsating flow on the turbine side; as it was also concluded from the analysis of figure 5.30, figure 5.31 and figure 5.32. On the right side of figure 5.33, turbine simulated efficiency is shown. Solid line represents turbine isentropic efficiency curve obtained with proposal of [131] for averaged reduced speed, instantaneous simulation of mechanical efficiency and turbine efficiency are shown in dotted grey and black lines respectively. The upper and lower boundaries for the fitted efficiency curve, (due to variations in speed and stagnation inlet temperature which affect K_3 parameter), are shown in dotted black. It is shown during simulations, as instantaneous efficiency values are placed between those boundaries limits. Instantaneous turbine isentropic and mechanical efficiency under pulsating flow conditions have been obtained from OpenWAM calculations. Turbine average efficiencies under these conditions have been calculated from previous instantaneous values, by weighting with turbine instantaneous power, according to the expressions 5.36 and 5.37.

$$\eta_T^{avg} = \frac{\sum \left(\dot{W}_{Ts}^{ins} \cdot \eta_T^{ins} \right)}{\sum \dot{W}_{Ts}^{ins}} \tag{5.36}$$

$$\eta_{mech}^{avg} = \frac{\sum \left(\dot{W}_{Ts}^{ins} \cdot \eta_{mech}^{ins} \right)}{\sum \dot{W}_{Ts}^{ins}} \tag{5.37}$$

Figure 5.34 shows the average turbine isentropic efficiency and average mechanical efficiency of the turbocharger for each of the VGT openings and the five operative points (showed by its average σ deviation). Both figures make distinctions between pulse amplitudes (grey tones) and frequency of the pulse (with symbols). Legend is related with table 5.2 and table 5.3. As it is shown in figure 5.34, points with higher average efficiency, both isentropic and mechanical, are obtained in operative points with minimum σ deviation. This

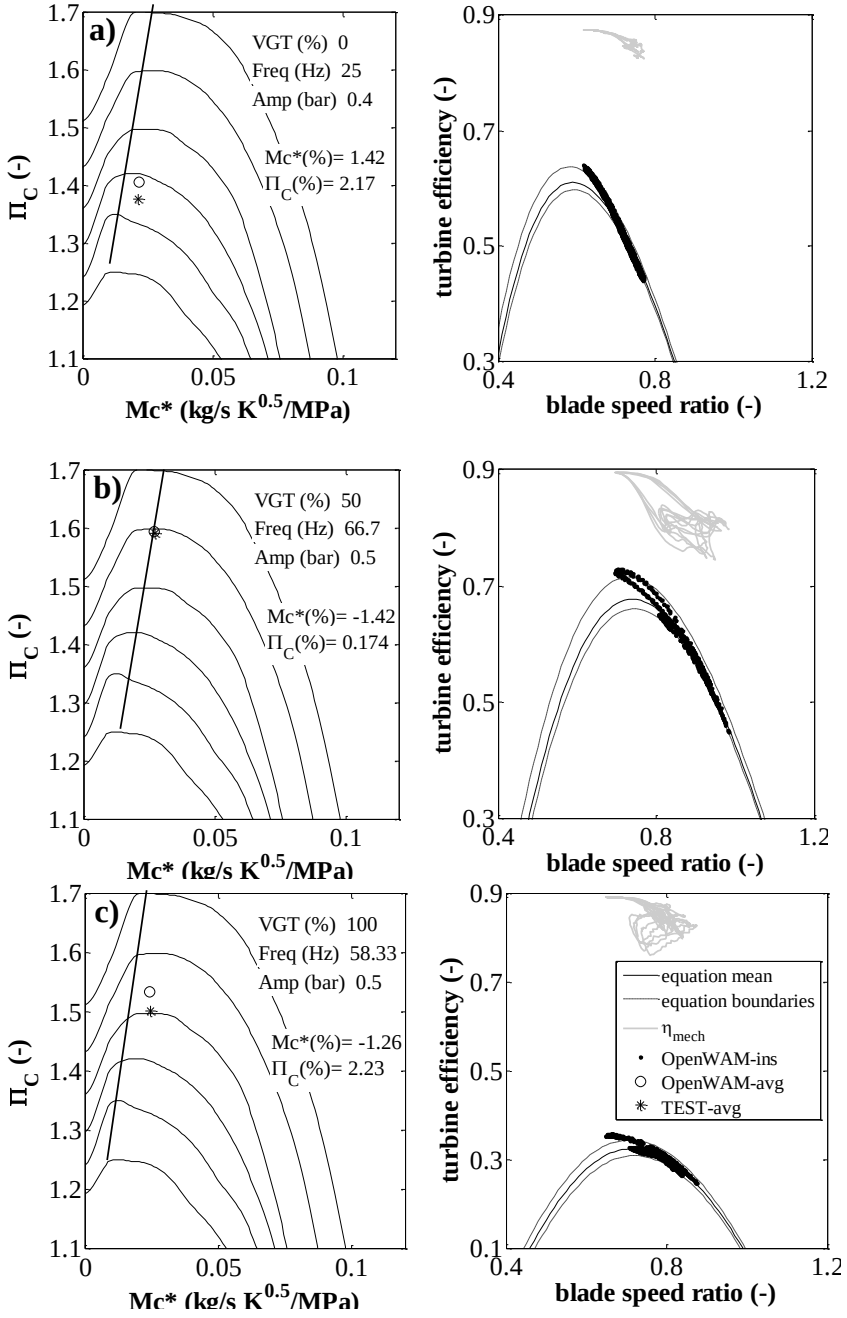

Figure 5.33: Modelling example, a) 0%, b) 50%, c) 100% VGT openings.

is the main conclusion of unsteady flow influence. The higher is the variation of σ with respect to σ of maximum efficiency the worst is average turbocharger efficiency.

Variations of efficiency with respect to σ deviation are 8 points in η_{Ts} (left side of figure 5.34) and up to 7 points in mechanical efficiency (right side of figure 5.34). It is also deducted from figure 5.34 that the closest are operative conditions to σ of maximum efficiency the less are η_{Ts} and η_m affected by the upstream flow unsteadiness (amplitude and frequency), this is especially evident at 50% VGT opening.

Analyzing now variations observed with pulses amplitude; left side of figure 5.34 shows that the higher is the pulse amplitude (A1 or black color) the lower is turbine efficiency (cases of 50% and 100% VGT opening are more evident). Left side of figure 5.34 shows that the effect of pulses amplitude on turbine isentropic efficiency is higher as the VGT opening increases. Amplitude phenomenon is also clearly observed on the left side of figure 5.34, where for a given frequency, the highest is the amplitude the lowest is the mechanical efficiency. Analyzing now fixed amplitude on left side of figure 5.34 (series with the same color) but different frequencies (different symbols) it is observed that for low amplitudes there is not any significant variation of performance with pulses frequency, as it would be expected. Finally, for the highest amplitude (A1) different trends depending on VGT opening are shown. In the 50% VGT case, the lowest efficiency values appear for the lowest frequencies (F6 and F5) even the differences are not very significant. In the 100% VGT case the lowest efficiency appear for medium frequencies (F3, F4 and F5) with differences up to 2 points.

Comparing both modelled and experimental results, it has been observed that mechanical efficiency model and turbine isentropic efficiency model (both fitted just with steady-flow data) can be used in a one-dimensional gas-dynamics code to reproduce turbocharger behaviour with reasonable accuracy. Errors below $\pm 5\%$ for most of the operative conditions have been obtained predicting compressor and turbine performance. It is worth highlighting that for the 50% VGT opening case, at which many data for η_{Ts} model fitting were available in the present study, errors were below $\pm$ 2%. The main conclusion of unsteady flow influence is that the higher is the variation of σ with respect to σ of maximum efficiency the worst is average turbocharger efficiency. It has been also concluded that turbine efficiency is less affected by flow unsteadiness (both pulses and amplitude) at VGT operative conditions close to σ of

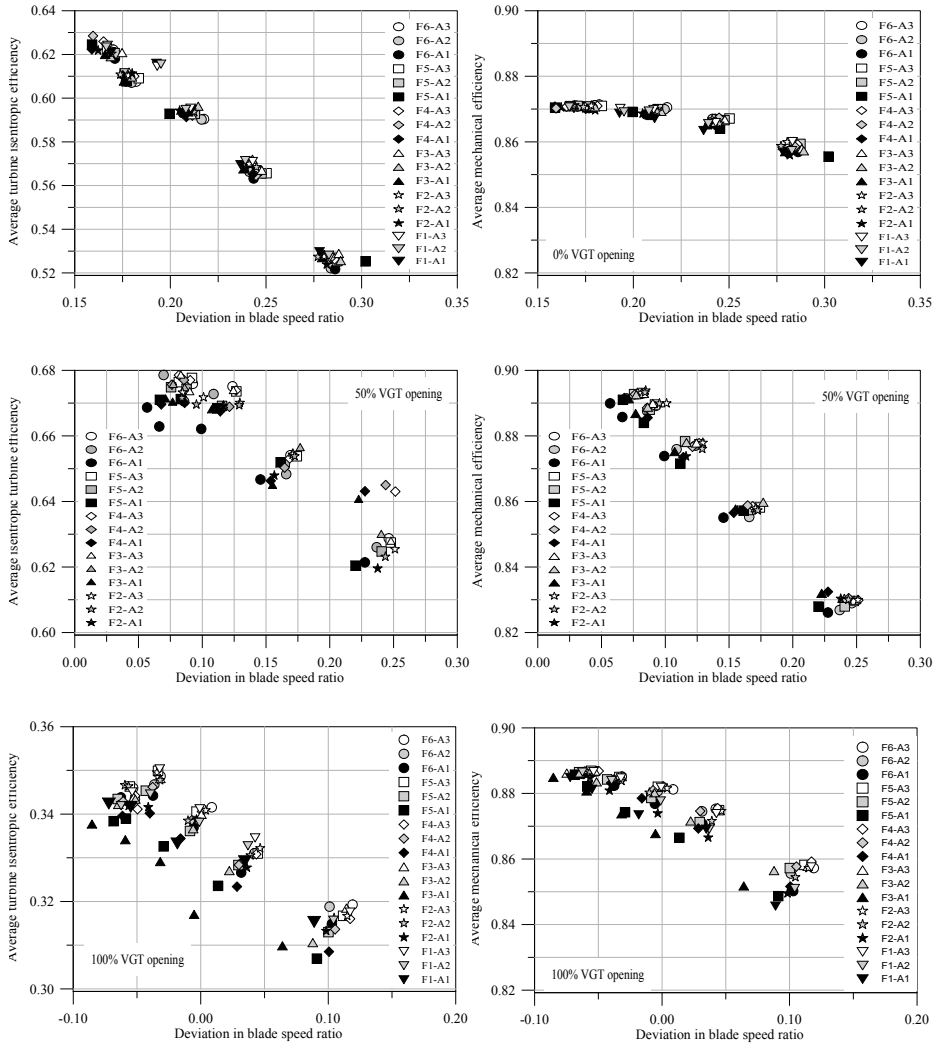

Figure 5.34: Effect of pulses frequency and amplitude on turbocharger efficiencies. Left: Average η_{Ts}, Right: Average η_m

maximum efficiency. Finally, it has been also check that the higher is pressure pulses amplitude the lower is the average VGT efficiency; in addition, such a turbocharger efficiency reduction due to pulses amplitude trends to grow with the VGT opening.

5.6 Summary

In the present chapter pulsating flow tests on the turbine side with high inlet temperature have been used to validate global turbocharger model. In a first section, interactions among different turbocharger sub-models have been discussed, since those models have been developed to be used in a quasi-steady way. As it was explained, mechanical losses model is affected by instantaneously pressure waves at compressor and turbine side since those pressures determine turbocharger axial thrust. Pulsating flow affects too the heat transfer model since instantaneous mass flow on turbine/compressor side affects to Reynold's number calculation inside that volutes that is used to estimate heat transfer coefficients.

In the next section, global model validation has been carried out simulating different engine conditions measured on the gas stand with steady and pulsating hot flow on the turbine inlet. Those points have been chosen to reproduce from low to high engine speeds and from partial to full load engine conditions. Computational simulations have been carried out using 1-D gas-dynamic code OpenWAM, averaged values from those simulations have been compared to averaged recorded parameters of the gas stand measurements. Those engine conditions have been simulated activating and deactivating HTM (Heat Transfer Model) in order to validate it under steady and pulsating flow conditions using gas-dynamic simulation code OpenWAM^{TM}. Simulations have been performed including or not HTM in order to show the improvement in compressor and turbine outlet temperatures prediction (COT and TOT). Histogram figures have been used in order to show how HTM reduced predicting errors and dispersion, mainly for the low load conditions. For those conditions (corresponding to NEDC), heat transfer losses at turbine and compressor cases exceed 50% of the available energy at the turbine inlet. The same analysis was done comparing enthalpy drops where the benefit of using HTM was observed too. As it has been discussed in that section, proposed turbocharger model provided accurate results for pulsating average turbocharger parameters such as corrected mass flows, pressure ratios and rotational speed. As it has been observed, turbocharger speed was well predicted independently of using or not heat transfer model. Nevertheless if turbine or compressor outlet temperature are desired to be determined accurately, HTM will be needed since big differences beyond 20 ºC will appear. In case of using commercial engine simulation codes without turbocharger heat transfer packages it will

be necessary to introduce a corrector efficiency chart in order to kept that temperature. Those tables will depend on engine speed, load, engine mass flow and pulsating characteristics. Using those tables make inoperative problem analysis since coefficients are not physically-based. Pulses analysis have shown good agreement with experimental measurements both in time and frequency domain for both turbine inlet and outlet pipes. Small shift at turbine inlet reflected pressure, for higher engine speed (higher frequencies) have been observed what will be due to the proposed turbine geometrical model is too simple to account for mass losses at turbine stator. Nevertheless for the studied engine speeds and loads, reasonably good results for sound pressure level prediction on turbine reflected and transmitted waves have been obtained.

In the last section, improvements of proposed turbocharger model have been shown comparing average and instantaneous results of pulsating hot flow simulations. In order to analyse the importance of the proposed model, those tests have been simulated using the same gas-dynamic code but following two different methodologies. First set of results will be provided using the standard source of information for commercial turbocharger simulation codes. That is turbine and compressor performance maps measured under hot steady flow conditions. No heat transfer or mechanical losses models will be needed since turbine efficiency will intrinsically include those effects. On the other hand simulations will be carried out using proposed turbocharger model including sub-models to extrapolate turbine isentropic maps and to account for heat transfer and mechanical losses effects. As it has been observed, big errors appear predicting compressor and turbine performance when only manufacturer maps are used. Those errors appear for the whole operative range of turbocharger power, but biggest errors are located for reduced loads mainly on outlet temperature prediction. Big errors in turbine mass flow prediction have been also observed when manufacturer maps are used to reproduce pulsating flow on the turbine side. That is due to pressure pulsation can move instantaneously turbine operative point far from the steady state map measurements. Proposed turbocharger model showed a good accuracy predicting turbine mass flow due to the extrapolation techniques presented in chapter 4.

In addition, a wide test campaign has been also designed in order to study the effect of pulses' frequency and amplitude in VGT efficiency calculation, developing a data base with 285 points. From comparing both modelled and experimental results, it has been concluded that the mechanical efficiency model and turbine isentropic efficiency model (both fitted just with steady-

flow data) can be used in a one-dimensional gas dynamics code to reproduce the turbocharger behaviour with reasonable accuracy. As it has been shown, reasonable accuracy means predicting compressor and turbine variables with errors below ± 5% for most of the operative conditions. It is worth highlighting that, for the 50% VGT opening case, at which many data for η_{Ts} model fitting were available in the present study, the errors were below ± 2%. The main conclusion of unsteady flow influence was that the higher the variation of σ with respect to σ of maximum efficiency, the worse the average turbocharger efficiency. It has been also concluded that the turbine efficiency is less affected by flow unsteadiness (both pulses and amplitude) at VGT operative conditions close to t of maximum efficiency. Finally, it has been also checked that the higher the pressure pulses' amplitude, the lower will be the average VGT efficiency. In addition, such a turbocharger efficiency reduction, due to pulse' amplitude trends to grow with the VGT opening, i.e., the average efficiency decreasing trend, due to pulses' amplitude, almost disappears when VGT is closed. The hypothesis is that pulse lamination downstream VGT reduces instantaneous pressure ratio variation and therefore stabilizes the average efficiency.

References

[67] J. Galindo, J.R. Serrano, F.J. Arnau, and P. Piqueras. "Description and analysis of a one-dimensional gas-dynamic model with Independent Time Discretization". In: *Proceedings of the ASME Internal Combustion Engine Division 2008 Spring Technical Conference ICES2008*. 2008 (cit. on p. 218).

[68] J. Galindo, J.R. Serrano, F.J. Arnau, and P. Piqueras. "Description of a Semi-Independent Time Discretization Methodology for a One-Dimensional Gas Dynamics Model". In: *Journal of engineering for gas turbines and power* 131 (2009). DOI: 10.1115/1.2983015 (cit. on pp. 7, 218).

[103] J.M. Luján, J. Galindo, and J.R. Serrano. "Efficiency Characterization of Centripetal Turbines under Pulsating Flow Conditions". In: *SAE Technical Paper* 2001-01-0272 (2001) (cit. on pp. 59, 71, 214).

[119] P. Olmeda, V. Dolz, F.J. Arnau, and M.A. Reyes-Belmonte. "Determination of heat flows inside turbochargers by means of a one dimensional lumped model". In: *Mathematical and Computer Modelling* 57.7-8 (2013), pp. 1847 –1852. ISSN: 0895-7177. DOI: 10.1016/j.mcm.2011.11.078. URL: http://www.sciencedirect.com/science/article/pii/S0895717711007631 (cit. on pp. 93, 104, 105, 233).

[131] F. Payri, J.R. Serrano, P. Fajardo, M.A. Reyes-Belmonte, and R. Gonzalo-Belles. "A physically based methodology to extrapolate performance maps of radial turbines". In: *Energy Conversion and Management* 55 (2012), pp. 149–163 (cit. on pp. 166, 233, 234, 260).

[147] J.R. Serrano, F. Arnau, P. Fajardo, F. Vidal, and M.A. Reyes-Belmonte. "Contribution to the modeling and understanding of cold pulsating flow influence in the efficiency of small radial turbines for turbochargers". In: *Journal of Engineering for Gas Turbines and Power* Vol 134, Issue 10 (2012), p. 10 (cit. on p. 253).

[148] J.R. Serrano, F.J. Arnau, V. Dolz, A. Tiseira, and C. Cervelló. "A model of turbocharger radial turbines appropriate to be used in zero- and one-dimensional gas dynamics codes for internal combustion engines modelling". In: *Energy Conversion and Management* 49 (2008), pp. 3729–3745 (cit. on pp. 59, 63, 160, 170, 189, 215, 216, 231, 234, 271, 275).

[151] J.R. Serrano, P. Olmeda, F.J. Arnau, M.A. Reyes-Belmonte, and A. Lefebvre. "Importance of heat transfer phenomena in small turbochargers for passenger car applications". In: *SAE Int. J. Engines* 6(2) (2013), pp. 716–728. DOI: 10.4271/2013-01-0576 (cit. on p. 218).

[153] J.R. Serrano, P. Olmeda, A. Tiseira, L.M. García-Cuevas, and A. Lefebvre. "Importance of mechanical losses modeling in the performance prediction of radial turbochargers under pulsating flow conditions". In: *SAE Int. J. Engines 6(2)* 6(2) (2013), pp. 729–738. DOI: 10.4271/2013-01-0577 (cit. on pp. 8, 46, 48, 49, 93, 132, 157, 189, 216, 217, 255).

[154] J.R. Serrano, P. Olmeda, A. Tiseira, L.M. García-Cuevas, and A. Lefebvre. "Theoretical and experimental study of mechanical losses in automotive turbochargers". In: *Energy* 55 (2013), pp. 888 –898 (cit. on pp. 8, 46, 48, 49, 93, 132, 157, 189, 216, 217, 223, 233, 255, 271).

[189] *www.Openwam.org*. OpenWAM, CMT-Motores Térmicos; Universitat Politècnica de València (UPV). 2012 (cit. on pp. 7, 152, 188, 214, 218, 228, 253).

Chapter 6

Conclusions and Future Works

Contents

6.1 Introduction

The main objective of the present Thesis has been the development of a turbocharger model appropriated to be used coupled to 1-D engine simulation codes. That turbocharger model has been designed to account for several physics phenomena taking place when the turbocharger is coupled to an internal combustion engine (ICE). In order to simplify that problem and with the aim of improving current turbocharger models, it has been decided to analyse each phenomenon separately. These are,

- Heat transfer effects.
- Mechanical friction losses.
- Pulsating flow inside compressor.
- Pulsating flow inside turbine.

In order to analyse and quantify the contribution of each phenomenon into turbocharger global performance, specific testing methodologies have been developed. Those experiments have been used to create and validate individual sub-models accounting for each isolated phenomenon. To validate all models working coupled together, hot pulsating flow tests on the turbine side have been performed.

Several turbochargers have been studied in this Thesis to validate turbocharger sub-models using more testing data. They ranged from turbochargers used in truck applications (named in the Thesis LSTT, MSTT, SSTT used for turbine extrapolation purposes) to turbochargers used in car applications from small size turbochargers to the biggest ones (for acoustic and heat transfer models). Figure 6.1 shows sub-models composing presented turbocharger model and the specific tests carried out to develop and validate them. In the following paragraphs main contributions of the present Thesis have been summarized.

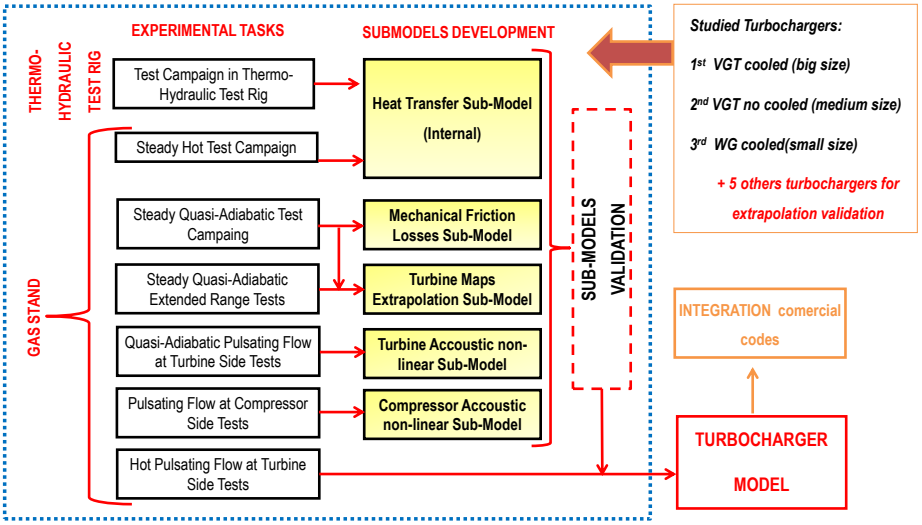

Figure 6.1: Schematic view of the turbocharger model

6.2 Main Contributions

Among the main contributions of this Thesis, the following topics can be pointed out.

- Development of a heat transfer model accounting for turbocharger internal heat transfer fluxes coupled to previously proposed models (mechanical losses [154] and fluid dynamic turbocharger models [148]).
- Validation of fluid-dynamics models for compressor and turbine accounting for acoustic non-linear effects.
- Development and validation of a physically-based methodology to extrapolate turbine performance maps.
- Integration of those models into a 1-D engine simulation code like OpenWAM^{TM} to simulate accurately turbocharger performance taking into account physics phenomenon described in the introduction section.

In that scenario, compressor/turbine isentropic maps are necessary as the data source for simulations, since performance represented there is independent from turbocharger/engine operative conditions. For that reason isentropic maps can be used to simulate turbocharger behaviour under any boundary conditions coupled to turbocharger submodels proposed in this Thesis. Later, proposed models have been used to account for particular simulation conditions (heat transfer, mechanical losses or pulsating flow). Although turbocharger modelling has been based on isentropic maps information and developed sub-models, having those maps is not the usual situation in engine modelling. That is due to the fact that manufacturer maps are not usually measured under adiabatic conditions (turbine is connected to an engine). In that situation, turbocharger proposed sub-models can be applied to discount heat transfer and mechanical losses from manufacturers maps, obtaining so adiabatic maps suitable to be used in turbocharger modelling. That procedure is necessary since manufacturer maps will only provide accurate simulation results in case of similar working operative conditions than those taking place when turbocharger maps were measured are being calculated. That assumption is not valid for engine off-design conditions or under urban driving conditions.

6.2.1 Heat Transfer Modelling

In the present Thesis a Heat Transfer Model (HTM) has been developed and validated to account for internal heat fluxes inside automotive turbochargers. To simplify internal heat transfer studies, the turbocharger unit was divided into 5 measurements planes. Those were placed according to the following criteria; one on turbine and compressor external cases and three measurements planes on the housing. The latest division was justified by housing complex geometry. Those three measurements planes were placed just in the housing middle section (where lubricating oil and coolant liquid enters the turbocharger), and the other two were situated near the compressor back-plate and near the turbine case. Three thermocouples were installed on each measurement plane, radially distributed to ensure one-dimensional assumption for heat transfer mechanism. That is, temperature difference across the axial direction was higher than radial dispersion. Once thermocouples had been installed on turbocharger cases, the unit was tested into a thermo-hydraulic test bench and into a gas stand to determine heat transfer correlations. Testing methodologies in both facilities have been presented and further described in

Chapter 3. Experiments on the first test bench were designed to determine turbocharger heat transfer properties depending only on turbocharger materials and geometry (conductive conductances between consecutive metal nodes and thermal capacitances of each node). Once conduction properties were determined, turbocharger unit was installed on the gas stand facility. There, steady hot flow tests were carried out in the turbine side to analyse convection between working fluids and metal nodes. Four working fluids have been considered, *Gas* for the exhaust gases passing through the turbine case, *Air* for the fresh air passing through the compressor case, *Oil* for the lubricating oil and *W* for the coolant liquid in case the turbocharger unit had a coolant circuit. Convective heat transfer correlations have been based on the form of Dittus-Boelter and Sieder-Tate equations in order to keep simplicity. Several assumptions have been done on presented heat transfer model, these are:

- Heat transfer on the turbine side has been considered to occur before rotor expansion.
- Heat transfer on the compressor side has been considered to occur after the adiabatic compression process, taking place at compressor diffuser and volute.
- Compressed air can receive or release heat from compressor case depending on compressor operative conditions.
- Heat transfer to the lubricating oil occurs according to the following order; oil receives first heat from housing node placed near the turbine case ($\dot{Q}_{H1/OH1}$), later oil temperature increases due to mechanical losses effects, after that process it can receive or release heat from housing central node *H2* depending on turbocharger operative conditions ($\dot{Q}_{H2/OH2}$).

Heat transfer validation showed good agreement predicting heat fluxes between metal nodes and working fluids. Importance of internal heat transfer, mainly at the low load region (low turbocharger speeds) was observed. As it was explained, experimental heat fluxes in that region could raise up to 50% of turbocharger available energy. At those conditions, simulations using proposed HTM showed better prediction of turbine and compressor outlet temperatures compared with simulations where heat transfer model was not included. In case not HTM was used in simulations, errors up to 50ºC in turbine outlet temperature prediction appeared. However, simulations including

HTM showed errors in the threshold of ±5ºC for most studied points. As a consequence of that prediction, turbocharger enthalpy calculation was considerably improved as it was observed in Chapter 5. Same trend was observed in compressor outlet temperature prediction, where errors in temperature reduced from the ±10ºC threshold to the ±6ºC. In addition most of simulated points showed an error below ±2ºC. Accurate results predicting average compressor and turbine outlet temperatures under hot pulsating flow conditions were observed too as it was discussed in Chapter 5.

6.2.2 Compressor Modelling

In the present Thesis a compressor geometrical model to account for acoustic effects has been validated. That model was based on 0-D and 1-D elements (pipes and volumes) to make it operative to be used coupled to 1-D gas-dynamic engine codes. That model was based on the proposal of Torregrosa et al. [172] consisting of two volumes to account for accumulative effects on compressor wheel and volute, connected to some pieces of pipes representing exact geometry from compressor inlet and outlet ports. A straight pipe with an equivalent length of 1/3 of compressor measured volute length was included between both volumes. A testing methodology to test compressor unit under pulsating flow conditions was developed. A rotary valve at compressor outlet was installed to simulate what would be engine intake valves. Arrays of three piezo-electric sensors at compressor inlet and outlet pipes were installed. Small fluctuations in pressure signals among those sensors has been used to decompose pressure signal into its components. Compressor geometrical model has been validated imposing second reflected pressure signal at compressor inlet (forward signal) and incident pressure wave at compressor outlet (backward signal). As it was observed good accuracy in rest of compressor wave components prediction was obtained both in time and frequency domain. As it was observed in Chapter 4, most of simulated engine points showed an error in the threshold of ±5dB mainly for the transmitted pressure wave.

6.2.3 Turbine Modelling

In the present Thesis a turbine geometrical model to account for acoustic non-linear effects has been improved and validated. That model was based on 0-D and 1-D elements (pipes and volumes) to make it appropriated to be

used in 1-D gas-dynamic engine simulation code OpenWAM. That model was based on the proposal of Serrano et al. [148] of two nozzles in series with an intermediate volume. First nozzle representing VGT vanes, and the second nozzle turbine rotor effective section. The intermediate volume accounts for accumulation effects during filling/emptying processes. That model has been improved by connecting to some straight and tapered pipes of precise dimensions related with turbine geometry as it was explained in Chapter 4. As it was observed good accuracy predicting turbine average values in pressure components and mass flow was obtained, in addition instantaneous results analysis showed good agreement with instantaneously measured pressures at turbine inlet and outlet pipes. Those tests were performed under cold pulsating flow on the turbine side. Turbine geometrical model to account for acoustics has been validated imposing forward signal at turbine inlet (incident pressure) and backward pressure at turbine outlet (second reflected pressure). Other components (reflected, transmitted and composed pressures) have been provided by turbine acoustic model and compared with instantaneous measures. Accurate results in both shift and mean value were observed for pressure components prediction. In addition peak and trough values were well predicted as it was observed in Chapter 4. Good results were obtained too predicting SPL (sound pressure level) inside turbine inlet and outlet pipes for most of the tested engines conditions and studied turbochargers. Most tested points showed an error in the threshold of $\pm$5dB for the second and fourth engine order for the adiabatic tests as it was observed on Chapter 4.

A physically based methodology to extrapolate turbine performance maps has been also developed and described on Chapter 4. That methodology has been based on Euler's turbomachinery equation to extrapolate turbine isentropic efficiency. Meanwhile momentum, energy and continuity conservation equations in turbine stator and rotor interface have been required in mass flow extrapolations. Although that model was physically-based, some fitting parameters accounting for small variations in geometrical stator and rotor areas were included. An extra fitting parameter was introduced to represent what would be velocity terms in stator and rotor blades. Finally a linear trend between stator flow angle (at its outlet) and blade speed ratio was assumed in order to account for turbine operative conditions.

Importance of having extra information for turbine performance (mass flow and efficiency) in the off design region for extrapolation purposes have been discussed. Differences up to 5 percent points in extrapolated peak efficiency

can appear from using the typical narrow range of measurements provided in turbine maps or using an extended methodology. For that reason several testing methodologies to obtain enough information in that region have been used and described. They range from testing compressor in a closed loop where its inlet pressure can be modified as desired, what would increase or reduce surge and choke limits, or reducing volume at compressor outlet in order to increase surge frequency what will reduce compressor damaging. Finally turbine lowest power point could be measured by subtracting compressor case and replacing compressor wheel just by a small ring to keep shaft balanced. In those conditions, turbine will provide the lowest possible power since it should only gain mechanical losses in the shaft and windage losses on the ring replacing compressor wheel.

As it was observed in Chapter 4 good prediction in turbine mass flow and efficiency maps extrapolation was observed for all analysed turbochargers. In addition better prediction was obtained using proposed methodology than the procedure followed by commercial engine code GT-Power.

6.2.4 Model Capabilities

Once turbocharger models have been developed and validated after studying each phenomenon individually, they have been applied instantaneously in a quasi-steady way to reproduce hot pulsating flow conditions on the turbine side. As it was observed in Chapter 5 turbocharger behaviour was accurately reproduced using adiabatic maps coupled to heat transfer model, mechanical losses model, turbine extrapolation methodology and turbine geometrical model. Despite the fact that heat transfer model was developed using steady flow measurements, good prediction reproducing compressor and turbine outlet temperatures for hot pulsating tests was demonstrated. Error drastically reduced in turbine outlet temperature prediction mainly for the low loads. Turbine geometrical and extrapolation models showed reasonably good results predicting turbine acoustics, most simulated points laid in the threshold of $\pm$5dB for second and fourth engine order. Same testing points were later reproduced using performance maps measured under steady hot flow conditions, but using manufacturers definition for compressor and turbine efficiency. In that case, heat transfer had been already included in compressor efficiency definition and also mechanical losses on turbine efficiency. Testing conditions were not similar when turbocharger hot map was measured and pulsating

flow tests were carried out. For that reason, turbocharger simulations using hot measured maps showed worse results than provided using adiabatic maps and turbocharger models. As it was observed, turbocharger speed was predicted with practically no error (unless the lowest load point) using adiabatic maps and turbocharger models. Meanwhile simulations using the traditional approach (manufacturer maps measured under hot conditions) showed big errors even for intermediate loads. Also big errors predicting mass flow through the turbine (around 5%) were observed using the traditional approach since no extrapolation methodologies were available. Errors in turbine and compressor outlet temperature prediction were nearly negligible using turbocharger proposed model, while errors between 10ºC and 20ºC were observed predicting compressor outlet temperature and between 20ºC and 40ºC for turbine prediction using previous typical approaches with adiabatic maps.

Once turbocharger models have been developed and validated, they can be applied to discount heat transfer and mechanical losses on turbocharger performance maps provided by manufacturers obtaining so its adiabatic performance. Doing so only internal irreversibilities for the turbocharger can be obtained from hot measured maps. The latter maps would only provide accurate results reproducing similar conditions to those appearing when turbocharger maps were measured. In other cases adiabatic maps coupled to proposed turbocharger models to account for particular heat transfer and mechanical losses have demonstrated to be an accurate tool to simulate turbocharger performance. As it was observed, compressor adiabatic efficiency obtained from hot measures by applying turbocharger models agreed with compressor efficiency from quasi-adiabatic measures. Meanwhile compressor efficiency defined directly from hot measures was far from previous definitions. That effect was increased as turbocharger speed reduced, since it was in that region where heat transfer and mechanical losses became more important. It was observed, how for high turbocharger speeds (and loads) both adiabatic efficiency and "adiabatized" obtained from hot tests were the same (and equal to compressor efficiency defined directly from hot measures), since there heat transfer and friction losses effects are insignificant compared to turbocharger power.

Input data and turbocharger model parameters described along this Thesis have been collect in Annex B.

6.3 Future Works

6.3.1 Heat Transfer Modelling

Turbocharger heat transfer model presented in this Thesis was developed to account only for internal heat transfer from hot turbine to lubricating oil, coolant circuit and cold compressor. Model was validated using hot steady and pulsating flow tests on the turbine side being the turbocharger fully insulated. Nevertheless turbocharger proposal did not account for external convection or radiation. Nevertheless, in case the turbocharger will be coupled to an ICE, external heat transfer effects will not be negligible. For that reason, proposed heat transfer models should be updated to include convective branches between metal model nodes and external ambient. Some experiments with the turbocharger exposed must be carried out in the future to validate those physically-based equations. For the case of external radiation, the following assumptions could be done in the future works:

- Turbine, compressor and housing cases should be considered as single cylinders in geometry.
- Radiation between each metal node and the ambient should be possible.
- Radiation between each metal node and the rest of metal nodes should be possible.
- Viewing factors from each single node to the rest of nodes should be calculated.

External convection could be calculated considering the following processes.

- Free convection.
- Forced convection.
- Combined convection (a mixture of the two above possibilities).

Equations from those mechanisms could be obtained from literature survey and should be applied to horizontal cylinders. Some extra measurements with

other turbochargers units should be tested in the future to obtain more data about heat transfer inside turbochargers. Those measurements will be used to validate turbocharger heat transfer model and try to get general correlations for heat transfer properties (K, h, C) based just on turbocharger geometry.

6.3.2 Turbine Modelling

In the present Thesis, a turbine geometrical model has been applied to account for acoustic effects on the turbine side. That model has been based on one-dimensional elements (straight and tapered pipes) to easily-adapt it to be used in 1-D gas-dynamic engine simulation codes. Observing pressure waves on the turbine inlet and outlet sides, a small shift on time domain analysis, and small errors predicting SPL for engine orders higher to the 8th were observed. Those effects were due to the simplification of turbine geometrical model, mainly on the pipe corresponding to the turbine volute. Since a straight pipe connected to a single nozzle placed at the end of that pipe was assumed. Nevertheless in real operation, mass flow can leave the turbine volute at any circumferential position by passing through one of the multiple orifices of turbine stator. So the next step to improve turbine acoustic model accuracy will be applying a second order model to reproduce stator internal geometry. In order to do so in the future it could be assumed each stator nozzle connected individually to each rotor nozzle, so turbine volute will be modelled as a series of nozzles installed in parallel connected by means of short pipes.

With respect to turbine extrapolating methodologies, it was observed how the proposed technique provided good results from a wide range of studied turbines and even for reduced turbocharger speeds and closed rack positions. Nevertheless, that methodology was developed only to be used for previously measured rack positions and iso-speed lines. In case of a new extrapolated turbine line; for a non-measured turbocharger speed, previously fitted coefficients from other iso-speed lines could be used to obtain an estimation for extrapolation coefficients for the new iso-speed line. In case it will be desired to extrapolate turbine map to non-measured rack openings, the proposed model should be improved to determine turbine effective area for non-measured positions. In addition extrapolation methodology presented here could be validated at extreme working conditions (lower expansion ratios, higher expansion ratios, low turbine power and turbine mass flow near zero).

References

[148] J.R. Serrano, F.J. Arnau, V. Dolz, A. Tiseira, and C. Cervelló. "A model of turbocharger radial turbines appropriate to be used in zero- and one-dimensional gas dynamics codes for internal combustion engines modelling". In: *Energy Conversion and Management* 49 (2008), pp. 3729–3745 (cit. on pp. 59, 63, 160, 170, 189, 215, 216, 231, 234, 271, 275).

[154] J.R. Serrano, P. Olmeda, A. Tiseira, L.M. García-Cuevas, and A. Lefebvre. "Theoretical and experimental study of mechanical losses in automotive turbochargers". In: *Energy* 55 (2013), pp. 888 –898 (cit. on pp. 8, 46, 48, 49, 93, 132, 157, 189, 216, 217, 223, 233, 255, 271).

[172] A. Torregrosa, J. Galindo, J.R. Serrano, and A. Tiseira. "A procedure for the unsteady characterization of turbochargers in reciprocating internal combustion engines". In: *The 4th International Symposium on Fluid Machinery and Fluid Engineering, November 24-27, 2008, Beijing, China*. 2008 (cit. on pp. 55, 56, 72, 149, 274).

Appendix A

Annex

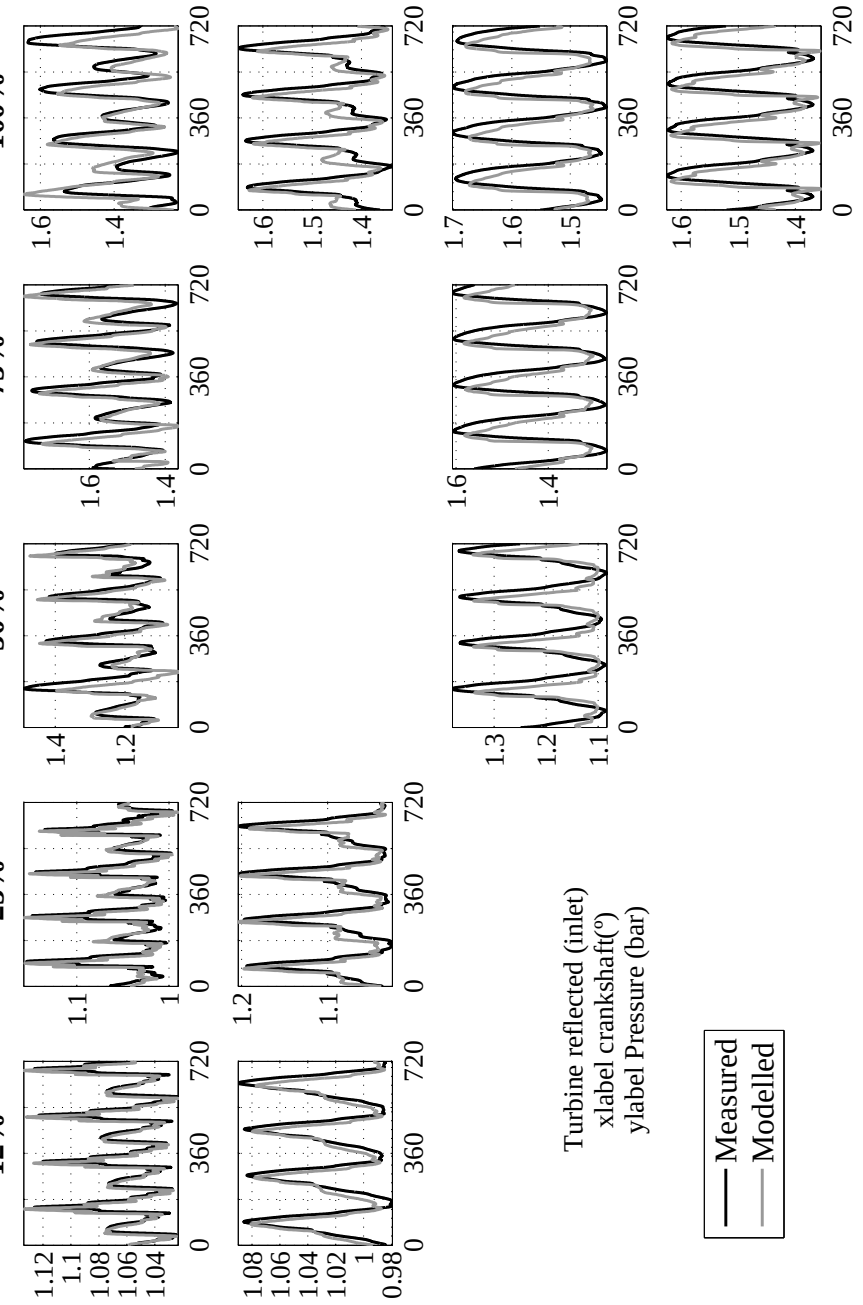

Figure A.1: Reflected pressure for turbocharger # 1 (Quasi-Adiabatic: measured vs. modelled).

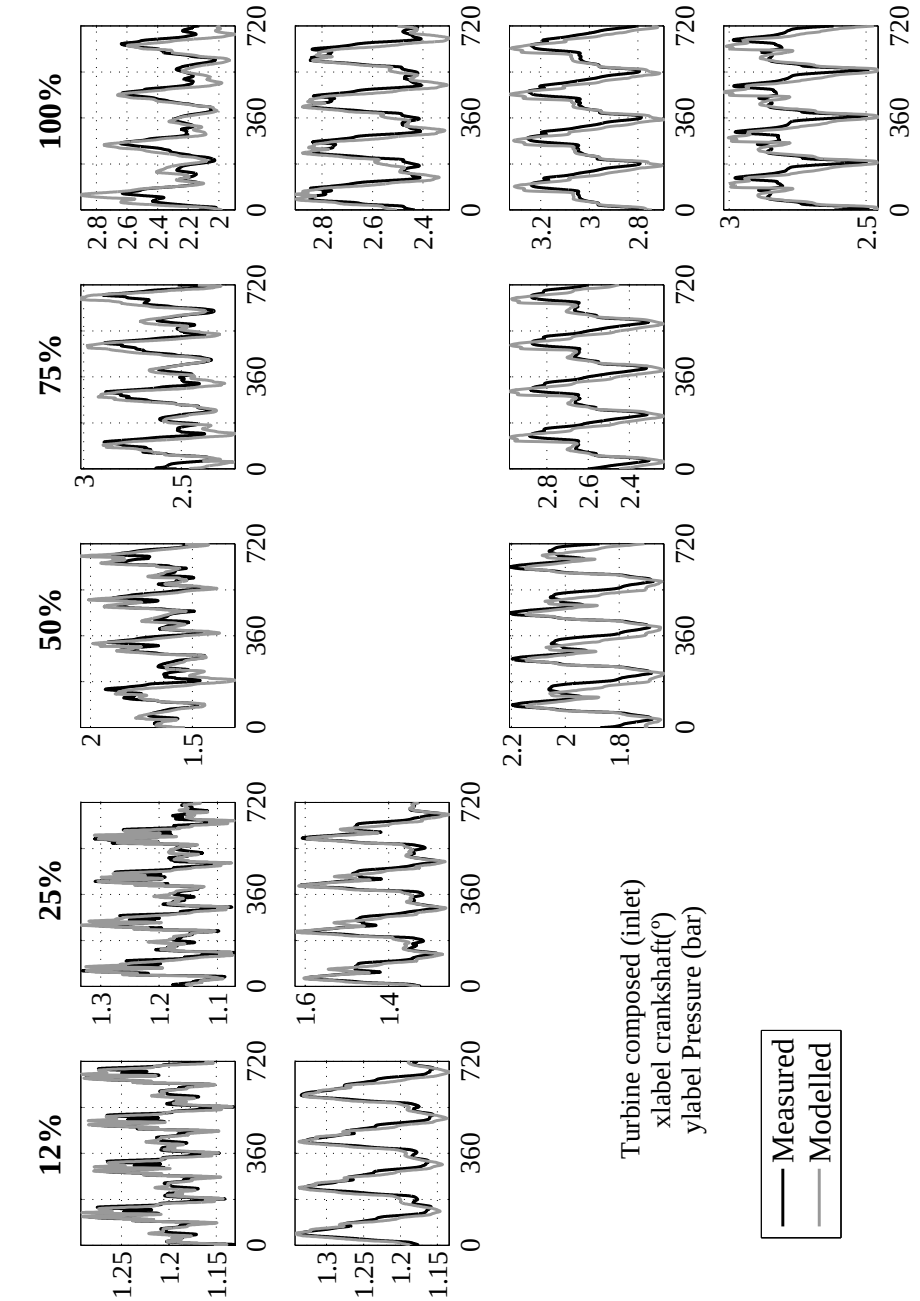

Figure A.2: Composed inlet pressure for turbocharger # 1 (Quasi-Adiabatic: measured vs. modelled).

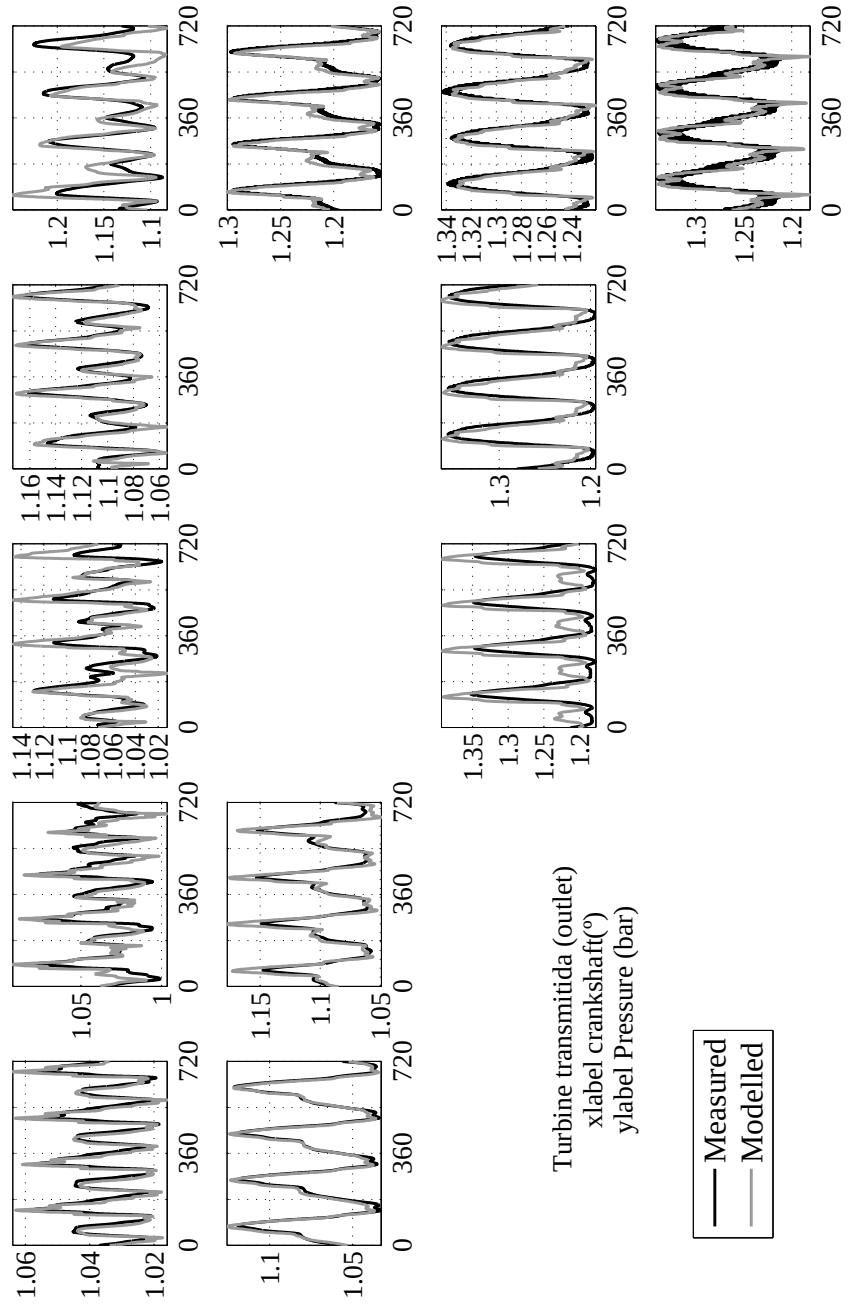

Figure A.3: Transmitted pressure for turbocharger # 1 (Quasi-Adiabatic: measured vs. modelled).

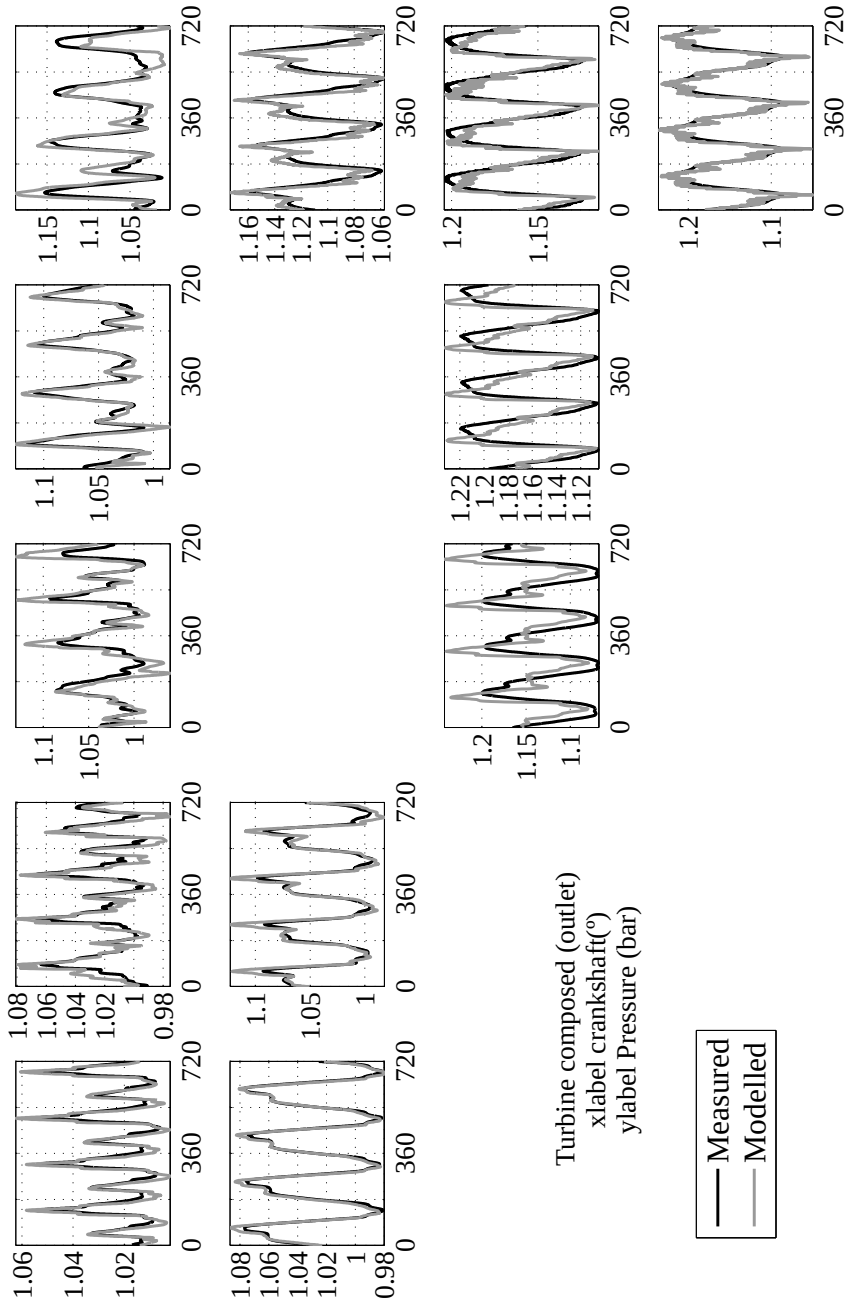

Figure A.4: Composed outlet pressure for turbocharger # 1 (Quasi-Adiabatic: measured vs. modelled).

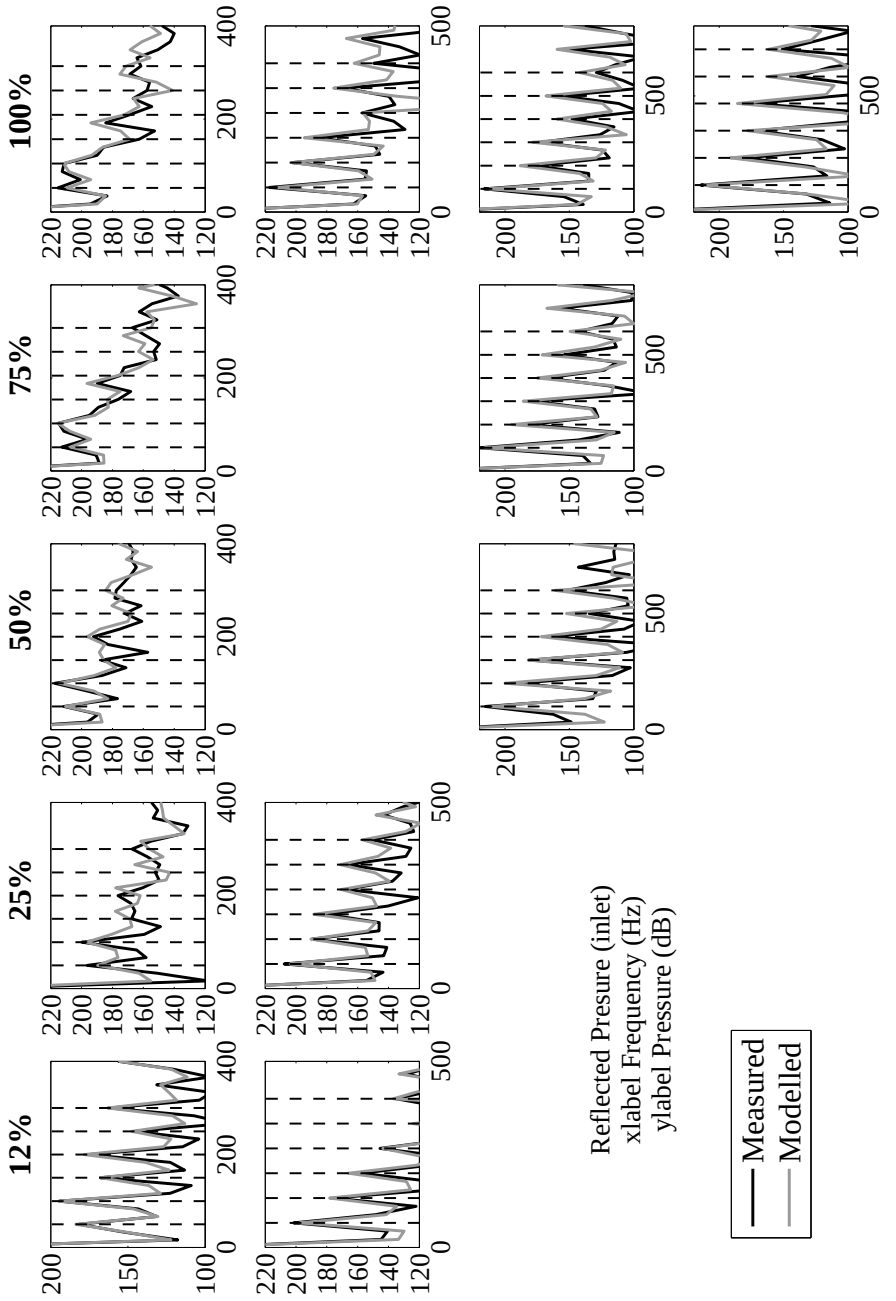

Figure A.5: Reflected pressure for turbocharger # 1 (Quasi-Adiabatic: measured vs. modelled).

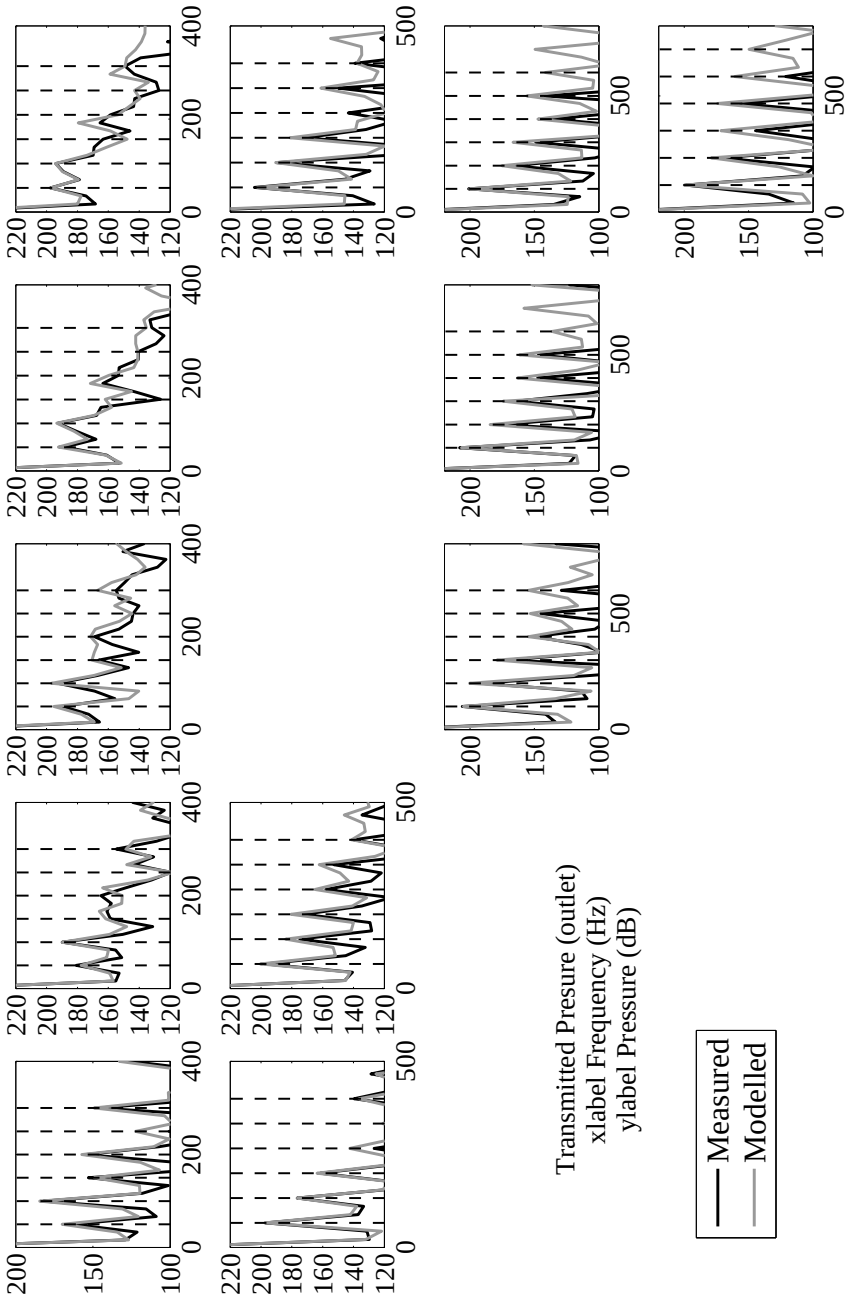

Figure A.6: Transmitted pressure for turbocharger # 1 (Quasi-Adiabatic: measured vs. modelled).

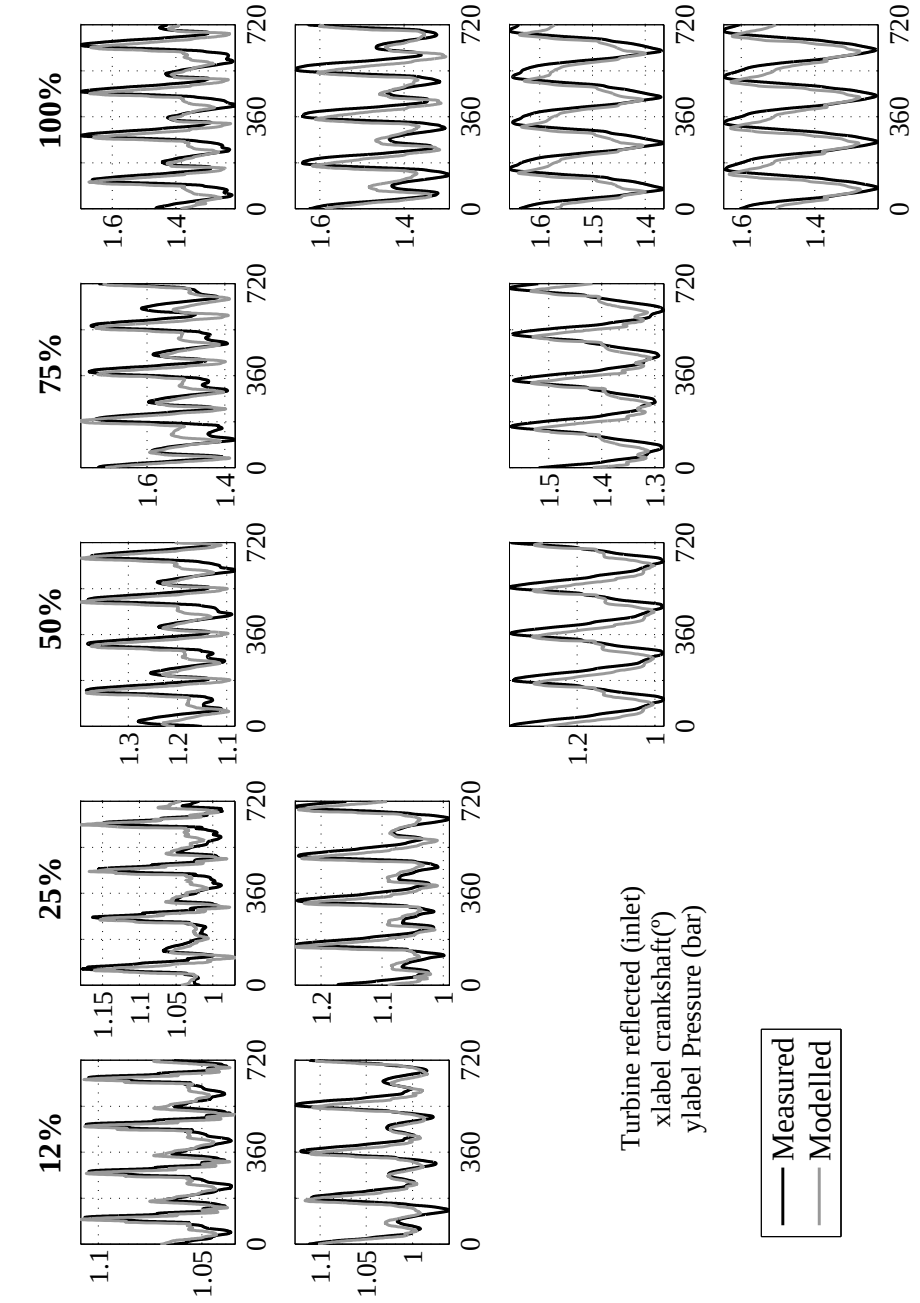

Figure A.7: Reflected pressure for turbocharger # 1 (Hot: measured vs. modelled).

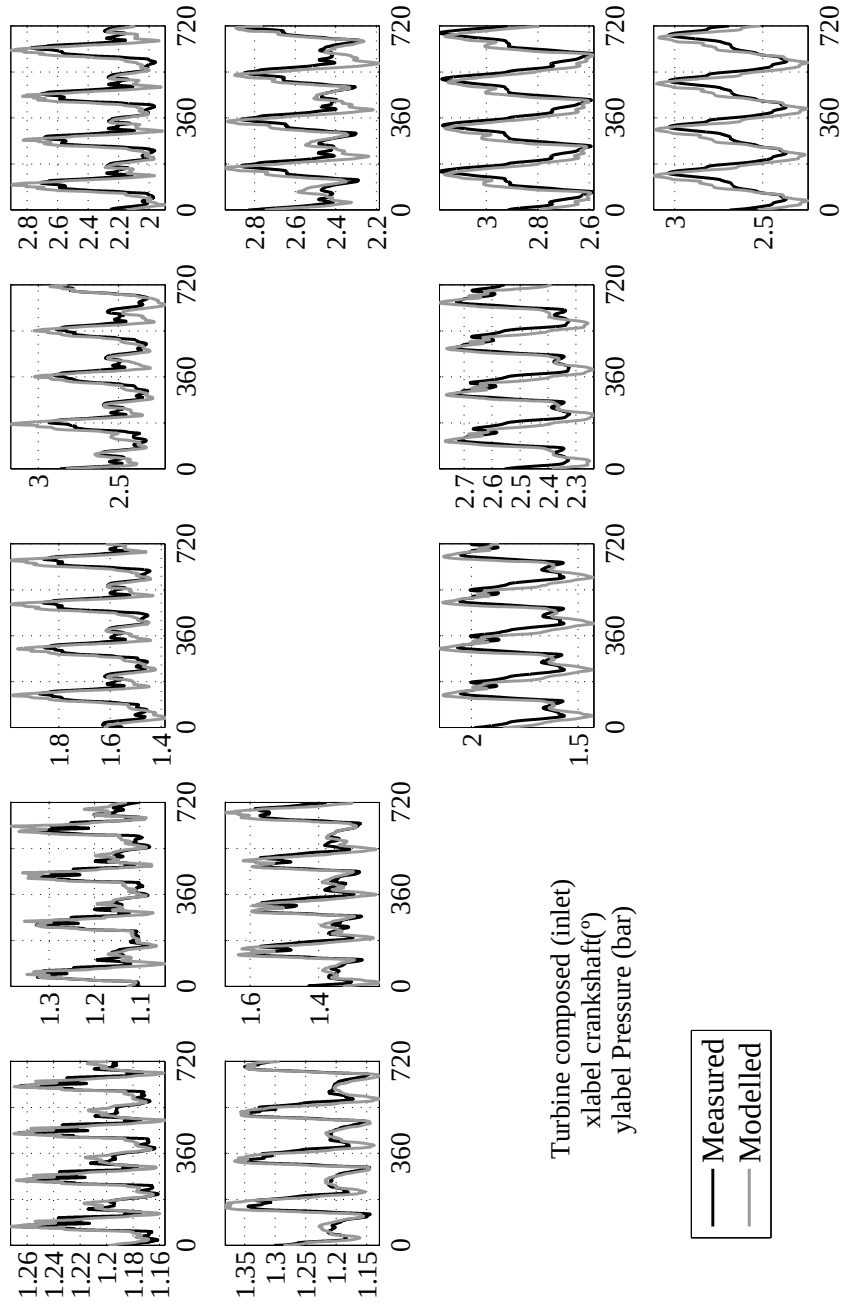

Figure A.8: Composed inlet pressure for turbocharger # 1 (Hot: measured vs. modelled).

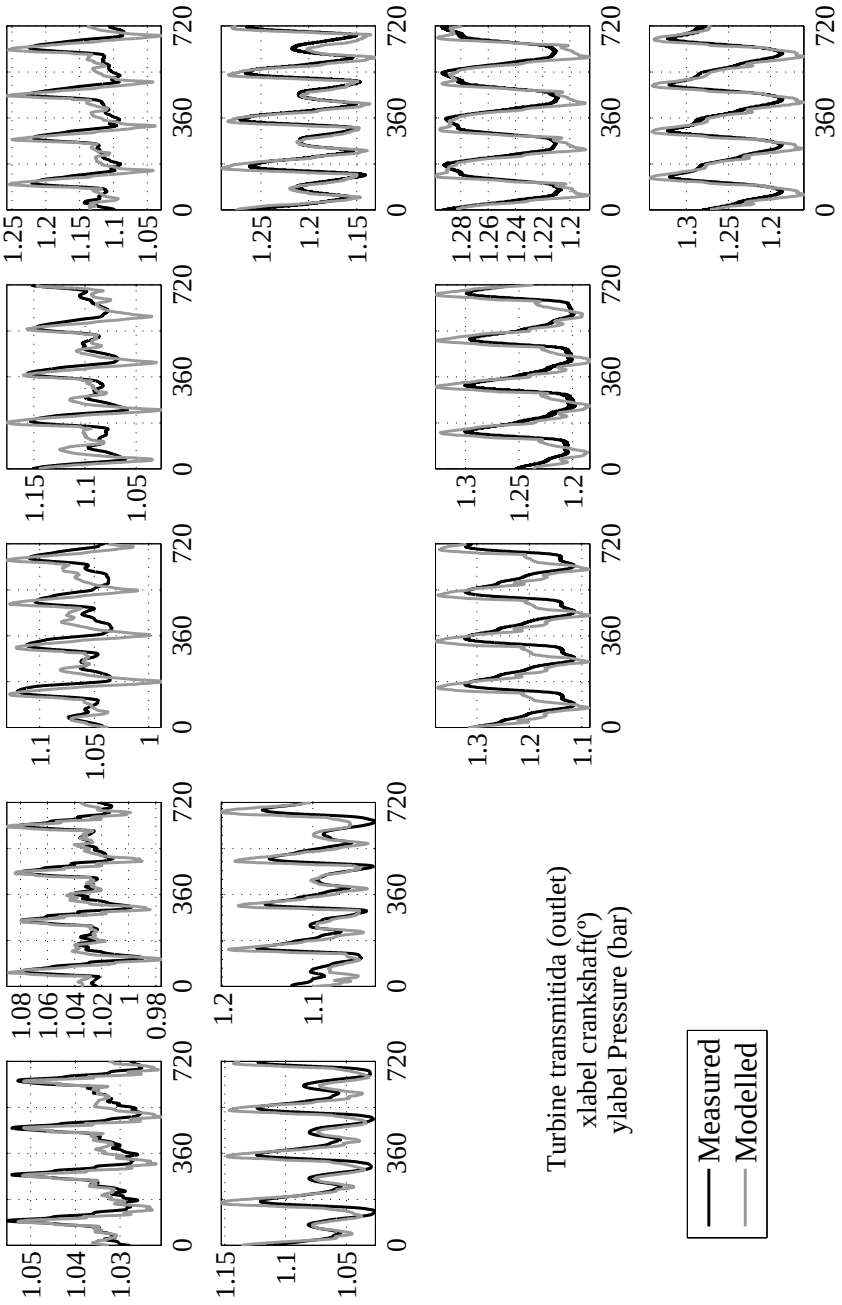

Figure A.9: Transmitted pressure for turbocharger # 1 (Hot: measured vs. modelled).

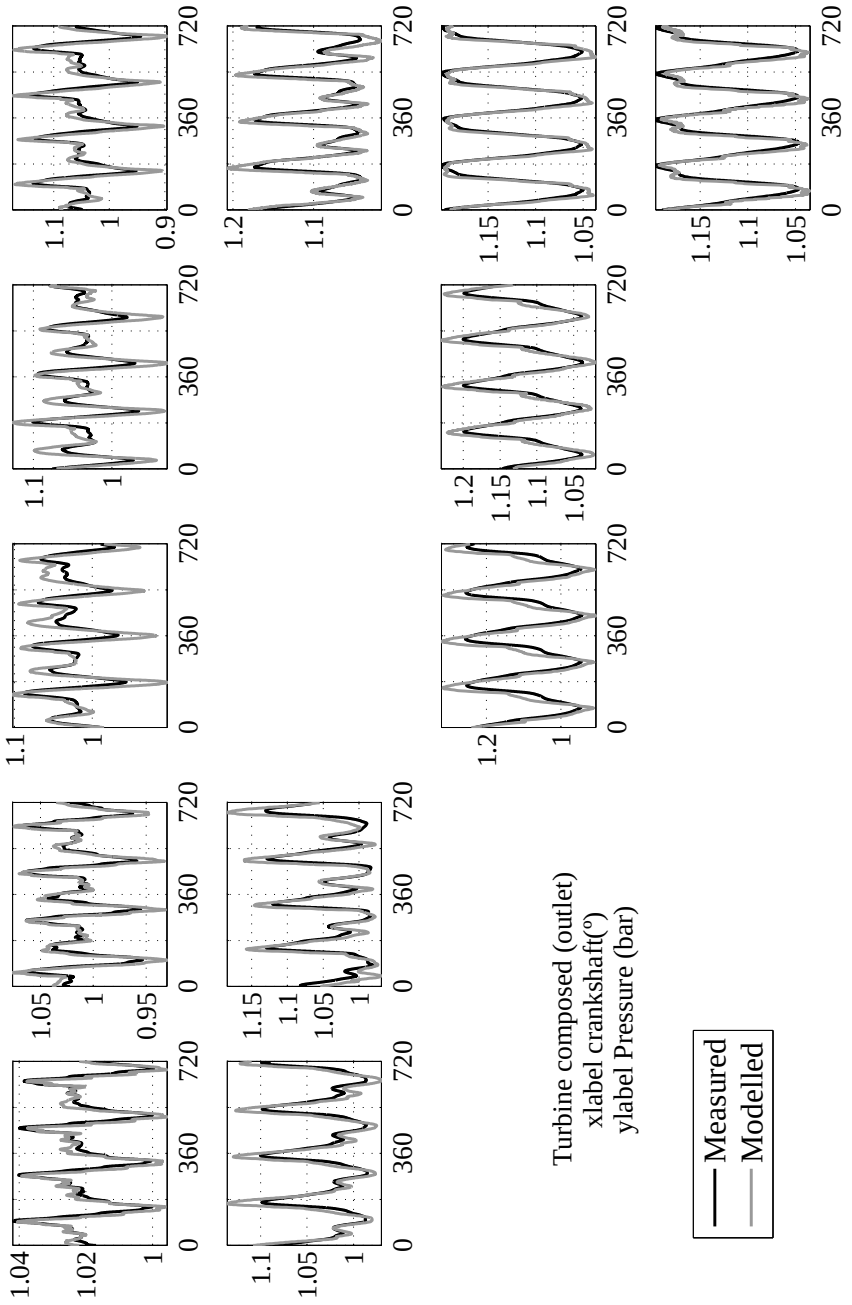

Figure A.10: Composed outlet pressure for turbocharger # 1 (Hot: measured vs. modelled).

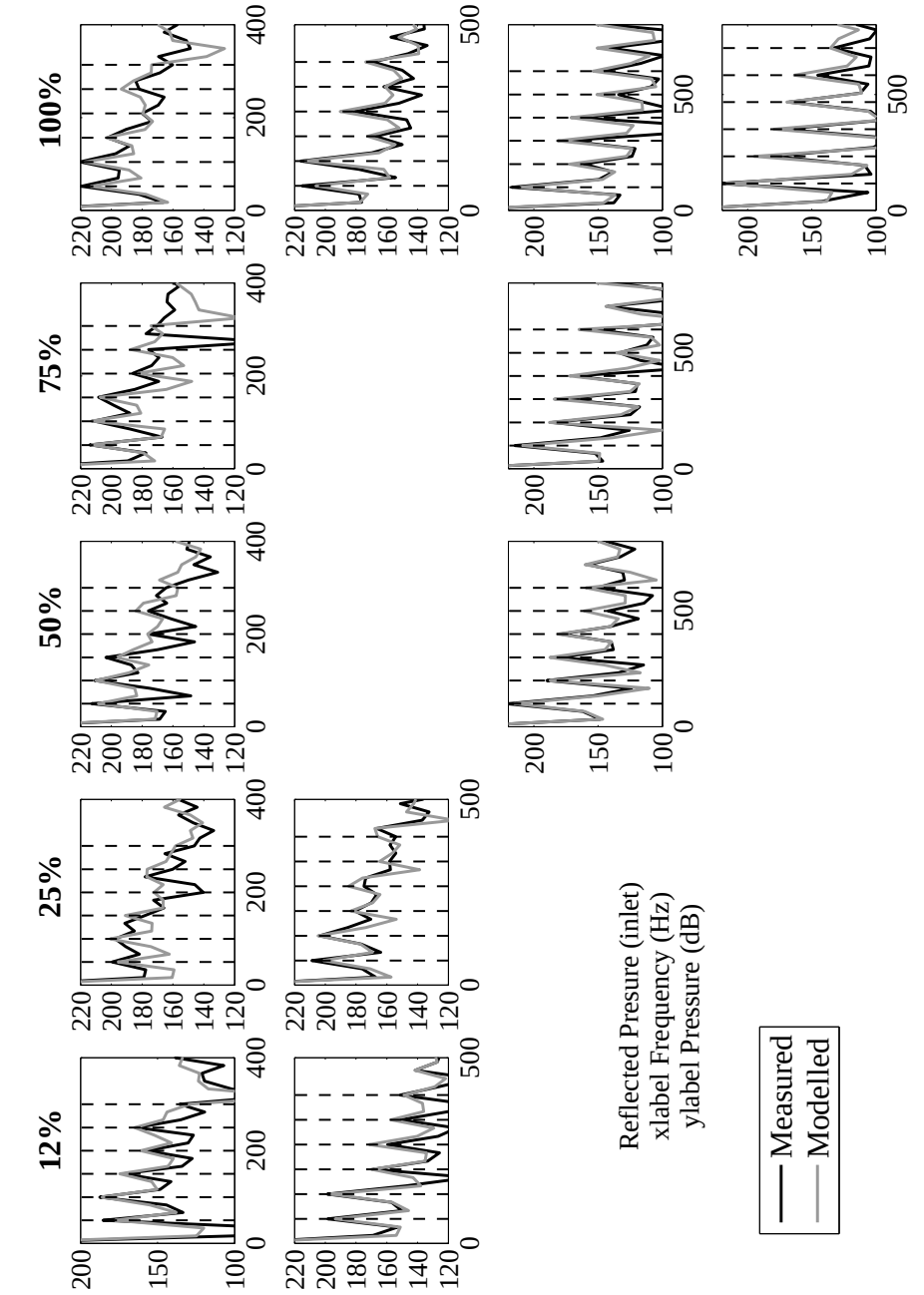

Figure A.11: Reflected pressure for turbocharger # 1 (Hot: measured vs. modelled).

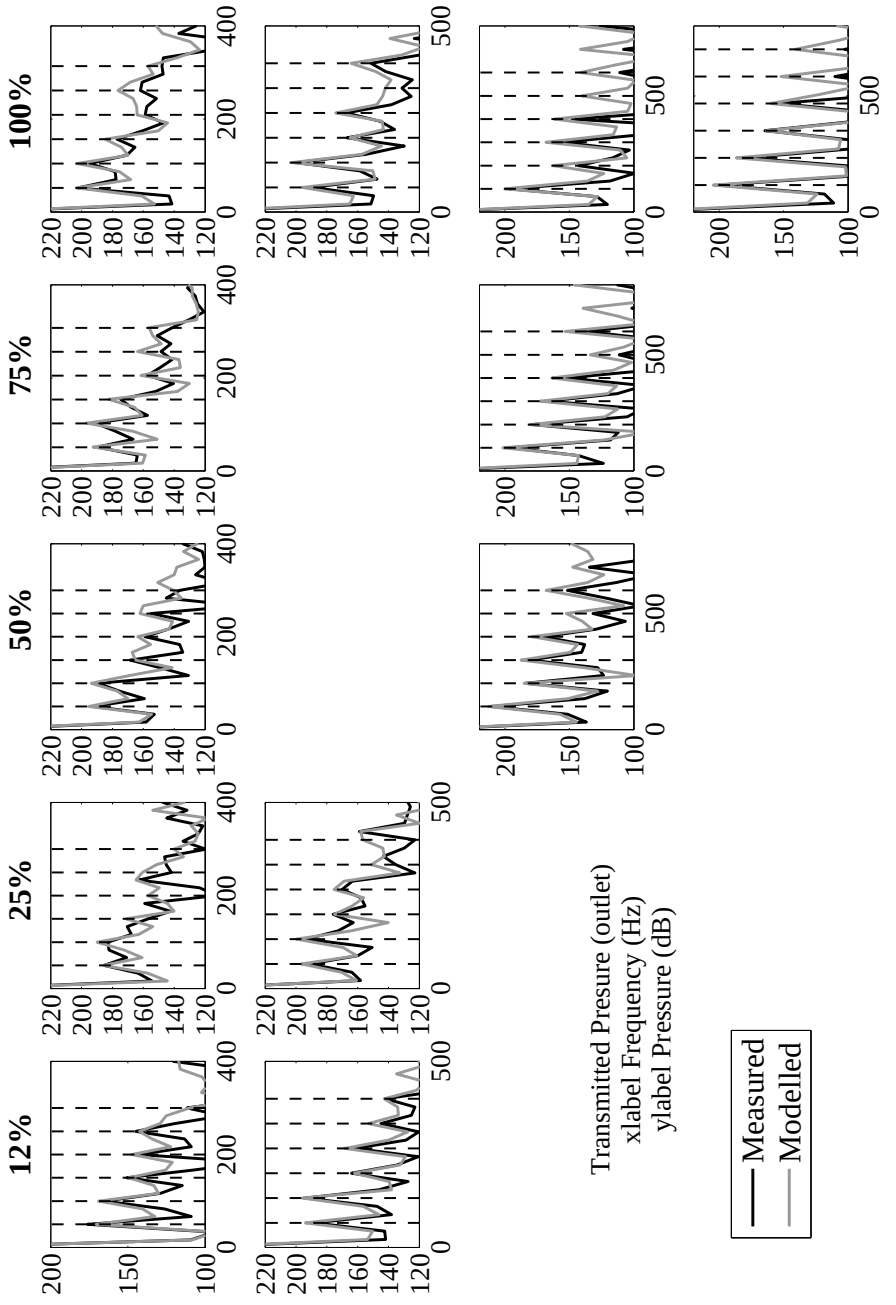

Figure A.12: Transmitted pressure for turbocharger # 1 (Hot: measured vs. modelled).

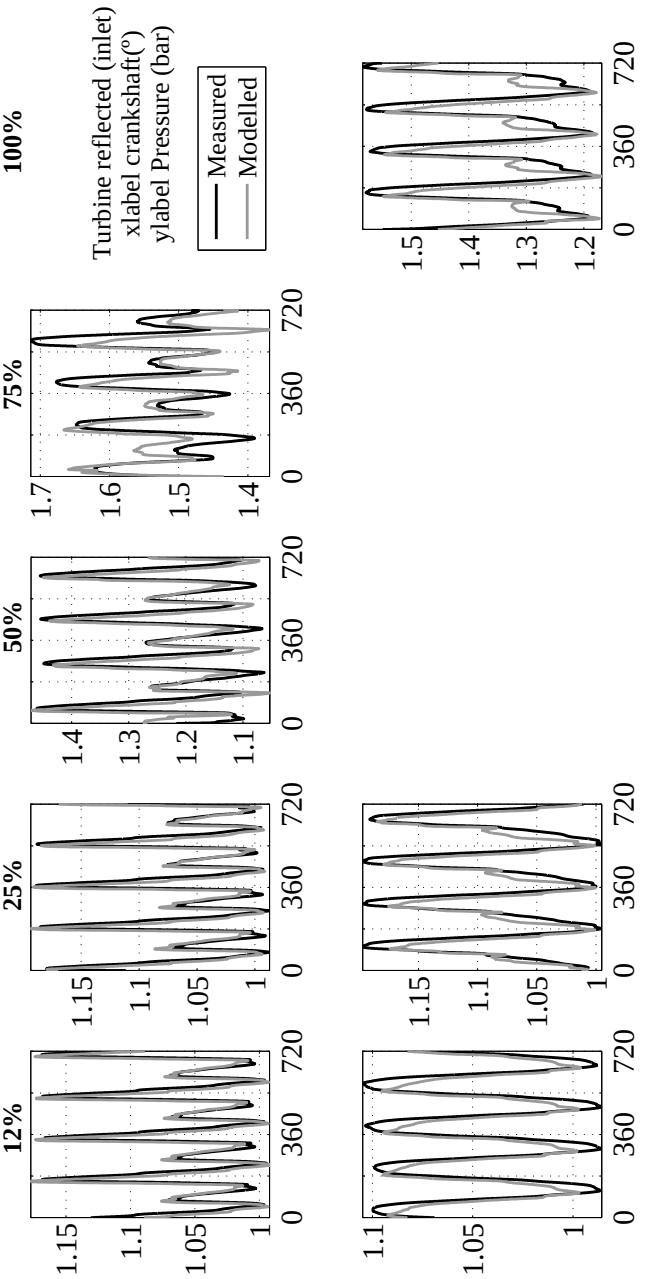

Figure A.13: Reflected pressure for turbocharger # 2 (Quasi-Adiabatic: measured vs. modelled).

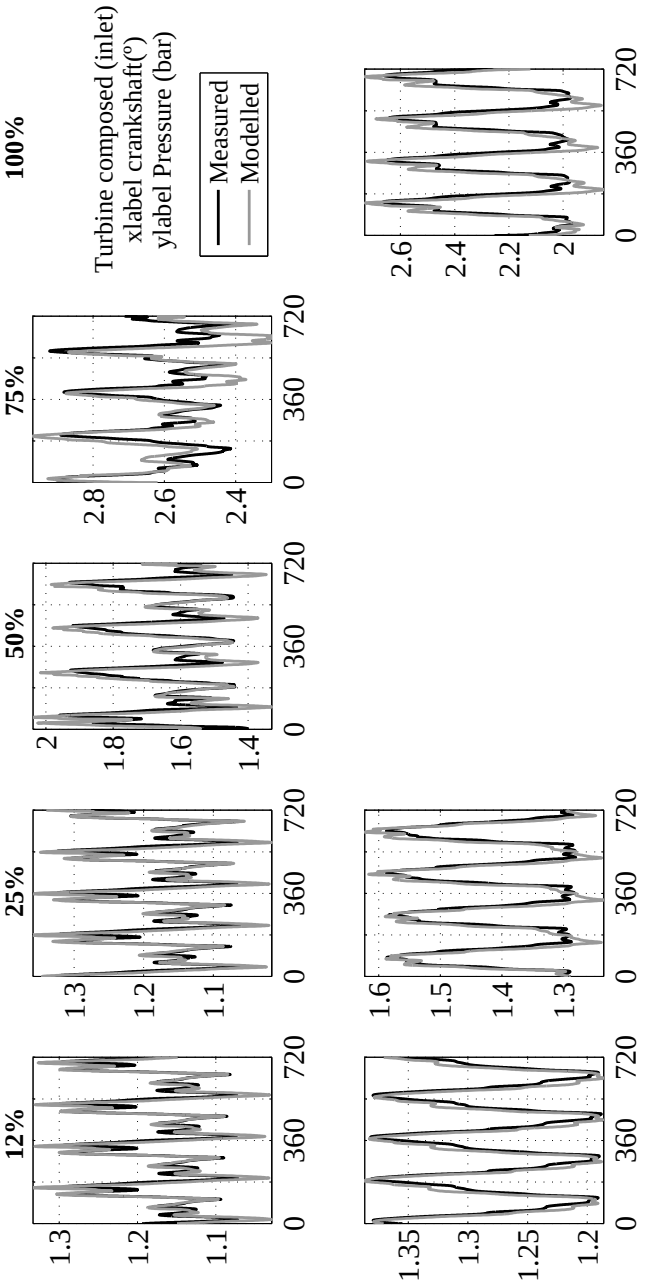

Figure A.14: Composed inlet pressure for turbocharger # 2 (Quasi-Adiabatic: measured vs. modelled).

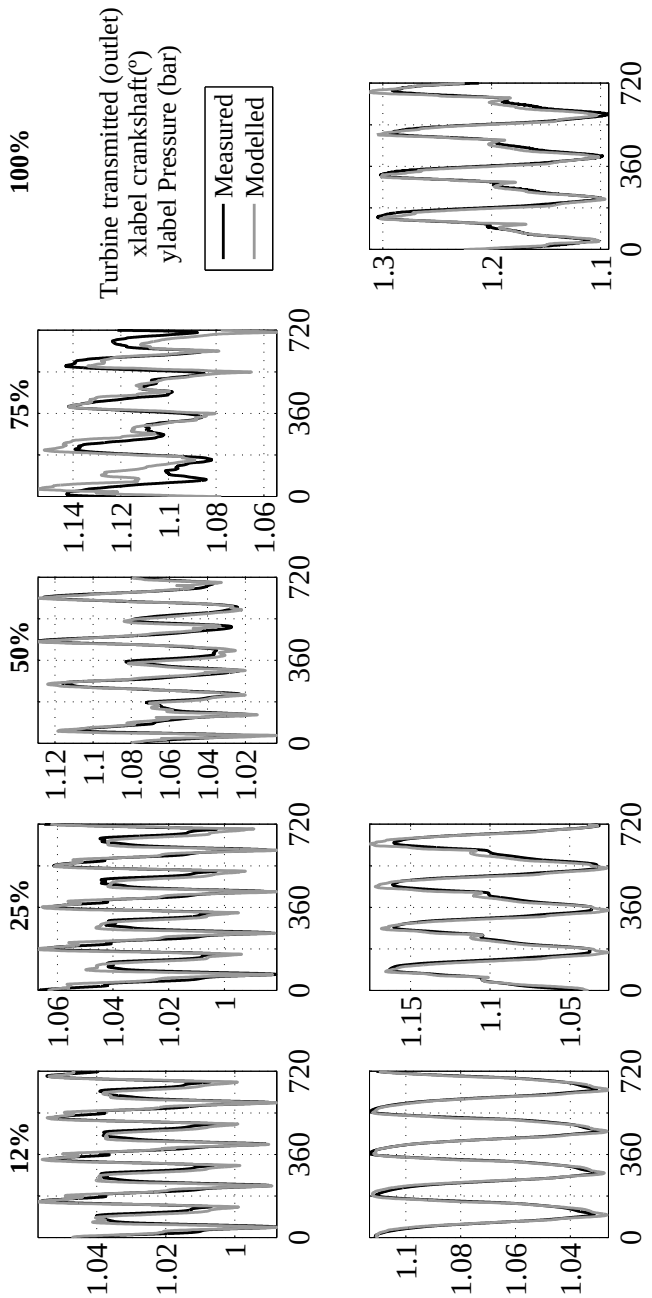

Figure A.15: Transmitted pressure for turbocharger # 2 (Quasi-Adiabatic: measured vs. modelled).

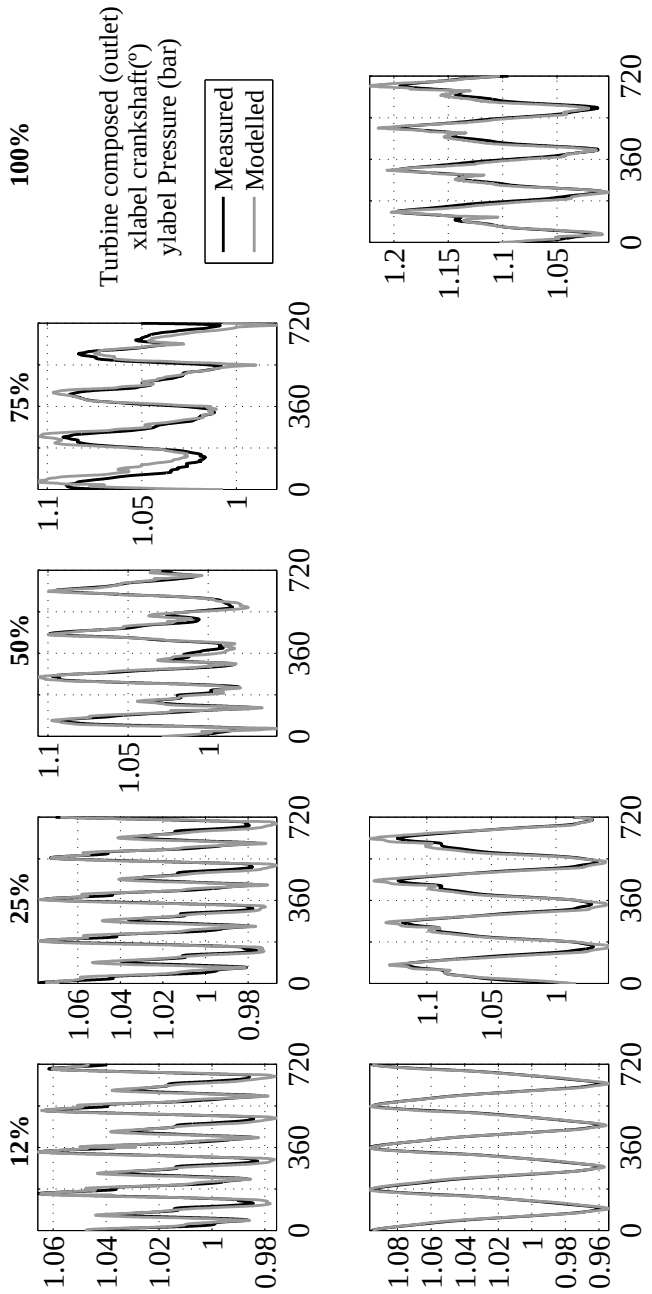

Figure A.16: Composed outlet pressure for turbocharger # 2 (Quasi-Adiabatic: measured vs. modelled).

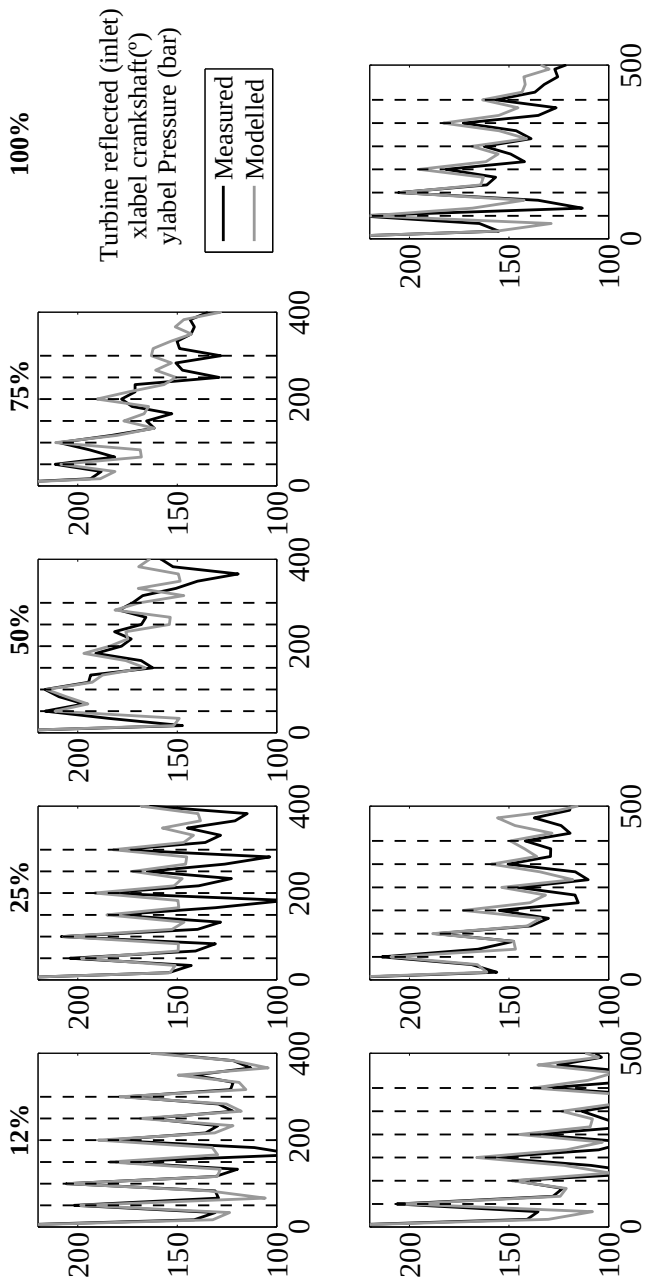

Figure A.17: Reflected pressure for turbocharger # 2 (Quasi-Adiabatic: measured vs. modelled).

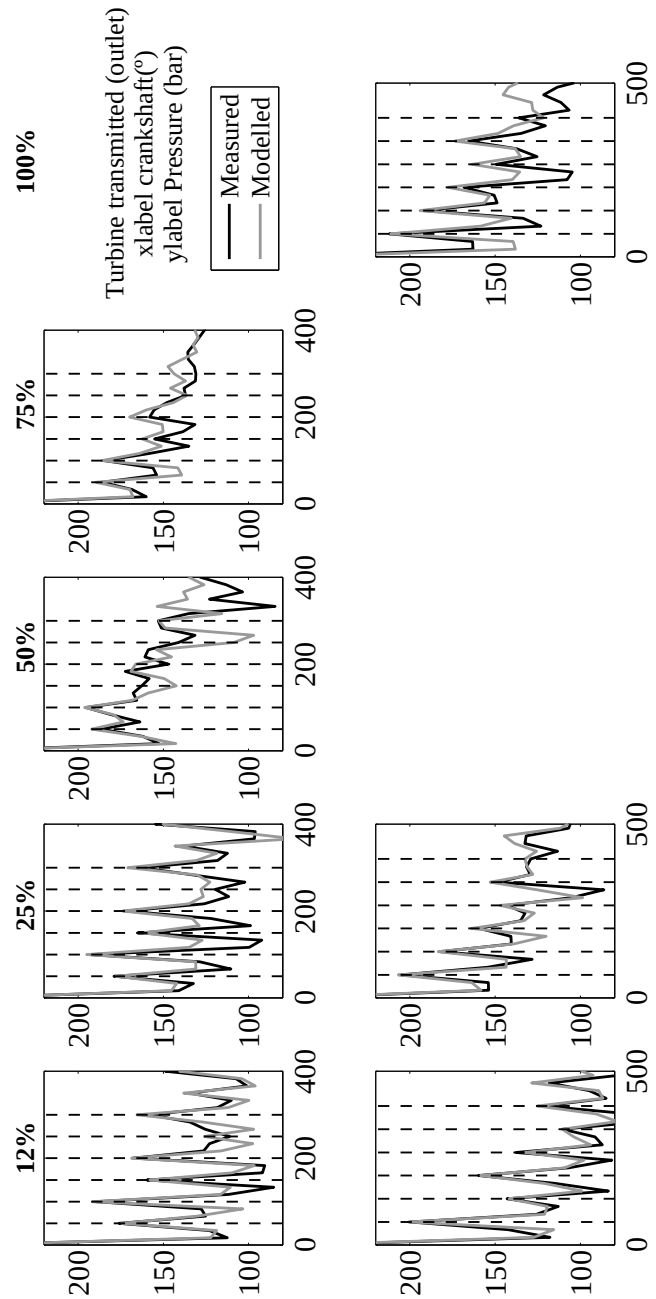

Figure A.18: Transmitted pressure for turbocharger # 2 (Quasi-Adiabatic: measured vs. modelled).

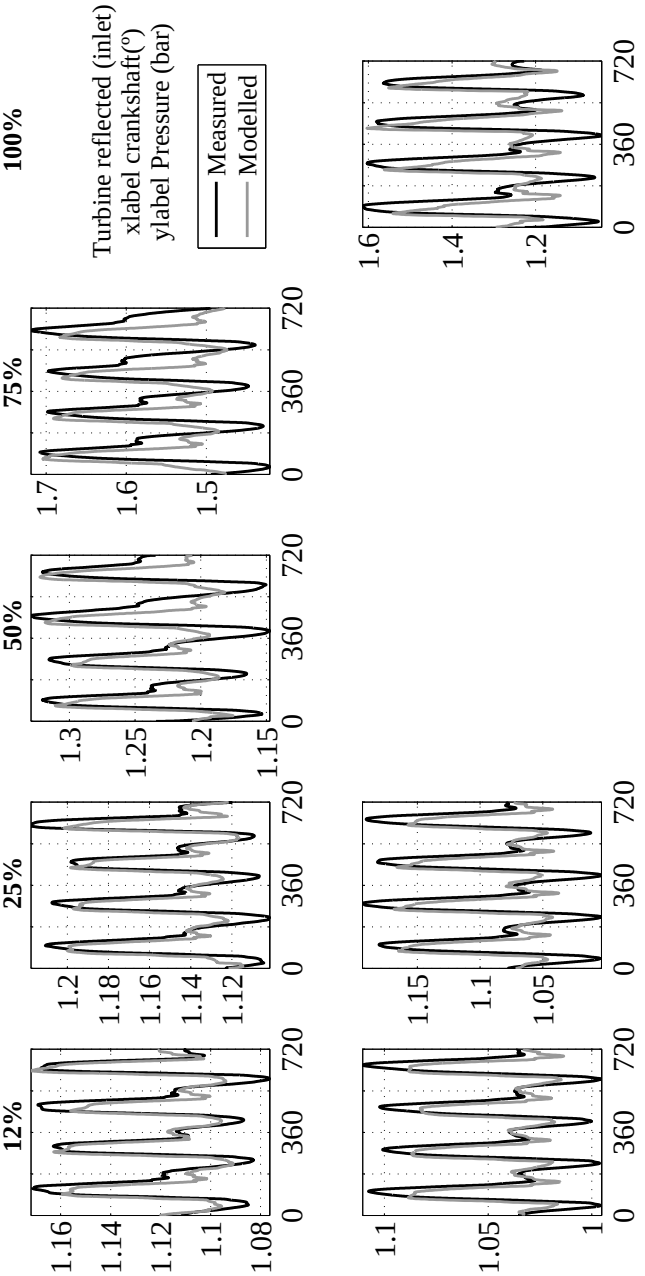

Figure A.19: Reflected pressure for turbocharger # 2 (Hot: measured vs. modelled).

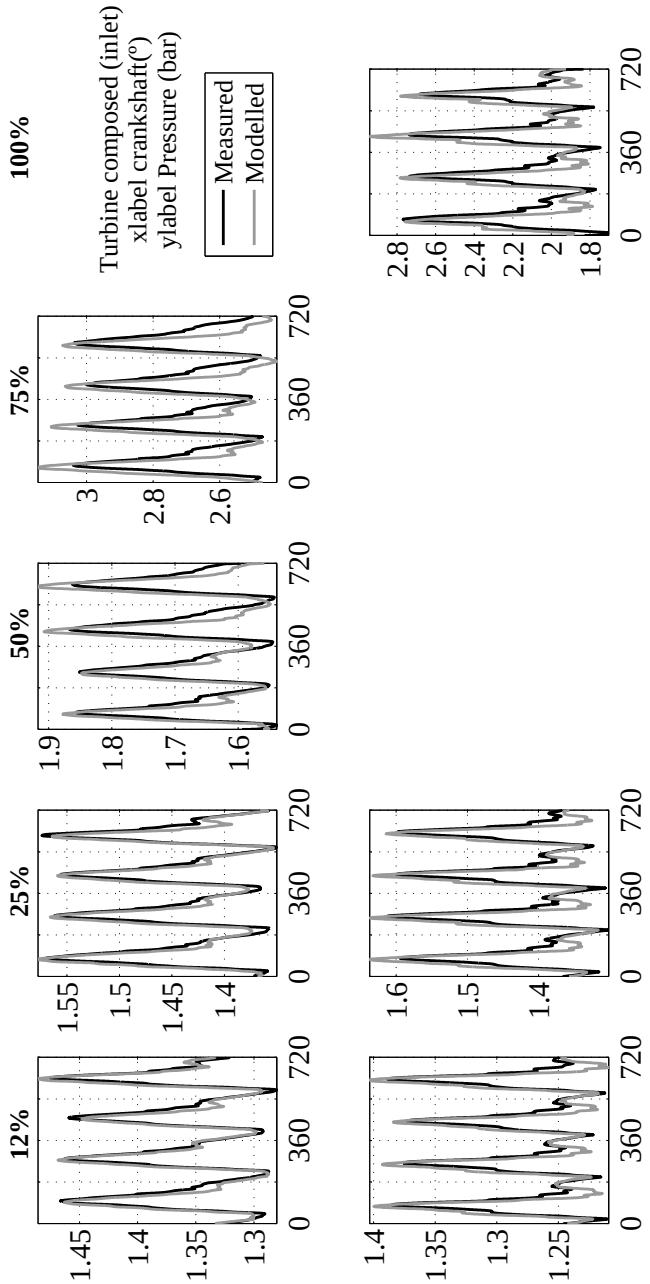

Figure A.20: Composed inlet pressure for turbocharger # 2 (Hot: measured vs. modelled).

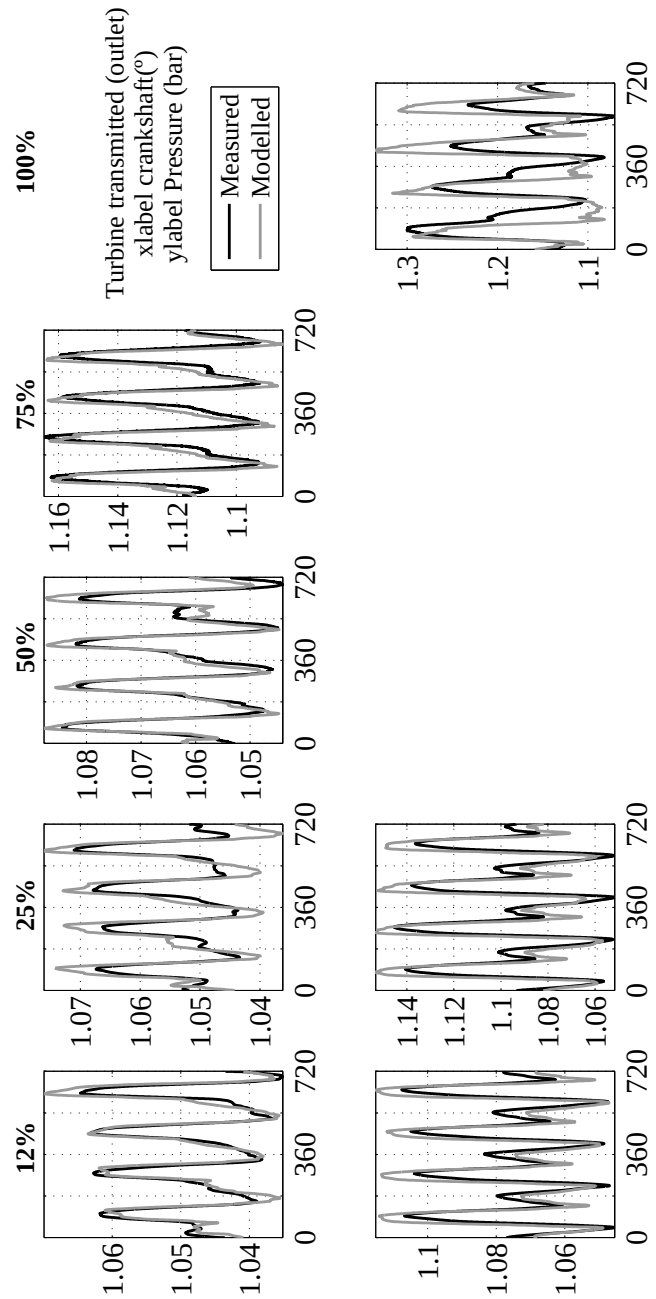

Figure A.21: Transmitted pressure for turbocharger # 2 (Hot: measured vs. modelled).

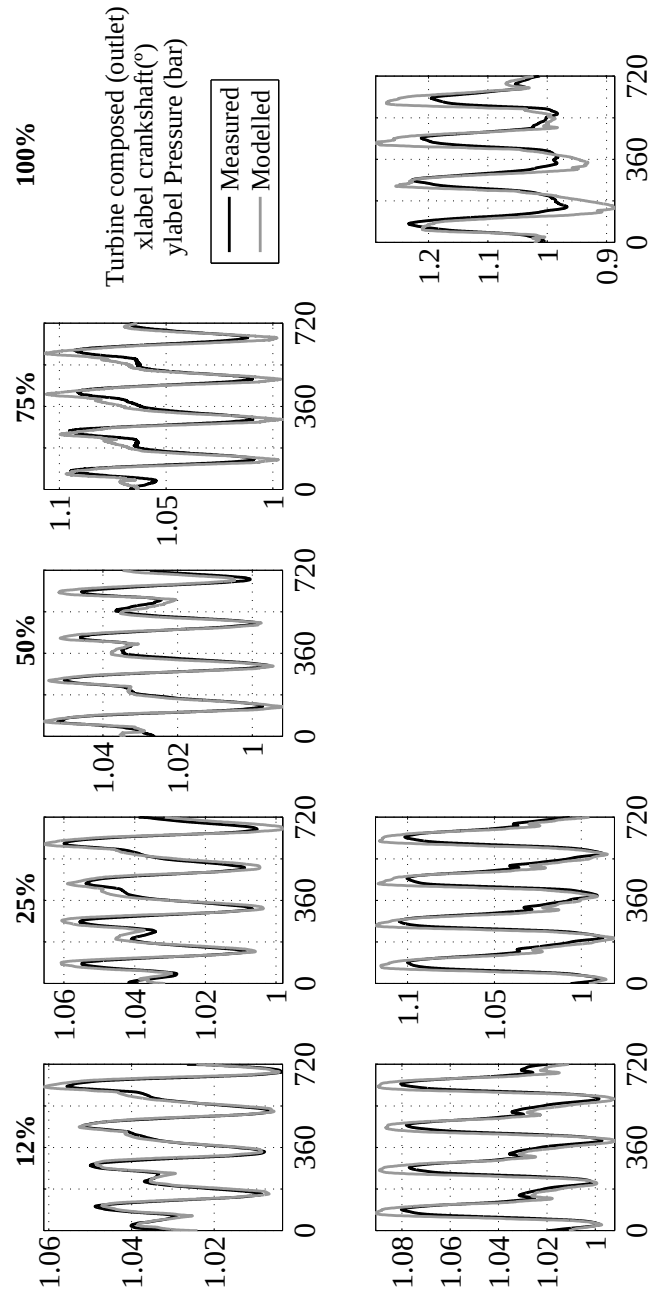

Figure A.22: Composed outlet pressure for turbocharger # 2 (Hot: measured vs. modelled).

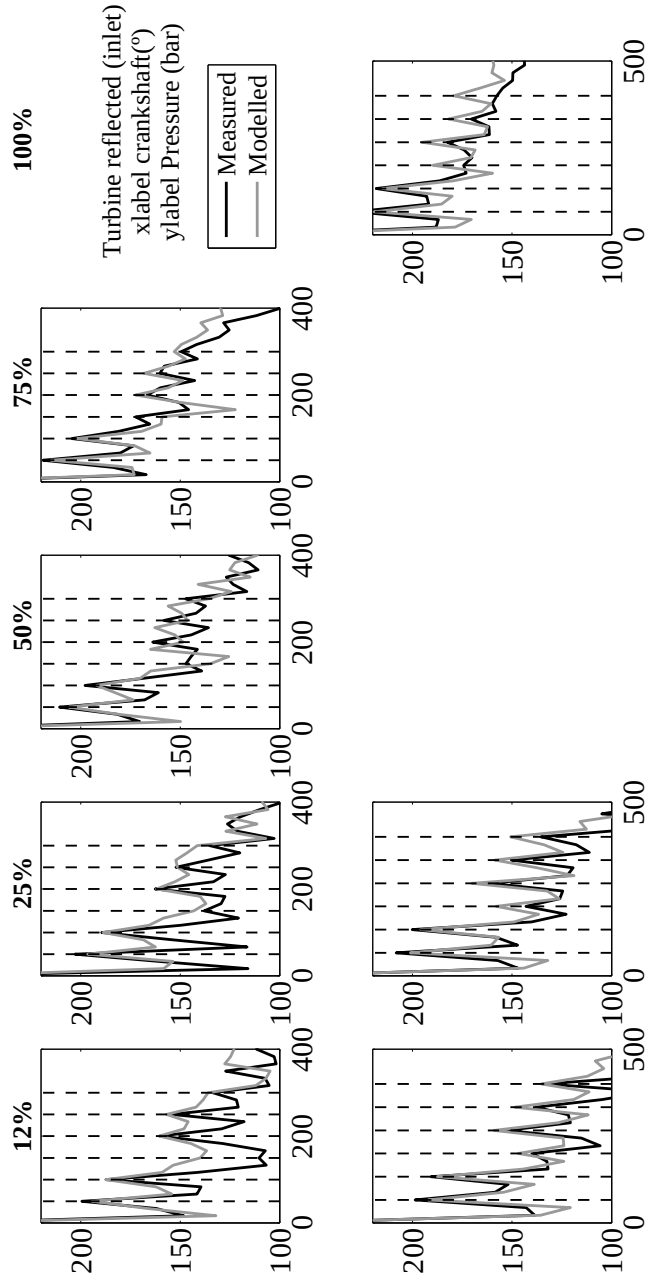

Figure A.23: Reflected pressure for turbocharger # 2 (Hot: measured vs. modelled).

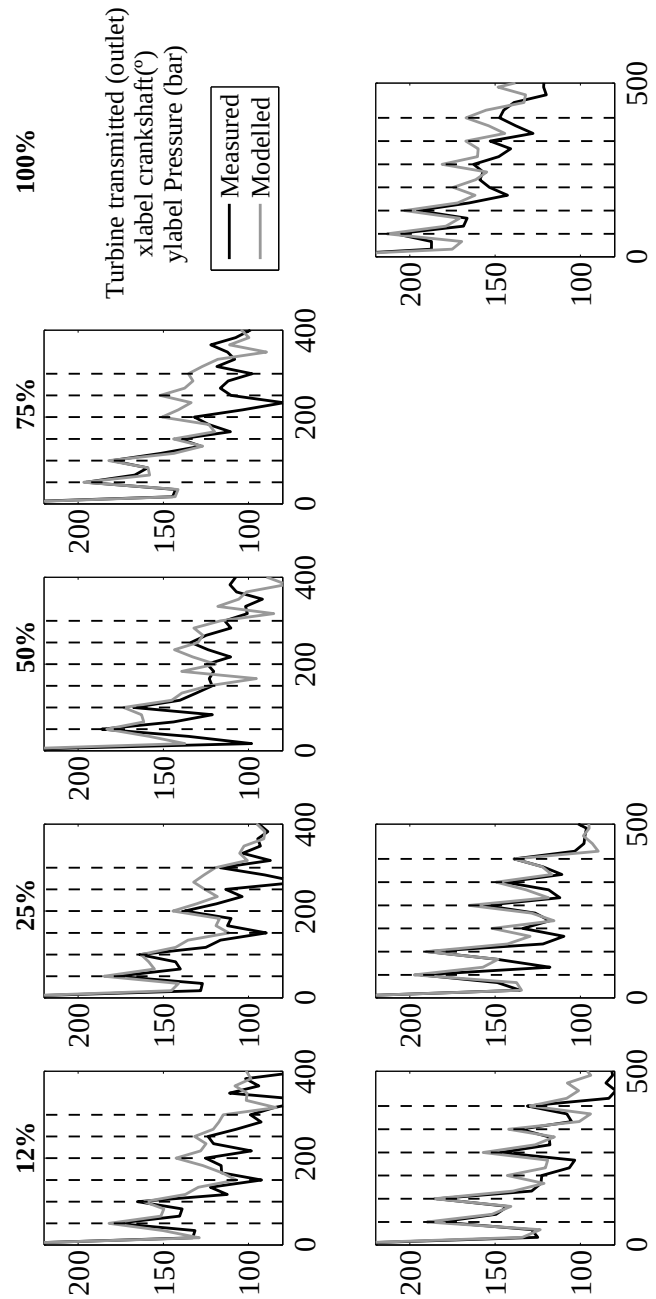

Figure A.24: Transmitted pressure for turbocharger # 2 (Hot: measured vs. modelled).

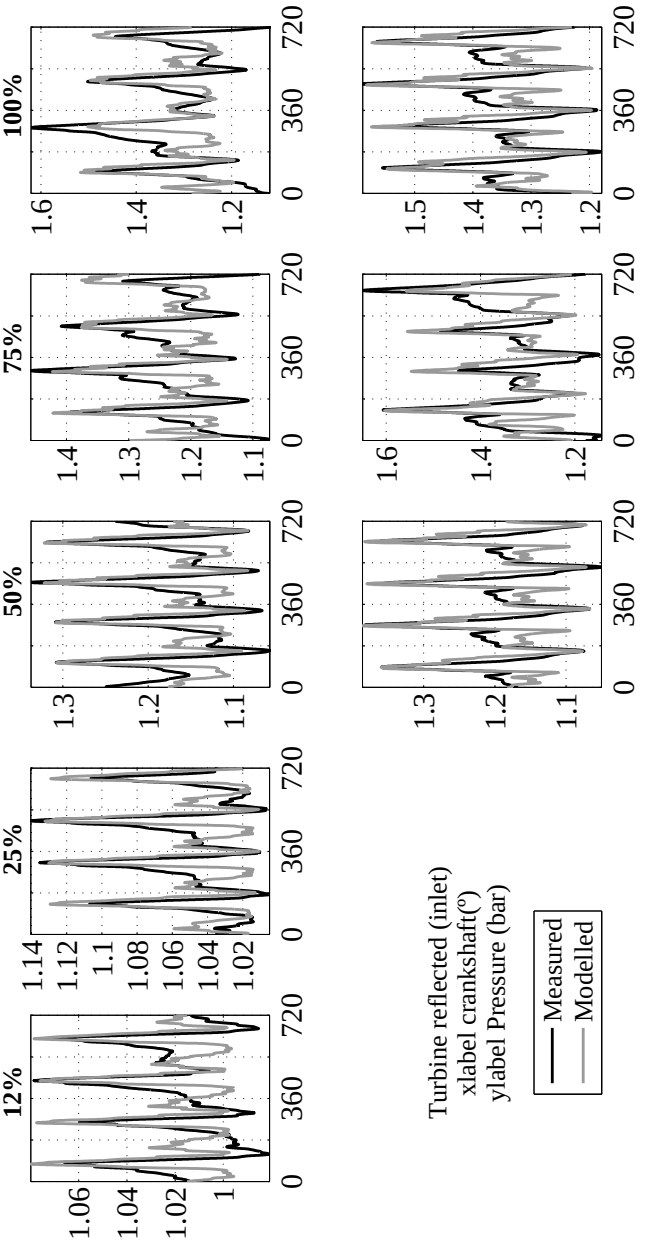

Figure A.25: Reflected pressure for turbocharger # 3 (Quasi-Adiabatic: measured vs. modelled).

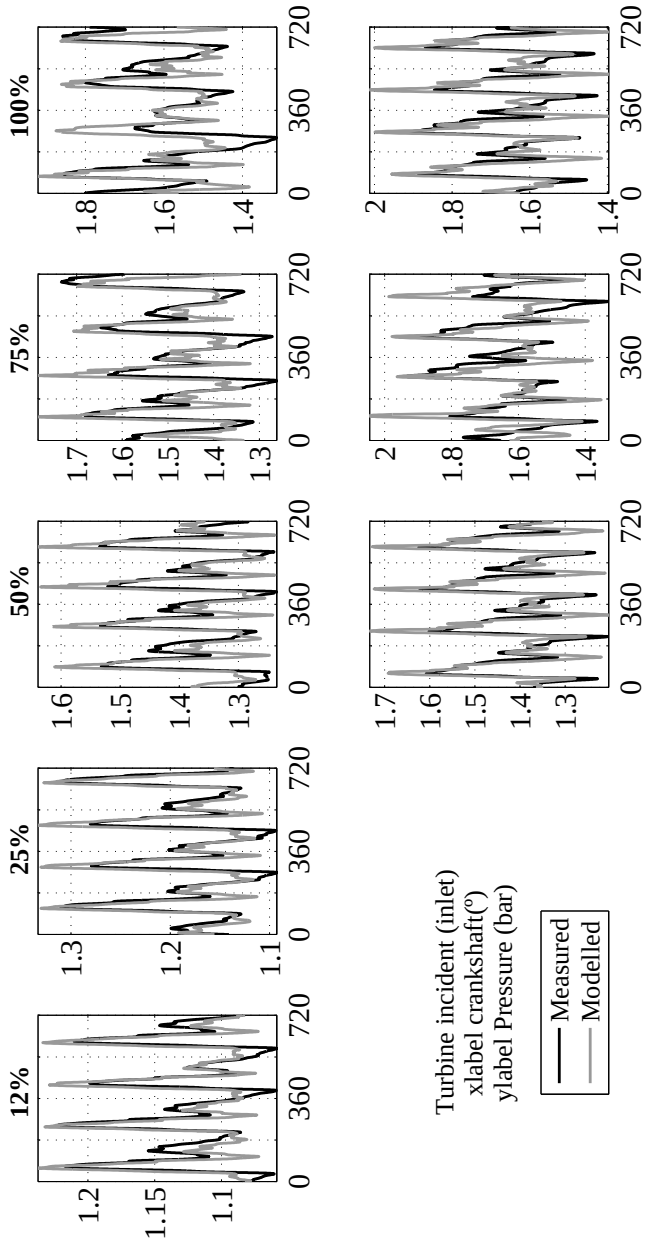

Figure A.26: Incident inlet pressure for turbocharger # 3 (Quasi-Adiabatic: measured vs. modelled).

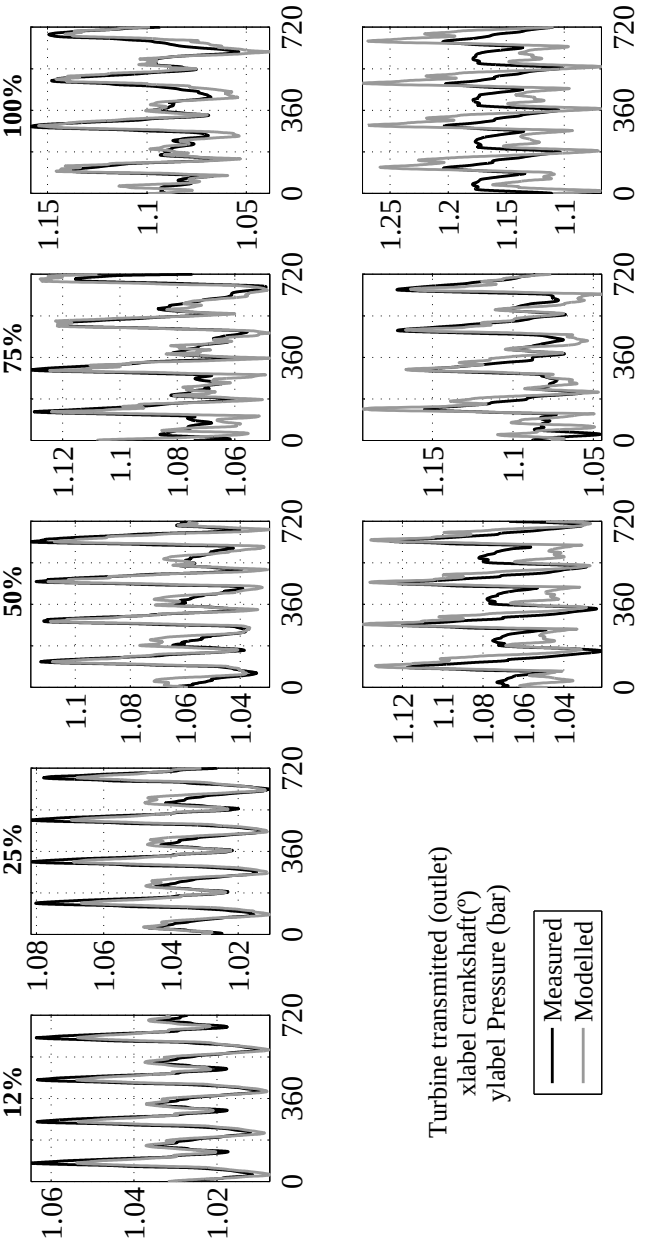

Figure A.27: Transmitted pressure for turbocharger # 3 (Quasi-Adiabatic: measured vs. modelled).

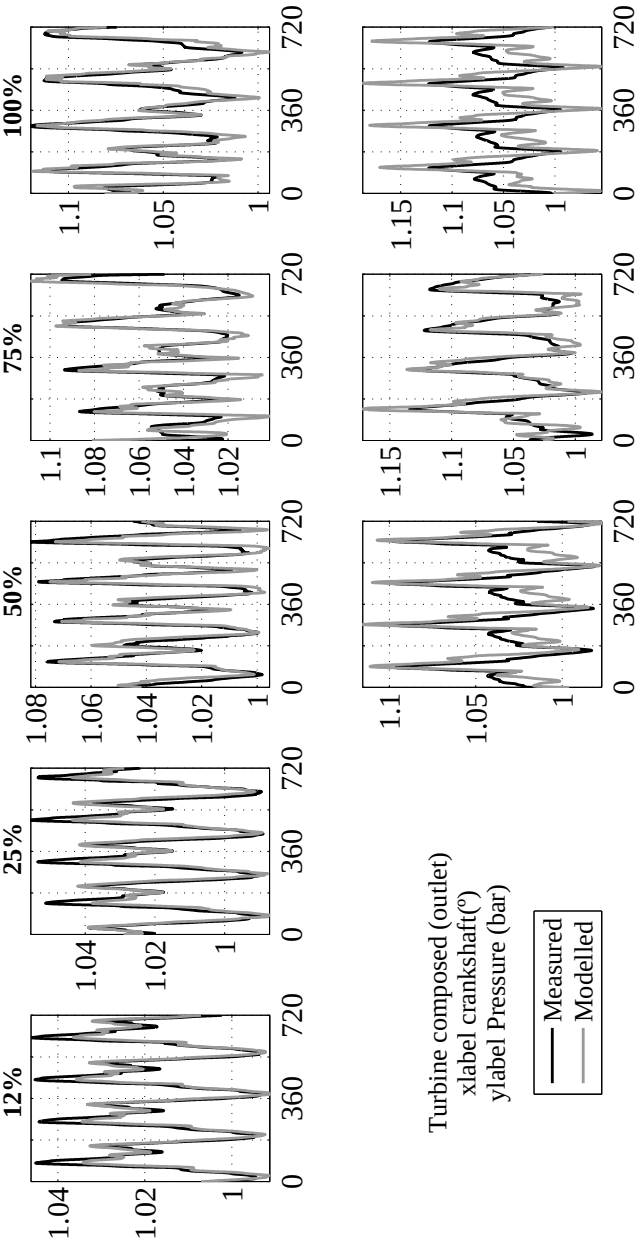

Figure A.28: Composed outlet pressure for turbocharger # 3 (Quasi-Adiabatic: measured vs. modelled).

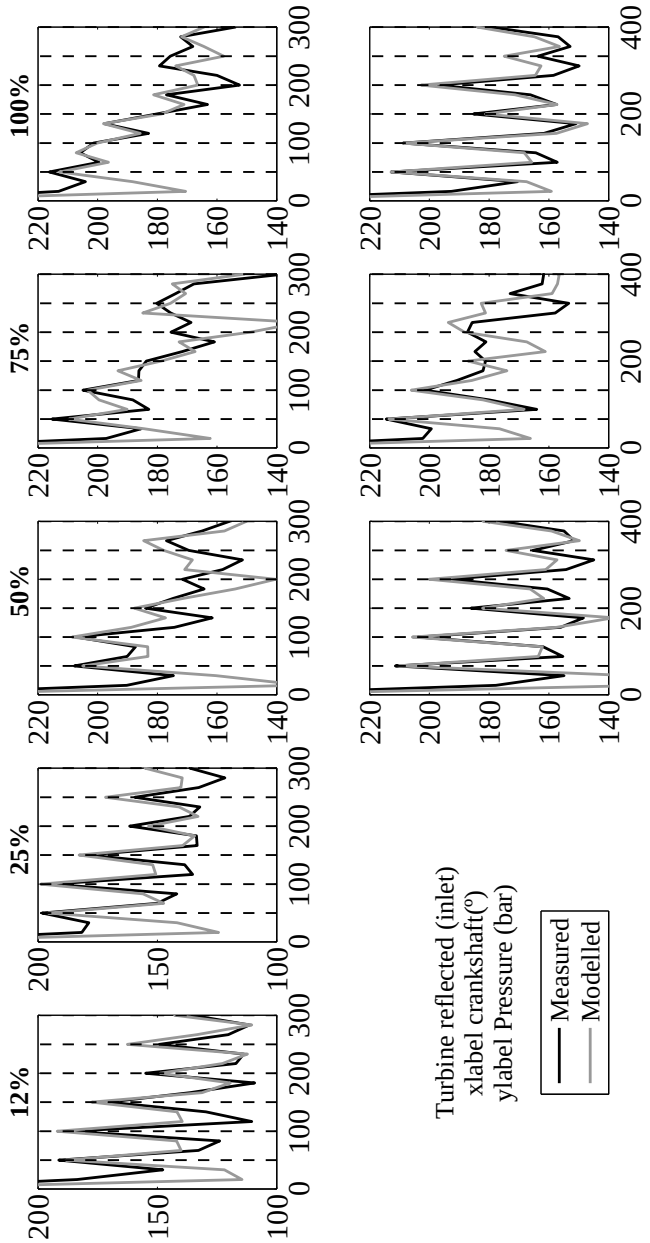

Figure A.29: Reflected pressure for turbocharger # 3 (Quasi-Adiabatic: measured vs. modelled).

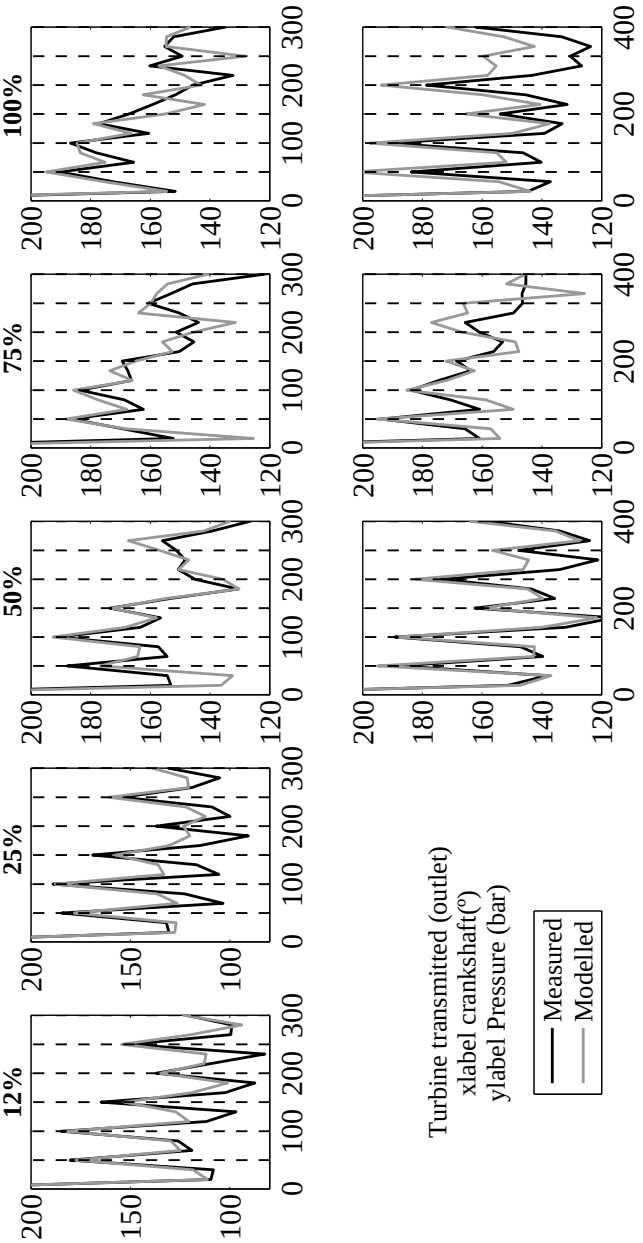

Figure A.30: Transmitted pressure for turbocharger # 3 (Quasi-Adiabatic: measured vs. modelled).

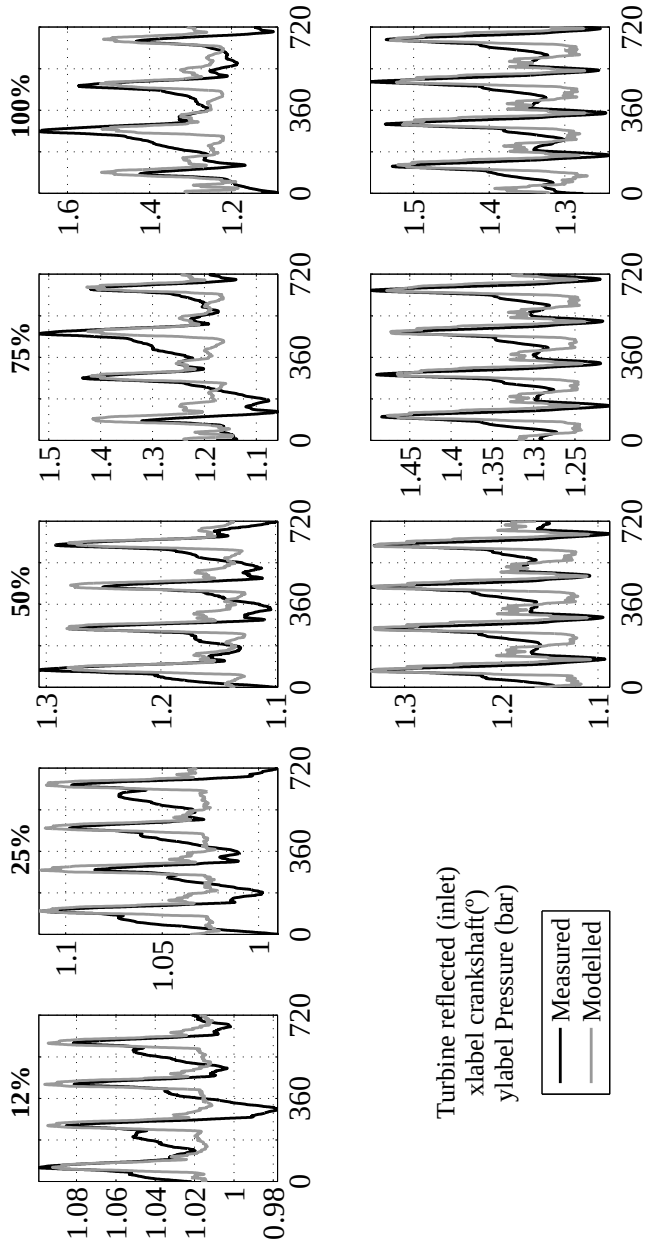

Figure A.31: Reflected pressure for turbocharger # 3 (Hot: measured vs. modelled).

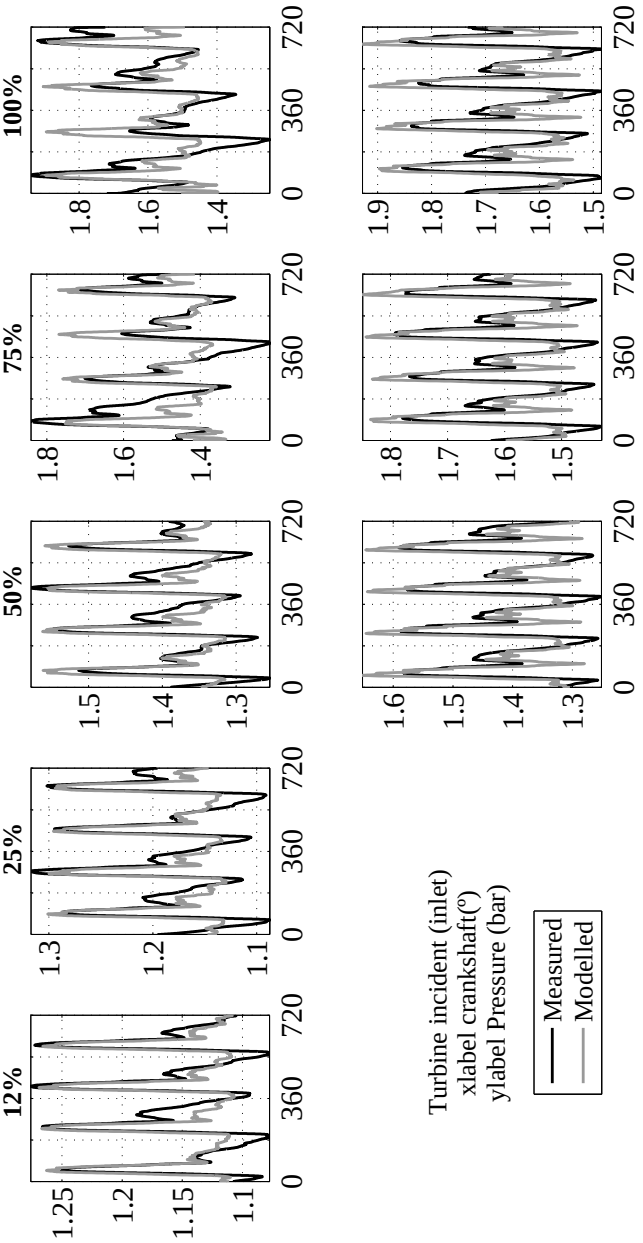

Figure A.32: Incident inlet pressure for turbocharger # 3 (Hot: measured vs. modelled).

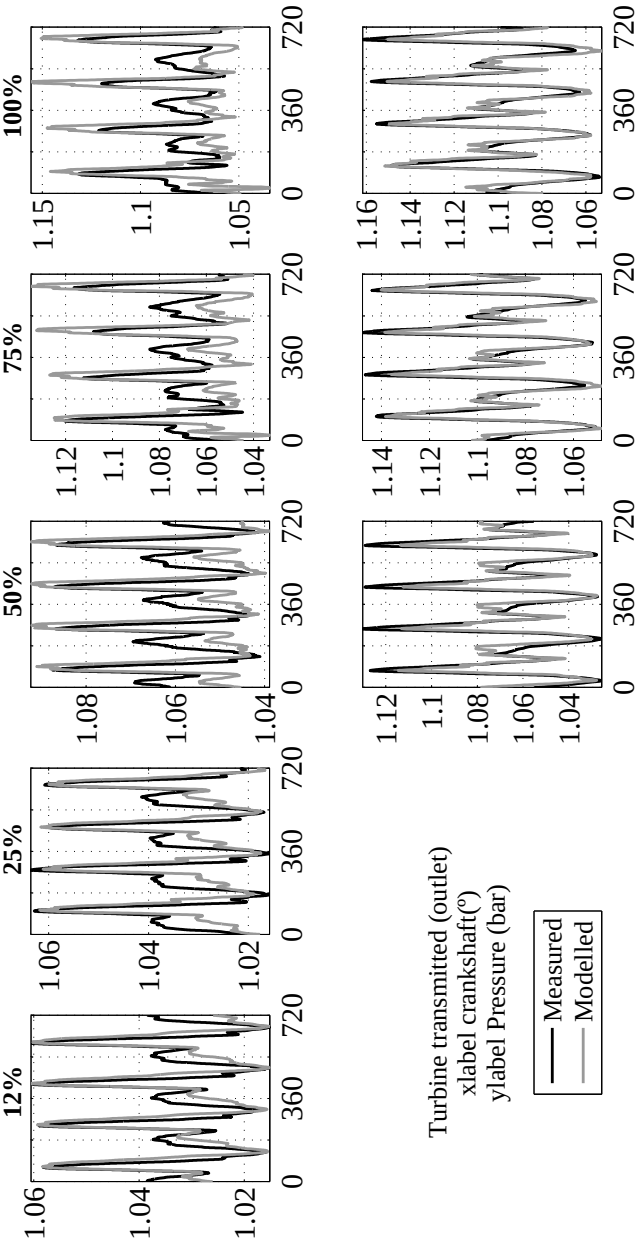

Figure A.33: Transmitted pressure for turbocharger # 3 (Hot: measured vs. modelled).

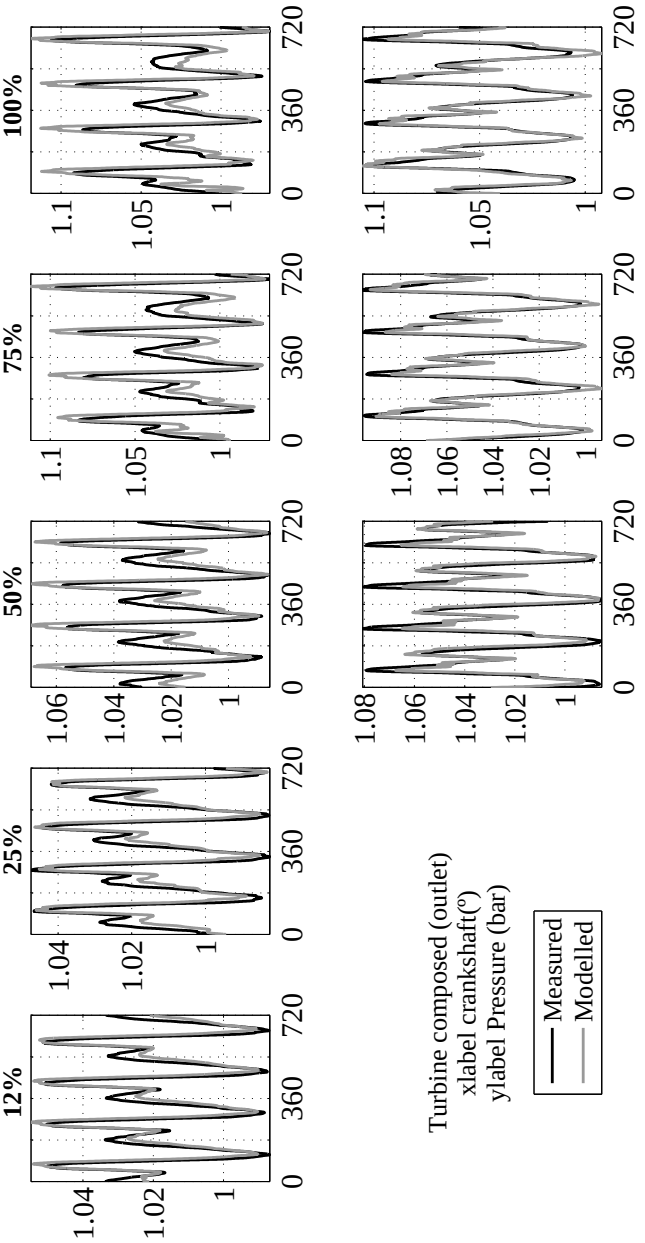

Figure A.34: Composed outlet pressure for turbocharger # 3 (Hot: measured vs. modelled).

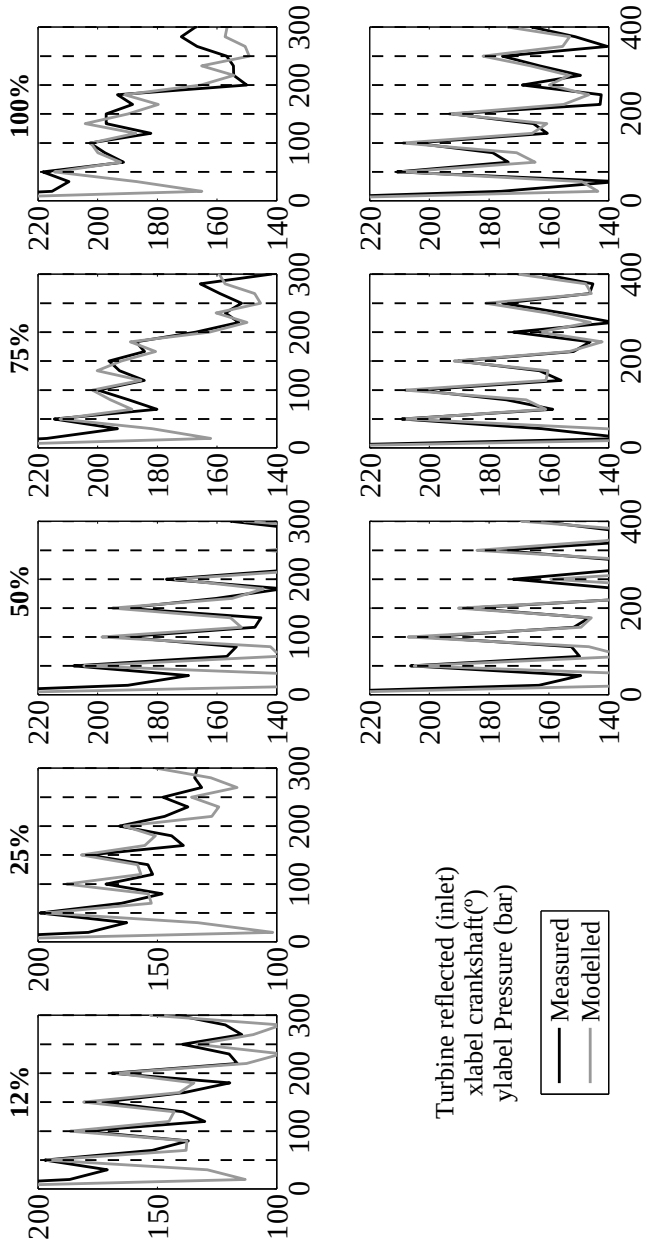

Figure A.35: Reflected pressure for turbocharger # 3 (Hot: measured vs. modelled).

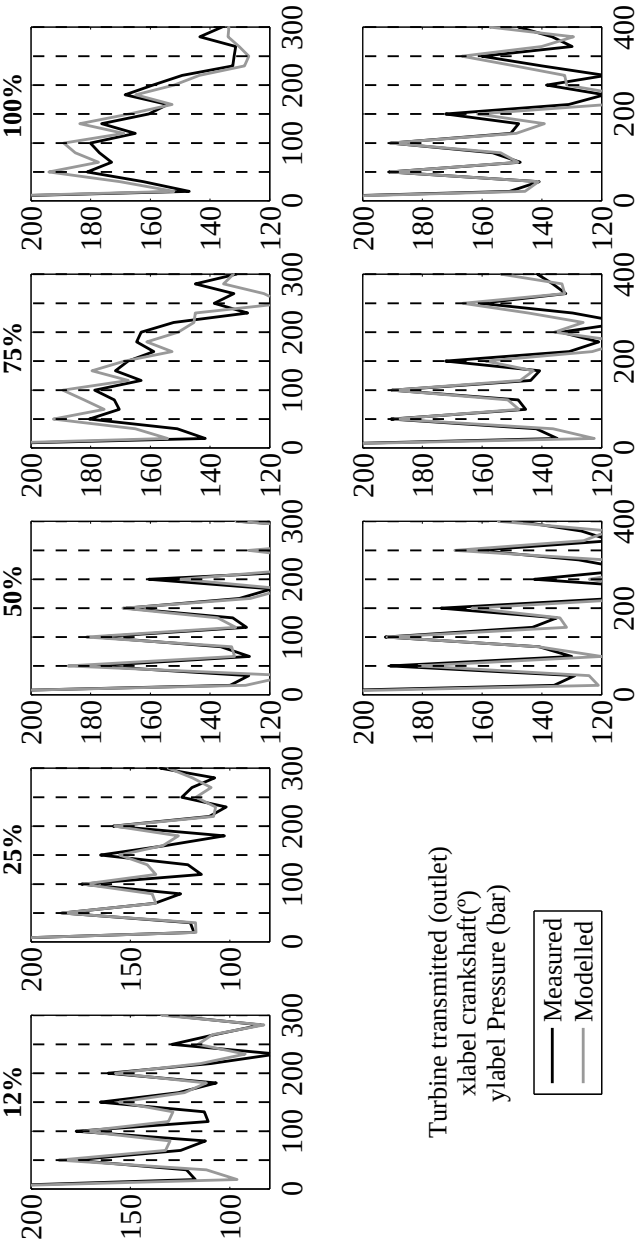

Figure A.36: Transmitted pressure for turbocharger # 3 (Hot: measured vs. modelled).

Appendix B

Annex

Contents

B.1 Introduction

As it has been discussed in this Thesis, obtaining more information about turbocharger behaviour than provided by manufacturers would help to improve accuracy of current modelling tools. These tools, like 1-D modelling, have increased their importance on engine division since they allow meeting with users demands and the stringent emission standards. Both objectives are currently achieved by reducing engine displacement but keeping the same power (*downsizing*), becoming boosting technologies crucial in that scenario. Turbocharger modelling has traditionally been a difficult task, since manufacturer maps do only provide information for a narrow operative range corresponding to mid-high load range, where heat transfer and mechanical losses effects are small compared to the turbocharger power. Information stored in those maps does not usually meet with engine operative conditions for urban driving conditions or partial load conditions. For those reasons, performance maps coupled to turbocharger models accounting for heat transfer, mechanical losses and extrapolation abilities will be the new tool providing accurate turbocharger modelling results.

In this section, extra information that turbocharger manufacturers should provide with their maps is described. That information will be used to feed up turbocharger models described in this thesis, in order to get an accurate turbocharger modelling tool.

B.2 Geometrical Data

Apart from turbocharger working operative conditions, internal data for compressor and turbine geometry is necessary to develop compressor and turbine models to account for acoustics. In addition rotor wheel dimensions is needed for extrapolation purposes. Shaft and bearings geometry is necessary to fill up friction losses model. Eventually lengths and diameters from turbocharger cases are necessary to apply convective heat transfer model. In this section, detailed geometrical information needed for turbocharger model is described.

B.2.1 Compressor Geometry

Geometrical parameters described in figure B.1 and sorted in table B.1 are needed to develop 1-D compressor model to account for acoustic and heat transfer effects.

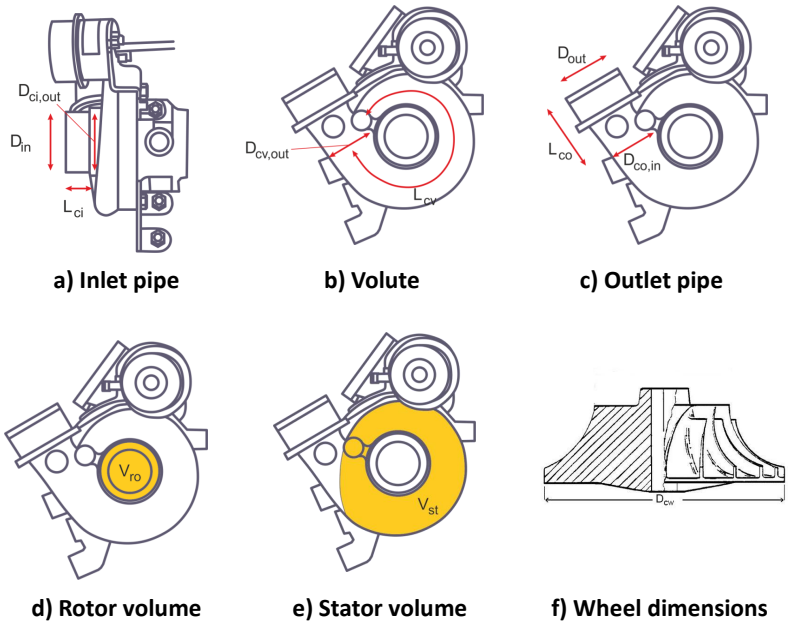

Figure B.1: Compressor geometry for 1-D modelling.

B.2.2 Turbine Geometry

Geometrical parameters showed in figure B.2 and table B.2 are needed to develop turbine 1-D geometrical model to account for acoustics and heat transfer effects. In addition detailed information about turbine rotor geometry is necessary to extrapolate turbine performance maps.

Table B.1: Compressor geometrical parameters

Description	Parameter	figure B.1
Inlet port (diameter from inlet section)	D_{in}	a
Inlet port (diameter from outlet section)	$D_{ci,out}$	a
Inlet port length	L_{ci}	a
Volute length	L_{cv}	b
Volute outlet diameter	$D_{cv,out}$	b
Outlet port (diameter from inlet section)	$D_{co,in}$=$D_{cv,out}$	c
Outlet port (diameter from outlet section)	D_{out}	c
Outlet port length	L_{co}	c
Rotor volume	V_{ro}	d
Stator volume	V_{st}	e
Rotor wheel diameter (outlet)	D_{cv}	f

B.2.3 Shaft Geometry

In order to apply mechanical losses model, geometry from turbocharger bearings should be supplied by manufacturers. That information is showed in table B.3 and figure B.3 for journal bearing geometry and in table B.4 and figure B.4 for turbocharger axial bearing. In addition inertial momentum of the rotary assembly should be provided too.

B.2.4 Turbocharger Geometry

Turbocharger geometry showed in table B.5 and figure B.5 is necessary to apply heat transfer model, since convective internal heat transfer correlations have been fitted using turbocharger geometry easy to measure. In addition material properties shown in table B.6 for the turbocharger are also needed to complete the conductive and convective part of heat transfer model.

B.3 Testing data

Apart of getting detailed information about shaft, bearings, wheels and volutes geometry presented above, turbocharger testing parameters showed in

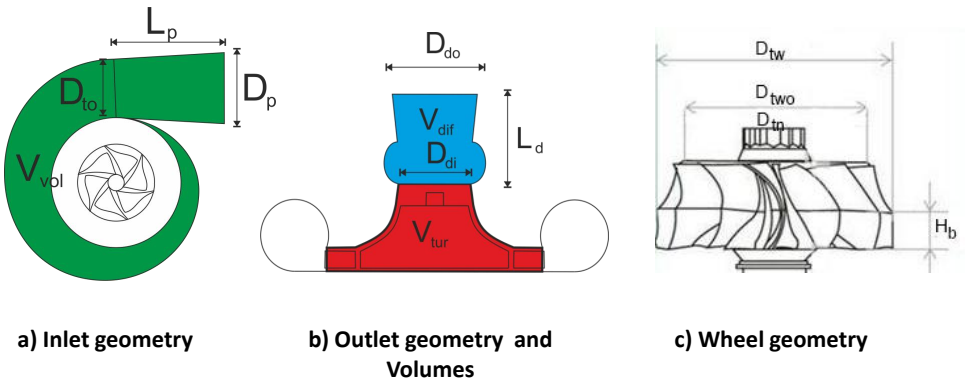

Figure B.2: Turbine geometry

table B.7 should be included to complete information provided in current turbocharger maps. That information is necessary to discount heat transfer and mechanical losses effects to the compressor manufacturer map (the original). In addition inlet flow conditions for the compressor (pressure and temperature) should be given too since real mass flow passing through the compressor will be necessary to discount heat transfer effects instead of the corrected mass flow showed in manufacturer maps. Testing information and geometrical data presented before will be used coupled to heat transfer and mechanical losses models to correct compressor efficiency (given in the map) obtaining so the adiabatic efficiency.

Table B.8 shows the extra information needed to determine turbine adiabatic efficiency from the information stored in manufacturer map (original). For doing so it is necessary to determine turbine real mass flow (using turbine inlet conditions), since that mass flow is used to determine the amount of energy lost inside the turbine (named as $\dot{Q}_{Gas/T}$). Mass flow passing through the compressor is necessary to discount heat transfer on the compressor side what updates nodes temperatures of heat transfer model. Pressure ratio at compressor and turbine side are needed to determine axial forces for thrust bearing model. Turbocharger speed, and oil conditions are used to discount heat transfer and friction losses from manufacturer map. Eventually, coolant properties are used in the heat transfer model.

Table B.2: Turbine geometrical parameters

Description	Parameter	figure B.2
Turbine volute volume	V_{vol}	a
Tongue diameter	D_{to}	a
Inlet port diameter	D_p	a
Port Length	L_p	a
Diffuser volume	V_{dif}	b
Diffuser Inlet diameter	D_{di}	b
Diffuser Outlet diameter	D_{do}	b
Inlet wheel diameter	D_{tw}	c
Outlet wheel diameter	D_{tn}	c
Nut diameter	D_{two}	c
Inlet blade height	H_b	c

Description	Parameter
Shaft Diameter	$2 \cdot R_{jb}$
Total length of the bearing	L_{jb}
Minimum clearance	h_{jb}

Table B.3: Journal Bearing geometry

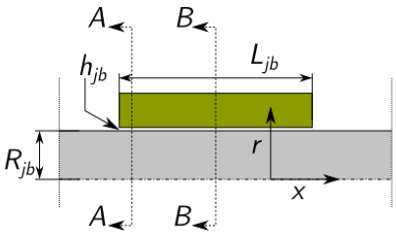

Figure B.3: Journal Bearing

Description	Parameter
Minimum Radius	$R_{tb,min}$
Maximum Radius	$R_{tb,max}$

Table B.4: Thrust Bearing geometry

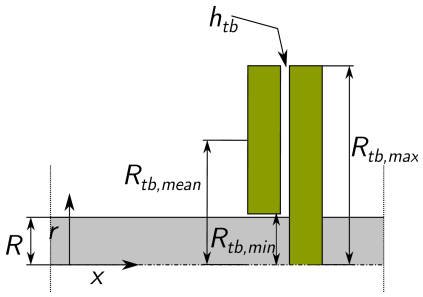

Figure B.4: Thrust Bearing

Description	parameter
Turbine external diameter	**Dt**
Turbine external length	**Lt**
Compressor ext. diameter	**Dc**
Compressor external length	**Lc**
Housing external diameter	**Dh**
Housing external length	**Lh**
Oil inlet port diameter	
Cooling inlet port diameter	

Table B.5: Turbo external geometry

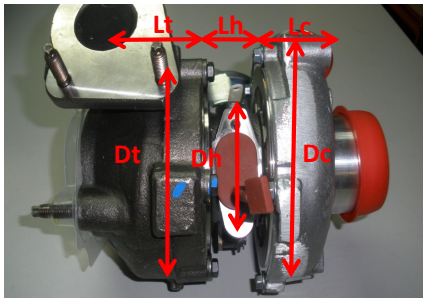

Figure B.5: Turbocharger geometry

Table B.6: Turbocharger material properties

Description	Parameter
Turbine density	ρ_T
Compressor density	ρ_C
Housing density	ρ_H
Turbine conductivity	κ_T
Compressor conductivity	κ_C
Housing conductivity	κ_H
Turbine capacity	C_T
Compressor capacity	C_C
Housing capacity	C_H

Table B.7: Extra experimental information to correct compressor manufacturer maps.

Parameter	Original Map	Heat Transfer Model	Mechanical Losses Model
from compressor measures			
Compressor Corrected Speed	✓		
Compressor Ratio	✓		
Corrected Mass Flow	✓		
Efficiency	✓		
Inlet temperature		✓	
Inlet pressure			✓
from turbine side			
Turbine mass flow		✓	
Turbine expansion ratio			✓
Turbine inlet temperature		✓	
from lube oil side			
Inlet temperature		✓	✓
Mass flow		✓	✓
from coolant side			
Inlet temperature		✓	
Mass flow		✓	

Table B.8: Extra experimental information to correct turbine manufacturer maps.

Parameter	Original Map	Heat Transfer Model	Mechanical Losses Model
from turbine measures	✓		
Turbine reduced flow	✓		
Expansion ratio	✓		
Reduced speed	✓		
Efficiency	✓		
Turbine inlet temperature		✓	
Turbine inlet pressure		✓	
from compressor measures			
Compressor mass flow		✓	
Compressor pressure ratio			✓
Compressor inlet temperature		✓	
from lube oil side			
Inlet temperature		✓	✓
Mass flow		✓	✓
from coolant side			
Inlet temperature		✓	
Mass flow		✓	

Bibliography

[1] *" Council Directive 91/441/EEC of 26 June 1991 on the Approximation of the Laws of the Member States Relating to Measures to Be Taken Against Air Pollution by Emissions from Motor Vehicles"*. Official Journal of the European Union, 30/08/1991, pp. 1-106, 1991. (Cit. on p. 2).

[2] *" Council Directive 98/69/EEC of 13 October 1998 on the Approximation of the Laws of the Member States Relating to Measures to be Taken Against Air Pollution by Emissions from Motor Vehicles"*. Official Journal of the European Union, 28/12/1998, pp. 1-65, 1998. (Cit. on p. 2).

[3] *" Regulation 715/2007 of the European Parliament and of the Council of 20 June 2007 on Type Approval of Motor Vehicles with Respect to Emissions from Light Passenger and Commercial Vehicles (Euro 5 and Euro 6) and on Access to Vehicle Repair and Maintenance Information"*. Official Journal of the European Union, 29/06/2007, pp. L171/1-16, 2007. (Cit. on p. 2).

[4] *7D-Soft High Technology Inc. 1stOpt manual, Release 3.0, http://www.7d-soft.com/ ; April 2010.* (Cit. on p. 66).

[5] M. Abidat and M. Hachemi. "Off-design performance of a turbocharger mixed flow turbine". In: *6th European Conference on Turbomachinery, Lille, France, 7-11 March.* 2005 (cit. on pp. 59, 64).

[6] M. Abidat, M. Hachemi, M.K. Hamidou, and N. Baines. "Prediction of the steady and non-steady flow performance of a highly loaded mixed flow turbine". In: *Proceedings of the Institution of Mechanical Engineers* 212 (1998), pp. 173–184 (cit. on pp. 59, 62).

[7] H. Aghaali and HE. Angstrom. "Improving turbocharged engine simulation by including heat transfer in the turbocharger". In: *SAE Technical Paper* 2012-01-0703 (2012) (cit. on p. 35).

[8] I. Al-Hinti, M. Samhouri, A. Al-Ghandoor, and A. Sakhrieh. "The effect of boost pressure on the performance characteristics of a diesel engine: A neuro-fuzzy approach". In: *Applied Energy* 86 (2009), pp. 113–121 (cit. on p. 4).

[9] J. Andersen, E. Karlsson, and A. Gawell. "Variable Turbine Geometry on SI Engines". In: *SAE Technical Paper* 2006-01-0020 (2006) (cit. on p. 57).

[10] P. Andersson. "Air Charge Estimation in Turbocharged Spark Ignition Engines". PhD thesis. Linköpings Universitet, 2005 (cit. on p. 52).

[11] T. Appenzeller. "End of Cheap Oil". In: *National Geographic Magazine* June (2004) (cit. on p. 2).

[12] C. Arcoumanis, I. Hakeem, L. Khezzar, R.F. Martinez-Botas, and N. Baines. "Performance of a mixed flow turbocharger turbine under pulsating flow conditions". In: *ASME International gas turbine and aeroengine congress and exposition* 95-GT-210 (1995) (cit. on p. 162).

[13] N. Baines, H. Mousthapa, M. Zelesky, and D. Japikse. *Axial and Radial Turbines*. ISBN 0 933283 12 0. Concepts NREC, Vermont, 2003 (cit. on pp. 144, 164, 173).

[14] N. Baines, K. Wygant, and A. Dris. "The analysis of Heat Transfer in Automotive Turbochargers". In: *Proceedings of ASME Turbo Expo 2009, GT2009-59618*. 2009 (cit. on pp. 24, 26, 27, 29, 37, 44, 111).

[15] N.C. Baines, A. Hajilouy-Benisi, and J.H. Yeo. "The pulse flow performance and modelling of radial inflow turbines". In: *Proceedings of the Institution of Mechanical Engineers, 5th International Conference on Turbocharging and Turbochargers* C484/006/94 (1994), pp. 209–220 (cit. on p. 60).

[16] J. Benajes, E. Reyes, and J.M. Luján. "Modelling study of the scavenging process in a turbocharged diesel engine with modified valve operation". In: *Proc. IMechE, Part C: Journal of Mechanical Engineering Science* 210(4) (1996), pp. 383–393. DOI: 10.1243/PIME_PROC_1996_210_210_02 (cit. on p. 145).

[17] R.S. Benson. *The thermodynamics and gas dynamics of internal-combustion engines*. Vol. 1. Clarendon Press Oxford, 1982 (cit. on pp. 160, 163).

[18] R.S. Benson and K.H. Scrimshaw. "An experimental investigation of non-steady flow in a radial gas turbine". In: *Proceedings of the Institution of Mechanical Engineers* 180 (1965), pp. 74–85 (cit. on pp. 44, 70).

[19] M.S. Bhatti and R.K. Shah. *Turbulent and transition flow convective heat transfer in ducts*. Ed. by S. Kakaç, R.K. Shah, and W. Aung. Vol. Handbook of Single-Phase Convective Heat Transfer, chapter 4. Wiley-Interscience, 1987 (cit. on p. 111).

[20] F.S. Bhinder and P.S. Gulati. "A method for predicting the performance of centripetal turbines in non-steady flow". In: *Proceedings of the Institution of Mechanical Engineers, 1st International Conference on Turbocharging and Turbochargers* (1978), pp. 233–240 (cit. on p. 60).

[21] D. Bohn, T. Heuer, and K. Kusterer. "Conjugate Flow and Heat Transfer Investigation of a Turbo Charger". In: *Journal of Engineering for Gas Turbines and Power* 127.3 (2005), pp. 663–669 (cit. on pp. 24, 26, 30).

[22] D. Bohn, T. Heuer, and K. Kusterer. "Conjugate flow and heat transfer investigation of a turbocharger: Part I: Numerical results". In: *ASME paper* GT2003-38445 (2003) (cit. on pp. 30, 37, 39–41).

[23] D. Bohn, N. Moritz, and M. Wolff. "Conjugate flow and heat transfer investigation of a turbocharger: Part II: Experimental results". In: *ASME paper* GT2003-38449 (2003) (cit. on pp. 27, 37).

[24] A. Boretti. "Towards 40directly injected, turbocharged, spark ignition ethanol engines". In: *Energy Conversion and Management* 57.0 (2012), pp. 154 –166. ISSN: 0196-8904. DOI: 10.1016/j.enconman.2011.12.011. URL: http://www.sciencedirect.com/science/article/pii/S0196890411003657 (cit. on p. 4).

[25] L. Bouard, M. Fillon, and J. Frene. "Comparison between three turbulent models application to thermohydrodynamic performances of tilting-pad journal bearings". In: *Tribology International* 29 (1996), pp. 11–18 (cit. on p. 50).

[26] BP. *BP Statistical Review of World Energy June 2012* (cit. on p. 3).

[27] M. Canova. "Development and validation of a control-oriented library for the simulation of automotive engines". In: *International Journal of Engine Research* 5 (2004), pp. 219–228 (cit. on p. 67).

[28] M. Canova, S. Midlam-Mohler, Y. Guezennec, and G. Rizzoni. "Mean value modeling and analysis of HCCI diesel engines with external mixture formation". In: *Journal of Dynamic Systems, Measurement, and Control* 131 (2009), pp. 1–14 (cit. on p. 67).

[29] C. Cervelló. "Contribución a la caracterización experimental y al modelado de turbinas de geometría variable en grupos de sobrealimentación". PhD thesis. Universidad Politécnica de Valencia, 2005 (cit. on p. 7).

[30] S.C. Chapra and R.P. Canale. *Numerical Methods for Engineers*. Ed. by New York 4th Ed. McGraw-Hill, 2002 (cit. on p. 54).

[31] H. Chen, I. Hakeem, and R. Martinez-Botas. "Modelling of a turbocharger turbine under pulsating inlet conditions". In: *Proceedings of the Institution of Mechanical Engineers, Part A: Journals of Power and Energy* 210 (1996), pp. 397–408 (cit. on pp. 59, 60, 62).

[32] H. Chen and D. Winterbone. "A method to predict performance of vaneless radial turbine under steady and unsteady flow conditions". In: *Proceedings of the Institution of Mechanical Engineers, Turbocharging and Turbochargers* (1990), pp. 13–22 (cit. on pp. 59, 61, 159).

[33] P. Chesse, D. Chalet, and X. Tauzia. "Impact of heat transfer on the performance calculations of automotive turbocharger compressor". In: *Oil & Gas Science and Technology. IFP Energies nouvelles* (2011) (cit. on p. 26).

[34] D.C. Clay and S.W. Moch. "Development of a new test facility for evaluation of turbocharger noise emissions". In: *IMechE Conference Transactions*. 7th International Conference on Turbochargers and Turbocharging C602/032/2002. 2002, pp 129–141 (cit. on p. 145).

[35] M. Cormerais, JF. Hetet, P. Chessé, and A. Maiboom. "Heat Transfer analysis in a turbocharger compressor: Modelling and Experiments". In: *SAE Technical Paper* 2006-01-0023 (2006) (cit. on p. 21).

[36] M. Cormerais, J.F. Hetet, P. Chesse, and A. Malboom. "Heat Transfers Characterization in a Variable Geometry Turbocharger: Experiments and Correlations". In: *Proceedings of ASME Internal Combustion Engine Division, Spring Technical Conference*. 2006 (cit. on p. 44).

[37] A.W. Costall, R.M. McDavid, R.F. Martinez-Botas, and N.C. Baines. "Pulse performance modelling of a twin-entry turbocharger turbine under full and unequal admission". In: *ASME paper* GT2009-59406 (2009) (cit. on pp. 59, 61–63, 159).

[38] A.W. Costall, S. Szymko, R. Martinez-Botas, D. Filsionger, and D. Ninkovic. "Assesment of unsteady behavior in turbocharger turbines". In: *ASME paper* GT2006-90348 (2006) (cit. on pp. 59, 62).

[39] C. Couderc, P. Chessé, and D. Chalet. "Comparison of the prediction performances of different models of radial turbine under steady and unsteady flow conditions". In: *Scientific Bulletin, Automotive series, year XVII, No.21(2)* (cit. on pp. 68, 70).

[40] R.C. Coy. "Practical applications of lubrication models in engines". In: *Tribology International* 31.10 (1998), pp. 563 –571. ISSN: 0301-679X. DOI: 10.1016/S0301-679X(98)00077-2. URL: http://www.sciencedirect.com/science/article/pii/S0301679X98000772 (cit. on p. 49).

[41] A. Dale. "Radial Vaneless Turbocharger Turbine Performance". PhD thesis. Imperial College, London, 1990 (cit. on pp. 59, 64, 162).

[42] A. Dale and N. Watson. "Vaneless radial turbocharger turbine performance". In: *Proceedings of the Institution of Mechanical Engineers* C110/86 (1986) (cit. on p. 59).

[43] M. Deligant, P. Podevin, and G. Descombes. "CFD model for turbocharger journal bearing performances". In: *Applied Thermal Engineering* 31.5 (2011). MNF 2009 Special Issue, pp. 811 –819. ISSN: 1359-4311. DOI: 10.1016/j.applthermaleng.2010.10.030. URL: http://www.sciencedirect.com/science/article/pii/S1359431110004692 (cit. on pp. 46, 49).

[44] M. Deligant, P. Podevin, and G. Descombes. "Experimental identification of turbocharger mechanical friction losses". In: *Energy* 39 (2012), pp. 388–394 (cit. on pp. 44, 46).

[45] M. Deligant, P. Podevin, G. Descombes, T. Lamquin, F. Vidal, and A. Marchal. "Effect of axial load on turbocharger friction losses". In: *Proceedings of the 13th EAEC European Congress, Valencia, Spain*. 2011 (cit. on p. 45).

[46] M. Deligant, P. Podevin, T. Lamquin, F. Vidal, and A. Marchal. "Experimental study of turbocharger's performances at low speeds". In: *Proceedings of the ASME 2010 Internal Combustion Engine Division Fall Technical Conference*. 2010 (cit. on p. 43).

[47] G. Descombes, F. Maroteaux, J. Jullien, and M. Pluviose. "Modelling of flow within a vaned channel in thermal engine". In: *International Journal of Thermal Sciences* 44.10 (2005), pp. 1000–1012 (cit. on p. 50).

[48] A. Diango, C. Perilhon, E. Danho, and G. Descombes. *Advances in gas turbine technology*. Ed. by Ernesto Benini. InTech, 2011. DOI: 10.5772/664 (cit. on p. 29).

[49] A. Diango, C. Perilhon, G. Descombes, and E. Danho. "Application of exergy balances for the optimization of non-adiabatic small turbomachines operation". In: *Energy* 36 (2011), pp. 2924–2936 (cit. on p. 44).

[50] V. Dolz, R. Novella, A. García, and J. Sánchez. "HD Diesel engine equipped with a bottoming Rankine cycle as a waste heat recovery system. Part 1: Study and analysis of the waste heat energy". In: *Applied Thermal Engineering* 36.0 (2012), pp. 269 –278. ISSN: 1359-4311. DOI: 10.1016/j.applthermaleng.2011.10.025. URL: http://www.sciencedirect.com/science/article/pii/S1359431111005631 (cit. on p. 4).

[51] P.G. Dowell and S. Akehurst. "Advanced Mapping Techniques for Radial Compressor for Use in Real-Time Engine Models". In: *SAE Technical Paper* 2010-01-1227 (2010) (cit. on p. 54).

[52] Pierre Duret, ed. *New Generation of Engines Combustion Processes for the Future?* Entretiens IFP Series. Editions Technip, 2002, p. 179. URL: ISBN-13:9782710808121 (cit. on p. 4).

[53] A.D. Ehrlich. "Characterization of unsteady on-engine turbocharger turbine performance". PhD thesis. Purdue University, West Lafayette, IN, 1998 (cit. on p. 63).

[54] A.D. Ehrlich, P.B. Lawless, and S. Fleeter. "On-engine turbocharger turbine inlet flow characterization". In: *SAE Technical Paper* 971565 (1997) (cit. on p. 63).

[55] L. Eriksson. "Modeling and Control of Turbocharged SI and DI Engines". In: *Oil & Gas Science and Technology. IFP Energies nouvelles* 62 (2007), pp. 523–538 (cit. on pp. 52, 69).

[56] L. Eriksson, J.B. Nielsen, F.P. Bergström, and P. Andersson. "Modeling of a Turbocharged SI Engine". In: *Annual Reviews in Control* 26 (2002), pp. 129–137 (cit. on pp. 54, 65, 70).

[57] P. Fajardo. "Methodology for the Numerical Characterization of a Radial Turbine under Steady and Pulsating Flow". PhD thesis. Universidad Politécnica de Valencia, 2012 (cit. on p. 7).

[58] X. Fang and Q. Dai. "Modeling of turbine mass flow rate performances using the Taylor expansion". In: *Applied Thermal Engineering* 30 (2010), pp. 1824–1831 (cit. on p. 68).

[59] X. Fang, Q. Dai, Y. Yin, and Y. Xu. "A compact and accurate empirical model for turbine mass flow characteristics". In: *Energy* 35 (2010), pp. 4819–4823 (cit. on p. 66).

[60] O. Flärdh and J. Märtensson. "Analysis of a Quasy-Steady Extension to the Turbine Model in Mean Value Engine Models". In: *SAE Technical Paper* 2010-01-1191 (2010) (cit. on pp. 66, 70).

[61] G. Fontana and E. Galloni. "Variable valve timing for fuel economy improvement in a small spark-ignition engine". In: *Applied Energy* 86.1 (2009), pp. 96–105. ISSN: 0306-2619. DOI: 10.1016/j.apenergy.2008.04.009. URL: http://www.sciencedirect.com/science/article/pii/S0306261908001013 (cit. on p. 4).

[62] R. Friedfeldt, T. Zenner, R. Ernst, and A. Fraser. "Three-cylinder Gasoline Engine with Direct Injection". In: *MTZ worldwide Edition* 05 (2012) (cit. on p. 4).

[63] S.M. Futral and C.A. Wasserbauer. *Off-design performance prediction with experimental verification for a radial-inflow turbine*. Tech. rep. TN D-2621. NASA, 1965 (cit. on pp. 162, 168–170, 172).

[64] J. Galindo, H. Climent, C. Guardiola, and A. Tiseira. "On the effect of pulsating flow on surge margin of small centrifugal compressors for automotive engines". In: *Experimental Thermal and Fluid Science* 33 (2009), pp. 1163–1171 (cit. on p. 43).

[65] J. Galindo, J.M. Luján, J.R. Serrano, V. Dolz, and S. Guilain. "Description of a heat transfer model suitable to calculate transient processes of turbocharged Diesel engines with one-dimensional gas-dynamic codes". In: *Applied Thermal Engineering* 26.1 (2006), pp. 66–76 (cit. on p. 20).

[66] J. Galindo, J.M. Luján, J.R. Serrano, V. Dolz, and S. Guilain. "Design of an exhaust manifold to improve transient performance of a high-speed turbocharged Diesel engine". In: *Experimental Thermal and Fluid Science* 28.8 (2004), pp. 863–875 (cit. on p. 145).

[67] J. Galindo, J.R. Serrano, F.J. Arnau, and P. Piqueras. "Description and analysis of a one-dimensional gas-dynamic model with Independent Time Discretization". In: *Proceedings of the ASME Internal Combustion Engine Division 2008 Spring Technical Conference ICES2008*. 2008 (cit. on p. 218).

[68] J. Galindo, J.R. Serrano, F.J. Arnau, and P. Piqueras. "Description of a Semi-Independent Time Discretization Methodology for a One-Dimensional Gas Dynamics Model". In: *Journal of engineering for gas turbines and power* 131 (2009). DOI: 10.1115/1.2983015 (cit. on pp. 7, 218).

[69] J. Galindo, J.R. Serrano, H. Climent, and O. Varnier. "Impact of two-stage turbocharging architectures on pumping losses of automotive engines based on an analytical model". In: *Energy Conversion and Management* 51.10 (2010), pp. 1958 –1969. ISSN: 0196-8904. DOI: 10.1016/j.enconman.2010.02.028. URL: http://www.sciencedirect.com/science/article/pii/S0196890410000944 (cit. on p. 4).

[70] J. Galindo, J.R. Serrano, C. Guardiola, and C. Cervelló. "Surge limit definition in a specific test bench for the characterization of automotive turbochargers". In: *Experimental Thermal and Fluid Science* 30 (2006), pp. 449–462 (cit. on pp. 57, 162, 163).

[71] J. Galindo, J.R. Serrano, P. Piqueras, and O. García-Afonso. "Heat transfer modelling in honeycomb wall-flow diesel particulate filters". In: *Energy* 43.1 (2012). 2nd International Meeting on Cleaner Combustion (CM0901-Detailed Chemical Models for Cleaner Combustion), pp. 201 –213. ISSN: 0360-5442. DOI: 10.1016/j.energy.2012.04.044. URL: http://www.sciencedirect.com/science/article/pii/S0360544212003428 (cit. on p. 4).

[72] E. Galloni, G. Fontana, and R. Palmaccio. "Numerical analyses of {EGR} techniques in a turbocharged spark-ignition engine". In: *Applied Thermal Engineering* 39.0 (2012), pp. 95 –104. ISSN: 1359-4311. DOI: 10.1016/j.applthermaleng.2012.01.040. URL: http://www.sciencedirect.com/science/article/pii/S1359431112000592 (cit. on p. 4).

[73] *Gamma Technologies, 2010, GT-POWER User's Manuals and Tutorials. GT-SUITE Version 7.1.* (Cit. on pp. 35, 63, 66, 70).

[74] P. Gautier, A. Albrecht, P. Moulin, A. Chasse, L. Fontvieille, A. Guinois, and L. Doleac. *"A New Simulation Step Towards Virtual Bench Through the Challenging Case of Two-Stage Turbocharger Diesel Engine Control Design"*. SAE Technical Paper 2008-01-0355, 2008. (Cit. on p. 6).

[75] E.G. Giakoumis. "Lubricating oil effects on the transient performance of a turbocharged diesel engine". In: *Energy* 35 (2010), pp. 864–873 (cit. on p. 45).

[76] L. Guzzella. *Introduction to modeling and control of internal combustion engine systems*. Springer, 2009 (cit. on pp. 21, 33, 50).

[77] L. Guzzella, U. Wenger, and R. Martin. "IC-engine Downsizing and Pressure-Wave Supercharging for Fuel Economy". In: *SAE Technical Paper* 2000-01-1019 (2000) (cit. on p. 20).

[78] D. Hagelstein, B. Beyer, J. Seume, M. Rautenberg, and H. Hasemann. "Heuristical view on the non-adiabatic coupling system of combustion engine and turbocharger". In: *C602/015/2002. Proceedings of 7th International Conference on Turbochargers and Turbocharging. Professional Engineering Publishing. Ltd. IMechE. London.* 2002 (cit. on pp. 26, 30).

[79] F. Hellström and L. Fuchs. "Effects of inlet conditions on the turbine performance of a radial turbine". In: *ASME paper* GT2008-51088 (2008) (cit. on p. 59).

[80] F. Hellström and L. Fuchs. "Numerical computation of the pulsatile flow in a turbocharger with realistic inflow conditions from an exhaust manifold". In: *ASME paper* GT2009-59619 (2009) (cit. on p. 59).

[81] F. Hellström and L. Fuchs. "Numerical computations of pulsatile flow in a turbo-charger". In: *AIAA Aerospace Sciences Meeting and Exhibit, Reno, Nevada,7-10 January.* 2008 (cit. on p. 59).

[82] J. Heywood. *Internal Combustion Engine Fundamentals.* Ed. by ISBN 007 028637 X. McGraw-Hill Science/Engineering/Math, 1988 (cit. on pp. 66, 163).

[83] J.H. Horlock and D.E. Winterbone. *The thermodynamics and gas dynamics of internal combustion engines. Volume II.* Oxford: Clarendon Press, 1986 (cit. on p. 69).

[84] K.G. Høyer. "The history of alternative fuels in transportation: The case of electric and hybrid cars". In: *Utilities Policy* 16.2 (2008), pp. 63 –71. ISSN: 0957-1787. DOI: 10.1016/j.jup.2007.11.001. URL: http://www.sciencedirect.com/science/article/pii/S0957178707000768 (cit. on p. 3).

[85] L. Hu, C. Yang, H. Sun, E. Krivizky, L. Larosiliere, J Zhang, and M.C. Lai. "Experimental and computational analysis of impact of self recirculation casing treatment on turbocharger compressor". In: *SAE Technical Paper 2010-01-1224.* 2010 (cit. on p. 47).

[86] X. Hu. "An advanced turbocharger model for the internal combustion engine". PhD thesis. Purdue University, West Lafayette, IN, 2000 (cit. on p. 63).

[87] X. Hu and P.B. Lawless. "Predictions of on-engine efficiency for the radial turbine of a pulse turbocharged engine". In: *SAE Technical Paper* 2001-01-1238 (2001) (cit. on p. 63).

[88] F.P. Incropera and D.P. De Witt. *Fundamentos de transferencia de calor.* Prentice Hall, 1999 (cit. on p. 104).

[89] J.P. Jensen, A.F. Kristensen, S.C. Sorenson, N. Houbak, and E. Hendricks. "Mean value modeling of a small turbocharged diesel engine". In: *SAE Technical Paper* 910070 (1991) (cit. on pp. 50, 54, 67, 70).

[90] W. Jiang, J. Khan, and R. Dougal. "Dynamic centrifugal compressor model for system simulation". In: *Journal of power sources* 158.2 (2006), pp. 1333–1343 (cit. on p. 50).

[91] M. Jung, R.G. Ford, K. Glover, and N. et al. Collings. "Parameterization and Transient Validation of a Variable Geometry Turbocharger for Mean-Value Modeling at Low and Medium Speed-Load Points". In: *SAE Technical Paper* 2002-01-2729 (2002) (cit. on p. 50).

[92] L.J. Kastner and F.S. Bhinder. "A method for predicting the performance of a centripetal gas turbine fitted with a nozzle-less volute". In: *ASME paper* 75-GT-65 (1975) (cit. on p. 60).

[93] T. Katrasnik. "Hybridization of powertrain and downsizing of IC engine - a way to reduce fuel consumption and pollutant emissions - Part 1". In: *Energy Conversion and Management* 48 (2007), pp. 1411–23 (cit. on p. 162).

[94] T. Katrasnik. "Hybridization of powertrain and downsizing of IC engine - analysis and parametric study - Part 2". In: *Energy Conversion and Management* 48 (2007), pp. 1424–34 (cit. on p. 162).

[95] B. Kegl. "Influence of biodiesel on engine combustion and emission characteristics". In: *Applied Energy* 88.5 (2011), pp. 1803 –1812. ISSN: 0306-2619. DOI: 10.1016/j.apenergy.2010.12.007. URL: http://www.sciencedirect.com/science/article/pii/S0306261910005143 (cit. on p. 4).

[96] U. Kiencke and L. Nielsen. "Automotive Control Systems: For Engine, Driveline, and Vehicle". In: *Measurement Science and Technology* 11.12 (2000), p. 1828. URL: http://stacks.iop.org/0957-0233/11/i=12/a=708 (cit. on p. 4).

[97] A.J. King. "A turbocharger unsteady performance model for the GT-Power internal combustion engine simulation". PhD thesis. Purdue University, West Lafayette, IN, 2002 (cit. on p. 63).

[98] I. Kolmanovsky, P. Moraal, M.J. van Nieuwstadt, M. Criddle, and P. Wood. *Modelling and identification of a 2.0 l turbocharged DI diesel engine*. Tech. rep. Ford internal technical report SR-97-039, 1997 (cit. on pp. 50, 53).

[99] F. Kreith. *Principles of heat transfer*. International textbook Company Scranton, Pennsylvania, 1967 (cit. on p. 29).

[100] J. Lam, Q. Roberts, and G. McDonnell. "Flow modelling of a turbocharger turbine unser pulsating flow". In: *Proceedings of the Institution of Mechanical Engineers, Turbocharging and Turbochargers* (2002), pp. 181–197 (cit. on pp. 59, 64).

[101] T. Lamquin and K. Gjika. "Power losses identification on turbocharger hydrodynamic bearing". In: *Proceedings of ASME Turbo Expo 2009: Power for Land, Sea and Air. Orlando, FL. USA*. 2009 (cit. on p. 45).

[102] R. Lang. "Contribución a la Mejora del Margen de Bombeo en Compresores Centrífugos de Sobrealimentación". PhD thesis. Departamento de Máquinas y Motores Térmicos - UPV, 2011 (cit. on p. 7).

[103] J.M. Luján, J. Galindo, and J.R. Serrano. "Efficiency Characterization of Centripetal Turbines under Pulsating Flow Conditions". In: *SAE Technical Paper* 2001-01-0272 (2001) (cit. on pp. 59, 71, 214).

[104] S. Marelli and M. Capobianco. "Steady and pulsating flow efficiency of a waste-gated turbocharger radial flow turbine for automotive application". In: *Energy* (2010) (cit. on p. 44).

[105] G. Martin, V. Talon, P. Higelin, A. Charlet, and C. Caillol. "Implementing Turbomachinery Physics into Data Map-Based Turbocharger Models". In: *SAE Technical Paper* 2009-01-0310 (2009) (cit. on pp. 50, 51, 160).

[106] R. Martinez-Botas. "Opportunities and challenges. Turbocharger trends and requirements forum". In: *Annex in the proceedings of the 8th International conference on turbochargers and turbocharging, London 15-18 May.* 2006 (cit. on pp. 69, 161, 162, 167, 170).

[107] I. Masanori, I. Nobuyuki, M. Youichi, and K. Toshiijo. "Comparison of Turbocharger Performance Between Steady Flow and Pulsating Flow on Engines". In: *SAE Technical Paper* 940839 (1994) (cit. on pp. 59, 71).

[108] A. Mohammadi, M. Shioji, Y. Nakai, W. Ishikura, and E. Tabo. "Performance and combustion characteristics of a direct injectionSI hydrogen engine". In: *International Journal of Hydrogen Energy* 32.2 (2007), pp. 296 –304. ISSN: 0360-3199. DOI: 10.1016/j.ijhydene.2006.06.005. URL: http://www.sciencedirect.com/science/article/pii/S0360319906002084 (cit. on p. 3).

[109] P. Moraal and I. Kolmanovsky. "Turbocharger modeling for automotive control applications". In: *SAE Technical Paper* 1999-01-0908 (1999) (cit. on p. 50).

[110] P. Moulin, J. Chauvin, and B. Youssef. "Modelling and control of the air system of a turbocharged gasoline engine". In: *Proceedings of the 17th World Congress. The International Federation of Automatic Control, Seoul, Korea, July 6-11.* 2008 (cit. on p. 68).

[111] M. Mrosek and R. Isermann. "On the parametrisation of the turbocharger power and heat transfer models". In: *IFAC AAC 2010, Munich. Germany.* 2010 (cit. on p. 21).

[112] M. Muñoz and F Payri. *Motores de Combustión Interna Alternativos*. ISBN 84 86043 01 9. Madrid: Sección de Publicaciones de la E.T.S. de Ingenieros Industriales Fundación General - U.P.M, 1989 (cit. on pp. 68, 164, 166).

[113] M. Mueller. "Mean value modeling of turbocharged spark ignition engines". MA thesis. DTU, Denmark, 1997 (cit. on pp. 50, 52).

[114] S.H. Nasser and B.B. Playfoot. "A turbocharger selection computer model". In: *SAE Technical Paper* 1999-01-0559 (1999). DOI: 10.4271/1999-01-0559 (cit. on p. 50).

[115] O. Nelles. "Lolimot - local linear model trees for nonlinear dynamic system identification". In: *Automatisierungstechnik* 45 (1997), pp. 163–174 (cit. on p. 33).

[116] S.A. Nelson, Z.S. Filipi, and D.N. Assanis. "The Use of Neural Nets for Matching Fixed or Variable Geometry Compressors With Diesel Engines". In: *Journal of Engineering for Gas Turbines and Power* 125.2 (2003), pp. 572–579. DOI: 10.1115/1.1563239. URL: http://link.aip.org/link/?GTP/125/572/1 (cit. on p. 54).

[117] S.A. Nelson, Z.S. Filipi, and D.N. Assanis. "The use of neural networks for matching compressors with diesel engines". In: *Spring Technical Conference, volum ICE-26-3, pages 35-42*. 1996 (cit. on pp. 50, 54).

[118] B. Nikpour. "Measurement of the performance of a radial inflow turbine". PhD thesis. Manchester, UK: UMIST, 1990 (cit. on p. 162).

[119] P. Olmeda, V. Dolz, F.J. Arnau, and M.A. Reyes-Belmonte. "Determination of heat flows inside turbochargers by means of a one dimensional lumped model". In: *Mathematical and Computer Modelling* 57.7-8 (2013), pp. 1847–1852. ISSN: 0895-7177. DOI: 10.1016/j.mcm.2011.11.078. URL: http://www.sciencedirect.com/science/article/pii/S0895717711007631 (cit. on pp. 93, 104, 105, 233).

[120] M. Orkisz and S. Stawarz. "Modeling of turbine engine axial-flow compressor and turbine characteristics". In: *Journal of Propulsion and Power* 16 (2000), pp. 336–339 (cit. on p. 65).

[121] J. Padet. *Convection thermique et massique*. Techniques de l'ingénieur. BE 8206 (cit. on p. 30).

[122] D. Palfreyman and R. Martinez-Botas. "The pulsating flow field in a mixed flow turbocharger turbine:an experimental and computational study". In: *ASME paper* GT2004-53143 (2004) (cit. on pp. 59, 64).

[123] S. Park, S. Yoon, and C. Lee. "Effects of multiple-injection strategies on overall spray behavior, combustion and emissions reduction characteristics of biodiesel fuel". In: *Applied Energy* 88 (2011), pp. 88–98 (cit. on p. 4).

[124] F. Payri. "Predicción de las actuaciones de los grupos de sobrealimentación para motores diesel de automoción". PhD thesis. Universidad Politécnica de Madrid, 1973 (cit. on p. 7).

[125] F. Payri, J. Benajes, J. Galindo, and J.R. Serrano. "Modelling of turbocharged diesel engines in transient operation: Part 2: wave action models for calculating the transient operation in a high speed direct injection engine". In: *Proceedings of the Institution of Mechanical Engineers, Part D: Jour* 216 (2002), pp. 479–493 (cit. on pp. 72, 145).

[126] F Payri, J. Benajes, J. Jullien, and Q. Duan. "Non-steady flow behaviour of a supercharger turbine". In: *Proceedings of the Third EAEC International Conference, pp. 347-351, Strassbourg.* 1991 (cit. on pp. 59, 159).

[127] F. Payri, J. Benajes, and M. Reyes. "Modelling of supercharger turbines in internal-combustion engines". In: *Journal of Mechanical Science* 38.8-9 (1996), pp. 835–869 (cit. on pp. 59, 60, 159, 160, 170).

[128] F. Payri, J. Galindo, J.R. Serrano, and A. Páez. "Experimental and modelling investigation on unsteady effects in compressor and turbines of current and future Diesel engines". In: *Société des Ingénieurs de l'Automobile (SIA).* 2008 (cit. on p. 73).

[129] F. Payri, J. Galindo, J.R. Serrano, and M.A. Reyes-Belmonte. "Experimental methodologies for a comprehensive characterization of automotive turbochargers". In: *13th EAEC European Congress, Valencia, Spain.* 2011 (cit. on p. 94).

[130] F. Payri, E. Reyes, and J. Galindo. "Analysis and modelling of the fluid-dynamic effects in branched exhaust junctions of ICE". In: *International Journal for Gas Turbine and Power: Transactions of the ASME* 123 (2001), pp. 197–203. DOI: 10.1115/1.1339988 (cit. on p. 145).

[131] F. Payri, J.R. Serrano, P. Fajardo, M.A. Reyes-Belmonte, and R. Gonzalo-Belles. "A physically based methodology to extrapolate performance maps of radial turbines". In: *Energy Conversion and Management* 55 (2012), pp. 149–163 (cit. on pp. 166, 233, 234, 260).

[132] F. Payri, J.R. Serrano, P. Olmeda, A. Páez, and F. Vidal. "Experimental methodology to characterize mechanical losses in small turbochargers". In: *Proceedings of ASME Turbo Expo 2010: Power for Land, Sea and Air. Glasgow, UK.* 2010 (cit. on pp. 22, 28, 44, 46, 47).

[133] G. Piñero, L. Vergara, and J.M. Desantes. "Estimation of velocity fluctuation in internal combustion engine exhaust systems through beam forming techniques". In: *Measurement Science and Technology* 11 (2000), pp. 1585–1595 (cit. on pp. 146, 158).

[134] P. Podevin, A. Clenci, and G. Descombes. "Influence of the lubricating oil pressure and temperature on the performance at low speeds of a centrifugal compressor for an automotive engine". In: *Applied Thermal Engineering* 31 (2011), pp. 194–201 (cit. on pp. 45, 46).

[135] P. Podevin, G. Descombes, A. Clenci, and C. Zaharia. "Researches regarding mechanical efficiency evaluation at turbochargers". In: *Proceeding of the International Automotive Congress, Brasov, Romania.* 2004 (cit. on p. 45).

[136] P. Podevin, G. Descombes, V. Hara, A. Clenci, and C. Zaharia. "Performances of turbocharger at low speed 1". In: *12 the EAEC Congress, Belgreade, Serbie.* 2005 (cit. on p. 45).

[137] P. Podevin, Toussaint M., Richard G., and G. Farinole. "Performances of turbocharger at low speed". In: *Proceeding of the SYMKOM02 congress, Lodz, Pologne.* 2002 (cit. on pp. 20, 45).

[138] B.V.V.S.U. Prasad, C.S. Sharma, T.N.C. Anand, and R.V. Ravikrishna. "High swirl-inducing piston bowls in small diesel engines for emission reduction". In: *Applied Energy* 88.7 (2011), pp. 2355 –2367. ISSN: 0306-2619. DOI: 10.1016/j.apenergy.2010.12.068. URL: http://www.sciencedirect.com/science/article/pii/S030626191000588X (cit. on p. 4).

[139] H. Pucher, R. Berndt, and P. et al Grigoriadis. "Erweiterte darstellung und extrapolation von turbolader-Kennfeldern als randbedingung der motorprozess-simulation". In: *FVV Informationstagung Motoren Heft R513, Frankfurt, Germany.* 2001 (cit. on p. 25).

[140] M. Rautenberg, A. Mobarak, and M. Molababic. "Influence of heat transfer between turbine and compressor on the performance of small turbochargers". In: *JSME Paper 83-Tokyo-IGTC-73. International Gas Turbine Congress.* 1983 (cit. on p. 21).

[141] A. Romagnoli and R. Martinez-Botas. "Heat transfer analysis in a turbocharger turbine: An experimental and computational evaluation". In: *Applied Thermal Engineering* 38 (2012), pp. 58–77 (cit. on p. 33).

[142] J1723 SAE Standards. *Supercharger Testing Standard.* Engine Power Test Code Committee. 1995-08-01 (cit. on p. 108).

[143] T. Sanchez, A. Muñoz, and F. Jiménez-Espadafor. *Turbomáquinas Térmicas.* Chapter 11, Section 7.4. ISBN 84-9756-185-6. Editorial Síntesis, 2004 (cit. on pp. 164–166, 173).

[144] S. Schmitt, W. Schmid, G. Hertweck, M. Schlegl, and S. Staudacher. "High-Precision Measurements of Friction Losses in Turbochargers". In: *Aufladetechnische Konferenz 2007, Desden, Germany.* 2007 (cit. on pp. 45, 46).

[145] N. Schorn, V. Smiljanowski, U. Späder, R. Stalman, and H. Kindl. "Turbocharger turbines in engine cycle simulation". In: *13th Supercharging Conference. Dresden, Germany.* (Cit. on p. 43).

[146] J.R. Serrano. "Análisis y modelado de transitorios de carga en MEC turboalimentados". PhD thesis. Universidad Politécnica de Valencia, 1999 (cit. on p. 7).

[147] J.R. Serrano, F. Arnau, P. Fajardo, F. Vidal, and M.A. Reyes-Belmonte. "Contribution to the modeling and understanding of cold pulsating flow influence in the efficiency of small radial turbines for turbochargers". In: *Journal of Engineering for Gas Turbines and Power* Vol 134, Issue 10 (2012), p. 10 (cit. on p. 253).

[148] J.R. Serrano, F.J. Arnau, V. Dolz, A. Tiseira, and C. Cervelló. "A model of turbocharger radial turbines appropriate to be used in zero- and one-dimensional gas dynamics codes for internal combustion engines modelling". In: *Energy Conversion and Management* 49 (2008), pp. 3729–3745 (cit. on pp. 59, 63, 160, 170, 189, 215, 216, 231, 234, 271, 275).

[149] J.R. Serrano, V. Dolz, R. Novella, and A. García. "HD Diesel engine equipped with a bottoming Rankine cycle as a waste heat recovery system. Part 2: Evaluation of alternative solutions". In: *Applied Thermal Engineering* 36.0 (2012), pp. 279 –287. ISSN: 1359-4311. DOI: 10.1016/j.applthermaleng.2011.10.024. URL: http://www.sciencedirect.com/science/article/pii/S135943111100562X (cit. on p. 4).

[150] J.R. Serrano, C. Guardiola, V. Dolz, A. Tiseira, and C. Cervelló. "Experimental study of the turbine inlet gas temperature influence on turbocharger performance". In: *SAE Technical Paper* 2007-01-1559 (2007) (cit. on pp. 23, 24, 27, 30).

[151] J.R. Serrano, P. Olmeda, F.J. Arnau, M.A. Reyes-Belmonte, and A. Lefebvre. "Importance of heat transfer phenomena in small turbochargers for passenger car applications". In: *SAE Int. J. Engines* 6(2) (2013), pp. 716–728. DOI: 10.4271/2013-01-0576 (cit. on p. 218).

[152] J.R. Serrano, P. Olmeda, A. Páez, and F. Vidal. "An Experimental Procedure to Determine Heat Transfer Properties of Turbochargers". In: *Measurement Science and Technology* 21 (2010), 14pp (cit. on pp. 89, 94, 100, 110).

[153] J.R. Serrano, P. Olmeda, A. Tiseira, L.M. García-Cuevas, and A. Lefebvre. "Importance of mechanical losses modeling in the performance prediction of radial turbochargers under pulsating flow conditions". In: *SAE Int. J. Engines 6(2)* 6(2) (2013), pp. 729–738. DOI: 10.4271/2013-01-0577 (cit. on pp. 8, 46, 48, 49, 93, 132, 157, 189, 216, 217, 255).

[154] J.R. Serrano, P. Olmeda, A. Tiseira, L.M. García-Cuevas, and A. Lefebvre. "Theoretical and experimental study of mechanical losses in automotive turbochargers". In: *Energy* 55 (2013), pp. 888 –898 (cit. on pp. 8, 46, 48, 49, 93, 132, 157, 189, 216, 217, 223, 233, 255, 271).

[155] J.R. Serrano, B. Pla, D. Ospina, and R. Gozalbo. "Estimation of the Extended Turbine Maps for a Radial Inflow Turbine". In: *SAE Technical Paper* 2010-01-1234 (2010) (cit. on pp. 59, 68).

[156] S. Shaaban. "Experimental investigation and extended simulation of turbocharger non-adiabatic performance". PhD thesis. University of Hannover, Germany, 2004 (cit. on pp. 21, 30).

[157] S. Shaaban and J. Seume. "Analysis of turbocharger non-adiabatic performance". In: *Turbochargers and Turbocharging, Inst Mech Engineers* (2006), pp. 119–130 (cit. on pp. 21, 26, 27, 30).

[158] S. Shaaban and J. Seume. "Impact of Turbocharger Non-Adiabatic Operation on Engine Volumetric Efficiency and Turbo Lag". In: *International Journal of Rotating Machinery* 2012 (2012) (cit. on pp. 24, 35).

[159] S. Shaaban, J. Seume, R. Berndt, H. Pucher, and H.J. Linnhoff. "Part-load performance prediction of turbocharged engines". In: *C647/019. Proceedings of 8th International Conference on Turbochargers and Turbocharging. Woodhead Publishing and CRC Press LLC. London.* 2006 (cit. on pp. 20, 89).

[160] P.N. Shah and C.S. Tan. "Effect of blade passage surface heat extraction on axial compressor performance". In: *Transactions-American Society of Mechanical Engineers Journal of Turbomachinery* 129.3 (2007), p. 457 (cit. on p. 21).

[161] S.M. Shahed. "Gasoline engine downsizing and boosting for CO2 emission reduction, California Air Resource Board, Climate Change". In: *International Vehicle Technology Symposium, Sacramento CA.* 2003 (cit. on p. 4).

[162] A. Sidorow, R. Isermann, F. Cianflone, and G. Landsmann. "Comparison of a turbocharger model based on isentropic efficiency maps with a parametric approach based on Euler's turbo-machinery equation". In: *18th IFAC World Congress. Milano (Italy) August 28 - September 2,* 2011 (cit. on pp. 30, 31).

[163] A. Sidorow, R. Isermann, F. Cianflone, and G. Landsmann. "Model based fault detection of the air and exhaust path of diesel engine including turbocharger models". In: *SAE 2011 World Congress, Detroit.* 2011 (cit. on pp. 30, 33).

[164] G. Sieros, A. Stamatis, and K. Mathioudakis. "Jet engine component maps for performance modeling and diagnosis". In: *Journal of Propulsion and Power* 13 (1997), pp. 665–674 (cit. on p. 65).

[165] P. Soltic. "Part-Load Optimized Si Engine Systems". PhD thesis. Swiss Federal Institute of Technology, Zürich, 2000 (cit. on p. 20).

[166] S. Sorenson, E. Hendricks, S. Magnusson, and A. Bertelsen. "Compact and accurate turbocharger modelling for engine control". In: *Electroni Engine Controls 2005 (SP-1975), SAE Technical Paper* 2005-01-1942 (2005) (cit. on p. 52).

[167] S. Szymko. "The development of an eddy current dynamometer for evaluation of steady and pulsating turbocharger turbine performance". PhD thesis. Imperial College, London, UK, 2006 (cit. on p. 162).

[168] M. Tancrez, J. Galindo, C. Guardiola, P. Fajardo, and O. Varnier. "Turbine adapted maps for turbocharger engine matching". In: *Experimental Thermal and Fluid Science* 35.1 (2011), pp. 146 –153. ISSN: 0894-1777. DOI: 10.1016/j.expthermflusci.2010.07.018. URL: http://www.sciencedirect.com/science/article/pii/S0894177710001755 (cit. on p. 59).

[169] A. Tiseira. "Caracterización Experimental y Modelado de Bombeo en Compresores Centrífugos de Sobrealimentación". PhD thesis. Departamento de Máquinas y Motores Térmicos - UPV, 2008 (cit. on p. 7).

[170] A. Torregrosa, F.J. Arnau, P. Piqueras, and M.A. Reyes-Belmonte. "Acoustic One-Dimensional Compressor Model for Integration in a Gas-Dynamic Code". In: *SAE Technical Paper* 2012-01-0834 (2012) (cit. on pp. 145, 149).

[171] A. Torregrosa, A. Broatch, P. Olmeda, and J. Martín. "A Contribution to Film Coefficient Estimation in Piston Cooling Galleries". In: *Experimental Thermal and Fluid Science* 34 (2010), pp. 142–151 (cit. on pp. 94, 95).

[172] A. Torregrosa, J. Galindo, J.R. Serrano, and A. Tiseira. "A procedure for the unsteady characterization of turbochargers in reciprocating internal combustion engines". In: *The 4th International Symposium on Fluid Machinery and Fluid Engineering, November 24-27, 2008, Beijing, China*. 2008 (cit. on pp. 55, 56, 72, 149, 274).

[173] A. Torregrosa, P. Olmeda, J. Martín, and C. Romero. "A Tool for Predicting the Thermal Performance of a Diesel Engine". In: *Heat Transfer Engineering* 32 (2011), pp. 891–904 (cit. on p. 87).

[174] A. Torregrosa, J.R. Serrano, F.J. Arnau, and P. Piqueras. "A fluid dynamic model for unsteady compressible flow in wall-flow diesel particulate filters". In: *Energy* 36.1 (2011), pp. 671 –684. ISSN: 0360-5442. DOI: 10.1016/j.energy.2010.09.047. URL: http://www.sciencedirect.com/science/article/pii/S0360544210005268 (cit. on p. 4).

[175] *Turbocharger Gas Stand Test Code (J1826)*. SAE International Surface Vehicle Recommended Practice, 1995-03-01 (cit. on p. 146).

[176] O. Varnier. "Trends and Limits of Two-Stage Boosting Systems for Automotive Diesel Engines". PhD thesis. Universidad Politecnica de Valencia, 2012 (cit. on pp. 7, 60).

[177] T. Verstraete, Z. Alsalihi, and R.A. Van den Braembussche. "Numerical study of the heat transfer in micro gas turbines". In: *Journal of Turbomachinery* 129 (2007), pp. 835–41 (cit. on pp. 21, 36–38).

[178] F. Vidal, A. Yammine, P. Chesse, A. Lefebvre, S. Guilain, and H. et al. Tartousi. "Diams: advanced diagnostics and modelling for turbocharging". In: *Conference internationale : Motorisations Diesel, face au defi de la competitivite. Rouen - INSA*. 2010 (cit. on p. 46).

[179] F.J. Wallace and G.P. Blair. "The pulsating-flow performance of inward radial-flow turbines". In: *Proceedings of the ASME Gas Turbine Conference and Products Show* paper 65-GT-21 (1965), pp. 1–19 (cit. on p. 59).

[180] T. Wang, Y. Zhang, J. Zhang, G. Shu, and Z. Peng. "Analysis of recoverable exhaust energy from a light-duty gasoline engine". In: *Applied Thermal Engineering* 0 (2012), pp. 414–419. ISSN: 1359-4311. DOI: 10.1016/j.applthermaleng.2012.03.025. URL: http://www.sciencedirect.com/science/article/pii/S1359431112002098 (cit. on p. 4).

[181] X. Wang, Z. Huang, W. Zhang, O. Kuti, and K. Nishida. "Effects of ultra-high injection pressure and micro-hole nozzle on flame structure and soot formation of impinging diesel spray". In: *Applied Energy* 88 (2011), pp. 1620–1628 (cit. on p. 4).

[182] N. Watson. "Transient performance simulation and analysis of turbocharged Diesel engines". In: *SAE Technical Paper 810338*. 1981. DOI: 10.4271/810338 (cit. on p. 145).

[183] N. Watson and S. Janota. *Turbocharging the internal combustion engine*. London: MacMillan Publishers Ltd, 1982 (cit. on pp. 23, 30, 58, 59, 69, 159, 163, 164, 173–175).

[184] N. Watson and M. Marzouk. "A Non-Linear Digital Simulation of Turbocharged Diesel Engines Under Transient Conditions". In: *SAE Technical Paper* 770123 (1977). DOI: 10.4271/770123 (cit. on p. 145).

[185] H. Wei, T. Zhu, G. Shu, L. Tan, and Y. Wang. "Gasoline engine exhaust gas recirculation - A review". In: *Applied Energy* 99 (2012), pp. 534–544 (cit. on p. 4).

[186] G. Winkler. "Steady state and dynamic modeling of engine turbomachinery systems". PhD thesis. University of Bath, UK, 1977 (cit. on p. 50).

[187] D.E. Winterbone, B. Nikpour, and G.I. Alexander. "Measurement of the performance of a radial inflow turbine in conditional steady and unsteady flow". In: *Proceedings of the 4th international conference on turbocharging and turbochargers. IMechE* C405/015 (1990), pp. 153–62 (cit. on p. 162).

[188] D.E. Winterbone and M. Yoshitomi. "The accuracy of calculating wave action in engine intake manifolds". In: *SAE Technical Paper 900677*. 1990 (cit. on p. 162).

[189] *www.Openwam.org*. OpenWAM, CMT-Motores Térmicos; Universitat Politècnica de València (UPV). 2012 (cit. on pp. 7, 152, 188, 214, 218, 228, 253).

[190] A. Yamagata, S. Nagai, and T: Kawakubo. "Prediction and measurement of turbocharger compressor wheel temperature". In: *Proceedings of 8th International Conference on Turbochargers and Turbocharging. Woodhead Publishing and CRC Press LLC. London.* 2006 (cit. on pp. 28, 29).

[191] W. Yan, Y. Xiaoli, and L. Guodong. "Experimental Measurement and Analysis of Performance of Heat Pipe Heat Exchanger Used in a Turbocharged Engine with Intercooling". In: *Heat Transfer Engineering* 33-14 (2012), pp. 1207–1216. DOI: 10.1080/01457632.2012.677727 (cit. on p. 4).

[192] S. Zahn and R. Isermann. "Crank angle synchronious modelling and real-time simulation of diesel engines for ecu function development and testing". In: *AVEC*. 2008 (cit. on p. 30).

[193] K. Zinner. *Supercharging of Internal Combustion Engines*. ISBN 3 540 085440. Springer-Verlag New York, 1978 (cit. on pp. 68, 164, 168).